Investigation of the microstructural parameters and deformation mechanisms until yield in Ziegler-Natta and Metallocene catalyst-based iPP beyond glass transition

Anne GOLDBERG

A dissertation submitted in fulfilment of the requirements of
the degree of *Docteur en Sciences*

2020 - 2024

Host University

Université de Mons (UMONS) - Laboratoire des Polymères et Matériaux composites

Secondment

Université Libre de Bruxelles (ULB) - Ecole Polytechnique de Bruxelles

Jury

Pr. Roberto Lazzaroni (UMONS - Chairman)

Pr. Philippe Leclere (UMONS - Secretary)

Pr. Jean-Marie Raquez (UMONS - Promoter)

Dr. Olivier Lhost (TotalEnergies - Co-Promoter)

Pr. Pierre Lambert (ULB - Co-Promoter)

Pr. Valérie Gaucher (Université de LILLE)

Pr. Philippe Dubois (UMONS)

Abstract

This thesis deals with the behaviour above glass transition of isotactic polypropylene (iPP) under its α-crystalline form in the linear visco-elastic and in the yield ranges. As iPP is known to undergo changes of its solid state microstructure under the action of time and temperature such as aging, annealing or thermo-oxidation, stabilised conditions have been identified before realising mechanical tests. Tensile quasi-static and DMTA experiments have been carried out with the aim to establish the link between both on the base of the analysis of their underpinning common mechanism, the diffusion of screw dislocations via helical jumps at the interface of the different phases. Six homopolymers produced with two catalytic systems have been analysed. Thanks to the Ree-Eyring model and a thermorheological approach new to the solid state, the equivalence between the levels of activation energies and their temperature range has been demonstrated, and a discussion on the relation with the microstructure carried out, with a proposal for a possible sketch. To our knowledge, it was the first time that the range of longer time and low to very low strain rates was explored in a systematic approach combining both types of tests on this type of material, and that an attempt to understand the physical signification of the activation constant in relation with the microstructure was proposed.

"Zog nit keynmol, az du geyst dem letstn veg - Ne dis jamais que c'est ton dernier chemin",

"La pensée est le dialogue de l'âme avec elle-même",
"Phédon", Platon

"Sans la croyance qu'il est possible de saisir la réalité avec nos constructions théoriques, sans la croyance en l'harmonie interne du monde, il ne pourrait y avoir de science."
"L'évolution des idées en physique", A. Einstein & L. Infeld

Acknowledgments

A toutes les femmes qui, parce que femmes, eurent à souffrir l'arrêt de leur projet,
A tous les hommes et toutes les femmes qui eurent à coeur de les soutenir,
A toutes celles et ceux qui, forts de ce combat, cherchent à mener leur entreprise à terme.

La boucle est bouclée.

Trente-cinq ans entre le début d'une thèse sur les propriétés de transport dans les plasmas collisionnels et sa fin dans le comportement à long terme d'un polymère qui, à ces températures, serait totalement vaporisé et ionisé, entre une licence en physique et un doctorat en chimie...

Trente-cinq ans pour réaliser ce vieux rêve...

Que soient ici remerciés tous celles et ceux qui m'ont aidée, encouragée et accompagnée sur le chemin escarpé et exigeant de la connaissance, celle de la nature qui nous entoure, celle des choses, celle des êtres humains mais aussi celle de soi.

Olivier (Lhost) et Philippe (Dubois), qui les premiers et chacun de leur côté, ont soutenu la timide proposition que je leur faisais et m'ont permis de transformer mon rêve en réalité; Jean-Marie (Ben pour les intimes) qui, cherchant avec moi les accompagnateurs scientifiques les plus légimitimes, m'a accueillie avec bienveillance dans le service SMPC, ainsi que tous les collègues avec lesquels j'ai eu de si nombreuses et enrichissantes discussions: Samira, Sébastien, Jérémy, Nathalie, Noémie, Sylvie, Guillem, Rossi, Olivier, Chiara, Nicolas, Charlotte, Gabriel sans oublier bien sûr Serena avec laquelle j'ai partagé tant de réflexions profondes.

Valérie et Pierre, mes accompagnateurs scientifiques, sans oublier non plus les collègues du service TIPS de l'ULB; Hervé, sans lequel je n'aurais pas pu réaliser mes essais de traction, ni Adam, sans lequel je n'aurais jamais pu traiter l'immense masse de données qu'ils ont suscitée, Charlotte, Thomas, Robin, Jonas, Jean sans oublier bien entendu Bernardo qui m'a très aimablement confié une des clés de son royaume.

Merci aussi aux membres de mon jury que je n'ai pas encore cités, Roberto qui m'a permis de prendre pied à l'université au travers de mes deux modules de cours - franchement, l'innovation, passe encore; mais quel risque de confier à une physicienne un cours pour chimistes sur l'histoire de la pensée scientifique! - , Philippe (Leclere) pour sa disponibilité à parler de ses équipements mais aussi pour ses encouragements.

Que ceux que je ne mentionne pas ici me pardonnent, vous étiez si nombreux!

A ma mère, si inquiète de mon activité intense, avec laquelle je me nourris de tant de nos échanges,
A mon père, qui, là où il est, contemple, je l'espère, sa fille, avec fierté et tendresse.

Et puis, je ne saurais passer sous silence l'attention affectueuse et constante de ma petite tribu.
A Marine et Nicolas, qui, lors d'un moment de désarroi, ont cru en mon projet.
A Luc, pour son soutien indéfectible et son infinie patience devant les visites culturelles différées, la table de la salle à manger transformée en salle de rédaction, et la manne débordant de linge propre posée dans le couloir telle une offrande aux mânes du ménage.

A la mémoire de mes ancêtres disparus que je ne connaîtrai jamais.

Table of contents

Preamble

Material science is a fabulous field of research.

Materials have been the companion of humankind since its very origin. The names of the prehistoric and historic periods bear testimony to this: paleolithic, mesolithic, neolithic for the stone, bronze age, iron age for ores and metals when these have been discovered four thousands years before the common era, without obviously forgetting clay. The mastery of the goldsmiths of antiquity revealed extraordinary skills and know-how, as did glass and metallurgy in the broadest sense.

Who has not been fascinated by the red glow of metal, by the incredible slabs of steel transported within factories and rolling mills, and by the human adventure of sweat and courage? Who has not been touched by the iridescent rainbow of colours and the swirls of opalescent paste skilfully moulded by the craftsman into crystal vases, decorative ornaments or simply table glass?

Synthetic polymers are far more recent and do not display such an external beauty; theirs lies in the realm of the infinitely small, because to remind the words of Ali S. Argon, one of the great scientists of mechanical engineering and fracture mechanics, if one had to describe the architecture of metals as classical, then that of polymers should be qualified as baroque.

One could think that everything has been discovered about polypropylene. It is indeed a very widely used commodity polymer the synthesis technology of which has been invented by Giulio Natta and Karl Ziegler in the '50. Its main applications find themselves in injection moulding, film extrusion, fiber production or thermoplastic elastomers [1].

However, the unique nature of polypropylene, especially isotactic polypropylene, makes it one of the most complex materials to understand: the sequence of monomers, the presence of defects or branches along the helical chain result, depending obviously on the thermo-mechanical history and chain remarkable flexibility, in crystalline polymorphism and epitaxy, and in disordered crystals co-existing together. Since the invention of the metallocene catalysis at the end of eighties, new routes have been open, adding still some extra layer of complexity.

Based on previous experience on the long term behaviour of polyethylene, we were curious to explore this material, understand the similarities between both, but also discrepancies.

We have not been disappointed.

Executive summary

This thesis deals with the behaviour of isotactic polypropylene under its α-crystalline form in the linear visco-elastic and in the yield domain, the two opposite limits of the small deformation range. Six homopolymers produced with two catalytic systems have been analysed.

The purpose is to establish the relation between these two limits, to understand the various processes at work and to make the relation with the microstructure that is itself dependent on the catalytic system and on the thermo-mechanical history, highlighting discrepancies and similarities.

More specifically, two aspects have been addressed: the influence of the catalytic system on the yield behaviour measured with quasi-static tensile tests, especially the presence of a double yield and its impact; and the relationship between the visco-elastic relaxations - measured with dynamic mechanical and thermal analysis (DMTA) - and the yield.

The results obtained in the range of the yielding behaviour have been modelled thanks to the Ree-Eyring approach and have shown that a double yielding phenomenon was indeed present, though it could not be ascribed clearly to the well known couple "heterogeneous/homogeneous" mechanism. By contrast, we suggest that it could result from the moreless strong competition between yield and cavitation leading to two mechanisms of heterogeneous yield, likely to be due to the multiphasic composition of the products.

The results obtained in the visco-elastic range have been modelled with a thermorheological approach usually carried out in the melt. This was compulsory because the strong overlap of the viscoelastic curves prevented a relevant exploitation of the time-temperature superposition principle and this type of model was particularly relevant in our case, being very sensitive to any small differences. Three to four mechanisms could be identified and their activation energy was put in relation with the activation energy found in the quasi-static tests, ranging between 100kJ/mol to 200kJ/mol. The DMTA tests unveiled more activated processes than those measured in quasi-static tests.

The influence of the catalytic system on the activation volume, energy and time constant was analysed from the viewpoint of the underlying diffusion of screw dislocations throughout the interfaces of the different phases, especially thanks to the helical jumps. The same mechanism was also used to explain the behaviour in the viscoelastic range.

Some preliminary structure/properties relationships were presented with respect to the crystalline thickness of lamellae and amorphous phase, to the isotactic length as well as to the yield and the viscoelastic properties. It was found that, comparing two of the three products exhibiting the same mechanism of deformation at yield, the flexibility of the amorphous phase due to the difference of catalyst was critical to explain the differences in the activation volumes, energies and time constants. It was also found that the lower α-transitions of the three products were occurring in a very narrow time-temperature frame, and seemed to correspond to the transition of the rigid amorphous fraction or of the conformationally disordered crystals, around 50°C-60°C. Finally, a proposal gathering the abovementioned considerations was attempted thanks to the sketch of a possible undeformed solid state microstructure for the two catalytic systems considered.

Several Matlab® programs were implemented to handle and analyse the data coming from the quasi-static and dynamic tests.

To our knowledge, it was the first time that the thermorheological approach was applied to the solid state. It was also the first time that a set of isotactic polypropylene products was systematically tested at low to very low strain rates, and that the link and interpretation of the activation constants was discussed in relation with its specific structure and not in general.

Chapter 1 : Introduction

1.1 General introduction

The worlwide production of thermoplastic polymers has evolved in fifty years from 50 millions to around 400.3 millions tonnes in 2022 among which less than 10% is recycled. China is currently the main producer, with one third of the total capacity. European converters demand around 50 million tonnes of plastic where packaging and building & construction account respectively for 40.5% and 20.4% of the market segments. Polyethylene and polypropylene are the biggest players with around 8.9 and 9.9 millions of tonnes of the demand [2].

The figure 1.1 gives the break down of the global polymer production by polymer where it can be seen that polypropylene contributes to around 20% of the total amount [2], [3].

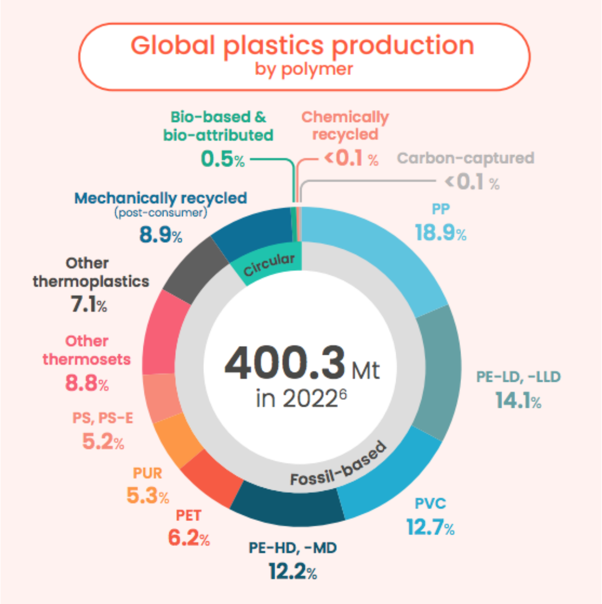

Figure 1.1: Global polymer production by polymer in 2023 [2], [3]

Figures 1.2 shows two types of distribution per region around the world: (a) the bio-based[1] and bio-attributed[2] plastics production and (b) the post-consumer recycled plastics production. In this latter case, it can be observed that the rest of Asia, China and Europe lead the way though the amount of 35.5 millions tonnes recycled is definitely still very low.

---

[1] According to ISO 16620-1, the biomass is the material of biological origin excluding material embedded in geological formations and/or fossilised and a bio-based synthetic polymer is a polymer obtained through chemical and/or biological industrial process(es), wholly or partly from biomass resources.

[2] According to European bioplastics association, due to the complexity of the supply chain, the term "bio-attributed" indicates that the use of renewable feedstock has been ascribed using mass balance approach compared to other methods to evaluate the amount of biogenic feedstock - see https://www.european-bioplastics.org/

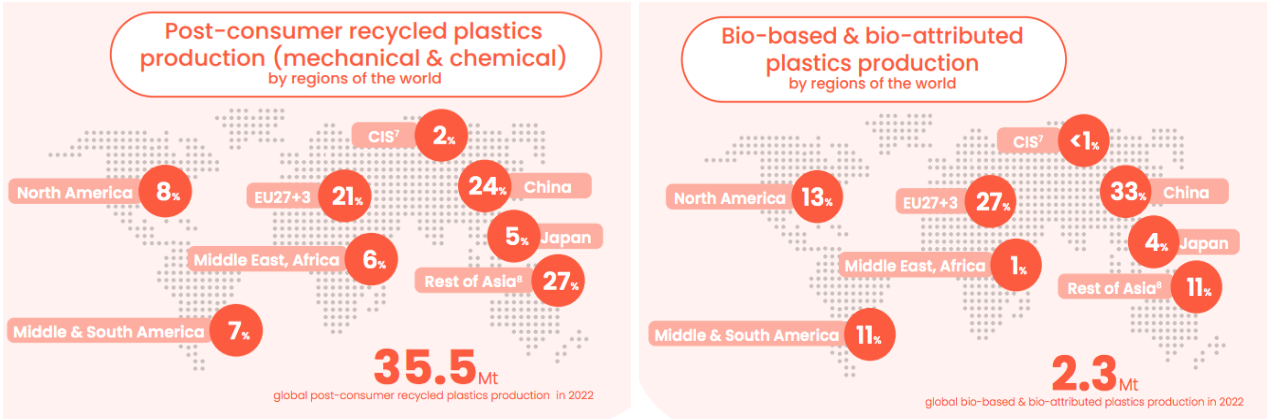

Figure 1.2: Distribution per region across the world of (a) the post-consumer recycled products and (b) the bio-based and bio-attributed plastics [3]

In the specific case of the European rigid packaging market, the figure 1.3 gives an idea of the competition between the various polymers.

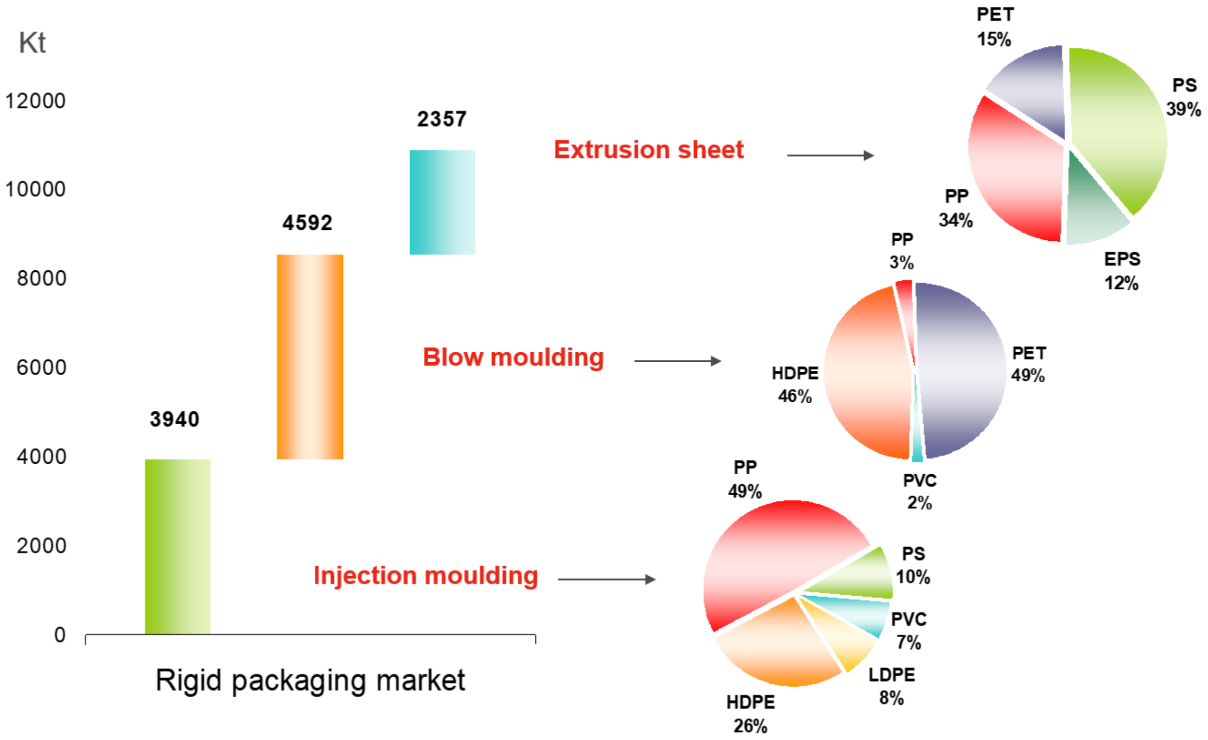

Figure 1.3: Break down of European rigid packaging market on the various polymers (Source: O. Lhost, TotalEnergies, 2018)

Polyethylene and polypropylene are part of the larger polyolefins family. Polypropylene is produced from the monomer propylene which general structure can be written as $CH_2 = CH - CH_3$. Its global market size is evaluated to be around EUR 113.30 billion in 2022 and is expected to expand at a compound annual growth rate (CAGR) of 4.7% from 2023 to 2030. The growth of the market is mainly driven by end-use industries such as automotive, packaging, and building & construction. In these markets, homopolymer is the largest segment and accounts for a market share of over 80% [4], [5]. The main applications find themselves in injection moulding, film extrusion, fiber production or thermoplastic elastomers [1] where the requested properties are in the range of short to mid-term characteristic times.

The table 1.1 summarises which applications supply which market.

Table 1.1: Summary of applications and markets for PP resins (source: O. Lhost, TotalEnergies, 2018)

Application	Markets
Injection	rigid food packaging, caps and closures, garden furniture, syringes, ...
Thermoforming	food packaging, non-food packaging
Blow-moulding	food packaging (multi-layers), detergency, containers
Textile	short fibres, multi-filaments, woven non-woven,..
Bi-oriented PP (BOPP)	monolayer, coextrusion, opaque, metallised: food packaging or not

Like many other semi-crystalline thermoplastics such as polyethylene (PE), polyamide (PA), polyvinylidene fluoride (PVDF) or polylactic acid (PLA), polypropylene (PP) and more especially isotactic polypropylene (iPP)[3] displays a series of domains and structures that are thermodynamically far from equilibrium and this has a strong influence on its main characteristics in the solid state: multi-scale hierarchically organised crystalline structures, sensitivity to ageing and annealing, to thermo- and photo-oxidation, to yielding and cavitation[4], ability to undergo changes of chain conformation and packing under thermal treatment or increasing strains.

A lot of research has investigated the influence of its molecular architecture on its crystallisation in solution or in the melt, namely from the viewpoint of the condensed state, and on the resulting solid state properties. The presence of co-monomers and defects was included in these studies.

The main mechanical properties studied in the literature have been dealing with stiffness and more generally quasi-static properties, impact resistance, brittle-ductile transition or fracture [6], [7], [8], [9], [10], [11], [12], [13], [14]. This has always been consistent with the requested end-use properties such as those mentioned above. The figure 1.4 displays the positionning of the various polypropylene structures in relation with the main requested end-use properties.

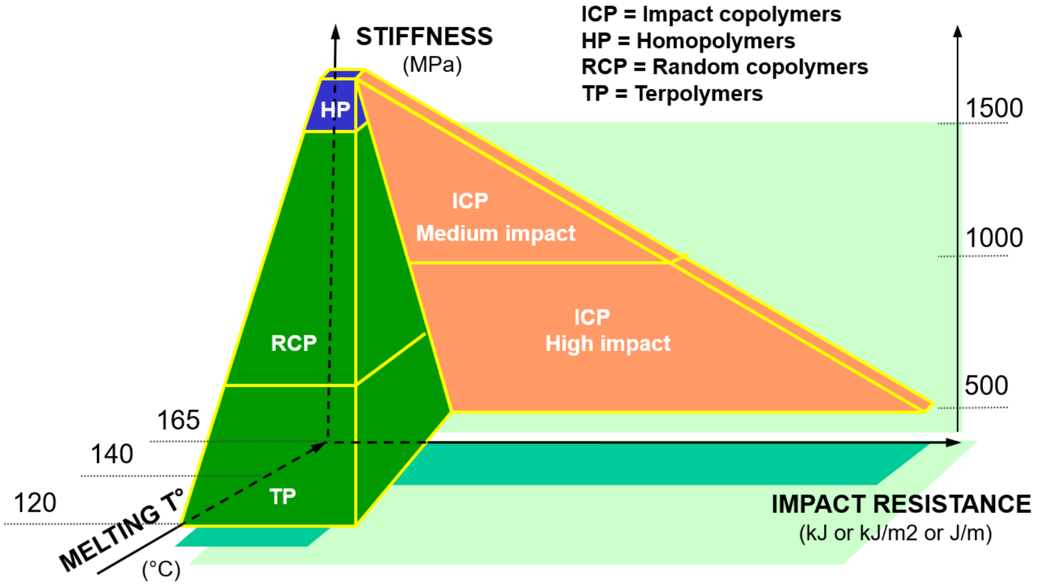

Figure 1.4: The pyramide of PP molecular structures in relation with their end-use properties (Source: reworked from O. Lhost, TotalEnergies, 2018)

Building on experience acquired on HDPE, we have more been interested in exploring the long-term properties of two types of isotactic polypropylene with the hope to better circumvent the behaviour of this material under these characteristic times and therefore open the door to new potential structures and maybe new long-term applications.

---

[3] the tacticity is "The orderliness of the succession of configurational repeating units in the main chain (backbone) of a regular macromolecule [...]" (source: IUPAC Gold Book). The polypropylene is qualified as isotactic when its methyl groups CH_3 are located on the same side of the main chain. See Chapter 2 for detailed explanations about iPP

[4] Cavitation is the tendency of a polymeric material to undergo a large number of small local density fluctuations leading to the creation of micro-voids which, by coalescence, lead to cavities on a meso- to macroscopic scale

By its very nature, material science is at the cross-road of chemistry and physics (without even talking about biological materials), and rely on four scientific domains: material, process, metrology and modelling & simulation at various scales, as illustrated on the figure 1.5 below. These graphs display, from top to bottom and left to right, (a) the path in terms of space and time scales to be followed from the chemical synthesis to the device, from the laboratory to the factory, with a variety of (b) experimental and (c) in silico methods[5].

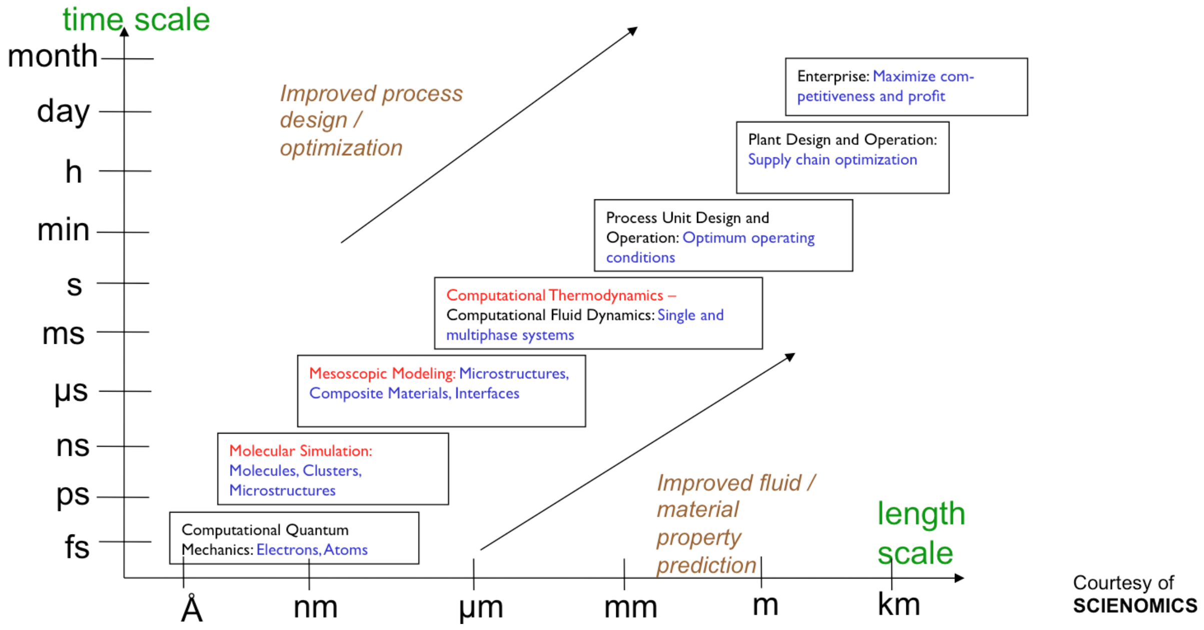

Courtesy of **SCIENOMICS**

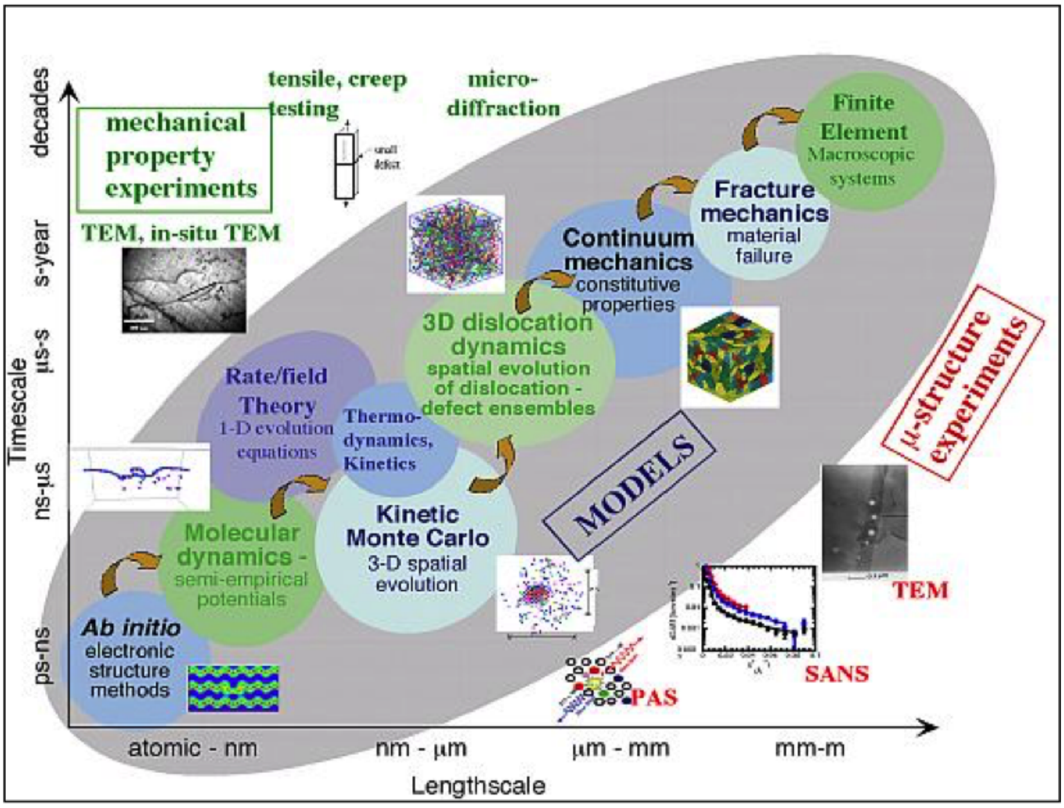

---

[5] As these graphs are presented for pedagogical purposes, their content has not been updated.

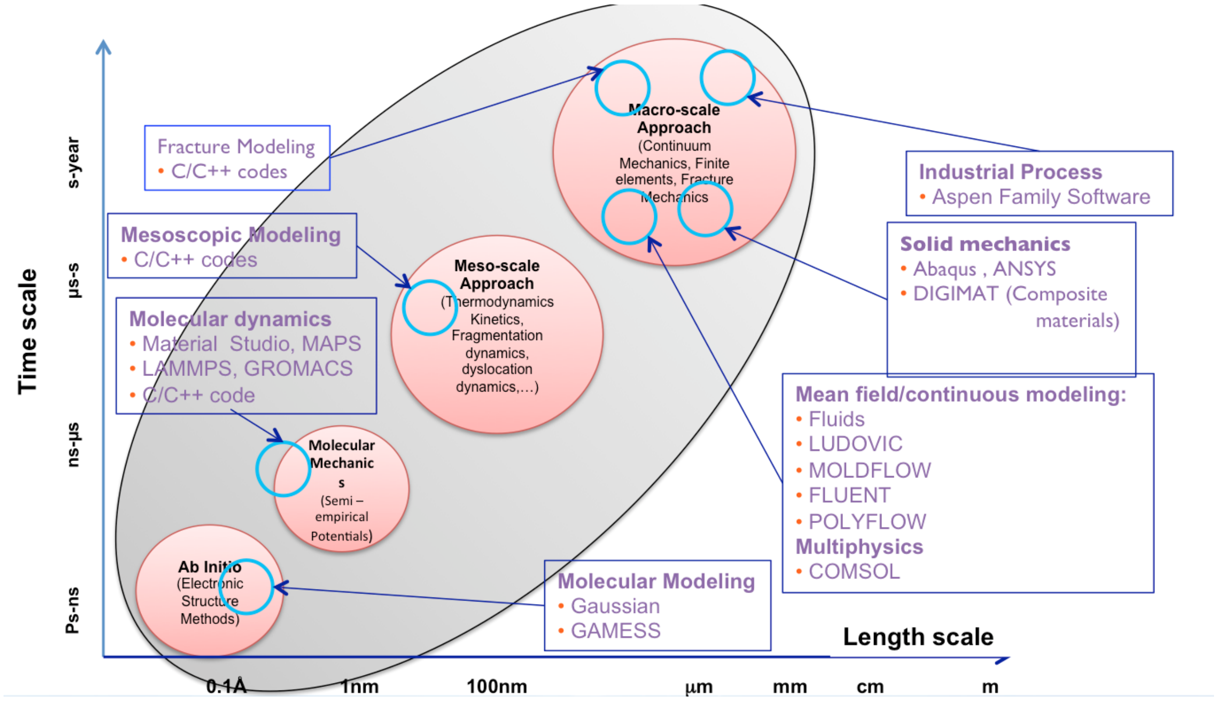

Figure 1.5: Hierarchical multiscale sketch of time and space with related structures, experimental and in silico tools and methods and their link towards down and upper level: (a) time and space scales from design to device and from lab to factory [15], (b) the variety of experimental methods (unknown source), (c) the variety of software [15]

Related to historical and industrial reasons, the literature does not cover the full knowledge chain and tackles scarcely together the influence of the macromolecular structure and of the thermo-mechanical history with the detailed understanding of the solid state microstructure. Despite incredibly huge progresses realised in the realm of modelling & simulation on the last decades, there still lacks a sound understanding of the micro-macro processes at work under deformation, that would be able to feed them appropriately. Researchers recognise this fact [16], [17].

This is thus the red line that we have taken, trying to bring some new systematic aspects and to contribute with our research to bring a small stone to this edifice.

1.2 Scope of this work

The purpose of our research about the isotactic polypropylene under its α-crystalline form is three-folded: first, to demonstrate, in the range of small deformation and low strain rates, the relationship between the visco-elastic and the yielding behaviour; secondly, to establish the relationship between the common underlying microscopic mechanisms at work and the micro-structure and finally to analyse the influence of the chemical synthesis route on both.

In this thesis, we will present the results obtained on two of these aspects: the influence of the catalytic system on the yield behaviour, especially the presence of a double yield and its meaning; and the relationship between both opposite limits of the small deformation range, i.e. the visco-elastic relaxations and the yield.

The work is disclosed into five parts: chapter 2 is a bibliographic study based mainly on polymer solid state behaviour and microstructure, chapter 3 deals with the characterisation of the microstructure in the solid state, chapter 4 deals with the evolution of the yield at low strain rates taking into account the two catalytic systems, chapter 5 deals with the comparison between viscoelastic relaxations and yield for all the products and finally a conclusion as last chapter.

The chapter 2 has been conceived with the red line that a special care should be brought to a pedagogical explanation of scientific fields usually handled separately. It proposes accordingly 1°) a general approach of deformation mechanisms in semi-crystalline polymers undergoing increasing strain, with a focus on the domain of small deformations (physical models, transitions such as glass/rubber or solid/solid, etc); 2°) a reminder of visco-elasticity and its link with time-temperature superposition, 3°) an overview of the molecular and solid state microstructure of iPP and 4°) a special case of environmental and chemical ageing, the thermo-oxidation.

The chapter 3 presents the six homopolymers that we have used for our research together with a set of results coming from the characterisation of the solid state microstructure. Two campaigns have been carried out on the materials, a first one tackling one chemical structure and three thermo-mechanical histories; a second one carried out on one thermo-mechanical history and tackling the influence of six different molecular architectures. The adequate balance between aging, annealing and degradation has been explored and stabilisation conditions found in order to mitigate degradation before and during mechanical tests.

The chapter 4 deals with the presence of two yielding processes occurring at longer term in mechanical tests and the influence on these mechanisms of the respective molecular architectures in relation with their catalytic system. The semi-empirical well known Ree-Eyring theory of plastic flow has been applied to three molecular architectures, two Ziegler-Natta and one metallocene homopolymers. This has allowed to determine the process constants for each product. To our knowledge, it is the first time that a detailed explanation is provided for isotactic polypropylene on the quality of the activation constants in relation with both the chemical structure and the thermo-mechanical history of the considered materials.

The chapter 5 deals with the influence of thermo-mechanical history and molecular structure on the visco-elastic behaviour above T_g at low to very low frequencies. The challenge was to identify the number and location in time and temperature of the relaxations, and where the transitions were occurring, as the viscoleastic curves were displaying substantial overlapping between each other, which has put at stake the application of the time-temperature superposition principle. A thermorheological approach, usually carried out in the melt, has been used because sensitive to small variations. An explanation about the different structural phases has been proposed: three to four mechanisms were identified, among which it was assumed that those occurring at lower temperature were related to the fragmentation of the lamellae, i.e. to the heterogeneous crystal slipping mechanism. This explanation was taking benefit of the assumption that the diffusion of screw dislocations at the interface between the different phases is the critical underpinning mechanism supporting the similarity between the visco-elastic and yielding behaviour.

Finally, in the conclusion, we review the physical interpretations of the various mechanisms occurring at the interface of the rigid amorphous fraction with crystalline phase on the one side and with the amorphous phase on the other. We sketch a few general structure/properties relationships dealing with the thicknesses of lamellae and amorphous phase, leaving a more detailed investigation of the role of stress transmitters and regio- and stereo-defects so characteristic of this polymer to a later study.

We would like to draw the attention of the reader that there could be some redundancies between the state-of-the-art of chapter 2 and the small literature review of chapters 3 to 5 as these are currently in the process of being transformed into articles to be submitted.

Chapter 2 : Polymer solid state behaviour and microstructure: a review

Table of contents

2.1 Introduction

The way this state-of-the-art has been organised corresponds to the scientific strategy that we have adopted to try helping to bridge the gap in scientists' understanding of their material, depending on whether they come from the synthesis world (the "chemists") or the process/end-use properties/design world (the "engineers" or "physicists").

Indeed, semi-crystalline polymers are, as reminded in the introduction, complex systems exhibiting a multi-scale multi-hierarchical structure in the solid state. Very schematically, the main inter-dependent pillars of a polymer-based device are the synthesis of the material, the process, the end-use properties, the design of device performances and the related equipments, all being supported by real and in silico experiments.

The current models used by the designers of devices are embedding the largest manufacturing and knowledge chain possible but they all rely on a correct description of local or long distance phenomena that depend themselves on the material structure at various scales. The general trends are known but the detailed description per material needed by the models is still missing.

The field of structure/properties relationships is thus a quite open field yet.

More precisely, the interface between these two disciplines lies on the understanding of the exact multi-component solid structure of materials far from equilibrium and the link with their microstructure in response to the whole range of deformation, temperature and time, and external environment possible during their utilisation.

The choice of isotactic polypropylene represents an interesting case as under relatively standard processing and end-use conditions, it presents a kaleidoscope of more or less organised and ordered domains coexisting within a solid-state microstructure and which are subjected in different ways to the influence of time, temperature, deformation and physical or chemical ageing; the solid state microstructure depending itself on the molecular architecture in function of catalytic systems used.

From the literature [18], [16], [19], [20] and overall [21], it appeared to us that, in particular, one of these domains within these semi-crystalline polymers plays a critical role in the macroscopic response of the material, i.e. the rigid amorphous fraction (RAF). In isotactic polypropylene, this phase, strongly dependent on the type of defects and therefore on catalyst, is made still more cumbersome because of its presence at the (confined) interface with various types of lamellae, with conformationally disordered crystals and other ordered mesophase. The visco-elastic behaviour of the solid state microstructure is an ideal tool to reveal the influence of the molecular architecture but also to fill in the gap with the end-use properties. In order to establish a relevant bridge between these two scales, it is therefore appealing to us to explore visco-elastic relaxations and their link with the yield point. These two behaviours have in common the underpinning process of nucleation and diffusion of dislocations, where the RAF plays a critical role.

We have applied traditional and systematic approaches from one field to another where they are not really used, and have therefore introduced two novelties: firstly, we have combined the "chemist" and "physicist" approaches by combining molecular architectures carefully selected and a large range of characteristic times, focusing on the longer ones (low to very low frequencies); secondly, we have combined the "rheologist" and "solid state" approaches of molecular relaxations by applying to the solid state a time-temperature superposition method usually dedicated to the very complex relaxation spectra of the molten state.

The state-of-the-art is thus broken down into four parts:

1. a general approach of deformation mechanisms in semi-crystalline polymers, its application to isotactic polypropylene and to the field of small deformations
2. the chemical and solid state structure of isotactic polypropylene and the influence of the two different catalytic systems
3. a specific type of chemical aging: the thermo-oxidation of isotactic polypropylene
4. a conclusion

2.2 General approach of deformation mechanisms in semi-crystalline polymers

Many models have been elaborated in order to describe the deformation mechanisms in high semi-crystalline polymers. Some of them are purely phenomenologic, other ones try to get a more semi-empirical understanding, though failing to involve the whole range of scales spanning the final macroscopic result.

In this section, we will first review what is known as "remarkable points", such as the yield point on a tensile curve and draw the attention to an important vocabulary aspect that concerns the term "failure"; secondly, we will give a broad outline of the mechanisms of deformation with increasing strain and finally, we will review in more details these processes at small deformation, with a focus on the plastic flow.

2.2.1 The tensile curve, remarkable points and deformation mechanisms

In order to bridge micro- and macro scales, it is worth to give first a few characteristics (i.e. remarkable points) of stress-strain curves in relation with the macroscopic event observed, as illustrated at figure 2.6 on a nominal (or engineering) stress-strain curve[6].

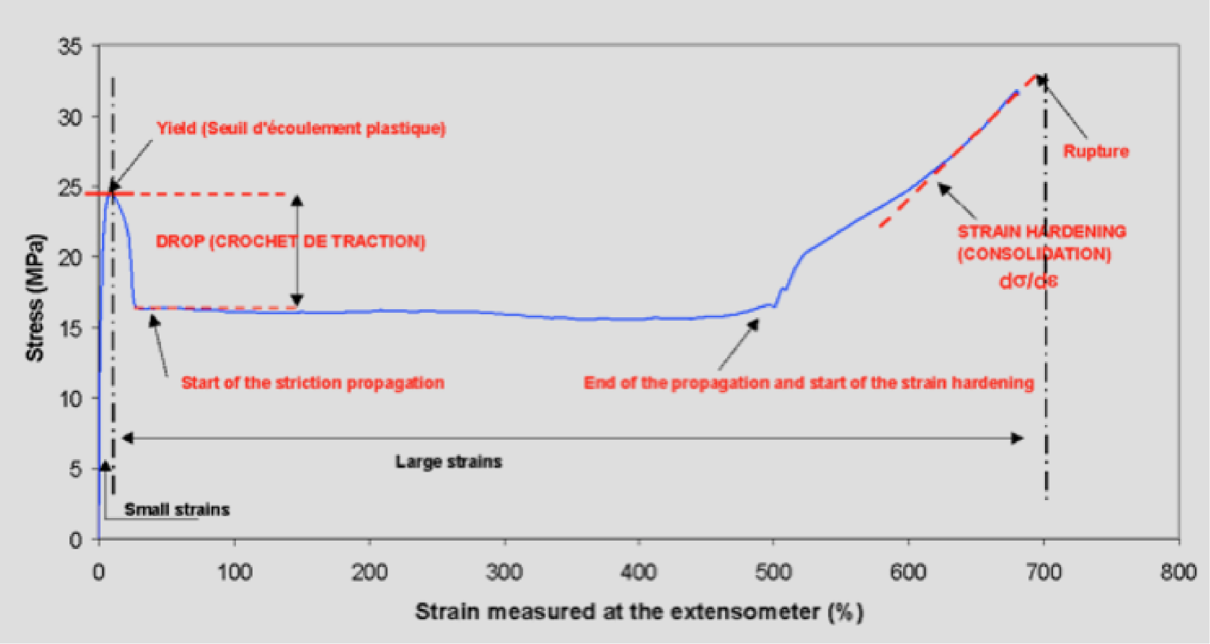

Figure 2.6: Stress-strain curve of HDPE in nominal values [22]

The deformation range up to the local maximum - the yield point - is considered as the range of small deformation. From this remarkable point to the fracture of the sample, the range is the one of the large deformations. The drop height and width are a signature of various events such as neck apparition and structure transformation. The material is said to have a viscoplastic or viscoelastoplastic behaviour, which is mainly an irreversible state. In this stage, and after the plateau corresponding to the propagation of the neck, the material can undergo strain hardening, as illustrated at figure 2.6, strain softening or break. The range of large deformations is characterised by two sets of quantities: the strain hardening coefficient (when existing), i.e. the local slope of the stress-strain curve and the stress and strain at break (Source: internal glossary on tensile quasi-static properties, Solvay, Ezio Gandin, Sandrine Hellinckx, Anne Goldberg).

Another way to represent the behaviour of a semi-crystalline polymer under increasing strain is to draw its true stress-true strain curve as illustrated at figure 2.7. True strain is used mainly when investigating and modeling material at large strains[7].

The true stress-true strain curve is obtained by assuming that the volume of the deformed section is conserved and that strain is uniform. Under these hypothesis, it is possible to write

$$\epsilon_{true} = \ln(1+\epsilon) \tag{2.1}$$

and

$$\sigma_{true} = \sigma(1+\epsilon) \tag{2.2}$$

---

[6] unless specified when tackling the stress-strain curve, ϵ and σ are the nominal values

[7] another quantity, the Hencky strain, is also found in the literature and gives similar information.

The remarkable points σ_y, ϵ_y and ϵ_h correspond to the yield stress, yield strain, and strain at onset of hardening, respectively. The two first quantities are obtained by searching the extrema thanks to the first derivative of the (ϵ, σ) curve.

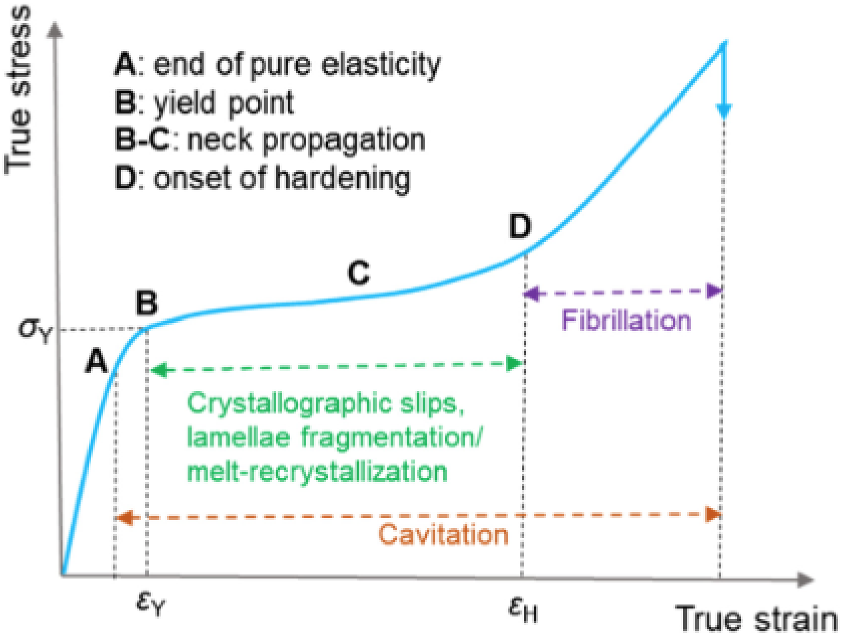

Figure 2.7: A typical true stress-strain curve of a semi-crystalline polymer [17]

There is no unified theory describing the behaviour of a polymer, its damaging and its ultimate failure by rupture of the C-C covalent bonds. A lot of various models exist that take various perspectives depending on the time, temperature and deformation considered. Just to mention a few, brittle-ductile transition, slow crack growth, strain hardening, activated fracture processes, etc. It is out of the scope of this literature review to address this topic. Let us just mention that usually, the macroscopic stress and strain at yield and break have always been considered as independent variables, the evolution with time or temperature of which is different and eventually competing together. They have also been considered as provider of interesting failure criteria. This results in a situation where the failure criteria, the damaging and the behaviour laws are not integrated and the choice of the failure criteria remains somehow arbitrary [23], [24], [25], [26].

We would like to finish this very short introduction to the tensile curve by drawing the attention to an important point: the very term ***failure*** itself can encompass in this context various situations and have different meanings if it is used at the macroscopic or the microscopic level: the *ultimate* failure refers clearly to the massive though nanoscopic rupture of the material covalent bonds whereas the macroscopic "*ductile*" failure refers to a moment where a more or less complex part is no more usable because it has locally crossed the yield and shifted to irreversible plastic deformations. The meaning of the word "failure" will thus be clarified later in this text by the context in which it is introduced [27], [24], [25], [26].

2.2.2 Structural approaches of relaxation and deformation mechanisms in semi-crystalline polymers

In this section, we will review the deformation mechanisms occurring under increasing strains up to the break of the material. Let us illustrate the mechanisms triggered all along the true stress-strain curve with their microstructural evolutions.

The whole deformation process consists of several stages with different micro-mechanisms involved at each stage. Generally speaking, the plastic deformation initiates at yield point (point B of figure 2.7) where the crystal lamellae experience crystallographic events like slips and interlamellar shear (or accompanied by partial melting recrystallisation), then the crystallites fragmented into lamellae blocks connected by oriented amorphous chains with the strain increasing (point B to C). Finally, at large strain (beyond point D), the lamellar crystals change into fibrillar crystals, allowing a significant hardening effect if chain disentanglement is not involved. In tensile deformation mode, the polymer may also cavitate during the whole stretching process. All in all, the critical deformation mechanisms may depend on a set of variables and factors linked to the material microstructure and test conditions, and follow irreversible or reversible paths, leading to changes in conformations or packing, when the stress is released. We summarize these aspects hereunder thanks to a model named "interpenetrated network" that will be explained later.

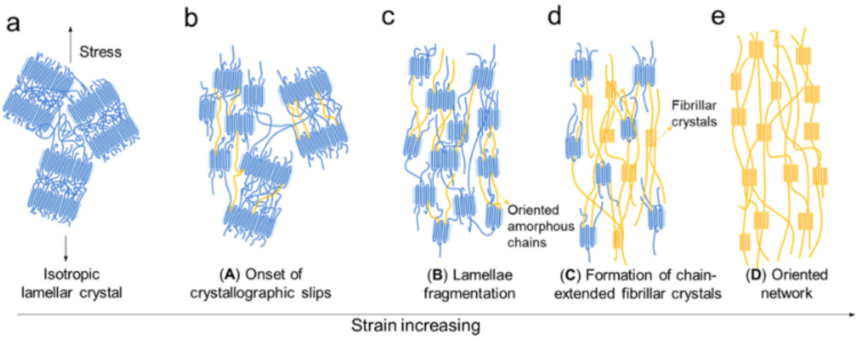

Figure 2.8: Characteristic deformation mechanisms of an interpenetrating model (see text for explanations on the various steps, with a special focus on the step (b)) [17]

The various existing models describing the microscopic deformation mechanisms are each based on different physical principles. The figure 2.8 describes one possible evolution of characteristic deformation mechanisms proposed at different critical strains in a model called the interpenetrated model or IPN (see infra). The deformation of isotropic lamellar crystals (see figure 2.8(a)) goes through four stages: (b) onset of individual crystallographic slips[8]; (c) collective activity of crystallographic slip and interlamellar shear leading to lamellae fragmentation; (d) formation of fibrillar crystals; (e) formation of a highly oriented network connected by fibrillar crystals. The critical strain points A–D correspond to different deformation stages marked in figure 2.7.

2.2.2.1 Deformation models

Here, we would like to take benefit from an excellent review published very recently by Xu et al [17] that presents a comprehensive overview of strain-driven structural evolutions from small to large deformations.

The objective of this paper is to get "*a comprehensive multi-scale vision regarding the structural changes involved during the whole deformation process from the beginning of plasticity to ultimate failure. Besides, how the strain-induced structural changes control over various physical properties and functions of crystallised polymer materials in practical applications has been rarely mentioned. We in this review summarize not only the classical deformation schemes but also the latest progresses on the multiscale and multi-stage structural evolutions covering each stage of deformation, particularly in terms of the crystal phase transitions, crystal morphology changes and damage mechanism.*"

Among many, four important models allow describing the molecular micro-mechanisms involved in multi-stage deformation process: 1°) crystallographic slipping, 2°) melting-crystallisation, 3°) micronecking and 4°) interpenetrated networks. These various models are based on different physical principles and do not always address the same deformation ranges.

One has also to bear in mind that the entire deformation process can involve several mechanisms, depending on the polymer, the initial microstructure and the testing conditions.

2.2.2.2 Crystallographic slipping models

Theoretical aspects: dislocations in crystals

The concept of dislocation comes from the metallurgy and the mineral crystals. According to Wikipedia ([28]-[29]) *"In materials science, a dislocation is a linear crystallographic defect or irregularity within a crystal structure that contains an abrupt change in the arrangement of atoms"*. It defines the boundary between slipped and unslipped regions and as a result, must either form a complete loop, intersect other dislocations or defects, or extend to the edges of the crystal. After the dislocation has exited the crystal, its order is restored but the atoms have moved from one position. When the crystalline order is not totally restored, the dislocation is named "partial".

There are two types of dislocation, edge dislocation and screw dislocation, as illustrated at figure 2.9 where have been represented (a) on the left hand side, an edge dislocation and (b) on the right hand side a screw

---

[8] Regarding the drawing itself, the authors have already included some lamellae fragmentation

dislocation. On this latter drawing, especially in the case of screw dislocation, the vector $\vec{DA}$ is located in the unslipped part and the vector $\vec{BC}$ in the slipped one. The dislocation thus created is defined by the geometric position of the dislocation line L and the force required to move the two lips of the discontinuity relative to each other [30].

The Burgers vector, named after the name of the Dutch physicist Jan Burgers, is defined as the vector required to complete an initially closed loop $ABCD$ in the perfect crystal (see figure 2.9 top), which is opened when it encircles the dislocation line (see figure 2.9 bottom). This vector is written **b** or $\vec{b}$ and represents the magnitude and direction of the crystal lattice deformation due to the dislocation. It is displayed in dark brown on figure 2.9. In the case of edge dislocation, $\vec{b}$ is normal to the dislocation line $\vec{L}$ (or dislocation line unit **u**) whereas in the case of the screw dislocation, $\vec{b}$ is parallel to $\vec{L}$.

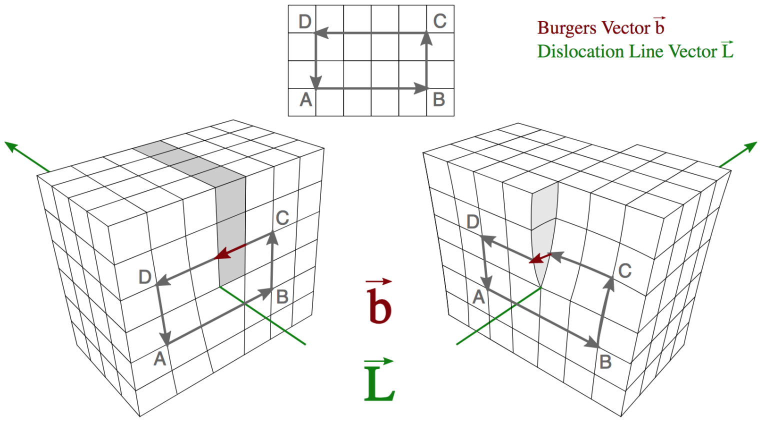

Figure 2.9: Top: closed loop $ABCD$ and bottom: dislocations of edge (left) and screw (right) type; the Burgers vector **b** (in brown/dark red) is (left) normal and (right) parallel to the dislocation line **L**; the crystallographic planes of the edge and screw dislocations are respectively parallel and perpendicular to their dislocation line $\vec{L}$ [31], [32]

From a physical viewpoint, the Burgers vector **b** describes the magnitude of the deformation carried by a dislocation. In mathematical terms, the Burgers vector is the integral of the displacement on the closed loop $ABCD$ embracing the dislocation line unit and it can be written as [30]:

$$\vec{b} = \int_{ABCD} d\vec{u} \tag{2.3}$$

Dislocations in polymers

As semi-crystalline polymers present various crystalline forms, an extension of dislocation theory from the metallurgy world to the polymer one was thus a quite natural way to tackle the problem of their viscosity and plasticity. We give hereunder some of its very basic elements. The number and configuration of the dislocations influence many properties of the solid material, especially its plastic flow.

Usually, dislocations in semi-crystalline polymers, are screw dislocations. Figure 2.10([9]) illustrates the phenomenon.

Regarding the microstructural aspects, and as can be see at figure 2.11, the slips in macromolecular crystals can be either (left) longitudinal along the chain axis (chain slip) or (right) transversal along the perpendicular direction (in the same plane) [17].

---

[9] In semi-crystalline polymers, the crystalline lamellae is said to be made of folded chains, or according to the IUPAC gold book "A polymer crystal consisting predominantly of chains that traverse the crystal repeatedly by folding as they emerge at its external surfaces. The re-entry of the chain into the crystal is assumed to be adjacent or near-adjacent within the lattice". See also section 2.3.3.1 for more details.

Figure 2.10: Remarkable electron micrograph of a stack of chain folded single crystals of PE that have all nucleated from a central screw dislocation site; the picture has been taken from a presentation by [33] that did not unfortunately mention any scale

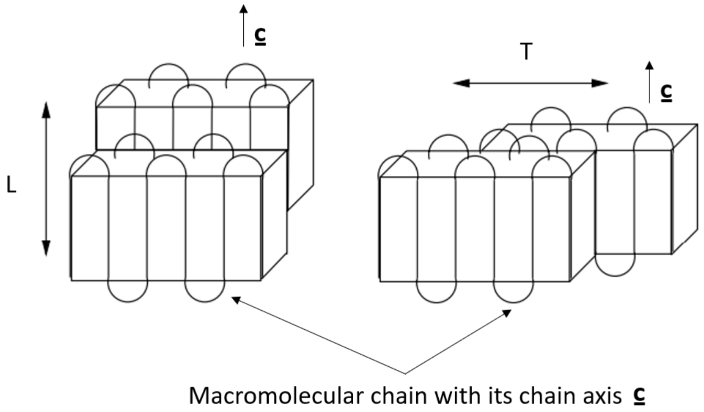

Figure 2.11: Longitudinal (L) and transverse (T) slip in crystalline lamellae; $\underline{c}$ is the chain axis [34]

Figure 2.12 illustrates the three main modes of slip propagation: fine, coarse and interlamellar slip (or shear). The two first occur in the crystal whereas the third one involves the amorphous layer between two lamellae.

The fine slip is an homogeneous slip process that causes the main axis of the chains **c** to tilt relative to the surface normal **n**. In other word, and as illustrated at figure 2.12(a), an angle appears between the normal direction to the crystal surface **n** and the chain axis **c**. The tilting of the chains in the crystallite is progressive and results eventually in the gradual thinning of the crystal lamellae.

The coarse slip is an heterogeneous shear process where the crystal blocks slide one past another without any modification between **n** with respect to **c**. The heterogeneity can be very strong and lead to the fragmentation of the lamellae followed by the formation of fibrillar structures if the strain increases further.

Fine slip seems to be the most common mechanism in semi-crystalline polymers, especially in compression though in tensile tests, fine and coarse slips coexist or compete. This depends on the material defects, the pre-deformation treatments and the experimental conditions.

The slipping process is a very flexible process as it accommodates a lot of deformation modes, making it a very general model. More importantly, it is associated to critical crystallographic events such as the ones described before that are also fundamental molecular processes. A link is thus established via this way between the micro- and the macro-scale that can be used in the deformation models [17].

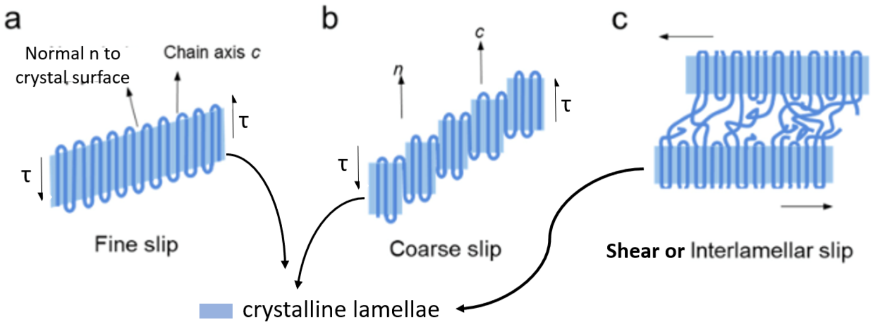

Figure 2.12: Main processes of slip propagation: (a) fine slip; (b) coarse slip; (c) shear or interlamellar slip. **n** and **c** represents the normal to crystal surface and chain axis, respectively [17]

Looking at the application of the dislocation process to the crystalline phase of iPP - also called α-relaxation, see section 2.2.4 for further details - Séguéla proposes a quite comprehensive view based on several articles, such as [35], [36], [37] or [38] so we relay on his analysis to summarise the situation. The migration of mobile localized conformational defects along the chain stem[10] results in the translation of the chain. We detail hereunder the various steps of that mechanism on the base of the isotactic polypropylene example studied by Séguéla [39].

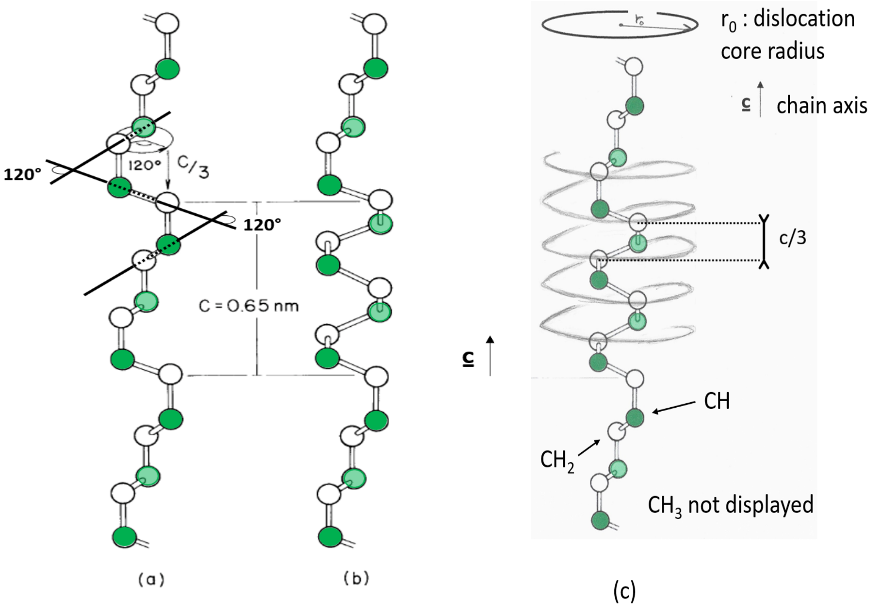

Figure 2.13: Polypropylene chain conformations (CH_3 groups are not displayed, CH_2 groups are in white and CH in green): (a) stable 3/1 helix in $(TG)_3$ conformation; (b) defective helix with a gauche link sequence involving 120° twist and c/3 compressive strain; (c) propagation of the defect along the chain axis (r_0 is the dislocation core radius) [39]

The figure 2.13(a) displays the helix of isotactic polypropylene in its stable $(TG)_3$ conformation[11]. To make the reading easier, the methyl groups CH_3 have not been represented. The CH_2 are in white and the CH in green. Each unit cell is constituted by three monomers along the main chain axis **c** and its value in that direction is $c = 0.65nm$. The bonds $CH_2 - CH$ undergo a torsion of 120° at each pitch the height of which is $c/3$ that brings the methyl groups moreless at the vertices of a triangle.

The figure 2.13(b) displays the case where a conformational defect has been brought within the helix pitch with an additional monomer unit. The chain involves then an extra 120° twist and a c/3 compression of the chain. This latter triggers the thermally activated nucleation and motion of a dislocation along the chain that results

---

[10] A stem is a crystallized, rodlike portion of a polymer chain connected to non-rodlike portions, or chain ends, or both. Source: IUPAC gold book

[11] The isotactic polypropylene structure will be described in details at section 2.3. The conformation we are referring to can be described as: "Conformations referring to torsion angles (A, B, C, D), where A, B, C, D are main-chain atoms, can be described as: cis or synperiplanar (C); gauche or synclinal (G); anticlinal (A); and trans or antiperiplanar (T)", source: IUPAC gold book

in an overall 120° rotation and c/3 translation of the stem. This is illustrated at figure 2.13 where the spirals illustrate the movement of the defect along the dislocation line.

At figure 2.14 it is shown how the sheared region helps to propagate the local compressive strain: a crystalline stem is initiated from one of the fold surfaces of the crystal as a response to the shear stress acting on this crystal (in this case, it was the left surface). Then it propagates along the chain (①) in a worm-like motion and finally exit the crystal at the opposite fold surface (②). The occurrence of such process, successively from stem to stem (③) in a given slip plane results in the generation and propagation of a screw dislocation [39], [40]. The implication from the viewpoint of the viscoelastic α-relaxation is that, below the crystalline relaxation temperature, the defective region is frozen and the conformational defects are likely to remain in the dislocation wake. We will discuss the implications of such situation from the viewpoint of deformation mechanisms linked to the plastic behaviour under that section.

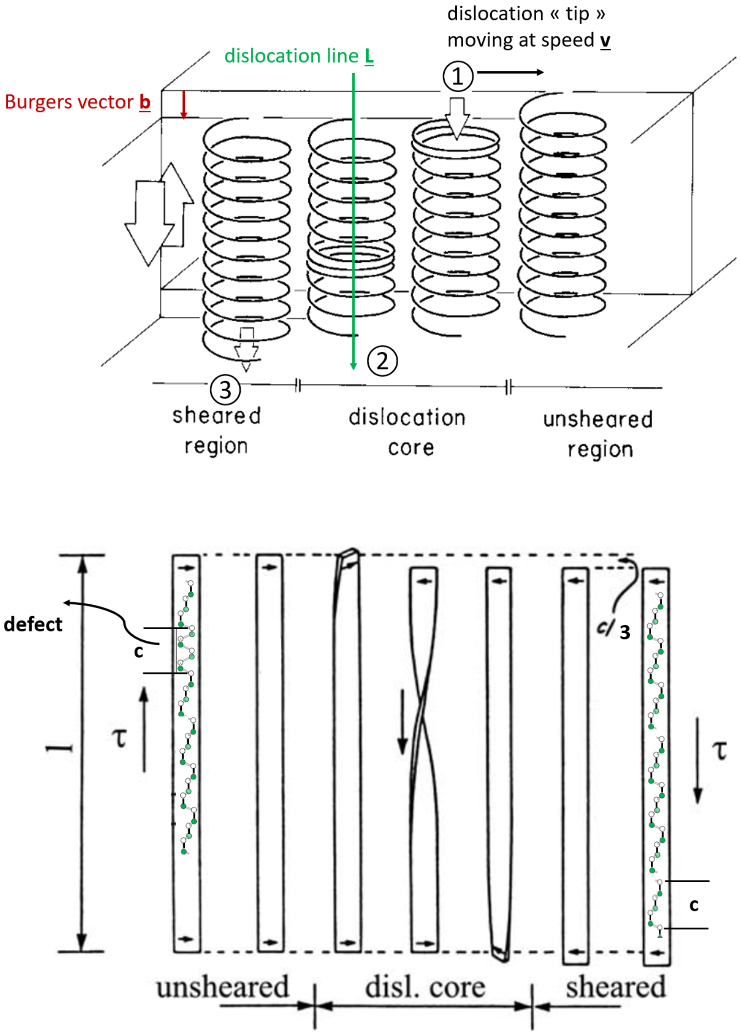

Figure 2.14: (a) Propagation of the compressive strain initiated by the local shear stress along the dislocation line (reworked from [39]); (b) another view of the same phenomenon illustrated with the same defect as figure 2.13(b) (reworked from [40])

2.2.2.3 Melting-recrystallisation model

The particularity of this model is to assume that polymer crystals undergo local strain-induced melting under deformation, resulting in a highly disordered intermediate state comparable to melt. The molten domains then recrystallise immediately forming new crystallites with chain oriented preferably along the stress direction. From a thermodynamic perspective, the propagation of plasticity is driven by locally reduced stress level due to predominant chain orientation. Though various experimental observations support this model, unclarity remains for several aspects, as discussed in the section 2.2.2.6.

Figure 2.15 illustrates such a model.

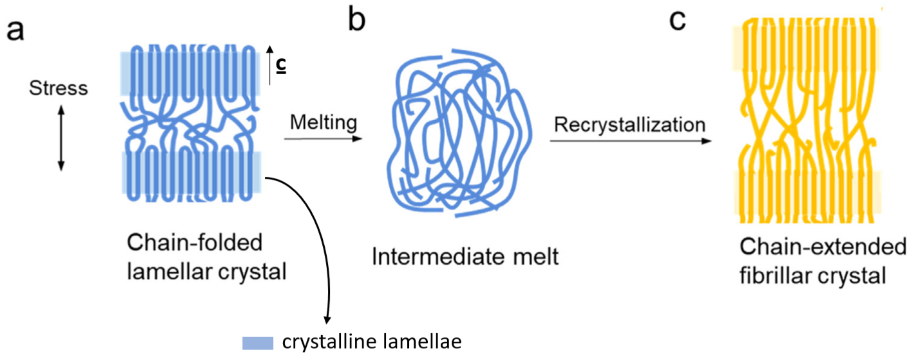

Figure 2.15: Stretching process modeled by melt recrystallisation: (a) original chain-folded lamellar crystal; (b) intermediate melting; (c) recrystallisation into chain-extended fibrillar crystal. The black arrows indicate the increasing strains [17]

2.2.2.4 Micro-necking model

In the micronecking model, Peterlin and coworkers also considered the change of crystal lamellae from a folded morphology into a partially-unfolded fibrillar structure as the global picture of deformation process - see figures 2.16 and 2.17. The key mechanism concerns the formation and propagation of many "micronecks" at the level of the crystalline lamellae and leading to the creation of microfibrils that occur in macroscopic neck of bulk sample and usually tend to concentrate at the boundary of microcracks[12] initiated at small macroscopic strain. The lamellae are first broken via this micronecking mechanism into small blocks that then rotate with the chain axis and align along the drawing direction. Calling for the presence of cracks, the model, applied with success to PE and iPP is somewhat limited.

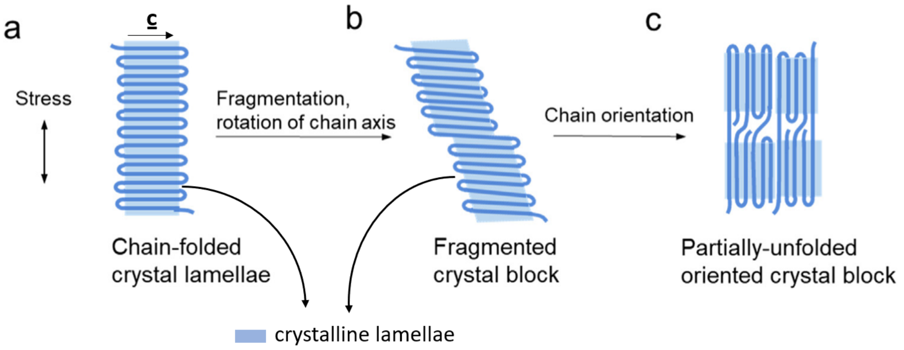

Figure 2.16: Stretching model by micronecking: (a) original chain-folded lamellar crystal; (b) fragmentation into crystal blocks; (c) reorientation into partially-unfolded fibrillar crystal. The arrows indicate increasing strains [17]

An illustration of the micronecking mechanism is also available at section 2.2.2.9, figure 2.27(a).

2.2.2.5 Interpenetrated network model

In the interpenetrated network model (IPN), a polymer system is considered to be built by two interpenetrating networks; one is the "skeleton" network consisting of rigid crystallites and the other one is the fluid, elastic amorphous phase (rubber-like phase above glass transition temperature T_g) as the entangled network. Such a network allows an homogeneous distribution of strain in both phases during deformation. This model was further refined into a two-step process, where the crystal block slipping and the stress induced disaggregation/melting-recrystallisation are the key mechanisms at small and large strains, respectively. Figure 2.8 gives an illustration of the whole deformation processes.

---

[12] the typical scale of microcracks is below the micron

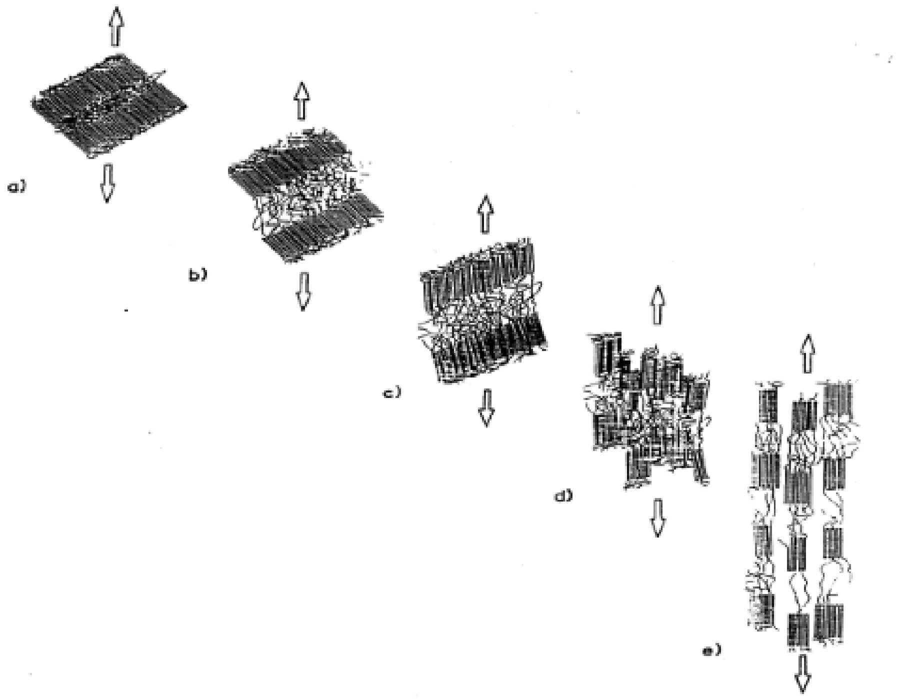

Figure 2.17: Complete solid-solid transformation process as seen by Peterlin [22]

2.2.2.6 A critical review of crystal slip versus melting-recrystallisation models

According to Seguela [41], the plastic behaviour of semi-crystalline polymers has been approached by the relevant concepts of solid state physics dealing with crystallographic slip processes involving thermal activation of dislocations.

The crystal slips leading to plasticity occur necessarily in the crystalline planes containing the chain stems in order to avoid the break of the intrachain bonds. In the Peterlin pioneer model, the original chain-folded lamellar morphology is transformed into a fibrillar structure where the chains are partially unfolded. In this model, plastic yielding is ascribed to the shearing of the crystalline lamellae followed by fragmentation into crystal blocks, as shown in the sketch of figures 2.16 and 2.17. The crystal blocks are further realigned into microfibrils, like strings of pearls with regular spacing between the blocks. However, if crystal slip models are able to account for the occurrence of plastic instability, they are unable to account for transformation such as chain unfolding. In this case, the large reo-organisation of the fold-unfolded chains result in large energy dissipation and likely chain melting. *"Therefore, melting-recrystallisation can be viewed as a corollary of plastic drawing whereas crystallographic slip and lamella fragmentation are its driving force."* [41].

This last aspect is quite worth to be highlighted, as melting-recrystallisation has long competed with dislocation theory, until it was clarified in that publication.

2.2.2.7 Strain-induced phase transition at crystal level

At section 2.3.3 we will describe the various polymorphs of isotactic polypropylene and their possible transformation of one metastable into another more stable under thermal activity. Let us clarify here the type of transformation that can occur due to mechanical deformation. There are two main types of strain-induced polymorphic phase-transition: reversible transitions and irreversible transitions. The former is usually a solid-solid process induced by reversible conformational changes between two crystal phases. The change occurs under the presence of a stress and disappear when the stress is removed.

The irreversible transformation concerns a stable crystal phase that transforms into a metastable state with a higher energy state conformation and interchain packing under strain. The inverse situation can also occur. This phase transition is quite cumbersome as it involves multiple structural evolutions.

Both types are illustrated at figures 2.18 and 2.19 where a, b and c are the axis of the undeformed unit cell and a', b' and c' the axis of the deformed one.

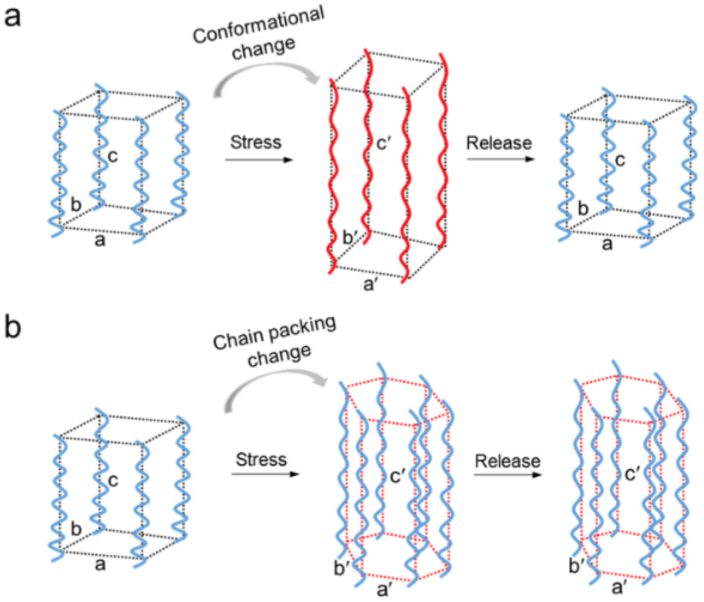

Figure 2.18: Two types of crystalline phase transitions upon application and release of stress: (a) reversible transition; (b) irreversible transition. For reversible transition, the blue and red chain represents two types of chain conformations before and after transition. The irreversible transition is illustrated by an evolution from an orthorhombic packing (black dotted frame) to a hexagonal packing (red dotted frame) [17]

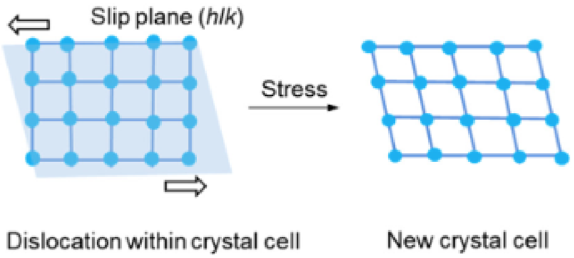

Figure 2.19: Strain-induced crystal phase transitions. Only crystallographic slip (within crystal cell) is represented here [17]

2.2.2.8 Strain-induced plasticisation at crystalline lamellae level

The previous section was focusing at the molecular level on the chain conformation and packing mode level and its evolution with deformation.

Let us consider now the level of the crystal lamellae and its evolution with increasing deformation and let us make the link with the macroscopic stress-strain curve.

"*From yield point to large strain, the original spherulitic structure of polymer is deformed in an irreversible way and changes into a fibrillar structure as the plastic deformation propagates. During this process, multiple events can take place, for instance the crystallographic slip, lamellae fragmentation, lamellae rotation, interlamellar shear, and eventually fibrillation*" as illustrated at figure 2.8 [17].

In this section, we will highlight the evolution of the microstructure according to three characteristic steps: 1°) prior to yield point, 2°) near yield point, 3°) beyond yield point till large strain.

Structural evolution before yield

Before the yield, structural deformations are tiny, though they can influence the structural processes at large deformation. A typical distribution of lamellae within a 2D-spherulite is presented at figure 2.20 where (a) the distribution of lamellae stacks before stretching and corresponding small angle X-ray scattering (SAXS)[13] pat-

---

[13] SAXS is a technique that measures the elastic scattering behaviour of X-rays when travelling through the material, recording their scattering at small angles. It allows to measure the thickness of crystalline lamellae

tern is presented and (b) lamellae stacks undergo Poisson effect in the meridional (or polar) region, interlamellar separation in the equatorial region, interlamellar shear in the diagonal region, respectively.

Three regions of lamellae stacks with different orientations of chain axis with respect to the stretching direction (SD) are identified: meridional, equatorial and diagonal. In the meridional case, stacks of lamellae approach to each other due to Poisson effect; in the equatorial case, lamellae are separated from each other under the interlamellar disentanglement of the macromolecules; and in the diagonal case, the interlamellar shearing dominates in their deformation.

It has been shown that lamellae fragmentation can occur in small spherulites, through sliding of crystal domains in the equatorial plane. This is direct evidence of the individual crystal slips at specific strain, as predicted by the IPN model, strain being identified on the macroscopic stress-strain curve. In order to address the difficulty of accessing local strains, other authors, such as Xiong, Lame, Séguéla [42], [43], [44] and Men [45] have studied the influence of crystal microstructure, chain topology and temperature. Their results confirmed the assumption of different modes occurring in different locations, and showed that the local strain is proportional to the macroscopic one.

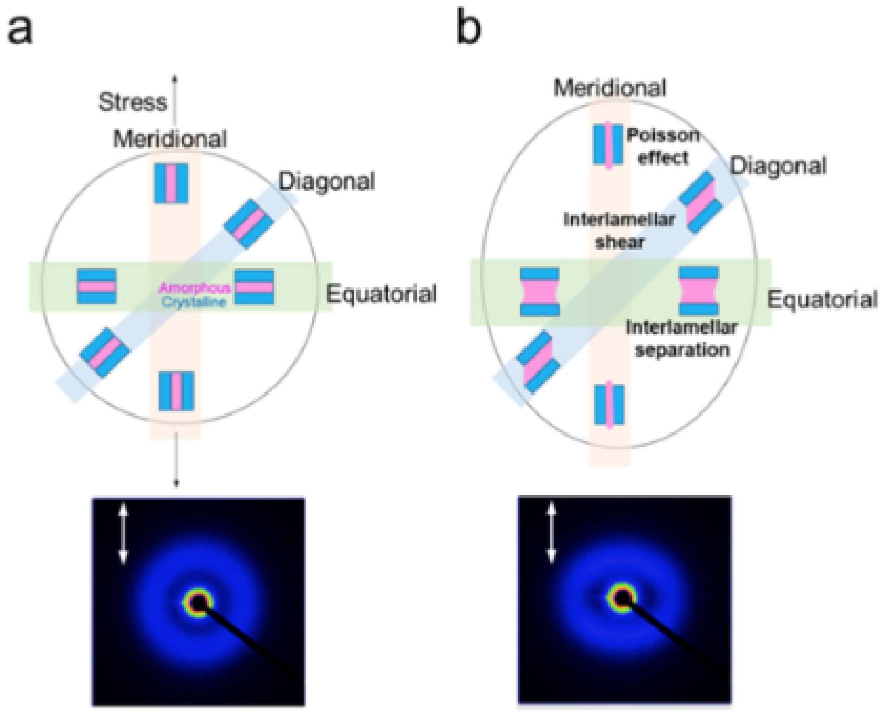

Figure 2.20: Deformation modes of lamellae stacks with different orientation states with respect to stretching direction (SD); they are identified as meridional (or polar), diagonal and equatorial - see text for more explanation; (a) before and (b) during stretching. A typical SAXS pattern of polymer obtained at strain prior to yield is also shown [17]

Structural evolution close to yield - the case of the single yield

At this stage, the lamellae stacks in equatorial and meridional (polar) regions begin to break into blocks, while the one in the diagonal region undergo intralamellar slip. These slipping mechanism could bring a shearing force on the equatorial lamellae fragments and oblige them to rotate along the stretching direction. In the region where neck propagates, continuous intralamellar slipping/damage of titled lamellae occurs, that could be named "melting" (with some care, cf supra 2.2.2.6) and that ends with the completion of the yielding instability. It has also be shown that the long period L_p increases just prior to the yield, reaches a maximum at this stage before going down. This could be interpreted as a melting-recrystallisation process.

Structural evolution close to yield - the case of the double yield

The double yield has been studied quite extensively in PE. The shape of the stress-strain curve can be in this region very dependent on deformation mode. A typical representation is given in figure 2.21 as well as a quite recent study on LDPE combining various characterisation techniques (see figure 2.22).

It seems that there is a consensus on the fact that the first yield originates from the slip of the lamellae. Regarding the second yield, it could be associated to pure crystallographic slips and lamellar kinking[14] - namely in compression [46] -, or to partial melting-recrystallisation.

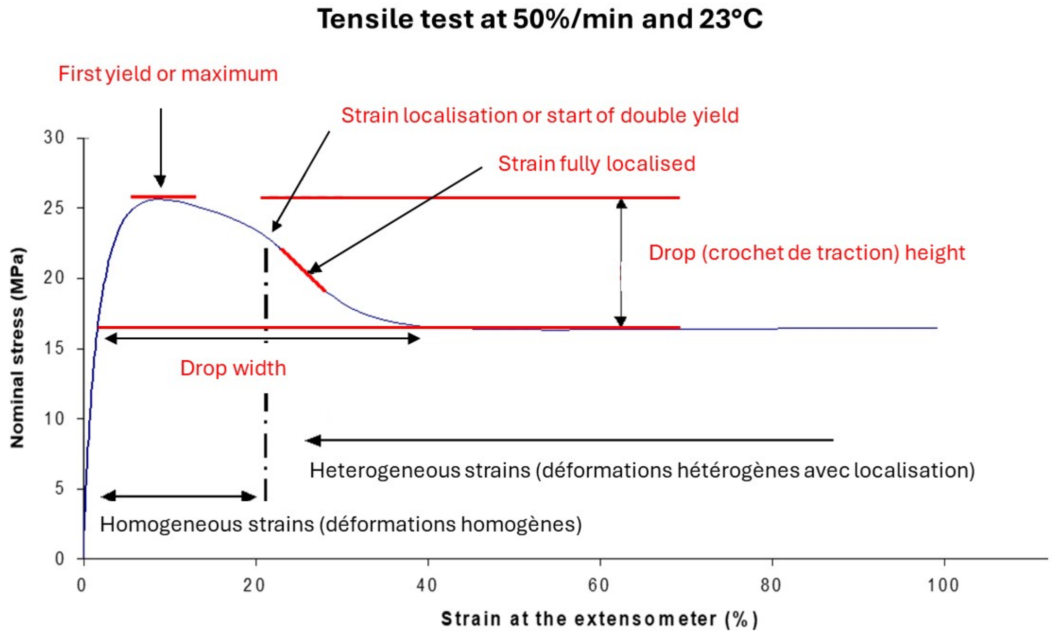

Figure 2.21: Double yield in a stress-strain curve measured on HDPE: zoom on small deformation (cf figure 2.6; the measure of the drop width is explained at section 2.2.2.13 where the term "drop" has been assimilated to the word "necking") [22]

In the work referred at figure 2.22[17], an heterogeneous deformation process between high-crystallinity and low-crystallinity parts at the scale of a spherulitic branch is presented. Combining the various technologies used for the test, the researchers proposed a partial melting-recrystallisation process. This observation has been supported by another work where an heterogeneous distribution of crystal domains with different stabilities plays a crucial role. The reorientation and slip of less stable domain initiate the first yielding and the plastic deformation of more stable domain leads to the second yielding and the further onset of hardening.

In his study already cited [39], Séguéla et al analysed the photographs of two samples of quenched polypropylene having undergone tensile test at respectively 25°C and 60°C; the picture was taken at around $\epsilon = 0,3$. As can be seen at figure 2.23, the sample tested at 25°C displays a sharp neck. The strain gradient is quite high, in width and thickness, and very coarse shear bands appear in the regions located beyond the neck. These two features suggest the presence of localized crystal slip at this temperature. In contrast, the sample tested at 60°C displays diffuse neck. The lower strain gradient is visible thanks to broader interference fringes; coarse bands are absent and beyond the necked region, the birefringence is uniform. These observations advocate for a highly active homogeneous crystal slip at 60°C.

---

[14] lamellar kinking is a kind of micro-buckling phenomenon of the lamellae

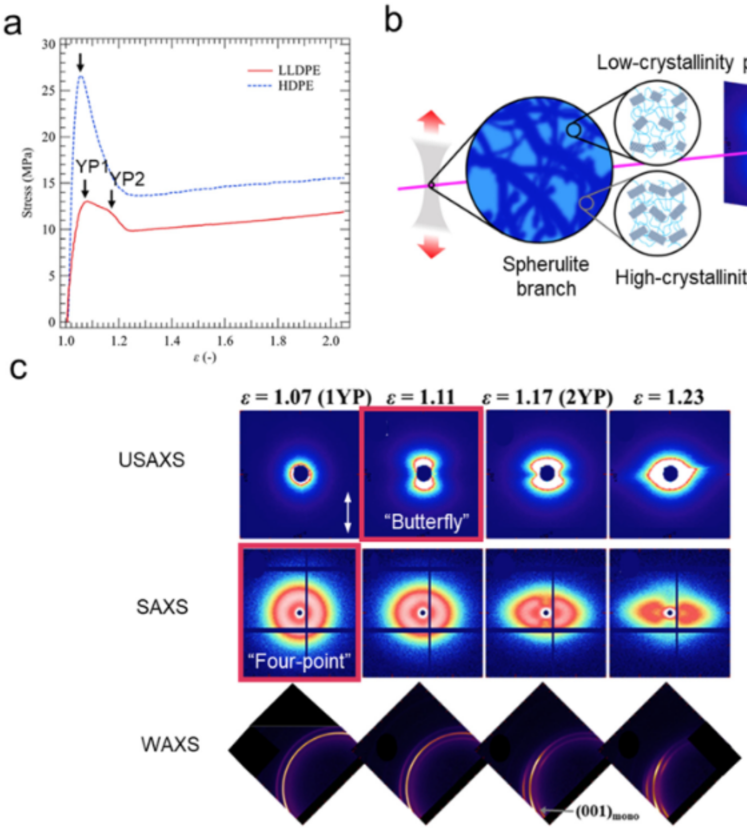

Figure 2.22: Multi-scale study of the double yielding behavior of linear LDPE. (a) Stress-strain curve showing first and second yield (YP1 and YP2). (b) illustration of proposed origin of double yielding, which is linked to the heterogeneous distribution on the submicron scale of high- or low-crystallinity parts of a spherulite branch (c) selected WAXS/SAXS/USAXS patterns obtained near the double-yielding strain range [17]

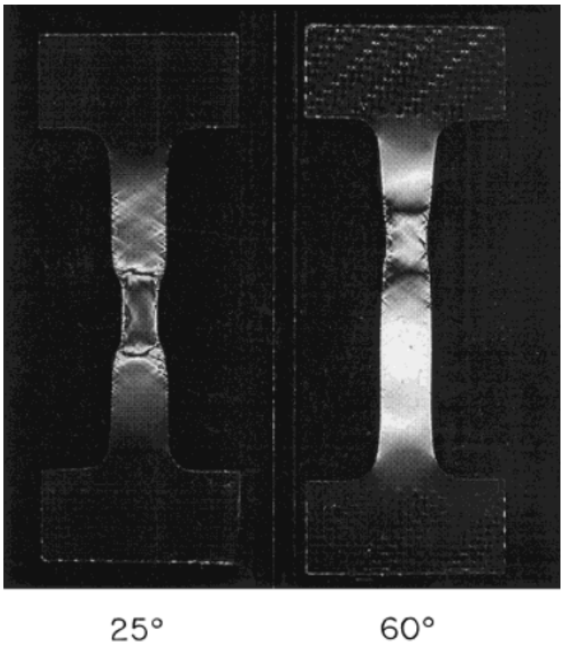

Figure 2.23: Quenched PP sheets drawn at 25 and 60°C up to $\epsilon = 0.3$ and at $\dot{\epsilon} = 1.0510^{-3} sec^{-1}$; the neck very pronounced at 25°C is accompanied by shear bands; the quite diffuse neck at 60°C is accompanied by rather uniform birefringence [39]

From these experiments, Séguéla et al concluded that there could be a competition between the two mechanisms, with crystal slip past each other in the fibrillar texture and uniform shear of the blocks. Moreover, their hypothesis is that

1. above the visco-elastic α-relaxation in the crystalline phase (see section 2.2.4), the molecular mobilities are high enough to allow thermally activated nucleation and propagation of screw dislocations in response to the applied stress. The high value of the activation volume measured during the experiments at high temperature is consistent with this assumption. This mechanism is a precursor of the homogeneous or uniform crystal slip, and reproduces fairly well other results obtained in PE
2. below the α-relaxation in the crystalline phase, dislocations are not able to nucleate and propagate at a rate high enough to accommodate macroscopic strain rate. Heterogeneous or localized crystal slip will occur either through defective interfaces within the lamellae or through the occurrence of partial dislocations involving the build up of stacking faults. The lower activation volume is consistent with this view, a reduced ability for thermal nucleation of dislocations. Microcracks are then likely to occur.

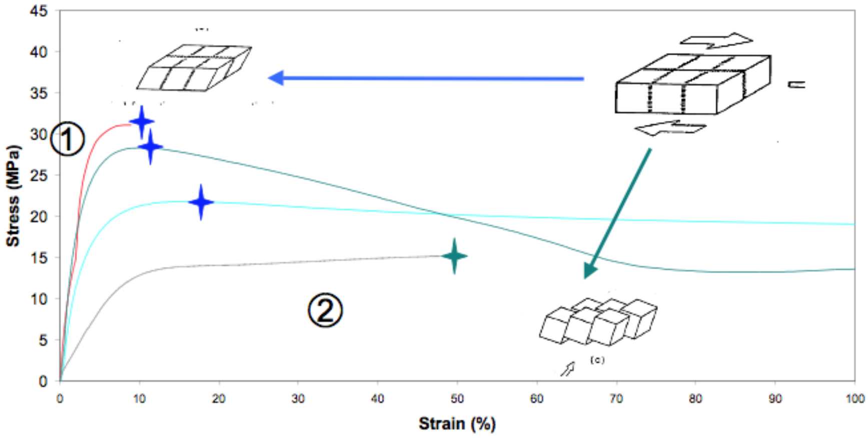

Figure 2.24: Positioning of the respective mechanisms in a stress-strain curve [22]

2.2.2.9 Strain-induced cavitation

Semi-crystalline polymers have been known for a long time to develop cavitation. This damage refers to the formation and propagation of cavities from nanoscale to microscale without any structure inside (voids). The cavities are damages that do not transfer the stress. Other types of phenomena are the crazes that are typical damaging mechanisms of polymer materials. As we will see later, crazes develop at the tip of notches and cracks, are composed of alternating voids and microfibrils and transfer the constraint from one side of the crack to the other side. Contrary to plasticity, a lot of studies have tackled cavities initiation and propagation in polypropylene, namely Pawlak, Galeski and Rozanski [47]. In this section, we review briefly the various mechanisms giving rise to cavitation initiation and propagation.

An interesting table can be displayed as an introduction, giving some information on key aspects of cavitation and microstructure.

Table 2.2: Microstructural and cavitation parameters; the length (along stretching direction) and radius (along transversal direction) of the cavities are referring to a cylinder-shaped objects model [17]

Polymer	X_c and L_p before drawing	T_d (°C)	Strain rate (sec^{-1})	Onset strain of cavitation; ϵ_y	cavity dimension (nm) length; radius
α-PP	50%; 16nm	30	$1.3.10^{-3}$	$0.08; 0.1$	$50 - 350; 40 - 240$

Another way to look at cavitation is to look at the competition between cavitation onset and yield, as presented in the table 2.3 and figure 2.25. In both cases, macroscopic events are usually monitored (except for the use of SAXS) that allow to identify simultaneously the value of the strain (third column on the table).

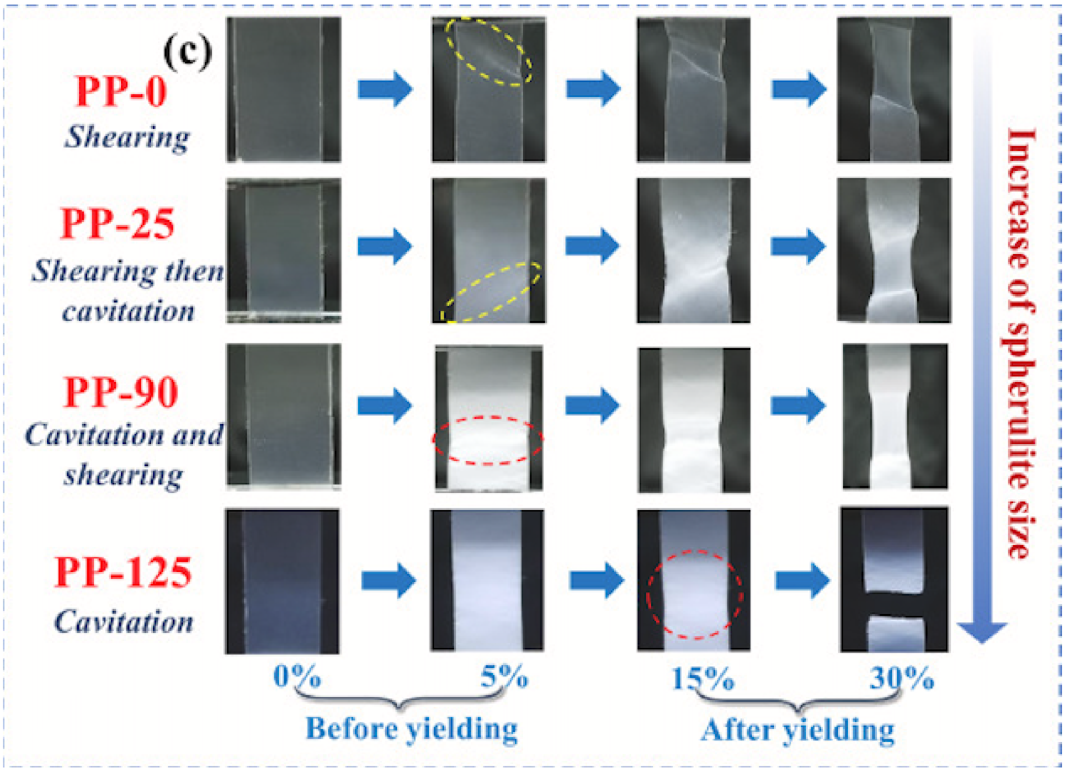

Figure 2.25: Four typical morphologies under increasing deformation (left to right); the competition between cavitation onset and shearing has been illustrated on samples of various spherulitic size (top down), thanks to the magnitude of the strain before yielding and in relation with the various optical events (strain localisation, whitening, ...); see text for further details [48]

Table 2.3: Cavitation and yield competition [47]

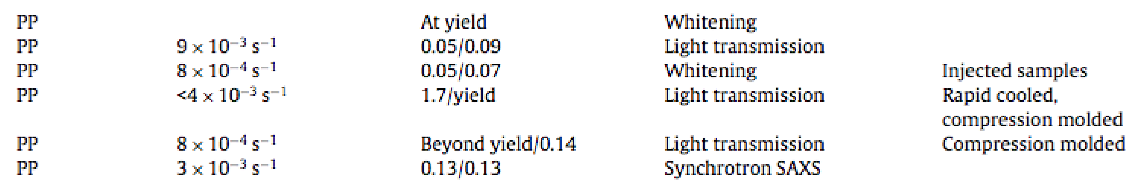

Polymer	Strain rate (sec^{-1})	Cavitation/yield ϵ_{true}	Detection method	Comment
PP		At yield	Whitening	
PP	9×10^{-3} s^{-1}	0.05/0.09	Light transmission	
PP	8×10^{-4} s^{-1}	0.05/0.07	Whitening	Injected samples
PP	$<4 \times 10^{-3}$ s^{-1}	1.7/yield	Light transmission	Rapid cooled, compression molded
PP	8×10^{-4} s^{-1}	Beyond yield/0.14	Light transmission	Compression molded
PP	3×10^{-3} s^{-1}	0.13/0.13	Synchrotron SAXS	

In many polymers, especially at lower temperature, cavities (voids) are formed during deformation. Due to hydrostatic pressure, cavitation is observed only during tensile test, never during compression or shearing. The very first characteristics of cavitation is stress whitening, observed usually around yielding. The further necking phenomenon can therefore be the combination of both cavitation as well as plastic instability phenomena. At figure 2.25, four types of samples with increasing spherulite dimensions have been tested (the spherulite size increases from top to bottom) and various optical events such as necking associated or not to whitening have been recorded (see dotted ellipses), together with the magnitude of the strain (indicated from left to right as "before yielding" and "after yielding"). The sequence at which whitening and necking appear illustrates their competition: if the necking occurs before whitening apparition, deformation mechanism is considered as pure shearing without any local volume increase; if the whitening appears before necking, the deformation mechanism is pure cavitation and is associated to an increase of local volume. The necking phenomenon decreases as the spherulite size increases and the whitening appears at earlier stage. The authors estimate that the results are not completely consistent because it is not clear whether some increase of volume noticed at large strains in polymers with weak crystals is a result of late cavitation or other structural changes.

Figures 2.26 and 2.27 illustrate the phenomenon at the spherulite level and at the crystalline lamellar level.

The top sketch of figure 2.26 presents (a) the tensile deformation of a spherulite; (b) the lamellae kinking and the formation of cavities in equatorial zones of a spherulite;(c) the lamellae fragmentation that occurs in polar fans of spherulites, potential cavities may be also expected. At the bottom of figure 2.26, AFM images of a spherulite equatorial region are presented for two strain levels (10 and 15%).

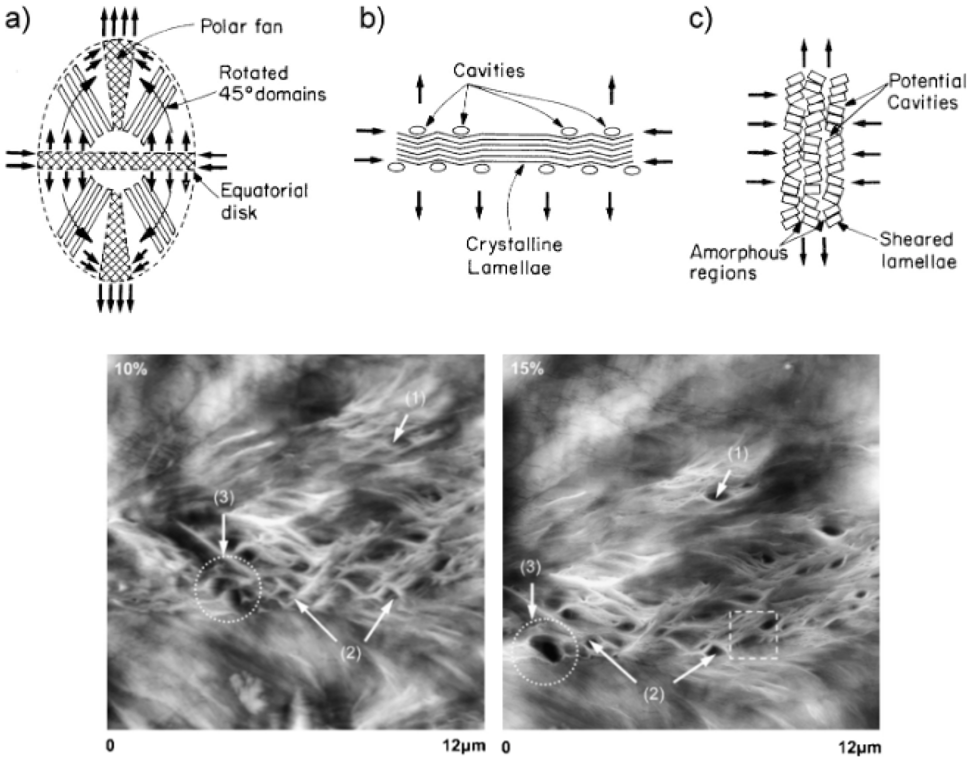

Figure 2.26: Top: tensile deformation of a spherulite, with lamellae deformation and cavities; bottom: AFM images with (1) void formation, (2) the growth and (3) the coalescence of cavities - see text for more explanations [47]

At figure 2.27, (a) the Peterlin model of microfibril and (b) the equivalent TEM picture are presented.

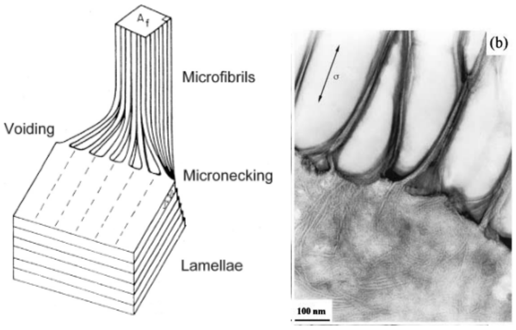

Figure 2.27: (a) Model of cavitating semi-crystalline polymer under tensile deformation [47] and (b) TEM section through a HDPE fracture surface taken 2mm from notch tip (the arrow indicates the drawing direction) [49]

The competition/cooperation between the cavitation and yielding respective kinetics leads to the well known phenomenon of crazing, as illustrated at figure 2.28 where the crack tip deformation zone of an HDPE notched sample tested in creep in air at $\sigma_i = 7MPa$ or $K_i = 0.3MPa.m^{1/2}$ is presented.

Usually, the cavitation process is observed in polymers having a spherulitic morphology, which means that cavitation could be expected to occur at the spherulite boundaries or inside. Cavitation inside a spherulite can be expected at the equatorial or polar parts, i.e. in regions where negative hydrostatic pressure dominates rather than shear. A good example on giant spherulites embedded in mesomorph material is presented at figure 2.29.

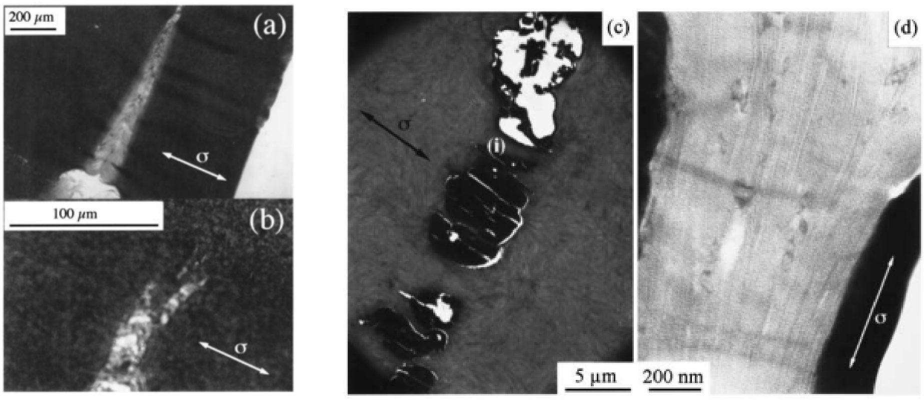

Figure 2.28: (a) Overview of deformation zone; (b) optical microscopy of deformation zone tip; (c) low magnification TEM image of deformation zone tip; (d) detail of internal structure of the region marked (i) in (c) (tensile axis as indicated by the arrows) [49]

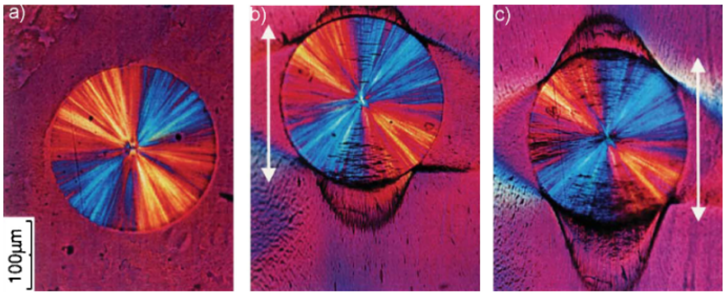

Figure 2.29: PP samples deformed at different temperatures. Deformation direction was horizontal. Internal structure was exposed by longitudinal sectioning and etching [47]

The way cavitation mechanism evolves according to its location is modelled for PP at figure 2.30 where, referring to initiation, two cavitation mechanisms are represented as a function of the alignment of the lamellae with the drawing direction: (a) initiation and propagation of cavities in interlamellar amorphous region for lamellae stacks in equatorial region; (b) initiation of cavities in crystal block boundaries for lamellae stacks in meridional (polar) region and further propagation across crystalline/amorphous regions (the distribution of lamellae stacks in different regions with respect to stretching direction is the same than in figure 2.20).

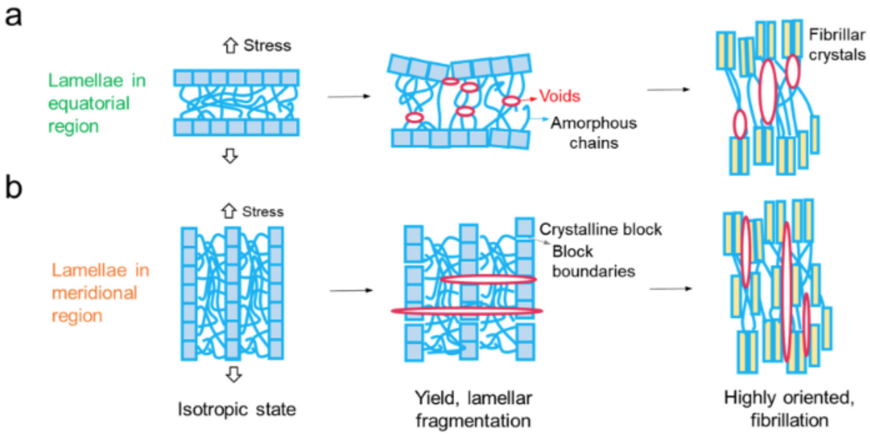

Figure 2.30: Two cavitation mechanisms: (a) for lamellae located in the equatorial plane and (b) for lamellae located in the meridional (polar) plane - see text for further details [17]

The evolution of those mechanisms with temperature and strain is illustrated at figure 2.31. It can be observed that around 25°C, the initial spherulitic morphology (upper left corner) is progressively lost with increasing strain (horizontal axis) while a lot of crazes appear that are totally oriented in the drawing direction for $\epsilon = 1.2$ (upper right corner). At 100°C, the spherulitic structure remain visible up to large strains and no crazes are visible at $\epsilon = 1.2$(bottom right corner).

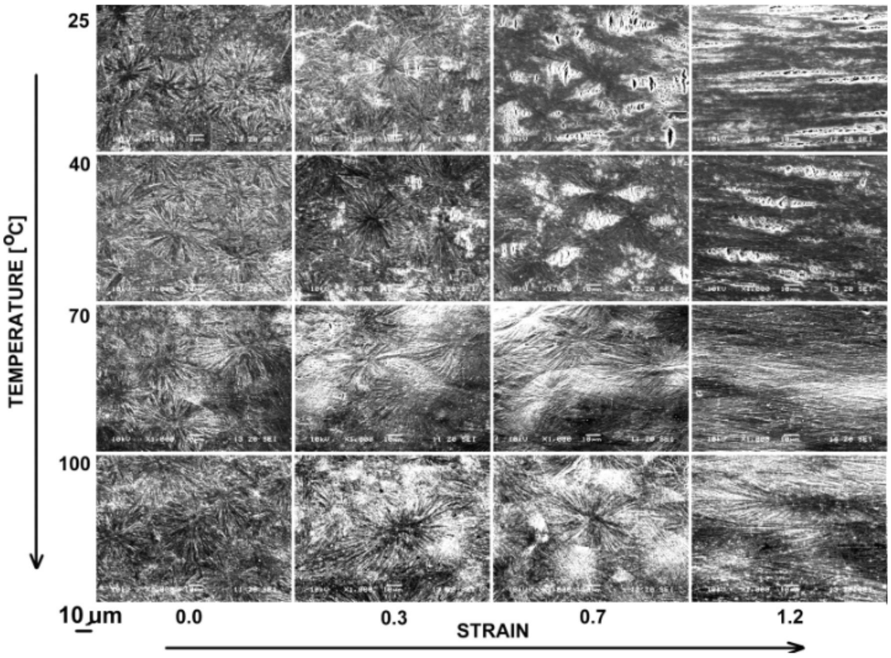

Figure 2.31: PP samples deformed at different temperatures and strains; deformation direction was horizontal; the evolution of the spherulitic structures is different at 25°C and 100°C and the number of crazes present at large strains decreases with increasing temperature [47]

Strain-induced cavitation: summary

The main factors influencing cavitation are the following ones: lamellae thickness and crystallinity, initial crystalline polymorph, molecular characteristics, drawing temperature and strain rate. The figure 2.32 is a good summary of the major factors influencing the cavitation process.

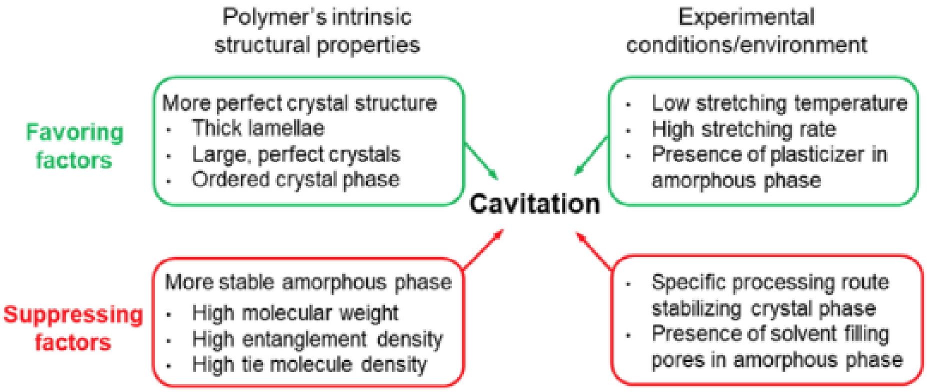

Figure 2.32: Some major factors influencing the cavitation process, including both intrinsic structural parameters of polymer and experimental conditions [17]

In conclusion, when the strength of the crystal is low, then it will be easier from the energetical viewpoint to activate dislocation mechanisms rather than to break the amorphous phase. In this case, the deformation process happens without cavitation. When it is easier to break the amorphous phase because the yield stress is very much enhanced f.i. at high strain rates or low temperatures, cavities are generated. The voids that appear are coupled with the crystals and the stress transfer changes, promoting deformation of crystals. The relations between the crystal strength and the amorphous phase can be modified by changing the quality of the amorphous phase (removal of low molecular weights, filling of free volume pores) or the presence of the defects in the crystalline phase (crystallisation conditions). The molecular weight plays also a role as it influences the number of entanglements [50], [47], [51].

Let us have now a look at the application of the abovemetionned concepts to two phases of isotactic polypropylene, the crystalline and the meso-phase.

2.2.2.10 Microstructural deformation mechanisms in single crystals

In this study, Cerra et al [52] have analysed the plastic deformation modes of single crystals of polypropylene under uniaxial strain and the way the crystallites deform under various orientations compared to the draw direction.

When crystals are moreless oriented in the direction of draw, microcracks developed at low strains and grow progressively larger as the draw ratio increased, spanned by fibrils of about 5 nm in diameter. The fibril diameter appeared to be independent of the imposed strain but its length was found to be proportional to the strain.

For crystals oriented at a large angle compared to the draw direction, simple and multiple shear, slip, as well as buckling appear. The authors compared their results with similar tests carried out on polyethylene, and found important discrepancies that we detail hereunder.

When the tensile axis is aligned with the *a*-axis of the crystallographic unit cell, localized cracking and micronecking occur, with formation of fibrils parallel to the draw direction. The chain is initially aligned with its *c*-axis, perpendicular to the lamella growing axis, it appears that, at some critical strain value, localized plastic deformation occurs by chains unpeeling and changing their molecular orientation. This is basically the mechanism of fibril formation. The fibre length then increases, in proportion of the applied deformation. No appreciable thinning of the lamella located at the edges at the fibrillar region was observed in the drawn region (see figure 2.33). This would mean that, contrary to PE, with crystal lamella thickness remaining the same and fibrils diameter also (around 5nm), the molecules do not tilt and slip but simply reorient themselves as indicated previously. Plastic deformation is triggered quite early, probably in regions with preferential presence of defects. The elastic energy stored in the part of the crystal adjacent to fibrils is released and the remaining part of the lamella relax to reach a new (temporary) equilibrium.

Another important difference between PE and PP crystals in their response to a deformation is the structure of the fold domain. PP seems to have only one domain as folds are believed to run only along or close to the *a*-axis - see figure 2.33(a). On the contrary, the fact that PE crystals grown from solution have a diamond shape means that these various folded domains are not parallel, hence will not be strained in the same way in each domain. Due to this single domain, the strain required to induce plastic flow are very low.

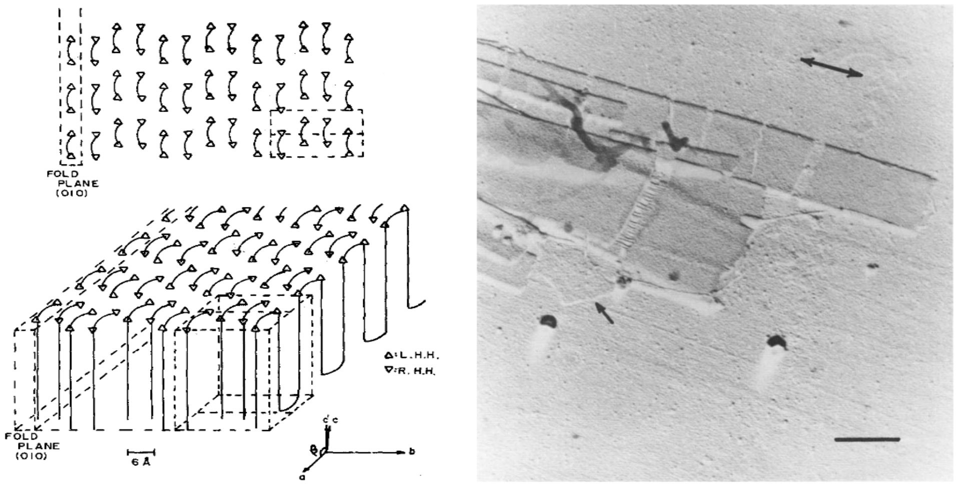

Figure 2.33: (a) Representation of a possible form of 010 fold packing [53] and (b) electronic microscopy of PP crystals drawn at 10% along the *a*-axis; the arrow indicate the drawing direction and the scale is 0.5μm [52]

When the *a*-axis is not aligned with the tensile axis, typically tilted with an angle of 45°, shear appears and considerable plastic deformation is observed. The shear strain component parallel to the *b*-axis is large and various blocks appear to have slipped relative to each other. The apparent slip surfaces seem to be aligned with the (110) plane. The slip lines appear to have developed in the already deformed twinned sections on the way to undergo upper deformation (see figure 2.34).

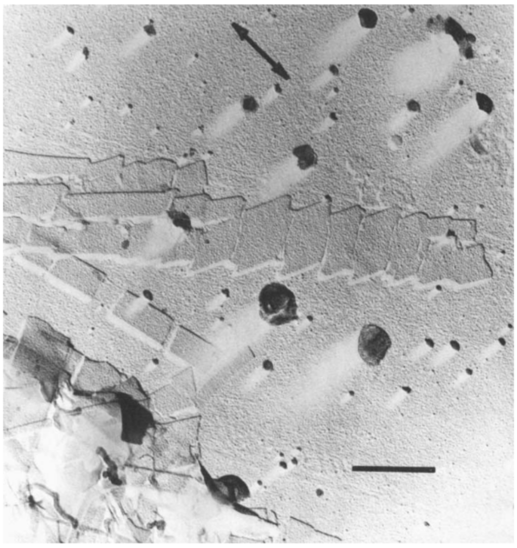

Figure 2.34: Electronic microscopy of 45° axis-tilted PP crystals drawn at 50%; the arrow indicate the drawing direction; the scale is 0.5μm [52]

2.2.2.11 Microstructural deformation mechanisms in mesomorphic materials

The work of Nitta and Odaka [54] focused on the influence of mesomorphic[15] phase on tensile properties, considering the material as a two phase composite according to Takayanagi model. They fabricate α-crystalline samples by varying cooling and annealing conditions: quenched at 0°C and then annealed ("crystallitic") samples that did not show up spherulitic superstructures and quenched at 80°C ("spherulitic") and annealed samples that showed up spherulitic structures. The mesophase has been considered as liquid-like lateral disorder with imperfect c-axis. The volume fraction of the various phases was determined thanks to density measurements, with

$$\rho_c = 936kg/m^3, \;\; \rho_a = 854kg/m^3, \;\; \rho_{meso} = 916kg/m^3 \tag{2.4}$$

and

$$E_c = 45GPa, \;\; E_a = 0,15GPa, \;\; E_{meso} = 5GPa \tag{2.5}$$

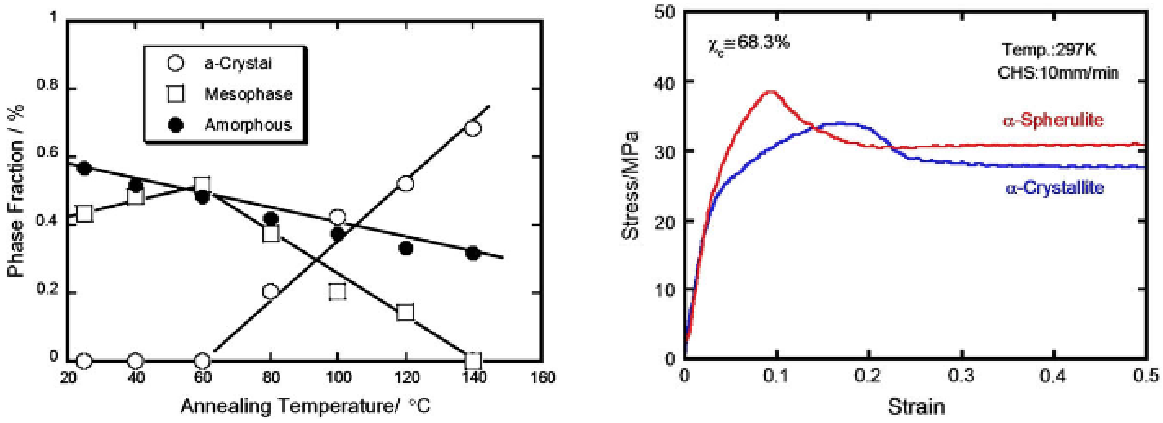

Figure 2.35: (a) Phase fraction plotted against the annealing temperature of "crystallic" samples and (b) stress–strain curves measured at 25°C and a cross-head speed of 10 mm/min of "crystallitic" iPP (C40) and "spherulitic" iPP (S140) having a fixed crystallinity of 68.3 %; the first yield is located approximately where the curves diverge [54]

---

[15] explanations about the mesophase are given at section 2.3

The evolution of the three phase fractions as a function of annealing temperature is presented at figure 2.35(a) for the "crystallitic" samples. The figure 2.35(b) illustrate the influence of the mesophase on the yield drop, the shape being very different, with inverse concavities for "crystallitic - C140" and "spherulitic - S140" samples annealed at 140°C with the same crystallinity (68.3%). There is no difference in stress–strain curves up to 3% of deformation, which illustrates the insensitivity to the spherulitic structures. The "crystallitic" sample annealed at 140°C displays clearly a double yield whereas the "spherultic" sample displays a sharp neck. The necking appeared at around the second yield peak for C-series samples while the necking of spherulitic iPP samples was initiated beyond the yield point. The second yield peak was related to the transformation of mesomorphic phase to α-crystal phase, indicating that the enhancement of the yield stress is a consequent of an increase in the perfection of the crystalline phase [54], [55]. The first yield has been identified as the point where both crystallitic and spherultic curves deviate from each other.

The dependencies of the stress–strain curves in mesomorphic iPP (C25) and "crystallitic" iPP (C140) samples on tensile speeds are summarised in the figure 2.36(a) and (b), respectively. The first yield point is more pronounced for the mesomorphic sample C25 while the second yield point is more pronounced for C140. Regarding the first, the dominant factor for the yield is likely to be the pulling-out processes of helical chains from these domains. The mesophase is indeed composed of loosely organized state of helical chains and the yield process is based on the plastic flow of helical chains from the mesomorphic domains. Therefore the dependence of the yield behaviour on elongation speed and temperature may be described by a thermally activated rate process. On the other hand, in the "crystallitic" C140, the second yield process will be associated with the irreversible structural re-organization into oriented state.

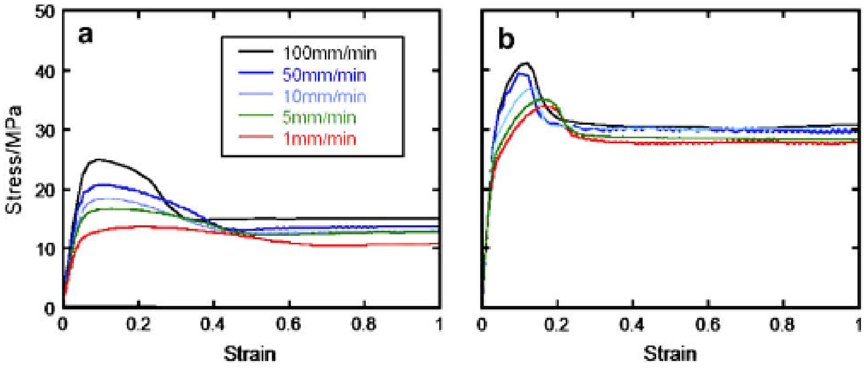

Figure 2.36: The tensile speed dependence of the stress–strain curves measured at 25°C for (a) mesomorphic iPP (C25) and (b) "crystallitic" iPP (C140) samples.

Looking at figure 2.37 that superimpose stress-strain curve and light transmittance for mesomorphic (C25), "crystallitic" (C140) and "spherulitic" (S140) samples, and taking into account the evolution of Poisson ratio (not shown), it is observed that the volume expansion occurs during yield deformation for the "spherulitic" iPP while no excess volume-changes take place during yielding for the "crystallitic" iPP. It was suggested from the stress-whitening observation that the volume expansion is caused by the formation of micro-voids and crazes. In any case, the yield stress of the mesomorphic material is much lower that the two other samples.

Finally, Nitta proposed also, with various co-authors, that an intermediary unit structure, the cluster of lamellae, plays an important role in the yield process [56], [57].

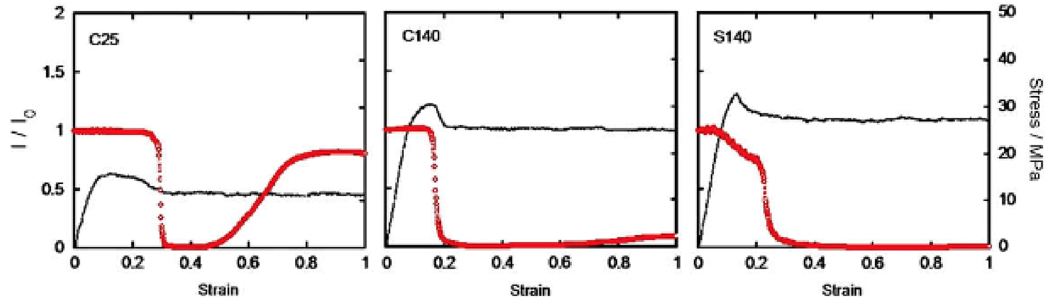

Figure 2.37: (a) Light transmittance intensity measured under a tensile test 25 °C and a cross-head speed of 10 mm/min for mesomorphic iPP (C25), (b) "crystallitic" iPP (C140), and (c) "spherulitic" iPP (S140); no volume increase was observed for (a) and (b) while volume expansion was present for (c)

2.2.2.12 Microstructure, strain rate, Young modulus and stress at yield

A lot of attempts have been implemented in order to find the microstructural causes explaining, on the one hand, the positive correlation always observed in many semi-crystalline polymers between the Young modulus, the yield stress and the crystalline parameters and, on the other hand, the influence of the strain rate on the Young modulus [34], [55], [58], [59], [60], [61], [62], [63], [64], [65], [66], Auriemma et al in [67]. We review some of them hereunder.

In their work, Zia et al [20] try also to establish the link between the modulus and the yield stress with the microstructure. In their approach, they first followed two cooling pathways, quenching and annealing or isothermal crystallisation; second, by comparing samples with the same level of crystallinities and crystallised at, or annealed at same temperature, they could demonstrate that the ones crystallised smoothly were constituted of lamellae of various sizes organised in superstructures (spherulites), leading to well known cross-hatched structure whereas the ones quenched and annealed were constituted of "nodules" which distribution is rather narrow, without any superstructure.

The replacement of cross-hatched monoclinic lamellae and spherulitic structure by randomly arranged nodules leads to the apparition of neck and therefore an important increase in elongation at break. The Young modulus and stress at yield are lower in the case of the nodular structure. AFM measurements show that the crystals undergo very small deformation, which would be attributed to the reduced mobility of amorphous phase interlocked in the regions between the cross-hatched lamellae (see [52]). This study demonstrates that the deformation at break is clearly driven by other parameters than crystallinity, confirming the study performed on PE by Humbert et al [68], [41]. These aspects will be discussed in the next section tackling with stress-transmitters.

Other studies dealing with the influence of the microstructure on the Young modulus have carried out experiments on quenched and annealed film samples tested at various strain rates [69], [60]. It is demonstrated [69] that the evolution of elastic component of stress at yield and the Young modulus with the annealing temperature is controlled by the physical cross-linking degree of the amorphous phase induced by the crystalline entities. As tests are performed at room temperature, the increase of modulus with strain rate comes from the behaviour of the amorphous phase around its glass transition. Regarding the drawability, it is controlled not only by the same parameters but also by the degree of perfection of the crystalline entities.

In [60], it is demonstrated that the stress–strain curves in the pre-yield region is independent of the size of spherulite when the comparison is made at similar crystalline and amorphous layer thicknesses. The initial modulus and stress depend only weakly on crystallite thickness, and strongly on interlamellar spacing. The increase in the Young's modulus and stress level with the degree of crystallinity can be attributed to the deformation imposed on the thinner interlamellar region because the modulus of amorphous phase is much lower than that of crystalline phase. Moreover, the tie molecules in the amorphous region where the deformation can be concentrated play important roles in the tensile deformation.

In Auriemma et al [67], it is shown that the Young modulus decreases with the increasing concentration of stereo-defects [rr][16] and that the correlation between the yield stress σ_y and the crystalline lamellae l_c follows the same trend as illustrated at figure 2.38 for a series of isotactic polypropylenes. This linear relationship between l_c and σ_y has been observed in many types of popylpropylenes and polyethylenes.

---

[16] see section 2.3.2.3 for explanations on defects

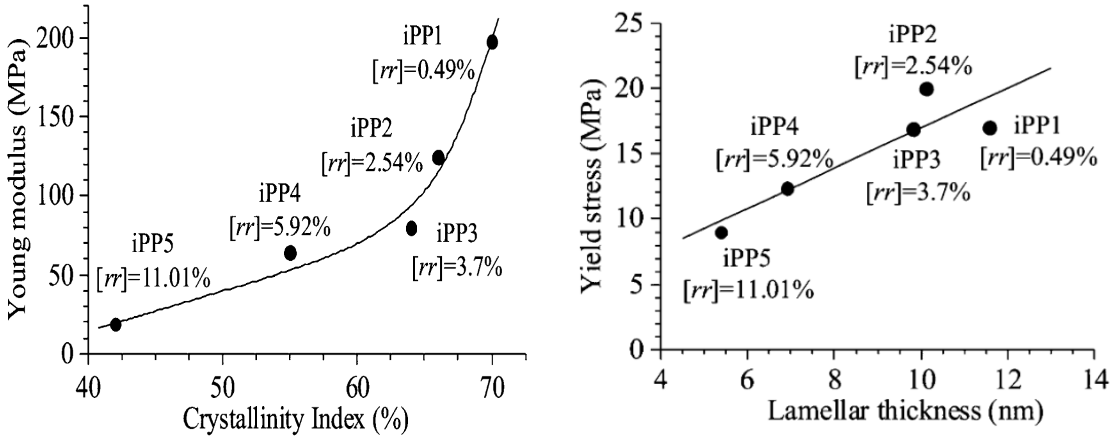

Figure 2.38: (a) Young modulus as a function of crystallinity index with increasing content of stereo-defects and (b) relationship between lamellar thickness l_c and the yield stress σ_y (Auriemma et al in [67])

We would like to finish this review with the excellent and recent work of Polinska et al [65], [66] that addresses the relationship between the Young modulus and the solid state microstructure by investigating the correlation between the modulus of the interlamellar amorphous phase and the microstructure of the crystalline components.

In the continuation of the researchs of Rozanski and Galeski - see namely [70] -, they developed a "universal" experimental method able to deform only the interlamellar amorphous layers of semi-crystalline polymers. The local deformation of the amorphous component was obtained by introducing a swelling agent as illustrated at figure 2.39(a). Three polyethylene structures (high and low density as well as ethylene-octane copolymer) were used to set-up the experiment that was also applied to polypropylene. As illustrated at figure 2.39(b), the distinction between the bulk rubbery amorphous phase and the confined one due to the thickening of the lamellae together with the change in order of magnitudes of the Young modulus was highlighted. The linear increase of the amorphous phase modulus, considered as confined, with the increase of crystal thickness is displayed at figure 2.40 and explained by the activation of the α-relaxation of the polyethylene crystalline lamellae. For a detailed analysis of this figure, we refer to the article.

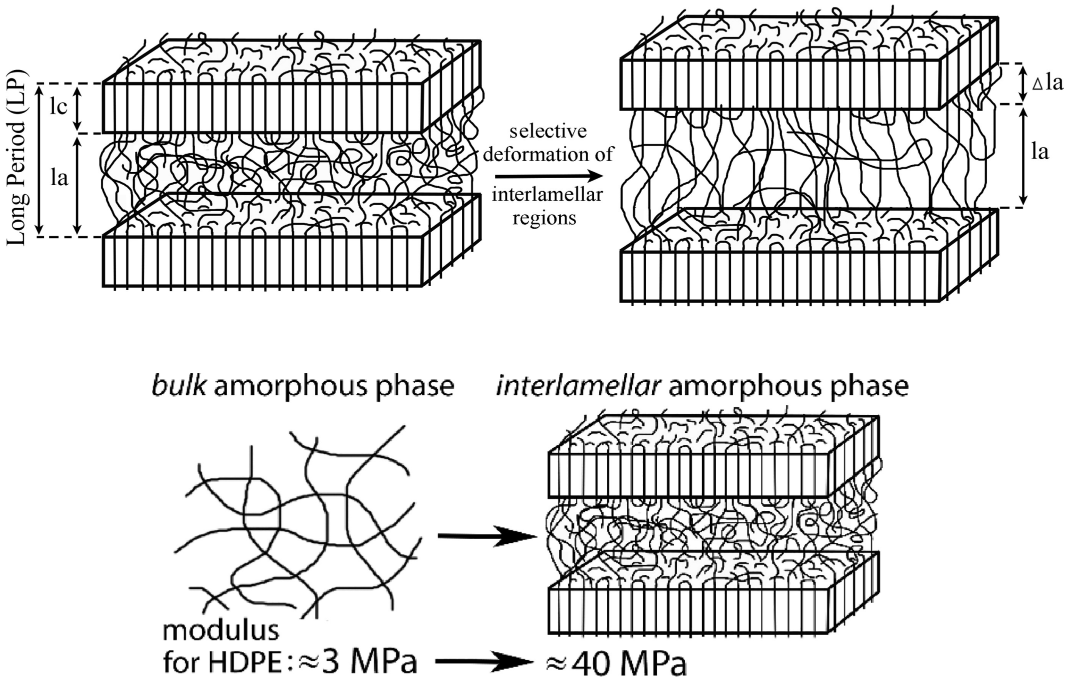

Figure 2.39: (a) Top: interlamellar distance changed thanks to swelling agents and (b) Bottom: evolution of the elastic modulus magnitude of the amorphous phase depending on its proximity to the crystalline phase [65]

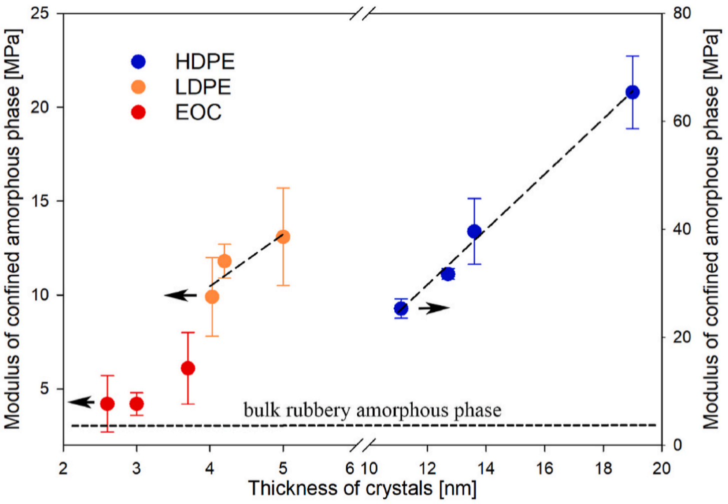

Figure 2.40: Evolution of the elastic modulus of the interlamellar amorphous phase as a function of the crystal thickness; left Y-axis: bulk rubbery amorphous phase and right Y-axis: confined amorphous phase [66]

The table 2.4 summarises some of the various structural parameters measured for both types of polyolefins where it can be seen that the elastic modulus of the amorphous phase ranges around 50MPa in the case of PP. Jourdan et al [71] found a value of moreless 10MPa for the shear modulus G_A of the amorphous phase that can be translated into around 30MPa for its Young modulus[17]. Nitta and Odaka found on their side (see section 2.2.2.11) a value of the amorphous modulus around 150MPa.

Table 2.4: Selected structural and mechanical parameters for polypropylene, low density polyethylene and ethylene-octane copolymers reference samples and hexane-swollen systems [65]

	long period (LP) [nm]	thickness of amorphous layers (l_a) [nm][a]	local strain of amorphous layers (ε_a)[b]	yield stress [MPa]	local stress of amorphous layers (σ_a) [MPa][c]	elastic modulus of the interlamellar amorphous phase [MPa][d]
PP	13.4	7.8		27.3		50.3 ± 3.5
PP/hexane	14.8	9.2	0.179	18.3	9.0	
LDPE	12.0	7.9		7.6		11.8 ± 0.9
LDPE/hexane	13.2	9.1	0.152	5.8	1.8	
EOC	11.4	8.4		4.9		4.2 ± 0.6
EOC/hexane	13.6	10.6	0.262	3.8	1.1	

All in all, Polinska et al summarised the various structural factors allowing to discriminate the respective bulk amorphous phase and the amorphous phase confined by the crystalline lamellae that impact its stiffness. They distinguish the factors that will respectively increase and decrease its stiffness. The factors promoting an increase are:

- high density of stress transmitters[18] coming from the intercrystalline tie molecules and an increasing number of entanglements
- the confinement of the molecular network between stiff crystalline lamellae, especially at the interface between the phases
- the lack of lateral contraction of the amorphous phase due to the very high aspect ratio of the flat and rigid crystalline lamellae

The factors promoting a decrase are:

- high density or content of chain ends and other (low weight) molecules present in the intercrystalline regions or rejected there during the crystallisation process.

It seems finally that the increase of the modulus with the crystallinity could be related to the lower deformation ability of the amorphous phase that could be coming from the increase of entanglements and tie molecules which impacts the stiffness of the interlamellar regions.

---

[17] The thermomechanical histories of both materials are not the same but we look at order of magnitudes by assuming a Poisson coefficient of 0.43 and using the relationship for isotropic materials $E = 2(1+\nu)G$.

[18] See section 2.2.2.13 for more details.

2.2.2.13 Stress transmitters (ST) definition and measurement

We would like to complete this general overview with a review of an important aspect of the link between microstructure and mechanical properties that builds on the notion of tie molecules [72], [73], [74], [75], [76], [77], the stress transmitters. For Humbert, Lame et Vigier [68], the link between crystalline lamellae thickness and yield which has been extensively studied does not provide any physical explanation. Furthermore, as some inconsistencies remain, there is a need of clarification of this correlation and a new notion, the stress transmitters, and a more accurate experimental way to characterize plasticity initiation are proposed.

The discrepancy observed in this important paper between the correlation of the yield stress with crystallinity on the one side and the poor prediction of the dislocation theory that considers the link between the stress at yield and the lamellae thickness on the other side has been solved by considering two new notions:

1. the threshold stress that is a signature of the transition of visco-elastic regime to a visco-plastic regime and
2. the stress transmitters (ST) density viewed as all the network linking two crystal lamellae (i.e. tie molecules, entanglements, loose loops, etc) as described on figure 2.41 below.

The ST constraints strongly the stress distribution on the lamellae edges. The correlation between the stress at yield and the crystallinity can be enlightened because the crystallinity involves indirectly the dislocations via the crystal lamellae thickness and the stress transmitters via the long period.

A new method that correlates the neck width and the Stress Transmitters (ST) density is proposed and enables to evaluate the ST concentration for each material as close as possible from the initiation of plasticity.

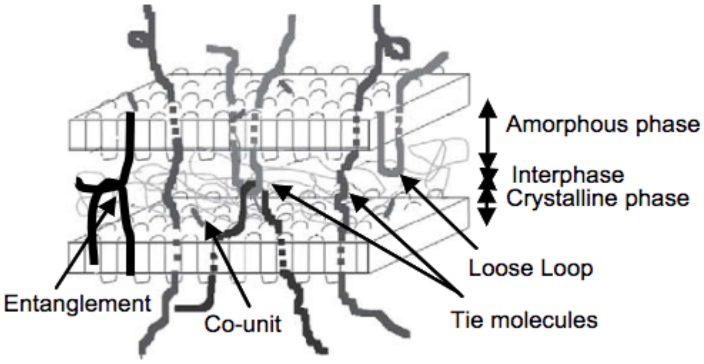

Figure 2.41: Crystalline and amorphous lamellae with their stress transmitters [77]

The global approach proposed is to take into account all the physical parameters that are involved in the initiation of plasticity. Their rationale follows the following sequence:

1. the dislocation model gives a relationship between the critical macroscopic tensile stress σ_c to shear a crystalline lamellae and its thickness l_c (or the stem length l)
2. usually, the critical shear stress σ_c is assimilated to the yield stress σ_y that is traditionally taken at the maximum of the stress-strain curve σ_{max}. However, at the maximum of the stress-strain curve, other deformation mechanisms can already be at work or triggered such as cavitation or plastic instability
3. the physical parameters of the dislocation theory based on activation processes, as has been explained in section 2.2.3 are all evaluated on undeformed micro-structure. This means that the theory makes sense only for the initiation of the plasticity
4. there is thus a discrepancy between the experimental values taken at the maximum (σ_{max}) where the damaging processes (plastic instability, cavitation if any) can be already at work and the initiation of the plasticity as described by the dislocation theory
5. there is thus a need to address this discrepancy first at the experimental level by carefully defining the macroscopic parameter taken from the stress-strain curve that will identify plasticity triggering. This parameter already exists in metallurgical approaches, defined by the loss of linearity on a true stress-true strain curve, using a strain parameter (see figure 2.42). In this research, the value of $\epsilon_{th} = 510^{-3}$ has been selected in order to get a sufficiently accurate value of σ_{th}. We detail somewhat hereunder the arguments used to link this stress to the microstructure

6. the stress transmitters are then defined, and a method is proposed to measure them as well. Taking benefit from literature experimental results, a relation between the neck width and the ST can be assumed that we detail also hereunder.

Regarding the threshold stress, taking then benefit of the wide literature using σ_y, two types of curves are drawn: σ_{th} as a function of crystallinity X_c and of the crystalline thickness l_c where a linear trend is highlighted for the former. Using

$$X_c = \frac{l_c}{L_p}\frac{\rho_c}{\rho} \tag{2.6}$$

it is possible to write

$$\sigma_{th} = K'\frac{l_c}{L_p} \tag{2.7}$$

with K' as a constant. This equation helps to show the dependence of the threshold stress to both the long period and the crystallisation conditions. Then, the authors assume that crystallisation conditions modify ST concentration and that ST concentration is in relation with the long period L_p. It is indeed observed that initiation of plasticity appears when a critical local shear stress τ_c is reached on a slip plan of a crystallite. This phenomenon depends on the orientation of the crystallite, the external macroscopic stress σ_{th} and also the local stress concentration. Indeed, the higher the amount of ST, the lower the stress concentration on the crystalline lamellae and the lower their influence on the local shear stress i.e. the local increase of τ is rather smooth and τ_c will be reached later. Consequently, at equivalent crystalline lamellae thickness l_c, the yield stress value increases with the concentration of ST.

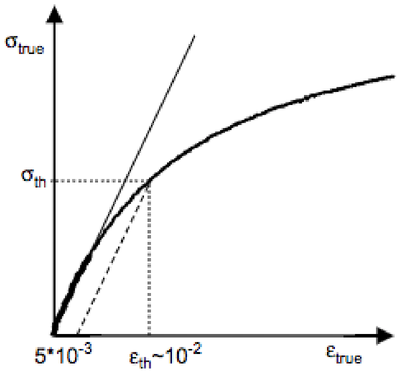

Figure 2.42: Method of sigma threshold σ_{th} measurement based on the value of $\epsilon_{th} = 5\ 10^{-3}$ [68]

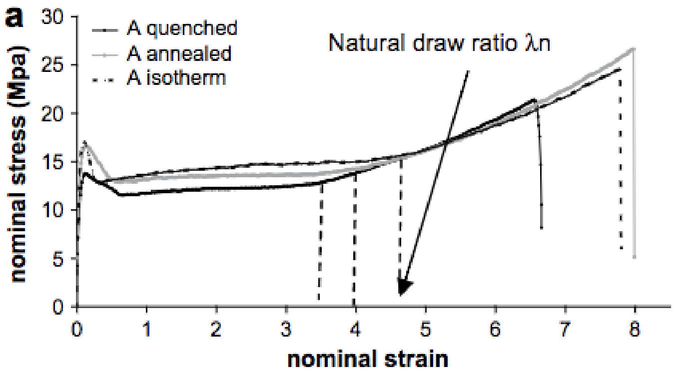

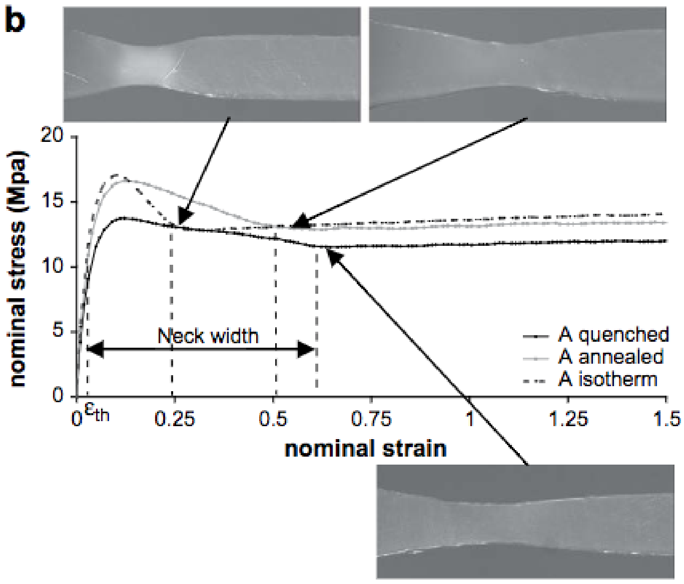

Figure 2.43: (a) Drawing and natural draw ratio of the PE A; (b) necking of the PE A and the corresponding photos [68]

A new method to measure ST is then proposed. It relies on the fact that on the one side, it is known from literature that sharp necking corresponds to important plastic instability during yielding, that, on the other side, chain topology and crystallisation conditions have an influence on neck shape as well as on the homogeneity and stability of the deformation, and finally that cavitation takes place during necking and is considered to be coupled with the plastic instability.

From these results, it is assumed that the lower the concentration of ST, the sharper the neck. The measurement of the neck width can then be selected as a ST concentration indicator, and it is measured as represented at figure 2.43. The neck width is thus a physical criterion, measured at the beginning of plasticity and it turns out that it is more sensitive to ST concentration than previous indicators, allowing more precise measurements. Thanks to the link established above between σ_{th} and L_p, the initiation of the yielding should be predicted with a good precision taking into account both l_c and ST concentration.

2.2.2.14 Conclusion of the review on strain-induced multiscale structural evolutions of crystallised polymers

A lot of difficulties are still present. There is still a lack of unified understanding of the various deformation mechanisms to explain the crystal phase transition and morphological transformations from a molecular viewpoint. In order to progress there, using models at various scales is really a fundamental tool as moreover, the traditional approach of looking solely at an increase of specific performances is hardly transposed and often non generalisable from one material to another [17]. From an experimental point of view, various aspects can be investigated, among other, building referentials of properties out of the traditional approach with standards and norms, by controlling the solicitation, the geometry of the samples and their solid state microstructure - via their thermomechanical history and molecular architecture -, and going from the simplest to the most complex. By doing so, the use of all the mechanical tests toolbox in the range of small and large deformation should be always underpinned by a micro-macro approach.

2.2.3 Small deformations: microstructural deformation mechanisms as a way to bridge visco-elastic and yielding behaviour

Before digging in the details of visco-elastic relaxations and yielding processes, we would like bridging these two limits of the small deformation range thanks to their common underlying microstructure deformation process viewed as activated processes.

Our focus is on the crystalline phase relaxations.

2.2.3.1 Activation volume

Digging further into the validity of dislocation model applied to plastic deformation, **Lefebvre and Escaig** [78] focused especially on the entropic effects, as the mechanical importance of these effects is a very distinctive feature of polymers vis-à-vis metals. They reviewed its main features by discussing its experimental relevance through various polymeric systems (PS, PMMA, PP and various polyesters): frequency of elementary deformation event, internal stress, activation parameters. Entanglements of the amorphous phase play here a critical role. The non-elastic deformation of glassy polymers was modelled by the nucleation and growth of localized slip nuclei or microshear band discs to which they applied a statistical analysis. Calculating the linear dislocation density, they found a rather low value for PP systems that they explained by the fact that the dislocation-like defects are assumed to be developed in the intercrystal amorphous phase which should be relatively entangled. Among the parameters that describe the entanglement barrier, one is related to the chain stiffness, and more specifically to the chain stem or to the chain persistence length[19]. They validated their model namely on PP and they confirm the important role played by the chain flexibility that controls the activation volume.

2.2.3.2 Dislocation kinetics

In an article dealing with the dislocation approach of plastic deformation in PE and iPP [79], Séguéla tries to establish a comparison between the dislocation kinetics and actual strain rate of homogeneous plastic deformation.

Figure 2.44 gives an illustration of dislocation initiation, propagation and exit from a crystalline lamellae as well as a sketch of the respectively undeformed (before dislocation passage) and deformed (after dislocation passage) regions.

In order to show that the activation of mobile conformational defects in the chain stems may fairly match the ability to develop homogeneous plastic flow or plastic instability, he makes a parallel between the conformational defects able to activate screw dislocations and those who activate α-relaxation in crystals.

The characteristics of defect thermal activation are shown to have a major influence on dislocation kinetics and therefore on plastic behaviour. The crystal lamellar thickness, as critical parameter of the plastic flow in the dislocation model, should especially be taken into account in the dislocation kinetics because its major influence on the chain twist activation.

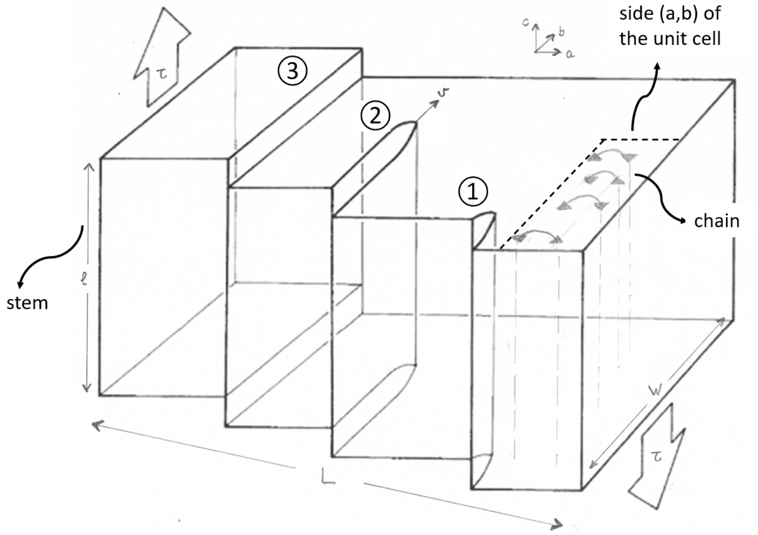

---

[19] The persistence length is a basic mechanical property quantifying the bending stiffness of a polymer. This is the maximum length for which the first and last monomer are correlated.

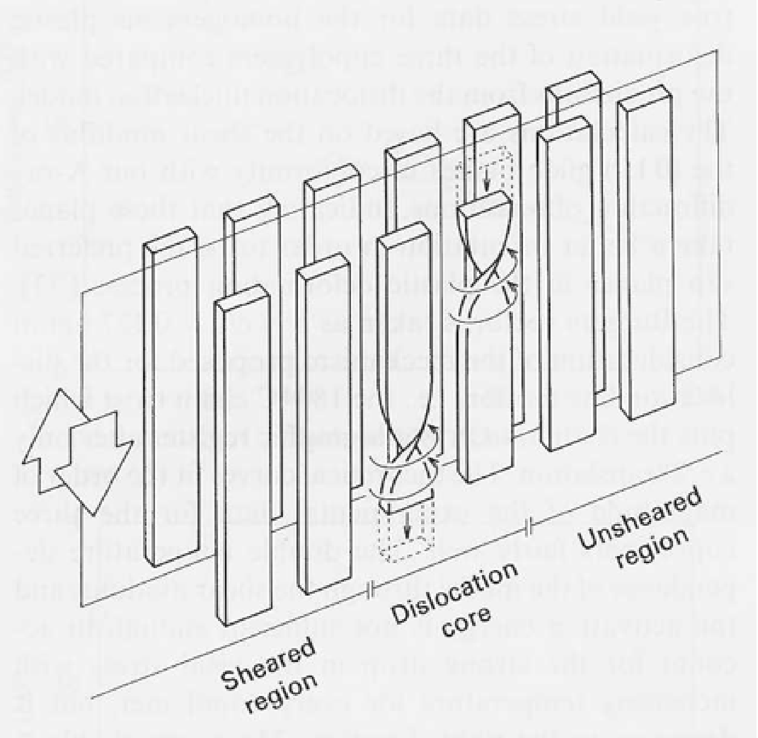

Figure 2.44: (a) Illustration of the nucleation and propagation of dislocation from stem to stem: ① initiation, ② propagation and ③ exit of a dislocation (reworked from [79]);(b) mechanism of advancement of a screw dislocation where the sheared region are the first to undergo the dislocation occurrence [39]

The following mathematical approach is described hereunder. The plastic deformation rate $\dot{\epsilon}$ for a dislocation governed process is:

$$\dot{\epsilon} = \rho \mathbf{b} v_d \tag{2.8}$$

where ρ is the dislocation density, $\mathbf{b}$ is the Burgers vector parallel to the chain axis c and v_d the dislocation velocity. For thin crystals lamellae, v_d is controlled by the rate of nucleation of the twist defects ahead of dislocation line, that maintain the forward jump of the dislocation in its glide plane (see figure 2.44).

The velocity can be expressed as:

$$v_d = a\nu_t \tag{2.9}$$

where ν_t is the activation frequency of the defect and a the cristallographic axis. By approaching the frequency ν_t with the crystalline relaxation frequency ν_c associated precisely with the chain twist activation in the crystals, it is possible to write:

$$\nu_t \approx \nu_c = \nu_0 exp(\frac{-E_a}{RT}) \tag{2.10}$$

where E_a is the apparent activation energy of the relaxation process. In PE, the activation energy was proved to be independent on the crystal content and morphology as long as the crystal thickness is larger than five to six monomers, i.e. the defect extension along the chain stem. Hence, the pre-exponential factor ν_0 could account for crystal thickness dependence of alpha relaxation by assigning it to the migration kinetics of the defects along the chain stem through the crystal thickness l. The dislocation density can be expressed by:

$$\rho = \frac{nlt}{Llw} \tag{2.11}$$

with $t = w/v_d$, Ll the crystal area at stake in the mechanism, w the lamellae width, n the number of screw dislocations of l length nucleated by time unit and t the lifetime of the dislocation. The maximum number n of screw dislocations that are nucleated every second from the lateral surface of any crystalline lamella relies on the number N of chain stems lying there according to :

$$n = \nu_t N \tag{2.12}$$

where $N = L/b$ with b the crystallographic axis in the growth direction L. The dislocation density can be then written as:

$$\rho = \frac{\nu_t t}{wb} = \frac{1}{ab} \tag{2.13}$$

The dislocation density is independent of the crystalline lamella parameters. The 3/1 helix of polypropylene undergoes, as already said elsewhere, a threefold rotation combined with a $c/3$ translation parallel to the stem axis. Assuming a Burgers vector $\mathbf{b} = c/3 = 0.22nm$, the calculated dislocation density is

$$\rho \approx 0.7\ \ 10^{18} m^{-2} \tag{2.14}$$

The temperature dependence of the α-crystalline relaxation frequency of iPP has been reported by [71] namely for PP samples annealed at 100°C and 140°C. The activation frequency is $\nu_c \leqslant 10^{-6} sec^{-1}$ at room temperature, leading to a theoretically attainable plastic flow rate $\dot{\epsilon} \leqslant 10^{-6} sec^{-1}$ at this temperature. This means that, under usual testing rates, i.e around or above $10^{-4} sec^{-1}$, this polypropylene will always give rise to heterogeneous deformation when tested at room temperature. In order to match the theoretical plastic flow with the experimental usual strain rate around $\dot{\epsilon} \approx 10^{-3} sec^{-1}$, the characteristic frequency of the crystalline relaxation should be around $\nu_c \leqslant 10^{-2} sec^{-1}$, which, according to figure 2.45 should occur around 100°C for the PP annealed at 140°C and 65°C for the one annealed at 100°C.

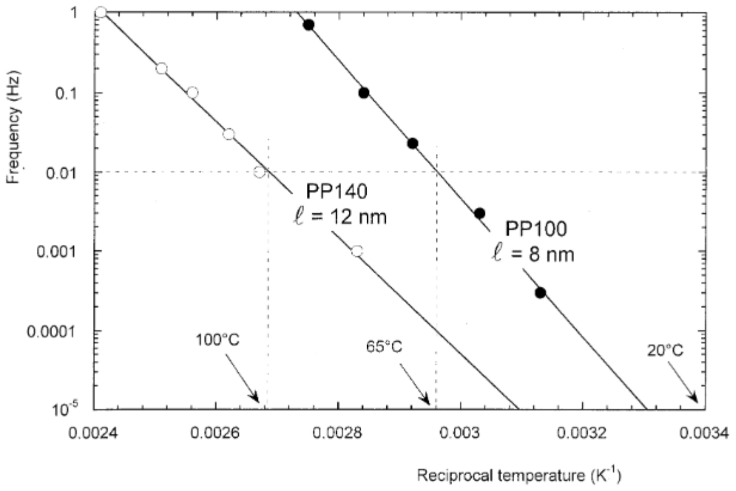

Figure 2.45: Frequency versus temperature dependency of the crystalline relaxation of PP100 and PP140 according to Jourdan et al [71] cited by Seguela [79]

2.2.3.3 Implementation of Ree-Eyring approach

We would like to finish this bibliographic review with the application of Ree-Eyring model to isotactic polypropylene[20]. In this last paper of van Erp et al [62], different molecular architectures (homo- and copolymers of iPP), additivation and solidification conditions have been tested at various temperatures and strain rates thanks to tensile quasi-static and creep tests. In the case of polypropylene, they indeed have noted that, while the vast majority of studies deal with various solidification conditions and micro-structures, only very few investigated the influence of these variations on a large range of temperatures and strain rates. Accordingly, building namely on own previous works as well as on those of Roetling [80], Alberola [69], Séguéla [39] and others, they validate the presence of two deformation mechanisms named I and II in the ranges $10^{-5} sec^{-1} \leq \dot{\epsilon}\ \leq 10^{-1} sec^{-1}$ and $25°C \leq T \leq 110°C$ on various α-iPP involving mesophase. Cooling conditions were ranging from $0.1°Csec^{-1}$ to $200°Csec^{-1}$. The various material used are presented in table 2.5 below.

---

[20] For the full description of this model, see section 2.5 "Small deformations: semi-empirical approaches of viscous flow".

Table 2.5: Molecular and physical properties of the materials used [62]

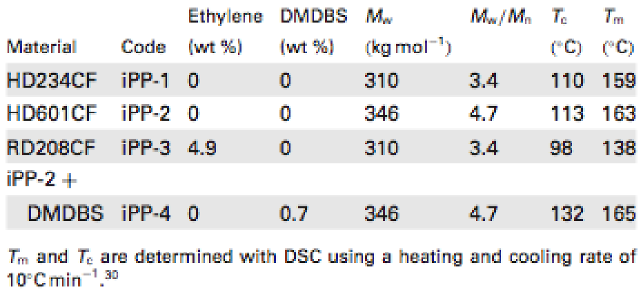

Material	Code	Ethylene (wt %)	DMDBS (wt %)	M_w (kg mol^{-1})	M_w/M_n	T_c (°C)	T_m (°C)
HD234CF	iPP-1	0	0	310	3.4	110	159
HD601CF	iPP-2	0	0	346	4.7	113	163
RD208CF	iPP-3	4.9	0	310	3.4	98	138
iPP-2 + DMDBS	iPP-4	0	0.7	346	4.7	132	165

T_m and T_c are determined with DSC using a heating and cooling rate of 10°C min^{-1}.[30]

The authors have also measured the crystal lamellae thickness as well as the crystallinity. As expected, they found a relationship illustrated at figure 2.46.

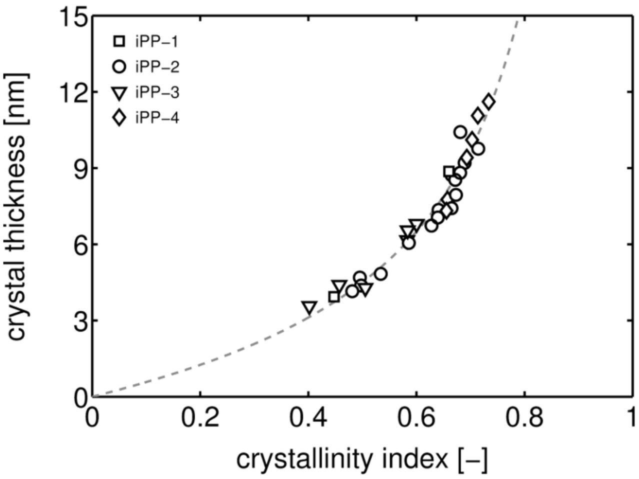

Figure 2.46: Crystal thickness as a function of crystallinity (determined with SAXS and WAXD) for all PP-based materials. The line is a prediction assuming a constant amorphous layer thickness

In order to preserve their microstructure, the mesomorphic phase samples were not tested beyond 60°C.

Typical (ϵ - σ) curves as well as ($\ln\dot{\epsilon}$ - σ_y) curves were obtained on iPP-2 cooled at 0.1°C/sec and iPP-1 cooled at 200°C/sec as illustrated at figure 2.47(a) and (b).

The slope in the high temperature and/or low strain rate regime is representative for the activation volume of mechanism I, whereas that one in the low temperature and/or high strain rate regime holds for the activation volume of mechanism I + II.

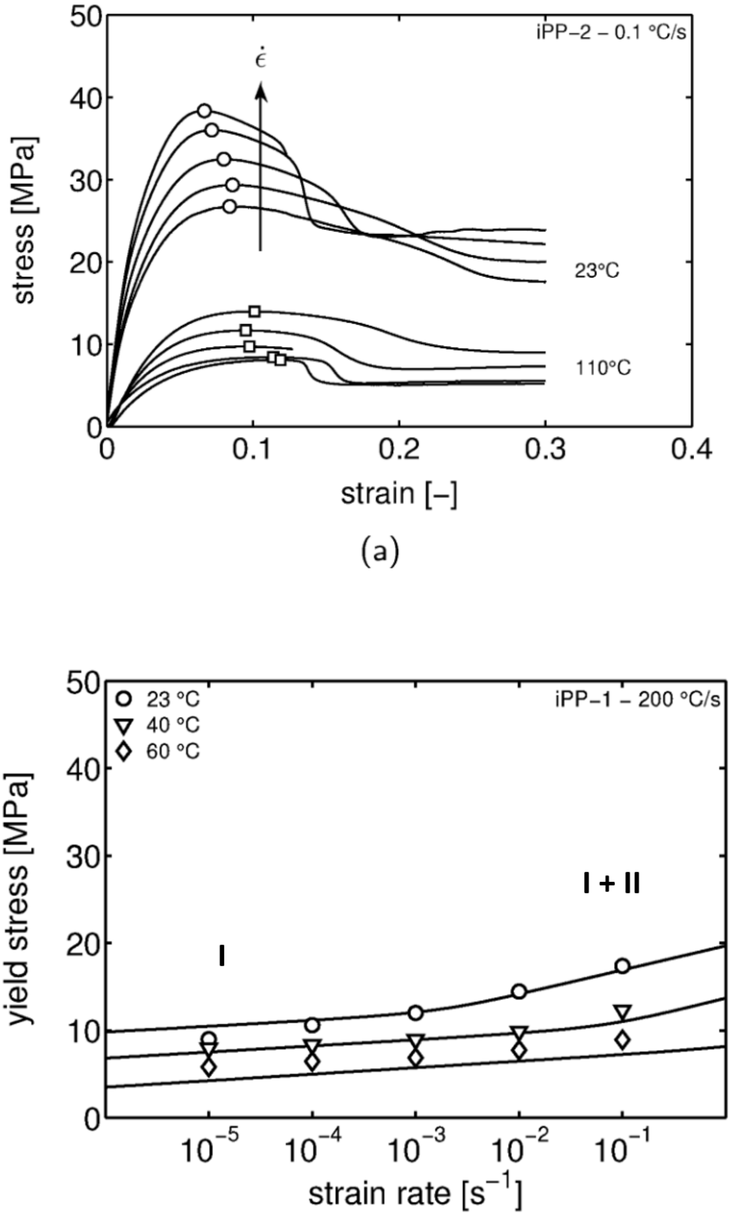

Figure 2.47: (a) Samples cooled at 0.1°$Csec^{-1}$ and tested at 23°C-110°C and $10^{-5}sec^{-1}$ to $10^{-1}sec^{-1}$; (b) yield stress as a function of strain rate for sample cooled at 200°$Csec^{-1}$ and tested between 23°C and 60°C. Symbols represent experimental data, and lines are optimal fits using Eyring equation with constant activation volumes - see table 2.6

It is thus possible as we will see later thanks to equation (2.36) to compute the activation energy E_a^i and activation volume V_i of each mechanism i as seen on table 2.6 below though some precaution have to be taken when reading the data because of the scattering.

Table 2.6: Ree–Eyring-Parameters for all PP-samples [62]

mechanism i	$V_i(nm^3)$	$E_a^i(kJmol^{-1})$
I	14.20	503.7
II	4.44	158.0

The author concludes that the activation volume does not depend on the cooling conditions for a specific molecular architecture. In fact, as displayed at table 2.6, the activation volume and energy of each mechanism i do not depend on the microstructure. The only parameter in the Ree-eyring model that translates the nature of the solid microstructure is the pre-exponential factor that will be discussed in details at section 2.2.5. As a matter of fact, the solid state microstructure is assumed to be constituted with a biphasic amorphous and crystalline phase. The morphology of the solid state can be quantified in terms of crystal thickness and of crystallinity and the authors find a strong non linear correlation between both. Hence, they argue that it was demonstrated - see figure 2.46 - that a unique relationship exists for all the considered compositions and microstructures between these two quantities. They also demonstrate that both crystal thickness and crystallinity decrease with increasing cooling rate and that crystallinity and crystal thickness of the α-phase is higher compared to the mesophase.

They try to link therefore the microstructure to the yield kinetics via the pre-exponential factor (which they name "rate constant") and conclude that *the yield kinetics of PP-based materials are satisfactory predicted using the crystallinity dependent rate constants* (see 2.48).

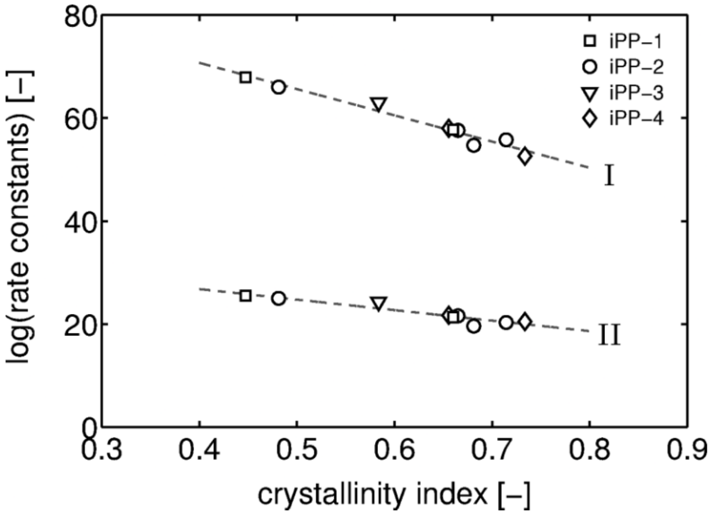

Figure 2.48: Logarithm of the pre-exponential factors (or rate constants) of processes I and II as a function of the crystallinity. Symbols represent experiments, and dashed lines are a guide to the eye [62]

The fact that the activation parameters do not depend on the cooling conditions is confirmed by the fact that the slopes of the quenched iPP-2 and of the same quenched then annealed iPP-2 sample are identical, as illustrated at figure 2.49 for the tests performed at room temperature. The same holds obviously for all the four structures.

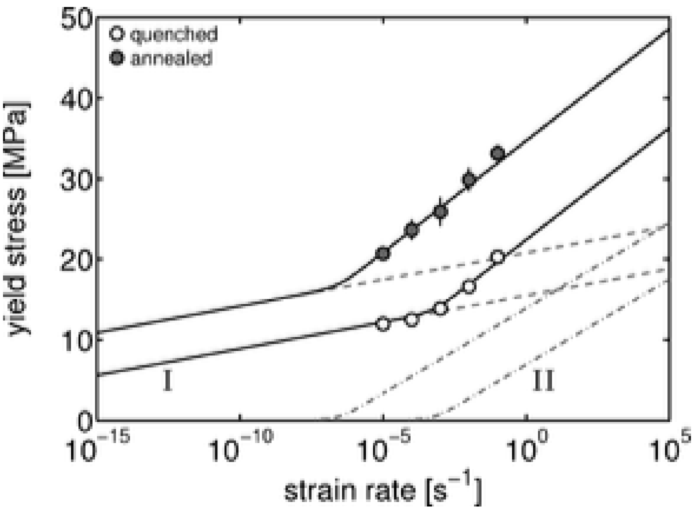

Figure 2.49: Yield stress of iPP-2 as a function of the strain rate. Symbols represent quenched and annealed (10min at 100°C) yield stress data, and lines are model predictions using crystallinity index dependent rate constants [62]

On the base of the above-mentioned research, the authors carry on an attempt to discuss the two mechanisms I and II in terms of crystal slip (mechanism I) and interface crystal-amorphous phase (mechanism II). They also discuss the values found for the activation energy. The magnitude of activation energy for mechanism I E_a^I is higher than the energy required for chain scission, as C $- C$ covalent bonds energy is in the range of 284 to $368kJmol^{-1}$ and in any case, such a break is not observed. The value of table 2.6 at $E_a^I = 504kJmol^{-1}$ however does not seem unrealistic as Alberola et al [69] found values of $470kJ/mol^{-1}$.

The mechanism II is, for what it is concerned, put in relation with the α-transition as the literature mentions that this latter occurs between 80°C and 100°C. The magnitude of activation energy for mechanism II $E_a^{II} = 158kJmol^{-1}$ is in the range of 146 to $167kJmol^{-1}$ found in the literature.

To summarize, the authors have covered a interesting range of compositions, microstructures, temperatures and strain rates. They have shown that two crystallisation regimes are competing, the monoclinic one and the mesomorphic one. The crystal thickness and crystallinity decrease with increasing cooling rate. These two regimes are translated into the Eyring formalism where it is shown that on the one hand, the activation volumes V_i and energies E_a^i are independent of the microstructure, i.e. the cooling conditions. On the contrary, these latter are captured in the pre-exponential factor.

2.2.4 Small deformations: visco-elastic behaviour of isotactic polypropylene

It is know from the literature that there are a lot of similitude between mechanical and electrical approaches to materials in the case of solid-state. Dielectric relaxation spectra and mechanical relaxation spectra display remarkable consistent measurements and provide very valuable information on the structure of the material, among other transitions located at the same temperatures [36], [81]. Furthermore, some important methodologies such as creep compliance or Cole-Cole diagrams come from theoretical and experimental methodologies dealing with electrical - or rather dielectrical in the case of polymers - properties, even on apolar ones.

According to [7], [81], isotactic polypropylene is known to have a series of six transitions which are located respectively around at 19K, 53K, 200K, 273K, 325K and 430K as explained hereunder. The origin of basic relaxations processes and their general trends are known. However, despite the amount of studies dedicated to them, the exact molecular origin and the morphological assignment of notably the α-relaxation are still a matter of discussion because of the variety of results and interpretations proposed by different authors.

About the relaxation around 430K, let us mention that it translates the very beginning of the primary crystals melting [7]. Let us call, for sake of clarity, the relaxations respectively below 100K (19K and 53K) and at 200K, 273K, 325K δ, γ, β and α. Nowadays, a consensus seems to emerge on the molecular origin of the two main lower temperature relaxations γ and β though this is not the case for α one as already said.

In dielectric relaxation measurements, the fourth relaxation δ, mainly below 100 K, is weak or absent and is attributed to the hindered rotation of CH_3 groups. Reported activation energies are about 5 kJ/mol.

The γ-relaxation is located between 150K and 230 K and is usually considered as local motions in the amorphous phase [82], most probably crankshaft type of $[C - CH_3]$ of the backbone chain [7]. The dynamic mechanical investigation has indicated that the initiation of thermal oxidation is concomitant with a partial vanishing of the γ-relaxation [81], [83], [84], [82]. In metallocene iPP, an increase of isotacticity results in a broadening of this relaxation, that partially overlaps with the left-hand side of the glass transition. The activation energies found for this relaxation vary between 25kJ/mol [81] and a range between 50 and 80kJ/mol for metallocene iPP [85].

The β-relaxation, located between 250K and 300 K and considered as the glass transition is usually assigned to the amorphous phase. Some authors [81] propose that the glass transition that is very broad, contains in reality two peaks, assigned to unconstrained regions of the amorphous phase [so called "mobile amorphous fraction"] and regions constrained by crystallites [so called "rigid amorphous fraction"] [71]; other authors point out to the lower transition as the one of amorphous phase rich in atactic chains and the upper one due to antioxidant contained in the amorphous phase which is rich in isotactic chains [86]. The Williams-Landel-Ferry (WLF) temperature dependence observed for this relaxation indicates cooperative behaviour related to the glass transition with the reported activation energies of 350-400 kJ/mol [71], [85].

According to Jourdan et al [71], the β-relaxation, related to the glass-rubber transition of the amorphous fraction behave in a similar way to that of a wholly amorphous polymer, with two characteristics: a high rubbery plateau, indicating a cross-linking effect by the crystalline phase, and a strong effect of interfaces in shear strain. When comparing the shift of respectively α- and β-relaxations with decreasing frequencies, there is a larger shift of the temperature T_α than T_β. This means that the apparent activation energy is larger for β than for α. Consequently, the shape of the β-relaxation curve is the more influenced by the presence of the

α-relaxation as the frequency is decreased; in other words, as the frequency decreases, the maximum value of tgδ increases, i.e., there is a lack of time-temperature superposition.

According to Hoyos et al [87], similarly to the α-relaxation, the temperature and relative intensity at which the β- and γ-relaxations occur are strongly related to the molecular architecture of the chains: there exists a critical value of the isotactic length n_{iso}[21] under which the motions associated to the β- and γ-processes occurring in the disordered phase are promoted against the motions in the crystals, i.e. the α-process. The associated variations of T_β and T_γ with n_{iso} suggest that the degree of constraint of the disordered regions play an important role in the mechanical relaxations. Therefore, the low-T_m crystals, constituted of subsidiary and transverse lamellae[22] appear to drive the respective contributions of β and γ to the whole dynamics of the disordered phase.

In general, the α-process appears below the melting temperature and its position varies with many factors such as the structure, the density, the thermal history, etc..

The origin of this process is controversial in the literature, but it undoubtedly requires the presence of a crystalline phase. According to [88], the α-relaxation process require the presence of both, the crystalline and the amorphous phase (MAF as well as RAF), because the deformation of the amorphous interphase layer (or RAF) takes place by a mechanical movement of the polymer chain. The temperature of the α transition T_α usually increases with the characteristic frequency of solicitation whereas the α-peak becomes broader. The temperature dependence of this transition follows an Arrhenius-law [89], [90] and the relaxation processes are exclusively triggered by relaxation processes in the crystalline phase that are mainly discrete, thermally activated and controlled by defects (see infra). The nucleation and propagation of these defects under thermal activity allows the deformation to be transferred from the crystalline phase to the amorphous phase via the interface [71].

It was also demonstrated that the underlying mechanisms are characterized by only a couple of sharp and defined relaxation times [36], [90], [91], [89], which means also that, under very small strains, the magnitude of the vibration frequencies are basically in the same range.

The solid state microstructure such as the mesophase or the spherulite size together with the molecular architecture significantly influence the nature and the number of components of the mechanical α-relaxation [92] thanks to the activation of various molecular mobilities. For instance, the decrease of both the spherulite size and the crystallite structure perfection leads to the enhancement of the crystallite mobility, resulting in an increased contribution of the intra-lamellar regions to the α-relaxation [81].

Multiple relaxations of α-process, consisting of two components, was also observed [84], for instance in samples cristallised from the glassy state. The low-temperature component ["low-T_α content"] is mainly attributed to the stress relaxation of the fraction of the non-crystalline phase containing strained molecules and segments of molecules belonging to the specific (irregular) arrangement of the surface layer of the crystallites. The high-temperature component ["high-T_α content"] of the α-relaxation is connected with the viscous slip of the crystalline elements within the non-crystalline phase [81].

In the study on thermo-oxidation of iPP made by Tiemblo et al [84],[83], the presence of the α-relaxation makes it possible for crystals to act as radical scavengers and thus stabilise the material at temperatures under 115 °C.

Mansfield and Boyd [93] investigated on their side the dielectric α-relaxation of PE and proposed the propagation of a twisted defect along the chain in the crystal lattice, resulting in a reorganisation of the crystal surface, though it is known that the amorphous phase is softened or deformed too. In the case of polypropylene, the α-process was found to follow an Arrhenius law due to less cooperative motions than in the case of the glass rubber transition, i.e. β-relaxation. Activation energies of the α-process were found in the range of 135kJ/mol and 150kJ/mol for metallocene based iPP [85], and 150kJ/mol and 200kJ/mol for ZN based iPP [71].

The influence of the ***molecular architecture*** has been studied by Hoyos et al [94], [87]. Recognizing that helical jumps through the RAF and chain-diffusion within the crystals are responsible for the α-relaxation in several semi-crystalline polymers such as PE or POM, it has been expected that tactic regularity would play an important role in iPP for the segment diffusion to take place. This means that chain characteristics (molecular architecture and molar mass) and morphology (crystalline content and size distribution of the crystals) will have an influence on this relaxation. Indeed, they control the average length of the isotactic segments able to be transferred between the crystalline and amorphous phases and some of the inter-chains associations could inhibit this dynamics by disabling the associated isotactic chain segments.

The authors carried out a research in which the main goal was to use materials of high molecular weight

---

[21] is the length between two isotacticity defects and is expressed in C_3H_6 monomeric units - see section 2.3.2 for the definition

[22] see section 2.3.2

and short average lengths in the chain. Considering copolymer as a defect, they synthesized three types of isotactic polypropylene structures, Ziegler-Natta homopolymers, Metallocene homopolymers and copolymers with varying molecular masses and isotactic lengths. The thermal history was approached in a (relative) way that would let each structure the same opportunity of ordering from the quenched status, meaning that the crystallisation temperature were different for each film when quenched from the melt.

In order to evaluate the amount of metastable mesophase, the low-T_m fraction, an empirical rule was used that assign this percentage to the area under the heat capacity up to $T_m - 8°C$, as illustrated at figure 2.50(a) and in order to evaluate the viscoelastic behaviour, they used a normalized method to compare the loss modulus E", by dividing it by the area under the β-relaxation process, i.e. the glass transition, as illustrated at 2.50(b). Computing the area under each peak, they could define the relative intensity of the transition. Finally, 2.50(c) displays the normalized loss modulus of various structures.

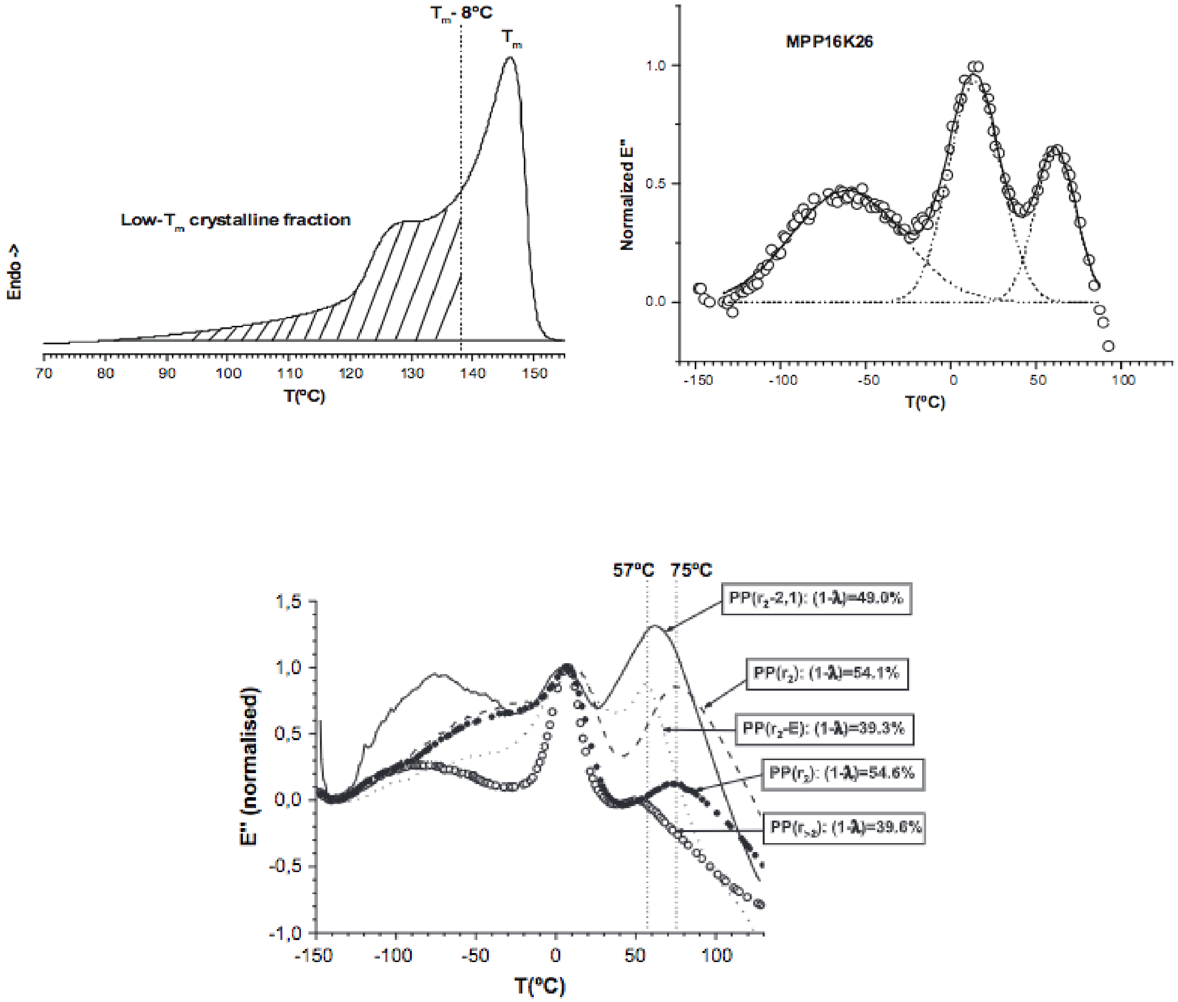

Figure 2.50: (a) DSC profile explaining how to calculate the amount of low-T_m fraction on a real sample, (b) normalized loss modulus curves (open circles: experimental data, continuous line: the fitted curve, dotted lines: deconvoluted peaks) and (c) normalized loss modulus of various structures

It has been known (see infra) that ZN catalyst displays almost zero regio-defects with stereo-defects inhomogeneously distributed, whereas metallocenes have both regio and stereo-defects homogeneously spread on the chain. Furthermore, it has also been possible to compare structures with the same amount and type of defects but with very different molar masses.

The result of this study states that the isotactic length n_{iso} plays an important role in the α-relaxation as illustrated at figure 2.51. It establishes that the total content of interruptions/defects determines the value of T_α - see 2.51(a) - where T_α has been drawn as a function of the isotactic length n_{iso} and that the intensity of the α-relaxation is mainly controlled by the crystalline distribution, provided that some molecular architecture requirements are fulfilled, i.e. the isotactic length n_{iso} is comprised in the range 20-500.

The correlation between the relative intensity of the α-relaxation and the low-T_m content illustrated by figure 2.51(b) supports the idea that the exchange of isotactic segments are at the basis of the α-relaxation and identifies the crystalline distribution as the main parameter to be controlled in order to modulate the intensity of this dynamics. Knowing also that this distribution come from the combination of the thermo-mechanical history and of the molecular architecture.

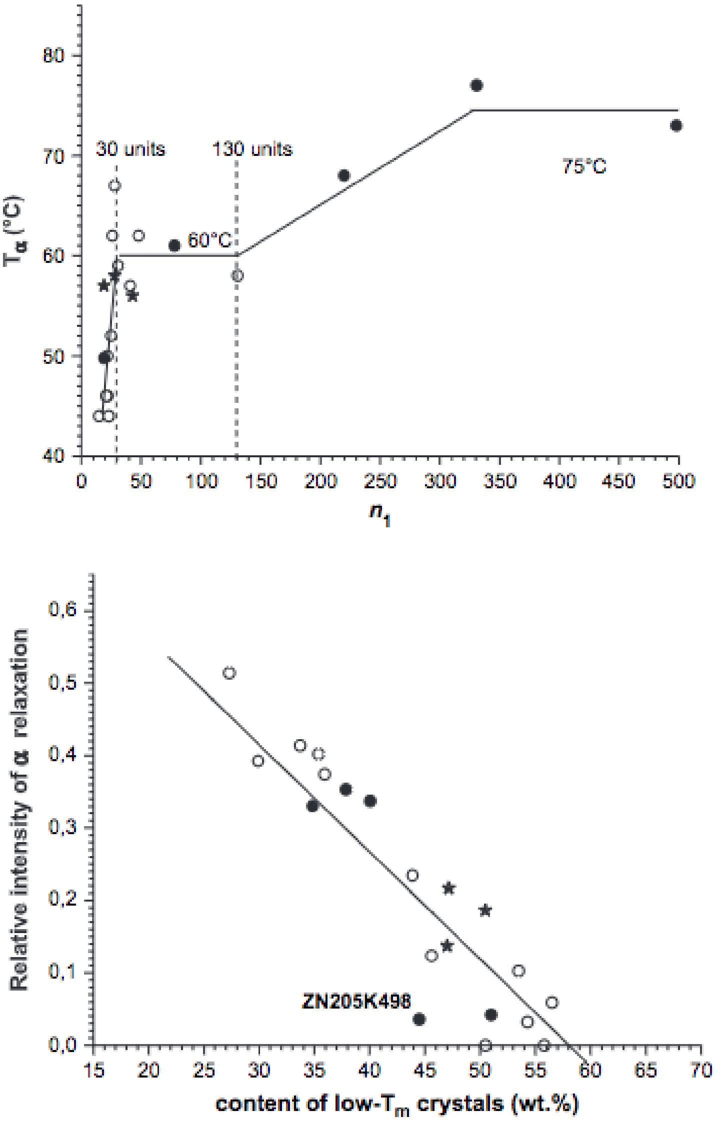

Figure 2.51: (a) T_α versus n_{iso} and (b) relative intensity α versus low-T_m content (open circles: MET, black circles: ZN, stars: copolymers)

The influence on the α-relaxation of annealing and more generally of ***the thermo-mechanical history*** has been studied by Séguéla et al [39] who has studied a $100\mu m$ film of iPP homopolymer (likely a ZN, Mw=257kDa) quenched at 30°C and annealed during 1h at 140°C. The WAXS spectra and the evolution of the DSC traces, storage modulus E' and loss factor tgδ are presented at figure 2.52.

These graphical representations are quite illustrative examples of the difference between both morphologies: on the WAXS spectra, the two broad peaks of the mesomorphic phase are well present for the quenched films and the four peaks of the monoclinic α-form for the annealed ones. For the quenched film, this is translated on the DSC traces into a small exothermic at 70°C followed by an endothermic peak at around 110°C that are characteristic to the reorganisation process of the mesophase into a monoclinic one. This latter melts at 165°C (sharp peak). For the annealed one, only one single melting peak is present at 167°C. Finally, regarding the dynamic and mechanical analyses, the two storage moduli $E'(T)$ are quite similar below the β-relaxation located around 10°C, that is the glass transition of iPP at 1hz.

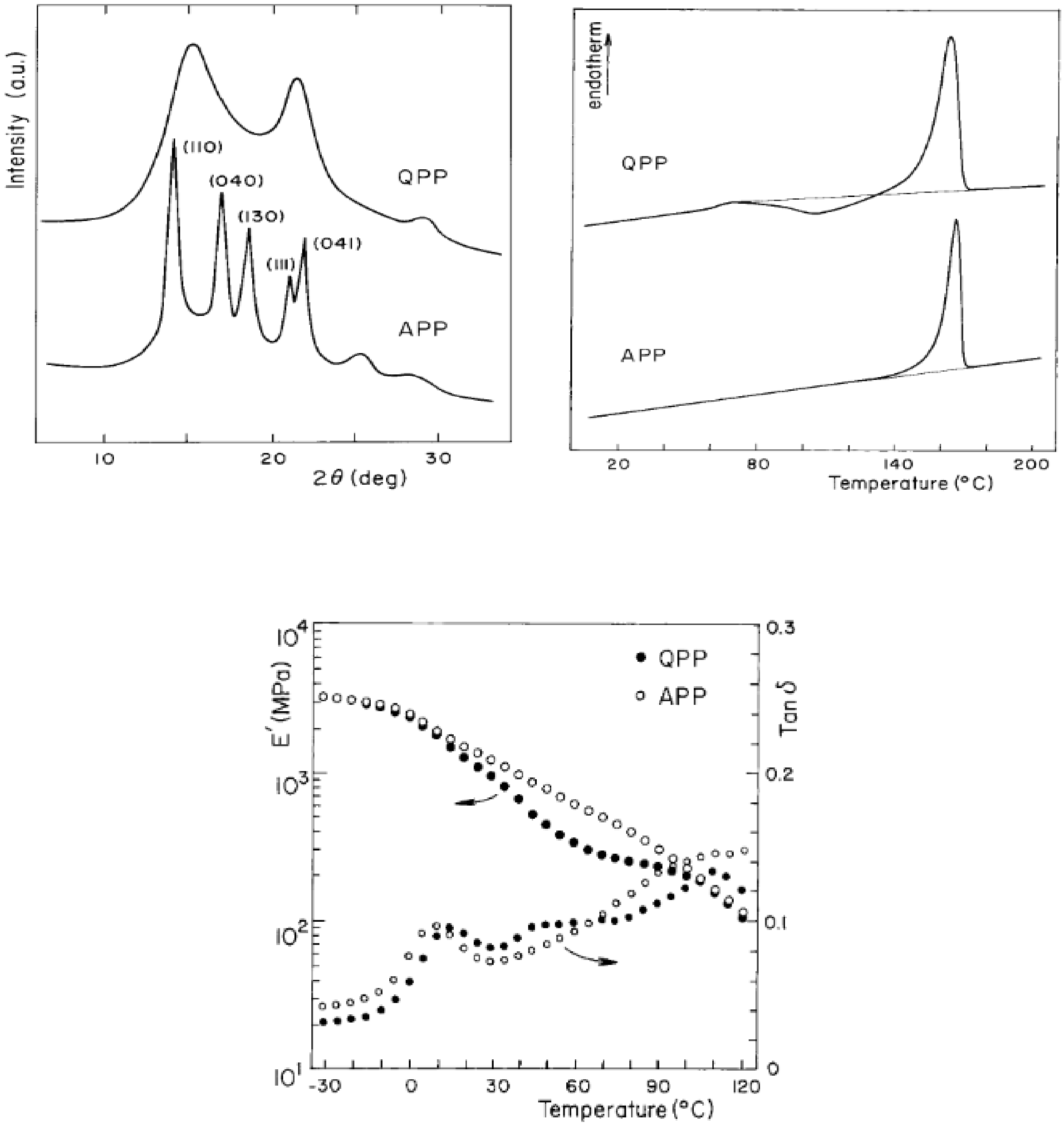

Figure 2.52: a) WAXS spectra, b) DSC traces, c) storage modulus and loss factor for respectively for quenched (black circles) and annealed films (open circles)

Above 10°C, the mobilities in the crystals are progressively activated leading to the α-relaxation. $E'(T)$ drops faster for the quenched film than for the annealed one because of the weaker elastic interactions in the mesophase than in the monoclinic one. This is confirmed by the higher tgδ level of the quenched sample between 10°C and 60°C due to higher energy dissipated by the more intense molecular movements. On the contrary, there is a limited difference in the mobility of the amorphous phase of both films. In the temperature range of 70°C and 110°C, the moduli start to converge and merge around 110°C. This is relevant to the transformation of the mesophase in the quenched sample into the monoclinic form thanks to the increasing activation of the molecular motions in the ordered phase. It can be also observed that the amplitude of the β-relaxation is the same for both samples, which means that the annealing treatment does not change significantly the amount of amorphous phase.

The mechanism of the α-relaxation can then be analyzed from the cristallographic viewpoint, via the nucleation and propagation of screw dislocations.

Chang et al [16] worked on their side on a iPP homopolymer using two processing approaches: isothermal crystallisation from the melt at various temperatures ranging between 90°C and 130°C and quenching in the water at 10°C and annealing at various temperatures ranging between 45°C and 150°C. Reminding that mesophase and polymorphs appear when cooling rate goes beyond 20K/sec, and that mesophase starts to melt around 40°C, they investigated the presence of the sole α-phase form. The expected influence of the annealing temperature on the long period and on the crystals distribution was measured via SAXS. Using a one dimension correlation function on the scattering angle data q and supposing that

$$L_p = l_c + l_a + 2l_i \tag{2.15}$$

with L_p the long period, l_c the crystal thickness, l_a the mobile amorphous phase thickness and l_i the thickness of the intermediate (i.e. rigid amorphous) phase, they were able to determine not only the long period L_p but also the thickness of the RAF phase. Among other results, in the annealing range between 60°C and 90°C, where the mesophase melts, two relaxations were clearly identified on the loss factor, T_{α_1} and T_{α_2} as displayed at figure 2.53.

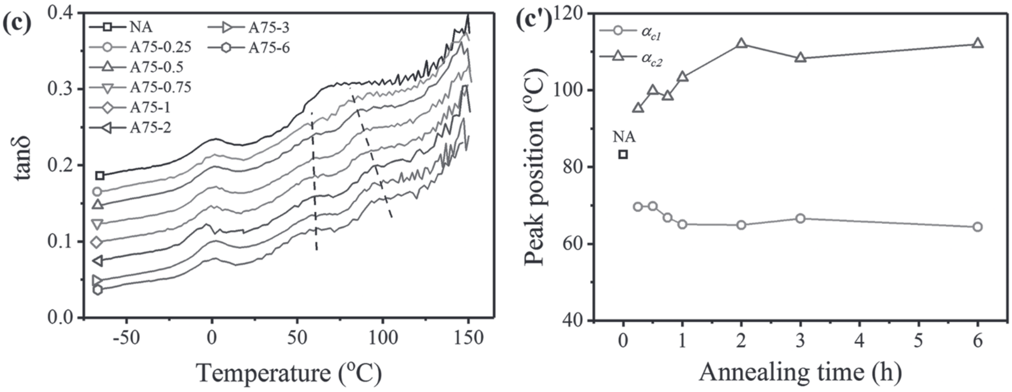

Figure 2.53: (a) Tangent of the loss factor as a function of temperature for samples quenched and annealed at 75°C for various times up to 6 h; (b) position of the peak of the tgδ

They have implemented the model of "continuum of mobility" proposed by Eposito et al [95], which assumes that polymer chains are strongly coupled between the various phases and that the continuum has a broad stress distribution. The polymer chains close to the crystals are strongly tied and the relaxation will happen at higher temperatures. The larger the distance of the polymer chains from the crystalline phase surfaces, the less they are influenced by the interfacial geometrical constraints and relax at lower temperature. This means that rather distinguishing RAF and MAF, they consider a smooth transition between those phases.

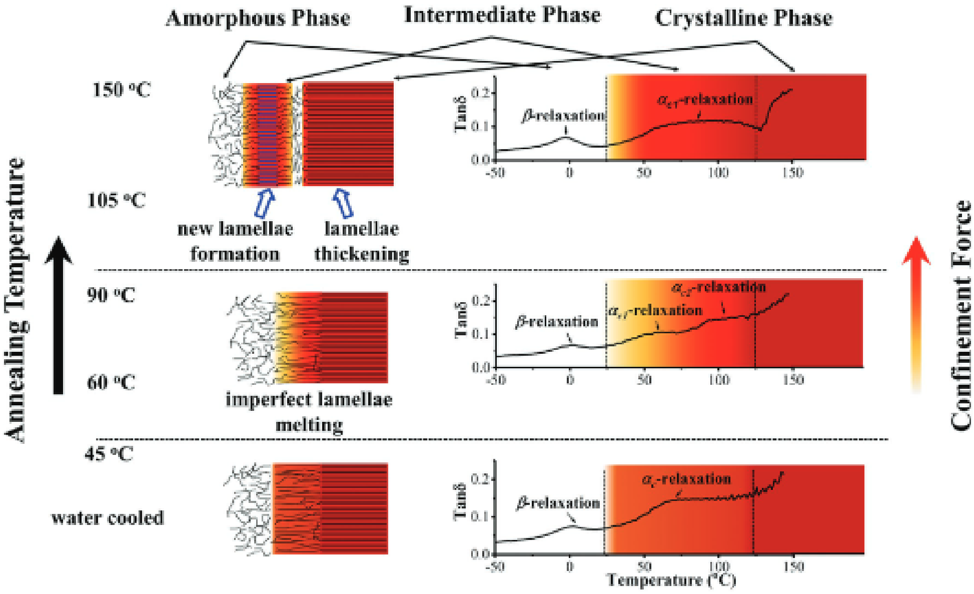

Figure 2.54: Relationship between intermediate phase and α-relaxation

The α-relaxation is described following this approach: α_1-relaxation at lower temperature could be ascribed to the helical jumps of polymer chains neighbouring the amorphous phase and α_2-relaxation at high temperature originates from the helical jumps of the polymer chains close to the crystalline phase. A schematic drawing is presented at figure 2.54.

To summarise, considering the annealing temperature T_a and the activation energy E_a :

1. for samples only quenched, polymer chains in the intermediate phase are constrained by crystallites with a broad size distribution, leading to one α-relaxation peak with $E_a = 53.4kJ/mol$
2. for $60°C < T_a < 105°C$, imperfect lamellae melting releases a part of the constraining force and two α-relaxation peaks are observed, α_1 and α_2. Both relaxation peaks shift to higher temperatures as T_a increases. The activation energy of the first mechanism E_{a1} decreases to 35.5 kJ/mol as the intermediate phase thickness increases from 2.0 to 2.2 nm
3. for $T_a > 105°C$, a new crystalline phase is formed, which enhances the constraining force on the polymer chains. The α_1-relaxation peak is broadened and its position shifts to a higher temperature. Moreover, the polymer chains between the initial and the newly formed crystalline phase are strongly confined and as a consequence, the α_2-relaxation becomes undetectable. The activation energy of the first mechanism E_{a1} decreases from 23.6 to 13.7 kJ/mol as the intermediate phase thickness increases from 2.3 to 3.0 nm.

This dependence of the activation energy to the thickness of the intermediate phase is illustrated in figure 2.55.

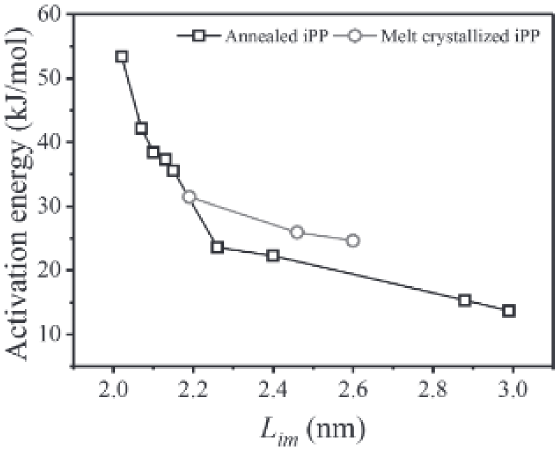

Figure 2.55: Activation energy as a function of the thickness of the intermediate phase

As a conclusion, α-relaxation depends strongly on the annealing temperature because its behaviour depends strongly on the confinement force on the polymer chains in the intermediate phase.

We would like to finalise this review with the paper of Syi and Mansfield [38] who examined the possibility to use a soliton model for the α-relaxation, not applied in many polymers and with some success to dielectric relaxations. The principle is to consider that the various molecular motions engaged in the relaxation mechanism, such as rotations and translations, as a particular case of a category of non-linear waves called solitons or solitary wave and to calculate and solve its motion equations.

Physically, the potential energy exerted by the surrounding crystalline stems on an individual one reflects the stem symmetry. For example, a complete rotation of the stem through 360° brings it back into its primary crystallographic position, as it does a translation along the chain axis through its unit-cell crystalline dimension. Other symmetries are possible in helical systems, namely screwing the helix in or out of the crystal. In the case of isotactic polypropylene, we know that it consists in a combined 120° rotation and c/3 translation, and in any case, the polymer stem finds itself moved forwards or back by one chemical repeat unit. One could consider motions within the crystal in which a stem jumps as a combined translation-rotation motion as a rigid rod - such as illustrated hereunder on figure 2.56. In other words, the motion allows the chain stem involved in the process to jump from one particular minimum energy position in the lattice to some other symmetry-equivalent position.

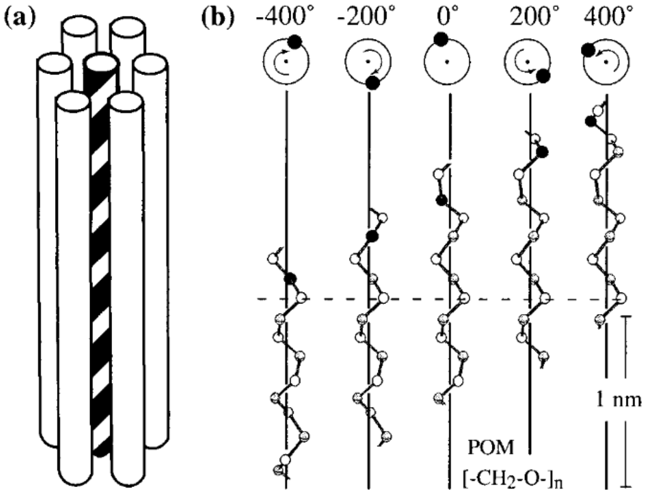

Figure 2.56: Helical jumps in crystallites [35]

The authors considered solitons producing net rotation and/or translation of crystalline polymer stems in four polymers. They were able to predict successfully the activation energy of the α-relaxation in both polyethylene and isotactic polypropylene, and to explain its absence in both syndiotactic polypropylene and isotactic polystyrene. Criteria controlling its absence or presence in any particular polymer crystal have been highlighted as 1°) the energy barrier opposing motion of each individual repeat unit of the stem, 2°) the elongational stiffness of the polymer stem and 3°) the number of bonds per repeat unit. They found that the minimum number of atoms per stem involved for the relaxation to exist is around 25 (see figure 2.57). A more careful comparison with the experimental results obtained by Hoyos et al would be interesting (see figure 2.51).

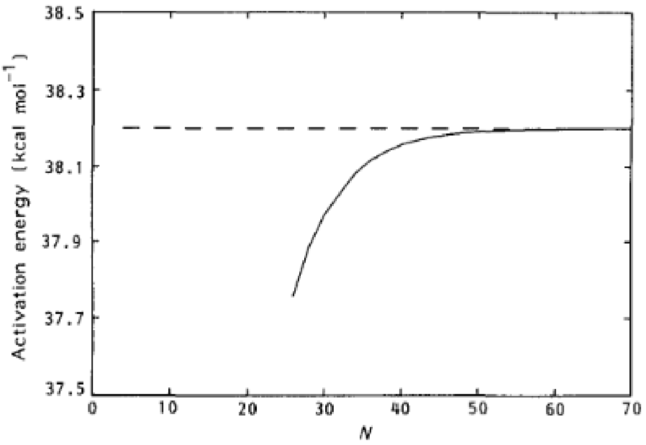

Figure 2.57: Activation energy as a function of the crystal thickness, where N is the number of atoms per stem

2.2.5 Small deformations: semi-empirical approaches of viscous flow

By controlling the conditions of time/frequency and temperature at which the tests will be performed, it is possible to better understand the influence of those variables on several values and processes, namely the viscous flow or the triggering of macroscopic plasticity. However, the tests have to be complemented in order to get a real access to the microscopic mechanisms involved at this stage. Hereunder, we describe two important theories, based on thermodynamic considerations.

The relation between the frequency f and the temperature T can be obtained from the dependence of the viscosity on the temperature. This expression is usually valid in a limited range of temperature. However, as we know, when semi-crystalline polymers are in a macroscopic solid-state, their viscous flow, and especially their yield, is obviously coupled with their microstructural components, i.e. their phases composition. Understanding how the respective phases (crystals, amorphous and mesomorphous phases) are interacting within the viscous flow, and which one is driving in a given slot of temperature or frequency because of internal molecular relaxations is not an easy task.

We review hereunder different models, that shed various lights on the behaviour of amorphous and/or semi-crystalline polymers.

Two models are presented in the following paragraphs, Williams, Landel and Ferry on the one side, and Ree-Eyring on the other side, the spotlight being put on this latter. In this paragraph, we follow mainly the references [96], [7] and [97].

First, **Williams, Landel and Ferry (WLF)** have obtained an equation that links the viscous flow of amorphous polymers to the temperature on the basis of the distribution of free volume for temperatures beyond glass transition. This distribution can be obtained by considering on the one side the probability for a free volume to have a magnitude larger than a specific value as expressed by Doolittle equation and on the other side the existence of a minimal free volume that is trapped into the polymer in its glass-like state. Indeed, according to Doolittle, the probability P for a free volume V_f to be larger than a given value V_{f0} can be expressed as

$$P = e^{-V_{f0}/V_f} \tag{2.16}$$

According to WLF, the free volume resulting from the creation of vacancies at temperatures above glass transition T_g is related to a minimal free volume V_{fg} and to the difference $\Delta\alpha$ between the thermal coefficients in the rubber-like and glass-like domains:

$$V_f = V_{fg} + \Delta\alpha(T - T_g) \tag{2.17}$$

Combining equations (2.16) and (2.17) leads to

$$P = exp\left(-\frac{V_{f0}}{V_{fg} + \Delta\alpha(T - T_g)}\right) \tag{2.18}$$

The viscosity η being inversely proportional to the probability P leads to the WLF equation

$$log\frac{\eta(T)}{\eta(T_g)} = \frac{-C_1(T - T_0)}{C_2 + (T - T_0)} \tag{2.19}$$

This equation is also quite often written as:

$$loga_T(T) = \frac{-C_1(T - T_0)}{C_2 + (T - T_0)} \tag{2.20}$$

Secondly, the **Ree-Eyring** theory is a theory of displacement and deformation linking the stress σ, the strain rate $\dot{\epsilon}$ and the temperature T. It was built in two steps and has been widely used for amorphous and semi-crystalline polymers, and modified since then: first the Eyring theory, then the Ree-Eyring theory as explained in the next pages.

Eyring has first based its description [98], [99] of the viscous flow by considering the way each segment of macromolecule has the freedom to move whereas each is prevented to do so because of the binding forces with other segments of macromolecules. In order to get a segment moving from position (1) to the close equilibrium position (2), a potential barrier E_a has to be overcome and the same amount of energy E_a has to be supplied[23].

Eyring assumes that the potential barrier is a symmetric one and that equilibrium positions (1) and (2) are separated by a constant distance λ at the temperature T_β. The displacement that is required to reach the top of the potential barrier is therefore $\frac{\lambda}{2}$ as illustrated at figure 2.58.

When there is no stress applied to the macromolecule (figure 2.58a), the segments move under the influence of thermal agitation (brownian motion) that leads to diffusion phenomenon. The probability for one segment to move is:

$$P = e^{-E_a/kT} \tag{2.21}$$

As the diffusion is totally random and homogeneous in the material no change is observed at the macroscopic scale.
When a stress is applied, this is no more the case (figure 2.58b).

---

[23] it should be highlighted that the height of the potential barrier is usually assimilated to the potential energy and more rarely to the enthalpy of the system which means that entropy contribution is usually ignored

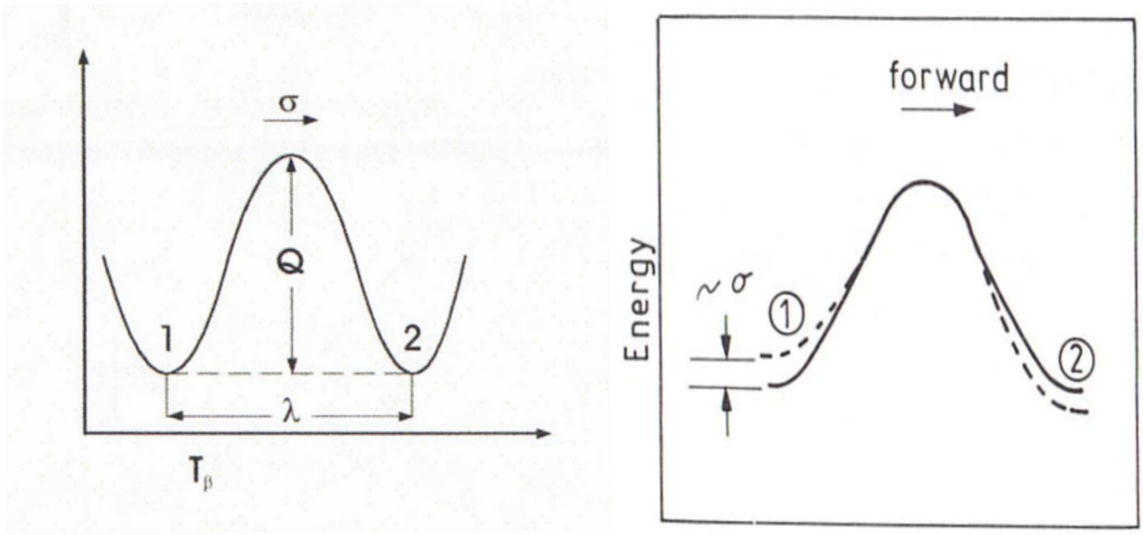

Figure 2.58: From left to right: (a) energy barrier between 2 equilibrium position 1 and 2 (with $Q \equiv E_a$) [97] and (b) influence of a stress on the decrease of the potential barrier in the flow direction [25]

The application of a stress σ will cause the apparition of a force vector, which direction will depend on the direction of the constraint applied to the segment. The work to be performed by the force is considered as equal to the potential energy. It will be positive or negative and the probabilities for the segment to cross the barrier become:

$$P_{1\rightarrow 2} = e^{-(E_a - W_\sigma)/kT} \tag{2.22}$$

$$P_{2\rightarrow 1} = e^{-(E_a + W_\sigma)/kT} \tag{2.23}$$

with k the Boltzmann constant (the perfect gas constant R could also be used) and W_σ the work performed by the force when the top of the barrier has been reached.

The deformation of the material is proportional to the difference of displacements (1) → (2) and (2) → (1), and can be written:

$$P_\sigma = P_{1\rightarrow 2} - P_{2\rightarrow 1} \tag{2.24}$$

or

$$P_\sigma = 2exp(-\frac{E_a}{kT})sinh\frac{W_\sigma}{kT} \tag{2.25}$$

If ϵ_0 is the shift corresponding to the elementary displacement of the segment from position (1) to position (2), $\frac{\epsilon_0}{2}$ the shift needed to reach the top of the potential barrier and V_0 the volume associated to the segment, then the work of the stress σ needed to reach the top of the potential barrier, acting on the shift plane of the segment and aligned with it can be expressed as:

$$W_\sigma = \frac{\epsilon_0 V_0 \sigma}{2} \tag{2.26}$$

The segment vibrates in the bottom of a symmetric potential, though it becomes asymetric when the stress is applied. If its energy is high enough, it can overcome the potential barrier. At each oscillation, it has the opportunity to cross the barrier once from left (1) to right (2) and once from right (2) to left (1). Let us consider J_0 as its vibration frequency. The frequency N of displacements excess in the direction of the stress is:

$$N = 2J_0 P_\sigma = 4J_0 e(-\frac{E_a}{kT})sinh\frac{\epsilon_0 V_0 \sigma}{2kT} \tag{2.27}$$

The deformation rate $\dot{\epsilon}$ is therefore equal to

$$\dot{\epsilon} = \epsilon_0 N \tag{2.28}$$

$$\dot{\epsilon} = 4\epsilon_0 J_0 e(-\frac{E_a}{kT})sinh\frac{\epsilon_0 V_0 \sigma}{2kT} \tag{2.29}$$

This relation can be simplified in 2 extreme cases:

1°) if $\sigma << 2kT/\epsilon_0 V_0$

$$sinhx \simeq x \tag{2.30}$$

and

$$\dot{\epsilon} \simeq 4\epsilon_0 J_0 e(-\frac{E_a}{kT})\frac{\epsilon_0 V_0 \sigma}{2kT} \tag{2.31}$$

or

$$\sigma \simeq \frac{kT}{2\epsilon_0^2 J_0 e(-E_a/kT)V_0} = \eta\dot{\epsilon} \tag{2.32}$$

which is the newtonian viscosity and is valid below T_g

2°) if $\sigma >> 2kT/\epsilon_0 V_0$, i.e. close to the yield point,

$$sinhx \simeq \frac{e^x}{2} \tag{2.33}$$

and

$$\dot{\epsilon} \simeq 2\epsilon_0 J_0 e(-\frac{E_a}{kT})e(\frac{\epsilon_0 V_0 \sigma}{2kT}) \tag{2.34}$$

This relation can still be written as:

$$\frac{\sigma}{T} = A^*(ln2C\dot{\epsilon} + \frac{E_a}{kT}) \tag{2.35}$$

with $A^* = k/V_0$ and $C = 1/\dot{\epsilon}_0$.

This equation encloses three adjustable parameters: A^*, C and E_a and is valid for a large range of temperatures except in the vicinity of T_g.

However, the theory elaborated by Eyring looked at one mechanism only and did not give results good enough in case of experimental deviations (this was especially the case for amorphous polymers at low temperatures). Modifying this theory into the well known "**Ree-Eyring theory**" the two authors involved the possibility to have deformation as the result of various molecular displacements combined together. In this case, each mechanism was translated into a different set of parameters, corresponding to each type of associated movement. Their main result was that the various processes terms are additive in the equation. This means that, assuming that N processes are involved in the viscous flow occurring at yield point and that each process i is associated with one relaxation time, it is possible to rewrite the Ree-Eyring equation as [100]:

$$\frac{\sigma}{T} = \sum_{n=1}^{N} A_i^*(ln2C_i\dot{\epsilon} + \frac{E_a^i}{kT}) \tag{2.36}$$

with $A_i^* = k/V_0^i$ and $C = 1/\dot{\epsilon}_0^i$ the constants of the process i and $\sigma >> A_i^* T$.

The physical meaning of these parameters can be highlighted by some observations:
1°) in the amorphous polymers, the activation energies E_a associated to the secundary transition β are identical to the one calculated via the dynamic mechanical analysis [101]
2°) in semi-crystalline polymers, the theory works as well in the range of the upper glass transition (corresponding to the mechanisms in the crystalline phase) and it has been demonstrated that in the presence of a threshold at high temperatures, the activated volume is similar to the volume of crystalline phase undergoing a fusion when the yield is reached [100]. An explanation taking into account the entropic aspects of the model is presented in chapter 4.

2.2.6 Time-temperature superposition or the method of the composite master curve

It is time now to present briefly the consequences of the dependence on temperature of viscoelastic functions and more generally of stress-strain curves.

The viscoelastic behaviour of high polymers can be modelled by more or less complex systems of springs and dashpots. The link between temperature and frequency (i.e. relaxation spectrum) can be obtained from the evolution of the viscosity with temperature, within a specific range [102].

In amorphous polymers, we know that under the glass transition temperature, the backbones of the polymer chains are immobilized and that none of the large changes in viscoelastic properties with time or frequency are observed. These tremendous changes appear in the transition zone, between the glass-like and rubber-like states. This behaviour can be understood qualitatively on the basis of relaxation and retardation times as these components of the viscoelastic spectra decrease rapidly with increasing temperature.

At low temperature, practically no configurational changes occur under deformation, the dynamic modulus $E'(\omega)$ is close to its equilibrium value E_e and $tan\delta$ is close to zero. At high temperatures, which correspond to mechanisms where a large number of molecular motions can occur, the relaxation spectrum H makes an important contribution to the relaxation modulus: E' becomes quite low, whereas E'' and tgδ increase dramatically.

However, a change in temperature can leave the shape of the relaxation spectrum unaltered, only shifting it along the time axis.

These specificities trigger the possibility to considerably enlarge the effective time or frequency scale available for experimental measurements and allow separating time from temperature on which viscoelastic properties relay. This experimental principle is called "*time-temperature superposition*" or "*thermorheological simplicity*" or *method of reduced variables*" or "*method of composite curve*", and should not be confused with the Boltzmann superposition principle.

2.2.7 Origin of the method of reduced variables

According to Ferry [102], the time-temperature superposition method, though demonstrated first experimentally, can be deduced, depending on the polymer under consideration, either from the dilute-solution theories for flexible random coils or from the theory for undiluted polymers (i.e. amorphous polymer with a low molecular weight that does not allow for the entanglement coupling to occur). It says schematically that all the contributions to the dynamic modulus E' should be proportional to the temperature and the density of the polymer ρ, and all relaxation times should have the same temperature dependence. This dependence is very largely due to changes in the friction coefficient of the monomeric entity of the polymer with temperature. The effect of shifting from temperature T to T_0 is to multiply E' by $T_0\rho_0/T\rho$, the density ratio being directly linked to the thermal expansion, and multiply the frequency scale by a shift factor a_T where this latter depends on the temperature, the monomeric friction coefficient, and mean square end-to-end distance per monomeric unit. Ferry observe that the proportionality of modulus and the assumption of one single friction coefficient "*are general principles that can be applied without assuming that the form of the time or frequency dependence follows any prescribed function*".

When applied to high polymers, i.e. polymers which the molecular weight is high enough so as to allow entanglement coupling to appear, the behaviour of the relaxation function has very schematically three main relaxation areas in its relaxation spectrum H as represented at figure 2.59.

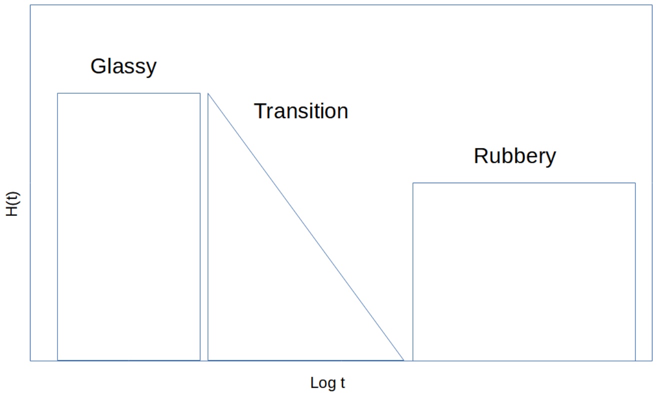

Figure 2.59: Schematic drawing of the relaxation spectrum H versus $log(t)$ for an amorphous polymer covering the glassy state, the T_g region and the rubbery plateau (inspired from [25] p.66)

In the transition zone, the relevant motions are governed by the monomer friction coefficient. The scheme is different in the terminal or rubbery zone when the polymer is molten, where the movements are governed by the friction coefficient of the entangled monomeric chains. The question of knowing if the same shift factor can be applied in both regions depends ultimately on the dependence of entanglement coupling to temperature. In the vicinity of the glassy zone, the configurational rearrangements of the polymer chains cannot be anymore related to the sliding of flexible chains. Furthermore, when other viscoelastic mechanisms are activated (side groups f.i.), two types of temperature dependence superposed on each other should be considered.

2.2.8 The shift factor and the Arrhenius equation

The Williams-Landel-Ferry equation has been assumed to be valid for amorphous polymer at temperatures between T_g and $T_g + 100$. For temperatures well below T_g, the influence of temperature on the position of relaxation curves along time scale cannot be described anymore by the WLF-equation, and the relaxation time is assumed to be following the Boltzmann statistics. This is the so called Arrhenius equation for the shift factor a_T

$$a_T(T) = exp(\frac{E_a}{R}(\frac{1}{T} - \frac{1}{T_0})) = \frac{f(T_0)}{f(T)} \tag{2.37}$$

with E_a the activation energy of the mechanism, R the gas constant and the shift factor being the ratio between the frequency at the reference temperature T_0 and the frequency at the considered temperature. This relation is usually used for secondary transitions of amorphous polymers and for the upper glass transition (i.e. α-transition) in semi-crystalline polymers. The activation energy can also enclose an entropy factor and is in this case an enthalpy rather than a potential energy.

In highly crystalline polymers, different mechanisms have different temperature dependence (motions in the crystal lattice, viscous flow of amorphous regions between crystalline lamellae f.i.). The structure of semi-crystalline polymers is rather sensitive to changes in temperature and they are linearly viscoelastic only at very low strain levels. The contribution of relaxation modulus decreases with increasing temperature as in glasses, but due to crystals, the macroscopic properties encompasses in reality a composite system. "*With extensive precise data, it is possible to analyze separate contributions with different temperatures dependence and determine their activation energies*"[69]. Empirically though, the composite curve is often achieved with vertical and horizontal shifts for a given viscoelastic function, "*but theoretical guides for performing such a manipulation are rather tenuous* "[69]. The numerous measurements performed on semi-crystalline polymers have demonstrated that, even in the glass transition region, the change of the viscoelastic function does not translate into steep changes in the slope: the curves are rather flat and broad. As has been examined at section 2.2.4 on the visco-elastic behaviour of iPP, this may be due to the cross-linking effect and filler action of the crystallites which impose a reduction in the segmental mobility.

2.2.9 Time-temperature superposition in practice

We have seen that the physical signification of time-temperature superposition means that it is possible to call for a mechanism either by increasing (or decreasing) the frequency or by decreasing (or increasing) the temperature. The point is to be cautious and to ensure that identical mechanisms are compared together and that the microstructure of the material remains constant. These are two pitfalls to be avoided especially when viscoelastic curves are overlapping when the frequency or the temperature is varied. This is why this kind of test is carried out at constant temperature and varying frequency, or the dependence to the temperature ramp of the microstructure is carefully checked.

Practically, applying a shift factor from an isothermal curve measured at T_0 to another isothermal curve measured at T_1 will lead to a so called master curve covering a broad range of strain rates or frequencies.

This is illustrated by the figure 2.60.

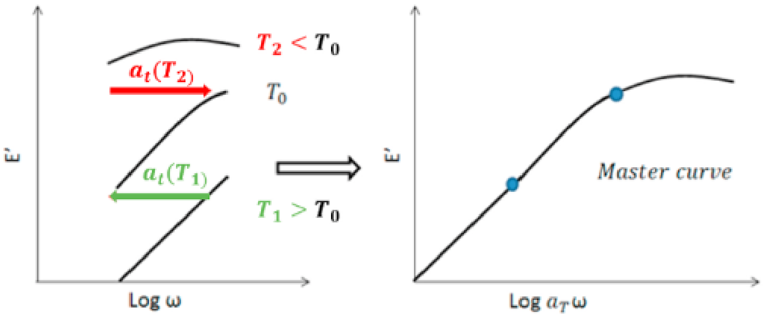

Figure 2.60: Building principles of a master curve [103]

The various relaxation times τ associated to a specific mechanism depend in the same way on the temperature according to the equation:

$$\tau(T_0) = a_T^*(T, T_0).\tau(T) \tag{2.38}$$

where T_0 is the reference temperature and $\tau = \frac{1}{f}$. Similarly, we can write:

$$\frac{1}{f}(T_0) = a_T^*(T, T_0).\frac{1}{f}(T) \tag{2.39}$$

We can thus write a similar expression for the frequencies $f(T)$:

$$f(T_0) = a_T(T, T_0)f(T) \quad or \quad a_T(T, T_0) = \frac{f(T_0)}{f(T)} \tag{2.40}$$

For each master curve, it is therefore possible to define a couple (shifted frequency, viscoelastic property considered). In the case of figure 2.61 that deals with a single crystal mat of PE, the presence of a single mechanism can be easily seen, as the loss factor amplitude and shape remain constant across the frequency range.

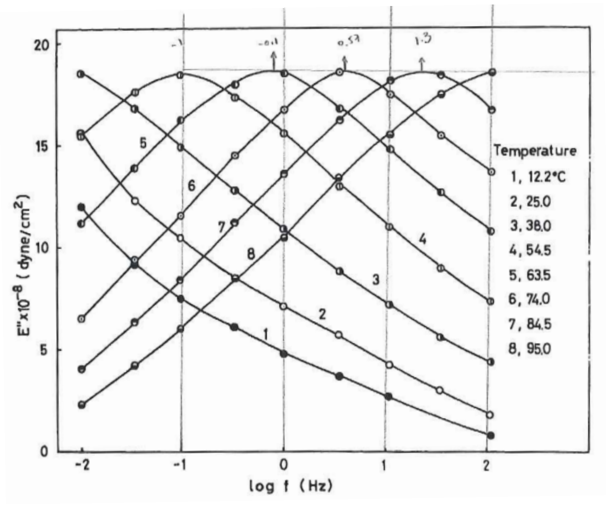

Figure 2.61: Isothermal curves of viscous modulus E" as a function of $logf$ for various temperatures [104]

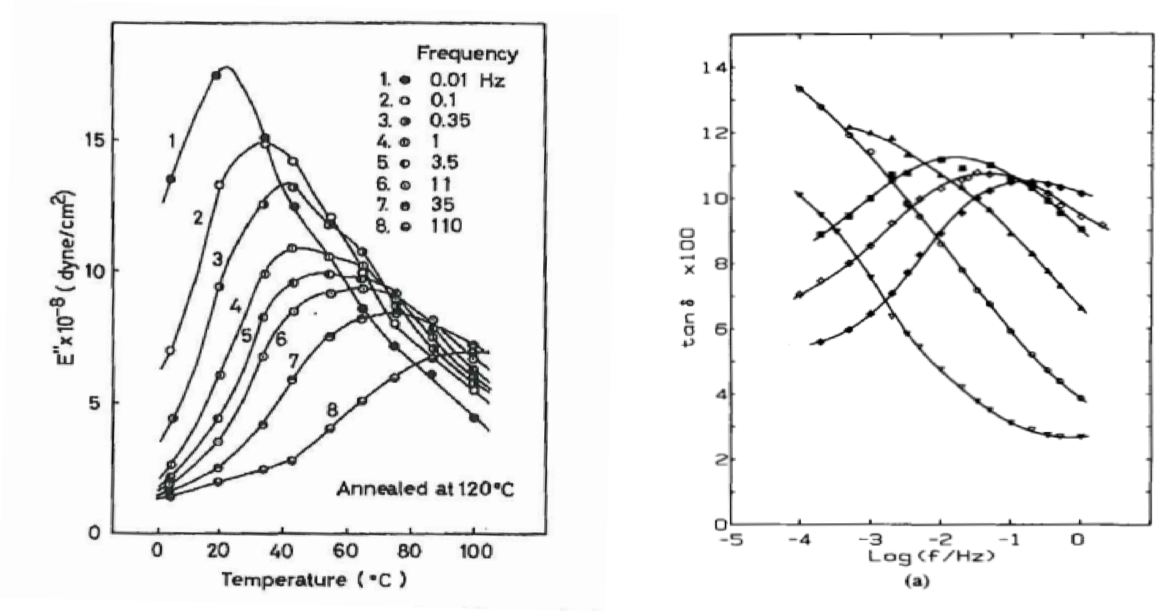

Figure 2.62: (a) The two α_1 and α_2 transitions in PE measured with the loss modulus E" as a function of temperature [104] and (b) the evolution of isothermal $tan\delta$ curves as a function of the frequency in iPP [71]

However, it is not always so obvious to get this type of curve and usually, several mechanisms are competing, as illustrated at figure 2.62(a) where two mechanisms are present, α_1 and α_2, the first one being emphasized at high frequencies or low temperatures and the second one at high temperatures/low frequencies.

The same type of transitions has been studied for iPP (f.i. [71], [80]) though to a really less extend than PE. This is illustrated in the case of an isotactic polypropylene [71] with similar properties as ours in the figure 2.62(b) and the table 2.63 below.

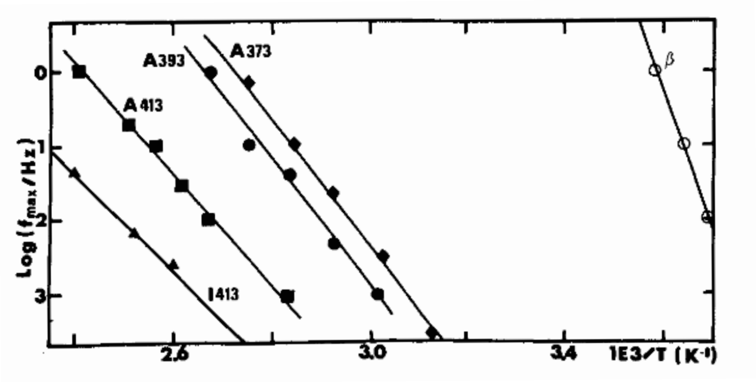

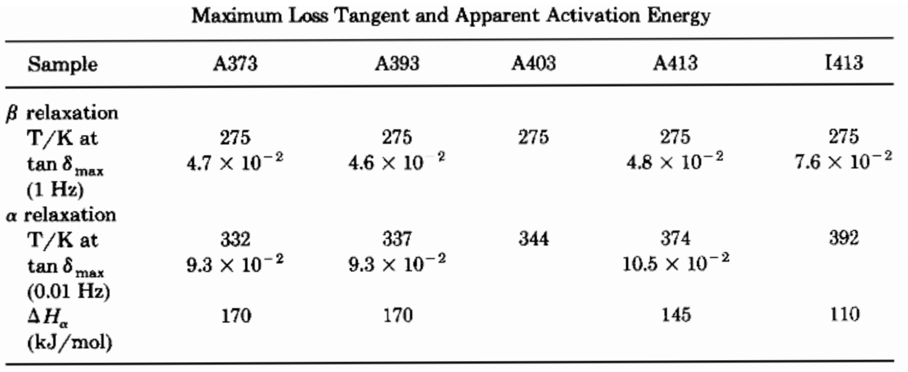

Maximum Loss Tangent and Apparent Activation Energy

Sample	A373	A393	A403	A413	I413
β relaxation					
T/K at	275	275	275	275	275
tan δ_{max}	4.7×10^{-2}	$4.6 \times 10^{\ 2}$		4.8×10^{-2}	7.6×10^{-2}
(1 Hz)					
α relaxation					
T/K at	332	337	344	374	392
tan δ_{max}	9.3×10^{-2}	9.3×10^{-2}		10.5×10^{-2}	
(0.01 Hz)					
ΔH_α	170	170		145	110
(kJ/mol)					

Figure 2.63: Top: Evolution of a_T as a function of $\frac{1}{T}$ and bottom: summary of activation parameters at various annealing ("A") and isothermally undercooled ("I") temperatures [71]

Though large similarities in the approach by the respective communities of solid and molten states, there are also somewhat differences, besides the type of solicitation: whereas the solid state community is used to deal with large ranges of temperatures and more narrow ranges of frequencies or strain rates, it is the contrary in the community of the rheologists. Also, storage and viscous modulus E', E" as well as tgδ are the preferred properties in the solid state, the phase angle δ together with G', G" are used as physical signatures to characterise the viscosity of the molten state considered. Keeping in mind a very simple type of Kelvin-Voigt, Maxwell or Zener models, when δ is approaching 0°, the material tends towards a pure elastic behaviour, whereas when it approaches 90°, it tends towards a pure viscous behaviour.

In order to show the mechanics of the master curve building, we follow the explanation given by Kessner et al in their article [105].

For thermorheological simple materials, i.e. polymers which all the relaxation times depend in the same way on temperature, the thermorheological behaviour follows equations (2.38) and (2.40). "*In order to determine reliable and comparable activation energies, the evaluation method is crucial*" because this quantity is the link with the molecular structure (or microstructure in the case of the solid state). Some literature uses, besides the shift factor along the frequencies a shift factor along the moduli. As already said, this has been quite controversial and in order to circumvent this pitfall, $tan\delta(\omega, T_0)$ or rather $\delta(\omega, T_0)$ is used:

$$tan\delta(\omega, T_0) = tan\delta(a_T\omega, T_0) \tag{2.41}$$

The activation energy E_a can be determined as the slope of the phase angle δ measured as a function of ω at different temperatures, and drawn as a function of $\frac{1}{T}$ according to the following equation:

$$\frac{\omega(T_0)}{\omega(T)} = exp(\frac{E_a}{RT}) \tag{2.42}$$

as illustrated at the figure 2.64 with ω the angular frequency.

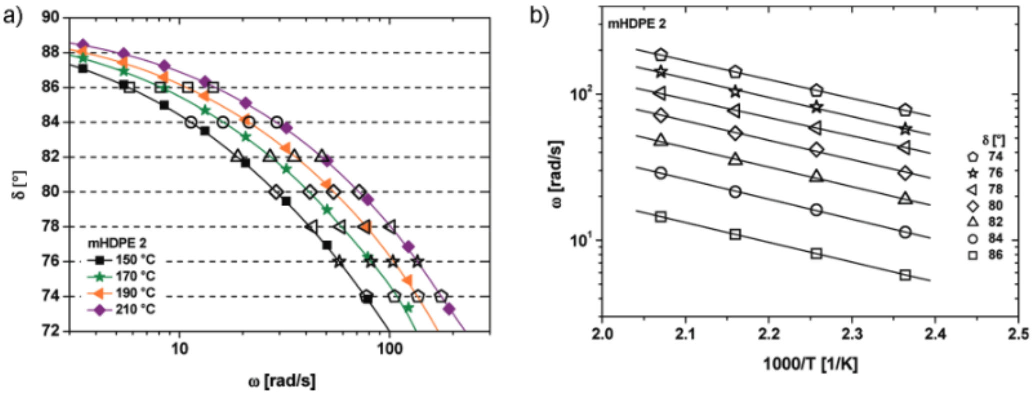

Figure 2.64: (a)δ as a function of $log\omega$ for increasing temperatures (bottom-up) and (b) ω as a function of $\frac{1}{T}$ for increasing δ (top-down in the graph) [105]

It can be observed from figure 2.64(a) that when δ increases or decrease, related relaxation times increase or decrease and from (b) that the slope is the same for all the curves, i.e. for all the values of δ used in this experiment.

Once the activation energies has been calculated, it is possible to plot E_a as a function of δ. When it is constant, it means that the mechanism at stake is "pure", as illustrated at figure 2.65.

According to the authors, this method is very powerful and sensitive to small differences, and its sensitivity can be exploited in the case of thermorheological complex polymers, if the range of frequencies ([and temperatures]) matches the internal time scales of the mechanisms at stake. We will see in the chapter 4 how this has been applied in the case of our polymers, and the obstacles that had to be overcome, keeping in mind that the movements considered in the molten and solid states are not the same.

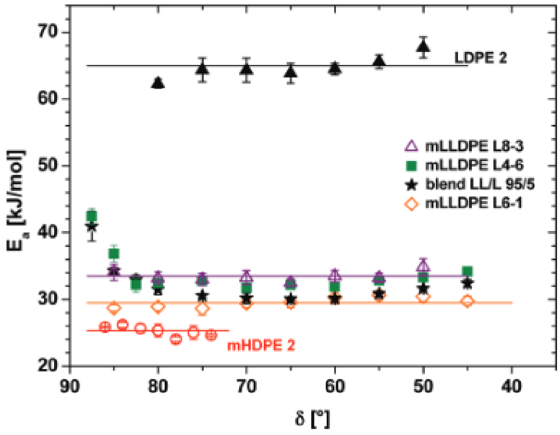

Figure 2.65: Activation energy E_a as a function of the phase angle δ [105]

2.3 Solid state microstructure of semi-crystalline polymers: application to isotactic polypropylene

2.3.1 The structure of the condensed matter: a brief overview

According to Wunderlich [106], when dealing with condensed matter physics, (macro)molecules can be categorized into small and large, rigid and flexible as illustrated in figure 2.66 where the type of polymeric macromolecules that we are dealing with in this work are considered as "large" and "flexible molecules".

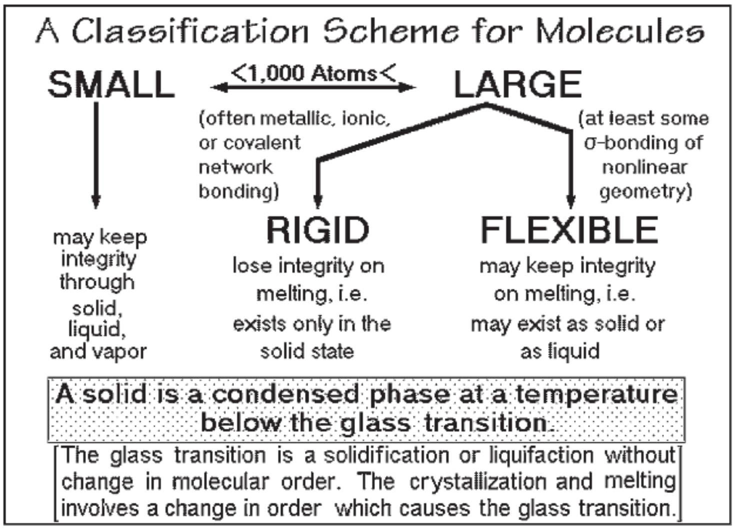

Figure 2.66: Types of (macro)molecules based on size and flexibility [106]

Semi-crystalline polymers are known to be materials that are composed of various (meta)stable multiphasic structures with superstructures going from macroscopic scale to nanometers. The figure 2.67(a) illustrates schematically the nature of the phases and their transitions, based on their molecular structure and motion. Moving top-down on this figure, and disregarding the gas phase, the phases are referred as solid, crystals and liquids. The mesophase has a special status and is drawn in blue and in orange on this scheme. According to [107], the thermodynamic analysis of phases and their changes can be based on the understanding of the glass transition and of the disordering transitions.

There are various types of solids and various types of mesophases [106], [108]. The amorphous solids (glass) has only short-range order. The fully ordered crystal shows long-range, three-dimensional order.

When the temperature is increased, the metastable mesophase can undergo, depending on its nature (glass or crystal), a glass transition or a melt. In both cases, there is a change in molecular or conformational mobility (enthalpic process) though in the case of the crystal, order is also lost (entropic process).

The liquid crystals are liquids with a small degree of orientational order, plastic crystals have a large degree of orientational disorder, and condis crystals a partial or complete conformational disorder[24]. The characteristics of these three mesophases and their mutual links via phase transitions are summarized in figure 2.67(b).

In their solid state, semi-crystalline polymers can be considered as globally metastable, multiphasic systems with phases ranging from micrometers to nanometers as illustrated at figure 2.68. Because of solidification conditions will determine the polymer macroscopic solid state structure, it is of utmost importance to understand the thermodynamic status of the phases, equilibrium or non equilibrium, because depending on it, irreversible transitions will occur or not during further thermomechanical history. Non-equilibrium states are reached by hindering the transition to thermodynamically more stable states, characterized by a lower free enthalpy G.

---

[24] There are various types of order (or disorder): orientational order refers to the alignment of the crystal with an average orientation; positional order refers to the extent to which the position of an average molecule or group of molecules shows translational symmetry (see https://uh.edu/ chembi/liquidcrystals.pdf), and conformational disorder refers to a "structural disorder, i.e. any deviation from the ideal three-dimensional regularity of the crystal structure, resulting from the statistical coexistence within the crystals of identical configurational units with different conformations" (see IUPAC gold book.)

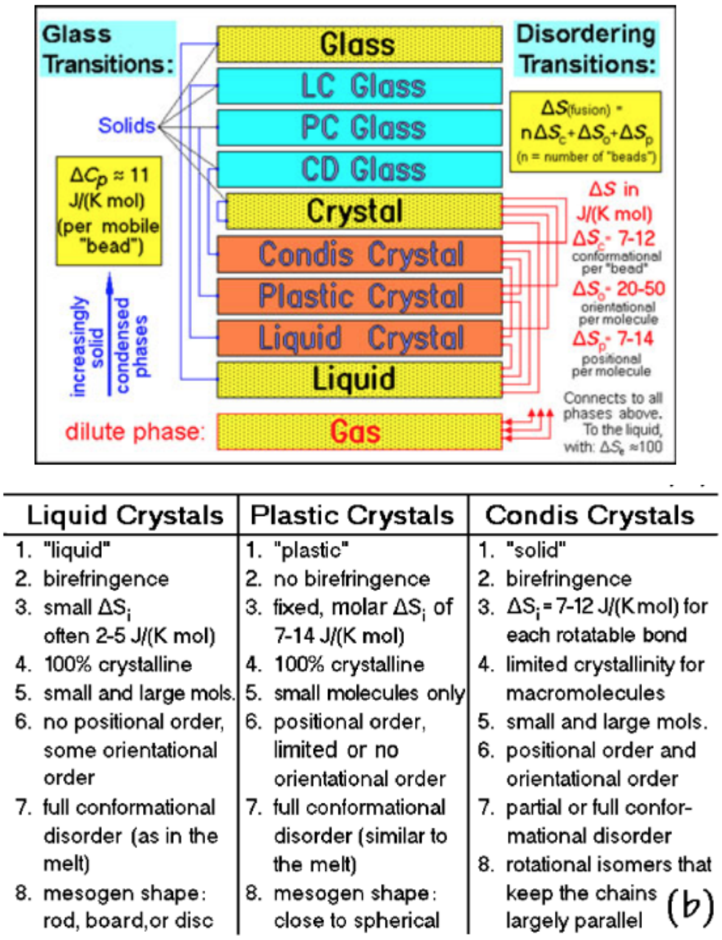

Liquid Crystals	Plastic Crystals	Condis Crystals
1. "liquid"	1. "plastic"	1. "solid"
2. birefringence	2. no birefringence	2. birefringence
3. small ΔS_i often 2-5 J/(K mol)	3. fixed, molar ΔS_i of 7-14 J/(K mol)	3. ΔS_i = 7-12 J/(K mol) for each rotatable bond
4. 100% crystalline	4. 100% crystalline	4. limited crystallinity for macromolecules
5. small and large mols.	5. small molecules only	5. small and large mols.
6. no positional order, some orientational order	6. positional order, limited or no orientational order	6. positional order and orientational order
7. full conformational disorder (as in the melt)	7. full conformational disorder (similar to the melt)	7. partial or full conformational disorder
8. mesogen shape: rod, board, or disc	8. mesogen shape: close to spherical	8. rotational isomers that keep the chains largely parallel

Figure 2.67: (a) Classification of phases and their transition, based on molecular structure and large-amplitude motions and (b) list of the typical properties of the three mobile mesophases [107]

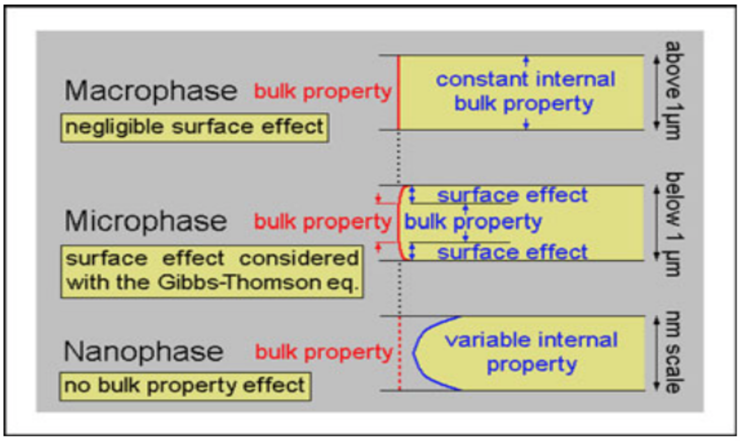

Figure 2.68: Effect of different phase dimensions on the properties within the phases [107]

The polymer molecules are usually longer than one $1\mu m$, cross the boundaries and decouple at the interfaces between the various phases, i.e segments of different lengths become independent from each other. This decoupling is usually not complete and, according to its level, will have various ranges of influence across the interfaces (see infra).

Regarding morphologies, crystals can be present as lamellar (single lamellae, hedrites, spherulites, dendrites), fibrous or nodular structures. The crystals are in most cases much smaller than the molecules. This means that, during crystallisation, the molecules are forced to form, from crystal nucleation seeds, either extended-chain crystals, fold-chain lamellae, fringed micelles, or intermediate crystal-forms [18], [109].

One possible representation of the various phases is presented at figure 2.69 (reworked from [110]).

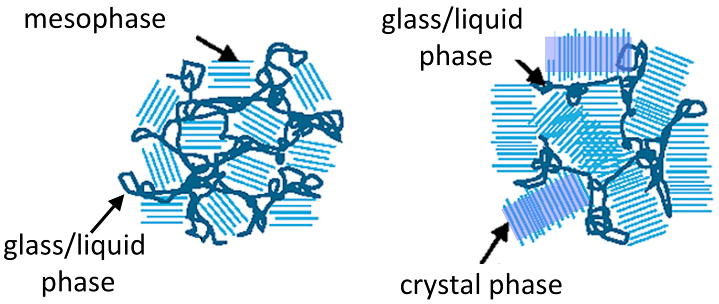

Figure 2.69: (a) Glass or liquid and mesophase and (b) glass or liquid and crystal phase; the filled blue color represents the crystal [110]

To understand those systems, it is important to know the crystal structures and the molecular motions. Let us observe that the field of crystallisation modeling is currently flourishing and old theories revisited [111].

A full thermodynamic description must consider the global, usually non-equilibrium nature of the sample and separate the different phases contributions. From this viewpoint, polymeric crystals can be characterised by their melting behaviour and non-crystalline phases by their glass transition T_g. When the coupling between crystalline and non-crystalline phases is weak, i.e. when segments of macromolecules of different lengths can act as independent components, the crystals are surrounded by an amorphous phases that is mobile and in the molten state above its T_g. It is called the *mobile amorphous fraction (MAF)*. This amorphous phase shows a broadening of the glass transition at higher temperatures. When the coupling is stronger, non-crystalline material remain solid at the transition of the bulk-amorphous phase and form a separate rigid-amorphous nanophase or *rigid amorphous fraction, RAF* (previously called "amorphous-crystal defect" because of its close coupling to crystal). The RAF undergoes its glass transition either below, at or even above the melting temperature and when present, the semi-crystalline polymers consist in a system of three or more type of phases with their own relaxation characteristics due to the coupling between the phases. From this perspective, a more general approach of decoupling can be elaborated, that will influence the final material microstructure.

When macromolecules are totally relaxed as in the molten (amorphous) state, they are considered to be in thermodynamic equilibrium. When the temperature is decreased close to glass transition, the cooperative large-amplitude movements slow down. Depending on molecular structure, their large amplitude motion can be constituted with intramolecular conformational movements. In the glassy or crystalline solid state, the small amplitude thermal motions can be separated into groups of vibrations and skeletal vibrations. The group vibrations are usually independent of the degree of disorder, and are therefore similar in glasses and crystals.

Figure 2.70 illustrates such types of motions.

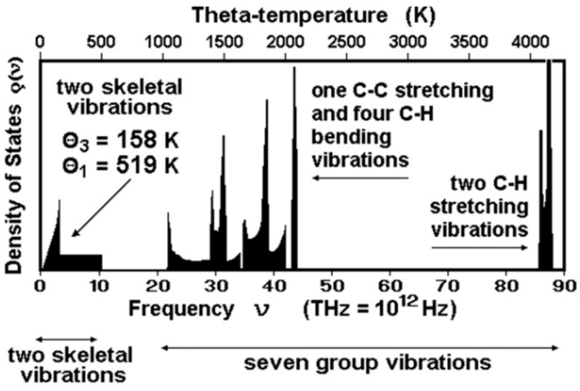

Figure 2.70: Approximate vibrational spectrum of crystalline PE measured with the C_p from 0°K to the beginning of large-amplitude motions [18]

2.3.2 The molecular structure of polypropylene

2.3.2.1 Polymerisation, chemical structure and tacticity

Polypropylene is part of the polyolefins family, produced by chain-growth polymerisation from the monomer propylene, i.e. sequential insertions of monomers into the chain thanks to a catalyst, the role of which is to ensure contact between monomeric molecules and to decrease the needed energy for them to react together. More specifically, it is a co-ordinated polymerisation, that was developed in the fifties with the Ziegler-Natta heterogeneous[25] catalysis. During a typical polymerization, there are a lot of competing reactions occurring simultaneously at different rates and orders. It is therefore very important to understand how the polymerisation conditions influence them and how specific steric or electronic requirements for a given mechanism can raise or lower the energy of a transition state in order to promote or discourage a desired reaction, or to control how a monomer is enchained (f.i. its stereo- or regioselectivity[26]) [112]. The use of stereoregular catalysts allows the synthesis of two types of stereoregular polypropylenes, syndiotactic and isotactic [7].

The structure of polypropylene is controlled schematically by (source: private training, 2000):

1. the multiple catalytic sites (nature of the catalyst, co-catalyst (nature, proportion) and stereoregulator (nature, proportion))
2. the process (batch or continuous, gas or liquid phase, comonomer and/or H2 feed, washing or not of the resins)
3. the finishing (presence of peroxides and depolymerisation, stripping of the resins when the liquid phase is used).

The polymerisation itself occurs via a three-step process: activation, thanks to a single site pre- or co-catalyst complex that is usually an alkyl-Al (with or without Cl)[27], initiation thanks to organometallic complexes of transition metals such as Ti or Zr and propagation thanks to an active center usually anionic that is constituted by a coordination complex between the monomeric moeity and the transition metal. At the end of propagation, termination or chain transfer can occur. Chain transfer is a statistical chain event that is not necessarily the termination of the final polymer chain, as many chain transferred products are reinserted afterwards. In the case of polypropylene, the reaction is terminated with an H_2. All these steps usually occur simultaneously in the reactor.

The stereochemistry of a polymerisation reaction is driven by the symmetry and the steric environment of the metallic centre and the growing polymer chain. The mechanism shown in figure 2.71 is the idealized enantiomorphic site-controlled enchainment of propylene. The symmetry C_2 mentionned on this figure refer to the symmetry axis, i.e. an axis around which a rotation by 360/n results in a molecule indistinguishable from the original. This is also called an n-fold rotational axis and abbreviated C_n (Source: Wikipedia).

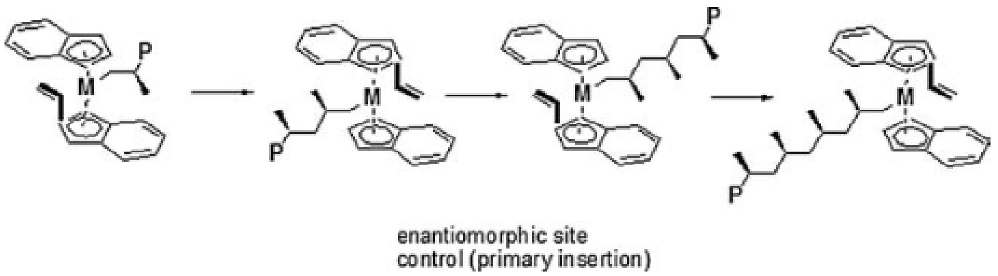

Figure 2.71: Chain propagation on a C_2 symmetric catalyst via enantiomorphic site control [112]

Polypropylene can exist under three mainly different stereostructures, that depend on catalysis technology (catalyst and support) and polymerisation conditions, atactic (aPP), syndiotactic (sPP) and isotactic (iPP)

---

[25] Catalysis can be classified as homogeneous catalysis, in which only one phase is involved, and heterogeneous catalysis, in which the reaction occurs at or near an interface between phases. Source: IUPAC gold book

[26] The stereo polymerisation is a polymerisation in which a polymer molecule is formed from a mixture of stereoisomeric monomer molecules by incorporation of only one stereoisomeric species. Stereoisomers possess identical constitution, but differ in the arrangement of their atoms in space. The regioselective reaction is one in which one direction of bond making or breaking occurs preferentially over all other possible directions. Source: UIPAC gold book

[27] Alkyls are univalent groups derived from alkanes by removal of a hydrogen atom from any carbon atom C_nH_{2n+1}; alkanes are hydrocarbons having the general formula C_nH_{2n+2} consisting entirely of hydrogen atoms and saturated carbon atoms. Source: IUPAC gold book

as illustrated at figure 2.72. In case of atactic polypropylene, the methyl group $[-CH3]$ is randomly aligned, alternating for syndiotactic polypropylene and evenly distributed for isotactic polypropylene [113].

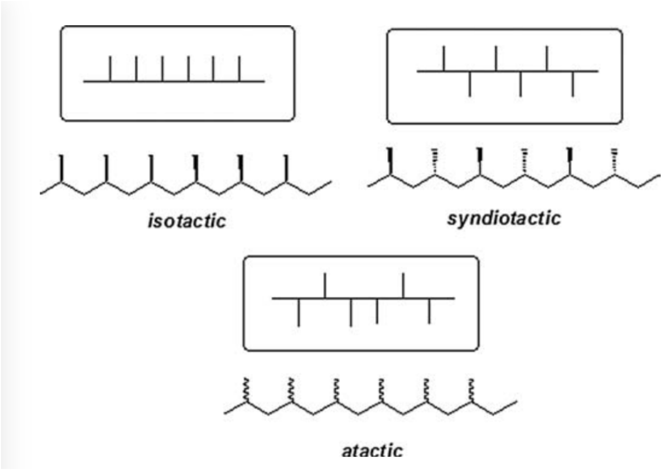

Figure 2.72: The three possible tacticity of iPP [112]

As illustrated at figure 2.73, the symmetry of the metallic centre controls also the enantiomorphism of the catalytic site. In the case of isotactic polypropylene, the symmetry is a C_2-type [112].

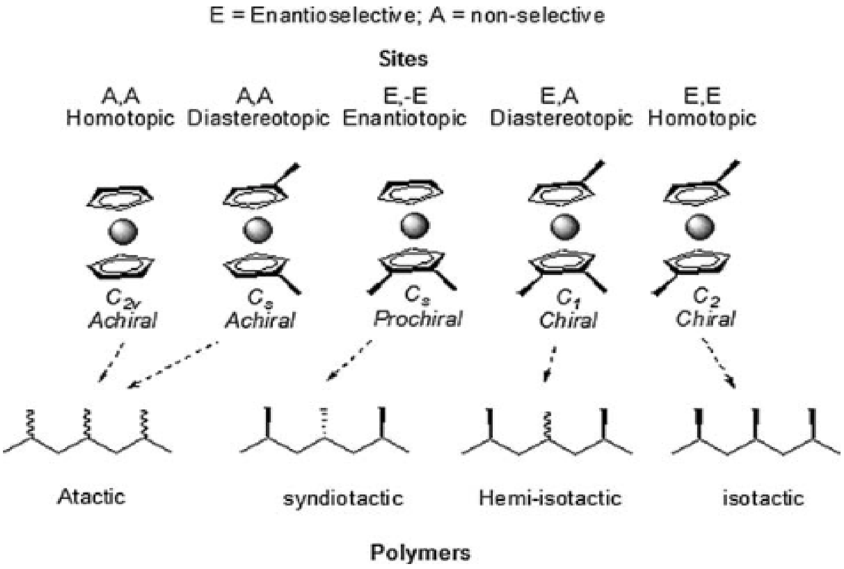

Figure 2.73: Ewen's symmetry rules [112]

In the heterogeneous Ziegler-Natta process, the complexes are formed at the surface of a crystal having a layer lattice, e.g. $TiCl_3$ under its α-form. The reaction goes on through successive additions of monomeric units to metal-carbon bonds of these complexes by the action of a metal-alkyl [114]. In the Metallocene process, the role of the surface is played by the aromatic ligand framework [115].

The multi-site nature of ZN systems has as consequence that the polypropylenes produced are complicated mixtures of macromolecules with different tacticity [112], [115]. However, the figure 2.74 that shows the correlation between the degree of isotacticity and DSC metling temperature for isotactic polypropylene suggests that ZN systems are the most convenient route to high-melting polypropylenes. The degree of isotacticity, expressed in % pentads or mmmm is defined at section 3.2.3.

On the other hand, metallocenes are suitable catalysts for the production of lower-melting iPP: by tailoring the aromatic ligand framework and reaction conditions, it is possible to tune the stereoselectivity, so as to produce homopolymer chains with the desired average length of crystallisable sequences.

In the ZN catalysis, the same result can be achieved by introducting controlled amounts of a co-monomer though this is made complicated by the broad distribution of copolymer composition. The way ZN and MET crystallise is also to be ascribed to the different distribution of stereodefects. It is often said that the γ crystalline form is favored by a low average polymer molecular mass but this is mainly due to the average length of the crystallisable sequences ranging around 10-30 monomeric units, a condition frequently matched by polypropylene samples produced with metallocene catalysts (which often happen to be of rather low molecular mass). On the other hand, Ziegler-Natta polypropylenes normally contain long, almost ideally isotactic sequences forming predominantly α-type crystal, along with sequences which are practically unable to crystallize [115].

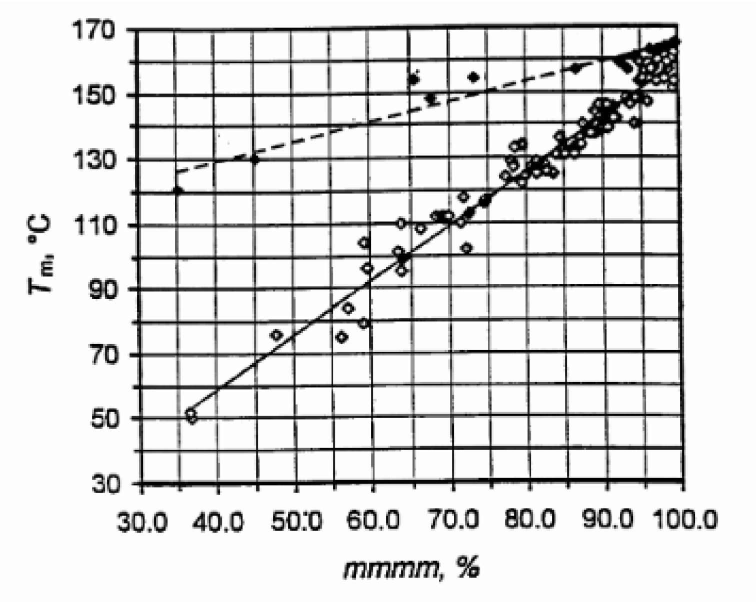

Figure 2.74: Correlation between degree of isotacticity expressed as % of mmmm pentad and DSC melting temperature Tm for predominantly isotactic polypropylenes (the upper curve refers to ZN data and the lower one to metallocene; the interpolating lines are only orientative [115]

The structure of the molecule can be seen at figure 2.75 hereunder.

$$\begin{array}{ccc} [CH_2 = CH - CH_3] & [-CH_2 - CH(CH_3)-] & [-CH(CH_3) - CH_2-] \\ \text{I} \quad\quad \text{II} \quad\quad \text{III} & \text{(A)} & \text{(B)} \end{array}$$

Figure 2.75: General structure of the monomer where the three carbon atoms are named I, II and III according to IUPAC rules. A and B are two stereo-regular structures [115].

The $[= CH(CH_3)]$ moiety is usually named "head" whereas the $[CH_2 =]$ moiety is named "tail". Each insertion is named $1,2$ or $2,1$ depending on which carbon atom I or II of the incoming monomer is bond to the active metal, as illustrated at figure 2.77. Alternative notations as primary and secondary are also of common use [115] - see figure 2.76.

Mt-P + CH_2=CH(CH_3) = Mt-CH_2-CH(CH_3)-P ***1,2 (primary) insertion***

Mt-P + CH(CH_3)=CH_2 = Mt-CH(CH_3)-CH_2-P ***2,1 (secondary) insertion***

Figure 2.76: Primary and secondary insertion [115]

Generally speaking, the enchainment of the propylene units is not random and one of the insertion mode is preferred for electronic or steric reasons. When only one mode occurs, the polymer is said to be stereo-regular and its structure can be described by one of the structures represented by (A) or (B) on figure 2.75.

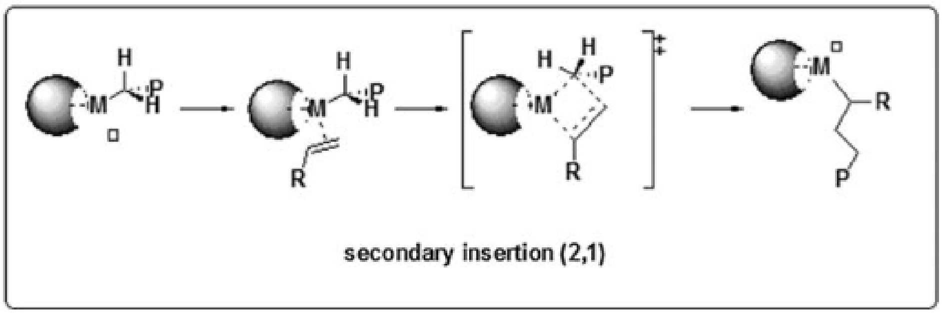

Figure 2.77: Mechanism of secondary insertion 2,1 [115]

2.3.2.2 Symmetries

According to [18], the intramolecular steric hindrance between the methyl groups forces backbone into the helical structure shown at figure 2.78. This polymer has, as for PE and PB repeating units of two backbone atoms. The class 2 helix of iPP with its *two* atoms completes after every *third* monomer *one* turn of helix. Accordingly, the helix is designated as 2*3/1. This configuration is the basic, low-energy conformation in all the polymorphs of iPP, though the helix symmetry is not part of the crystal symmetry. When talking about symmetries in the crystalline state, one rather prefer to describe the crystal symmetry with its screw axis notation, which introduces differences between right-hand side and left-hand side molecules, as only right-hand side rotations are used in the description of crystal symmetries. The right-handed 2*3/1 helix can be therefore described by a 3_1 crystallographic screw axis but it will not be for example the case of the left-handed molecule drawn at figure 2.78 that will need rotation and additional translation to achieve the same result.

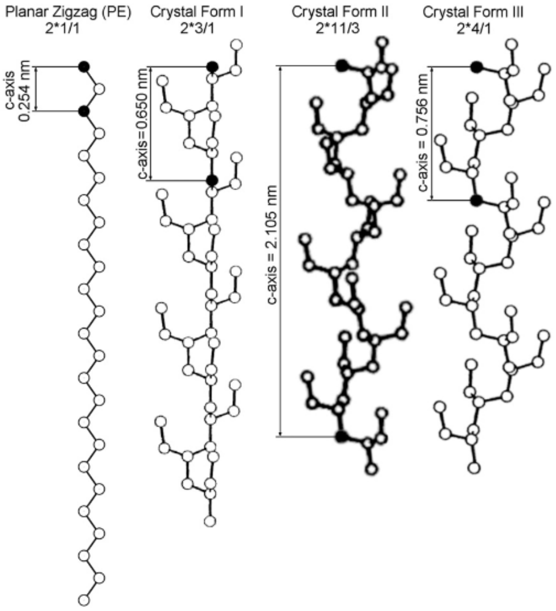

Figure 2.78: The four helix types of PE, iPP and iPB as a comparison; monoclinic iPP is the crystal form I with 2*3/1 helix; every segment is drawn for 12 molecular repeating unit [18];

In its isotactic form, the general conformation of the polypropylene chain is represented at figure 2.79. Another way to represent individual monomeric units is the modified Fisher projection [115], as shown at figure 2.80.

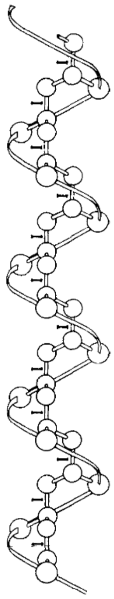

Figure 2.79: Conformation of an isotactic chain in the crystal state [114]

,

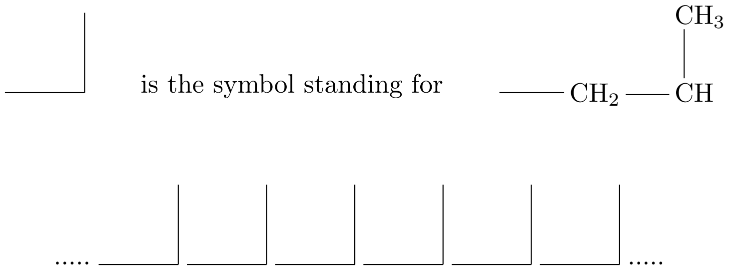

Figure 2.80: Top-down: (a) explanation of the symbols and (b) succession of monomeric units [115]

When looking at the configuration of the backbone tertiary carbon atoms, and in particular to those in consecutive couples of monomeric units, each of these is said to constitute a steric dyad. The two diads of figure 2.81 corresponding to equal or opposite relative configurations of the stereo-centers (see definition infra), can be labelled as "meso" abbreviated "m" or racemo, abbreviated "r". An infinite succession of meso diads results in an isotactic chain whereas an infinite succession of racemo diads results into a syndiotactic chain [115].

Figure 2.81: Diads *meso* "m" and *racemo* "r" [115]

2.3.2.3 Defects

According to [11], the regular insertion of monomers in the growing chain and therefore their more or less high regularity can be altered by the presence of defects. Let us define stereo centers as atoms bearing several groups whose identities are such that an interchange of two of the groups produces a stereo isomer. The carbon atom carrying the subsitutent (the methyl group) is a stereogenic center and the molecular structure of the polypropylene is described in terms of meso or racemo enchained neighbouring susbtituants. The regular manner that the stereo centers form the chain in their successive configuration results in a more or less overall ordered molecule, the tacticity.

Isotactic polypropylene displays two main types of defects in the chain, regio-error and stereo-error. Defects are enchained into a polymer during its all life-time, and can occur, f.i. via the mis-insertion of a monomer, as illustrated at figure 2.82.

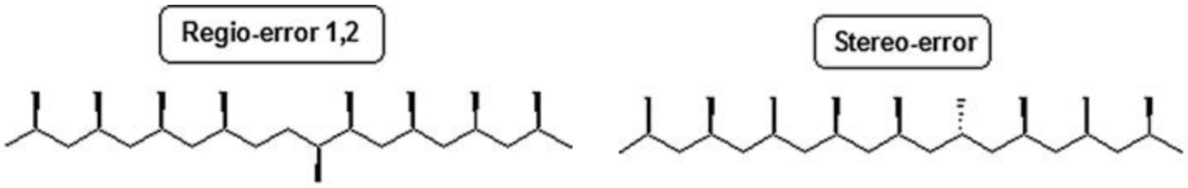

Figure 2.82: Schematic drawing of regio- and stereo-error defects [112]

Stereo-errors could be for instance the result of wrong incorporation of a monomer in the growing chain. Figure 2.83 displays the various possible stereo-defects.

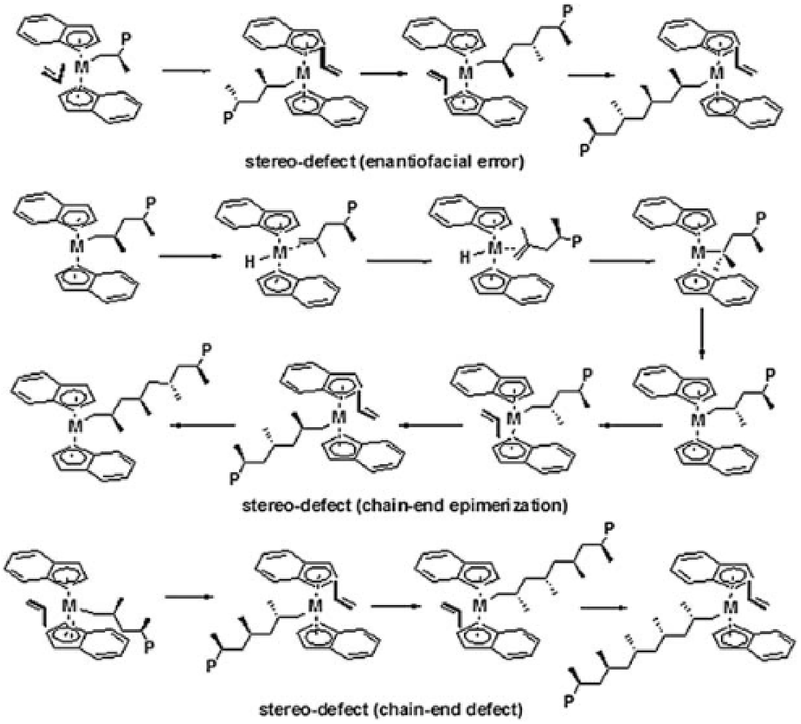

Figure 2.83: Formation of stereo-error defects [112]

In real polypropylene chains, a certain amount of regiodefects are always present. In most cases, these are isolated monomeric units with an enchainment that is opposite to the predominant one (head-to-head/tail-to-tail arrangements) as represented at figures 2.84 and 2.85.

$$-[CH_2\text{-}CH(CH_3)]_x\text{-}\mathbf{CH_2\text{-}CH(CH_3)\text{-}CH(CH_3)\text{-}CH_2}\text{-}[CH_2\text{-}CH(CH_3)]_y\text{-}$$

Figure 2.84: Regio-error defect such as head-to-head/tail-to-tail arrangement [115]

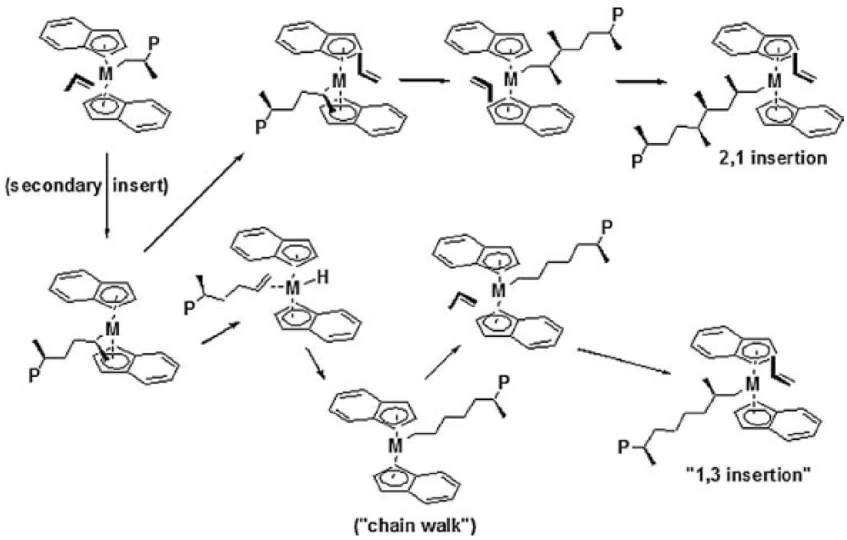

Figure 2.85: Regio-defects formation [112]

From ^{13}C-NMR spectra, it is possible to access the configuration of five neighbouring methyls named "pentad". Ten different configurations exist that are presented at figure 2.86.

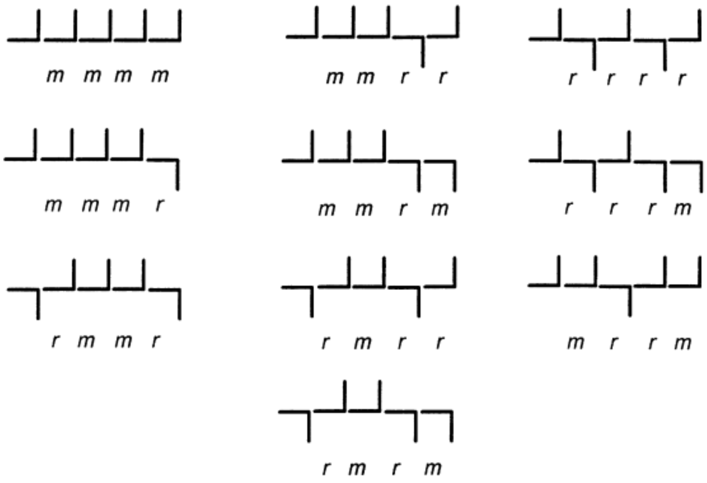

Figure 2.86: Pentads [115]

Defects in the backbone break the regularity of the chain in the similar way as the addition of a comonomer [112]. This has an impact on the crystallisation parameters. Moreover, defects are not randomly or equally distributed. They impact directly the average pure isotactic length n_{iso}, i.e. the crystallizable sequence between defects as illustrated at figure 2.87.

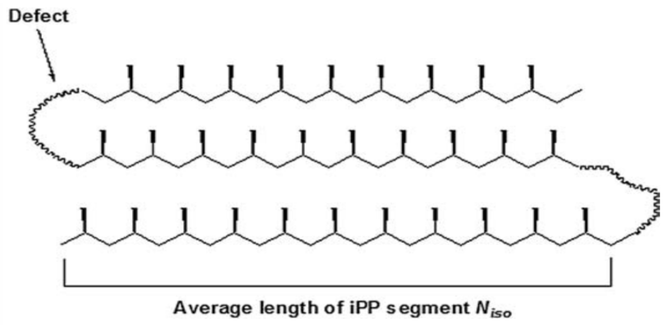

Figure 2.87: Average length n_{iso} of iPP isotactic sequences [112]

Single-site catalysts such as metallocene typically distribute their defect in an homogeneous way all along the polymeric chain, whereas multi-sites Ziegler-Natta catalysts rather gather them in blocks with very long isotactic segments in between. The consequence is that single-site catalysts have rather short isotactic segments n_{iso} and tend to crystallise in the γ-crystal form.

According to [116], "*the relationship between defect concentrations and mechanical (as well as thermal) properties is quite dependent on the extent of incorporation of defects into the crystalline regions. One of the principal mechanisms by which properties are thus modified involves changes that occur in the crystalline phase of the polymer. At the level of the unit cell, changes in defect concentrations can alter the level of crystallinity as well as the thickness and melting point. A key piece of information for understanding the role that each kind of defect plays in property modification is the break down of defects between the crystalline and the noncrystalline regions*" [117].

According to [11] and [118]

1. the influence on the melting of the regio-defect is much larger than stereo-defects, resulting in a strong linear decrease in melting points as function of the amount of defects
2. the influence of stereo-defects is independent of the presence of regio-defects
3. it is more difficult to incorporate a regio-defect in the crystal lattice than a stereo-defect
4. the excess free energy to incorporate a stereo-defect into the crystal phase is lower for β-phase than for α-phase, resulting in higher number of defects in β-phase
5. looking at the different crystal phases and types of defects, exclusion of the defects, especially regio-defects, from the crystal phase cannot account alone for the reduction of T_m, and a certain number of them must be present in the crystalline lamellae as non-equilibrium defects [10], [116]. Indeed, for a lamella to evolve laterally, the flux of energy associated to the large amount of chains transport and answering the crystallite formation needs, involves a significant amount of chain bending or folding that leads to dissipating free energy. Because the energy penalty of regio-defects, when inserted into a crystal lattice, would be large and the surrounding stacked layers strongly suppresses chain diffusion, the chain cannot fold back easily, or be inserted into the crystal lattice. Therefore long chain containing defects will remain for a longer time in the melt. Upon formation of the initial crystals (α-phase), there will be an increase in concentration of chain entanglements and defects in the melt. A certain number of regio-defects must be partitioned into crystal lattice as non-equilibrium defects. Stereo-defects on their side are not rejected from the crystal
6. this is illustrated at figure 2.88 which is a schematic representation of the two limiting cases of polymer crystallisation including defects: total exclusion (left) and uniform inclusion (right) according to Sanchez et al theory [118].

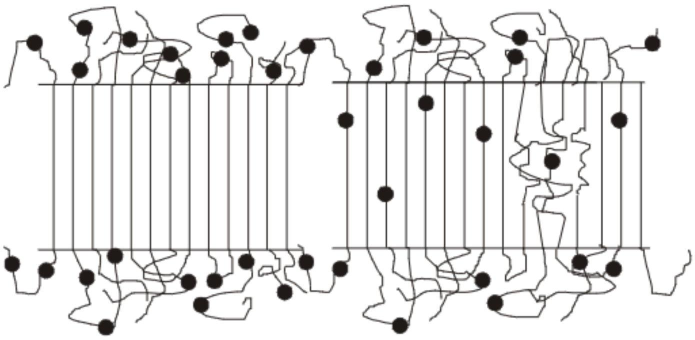

Figure 2.88: Two limiting cases of polymer crystallisation in presence of defects - see text [11]

2.3.3 The solid state microstructure of iPP

We will now review the structure of the isotactic polypropylene at the phase levels (a few tenths of nm) and to a less extend at the spherulite level (a few tenths of μm).

2.3.3.1 Structure and morphology of iPP: polymorphism analysis

Due to its molecular structure, isotactic polypropylene has a large range of microstructures, mainly due to original combination of helices with different hands and/or original packing schemes combined with specific molecular weight, degree of isotacticity, presence of defects and thermal treatment of the samples.

The shape of the macromolecules is intrinsically anisotropic, and this favors parallel packing in the crystalline states. Two typical modes of crystal nucleation are illustrated at figure 2.89: one is the chain-folding configuration named intramolecular crystal nucleation for a parallel alignement of consecutive chain segments, and the other is the fringed-micelle configuration named intermolecular crystal nucleation where the entangled chains in small local domains adopt regular packing where nearby chain segments are parallel to each other [119], [111]. We think that, according to the type of crystallisation conditions and molecular architecture, the intramolecular crystal nucleation of figure 2.89(a) will promote the crystalline phase and the intermolecular nucleation of figure 2.89(b)is likely to promote the mesophase.

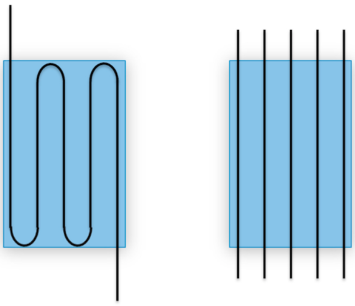

Figure 2.89: (a) Fold chain lamellae from intramolecular crystal nucleation and (b) fringed micelles from intermolecular crystal nucleation; the blue color represents the crystal [119]

Once crystallised, isotactic polypropylene crystals display thus a high capacity to induce epitaxial crystallisation with their chain axes titled at large angles relative to the helical axis direction. One of the most striking phenomenon [120] is certainly the homoepitaxy[28] with a 80° angle as will be illustrated at figure 2.93.

The polymorphism of the iPP allows also transitions between different crystalline forms that can be triggered either by different thermal treatments but also by mechanical stress. A very extensive bibliography has been devoted to this wide realm which analysis goes beyond the scope of this PhD, but not of this research (among others [67], [18], [117], [121], [69], [122], [16], [19], [10], [123], [20]).

In this section, we present the main aspects of polymorphism in iPP from the perspective of the undeformed structure and with a focus on α-phase. Whereas we will address the influence of thermal treatments, the influence of the mechanical stress on the microstructure has been tackled in section 2.2.2 sqq.

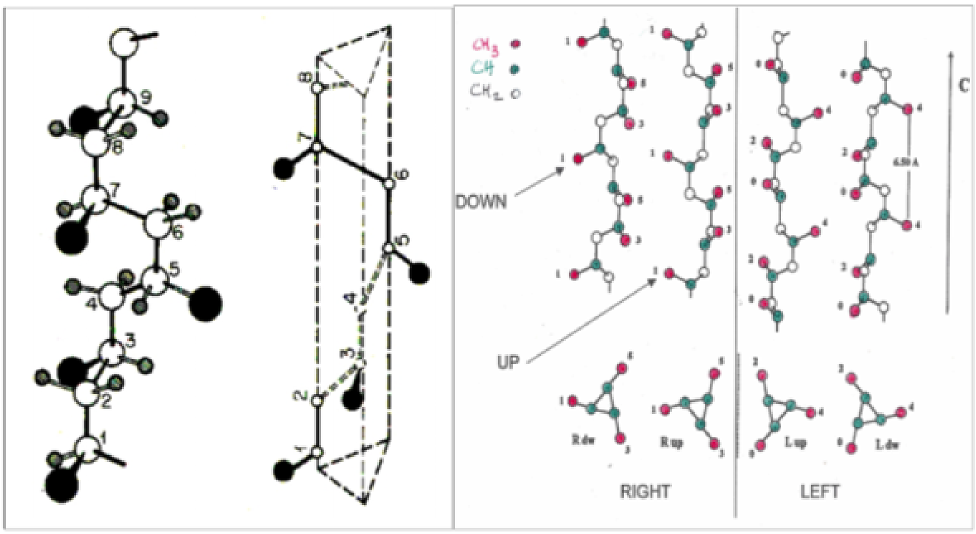

Figure 2.90: (a) iPP chain in its crystalline form [11] and (b) right and left handed three-fold minimum energy conformations; $[CH_3]$ in red, $[CH]$ in green and $[CH_2]$ in white [120] - see text for numbers and triangles signification and further explanation

---

[28] epitaxy "refers to a type of crystal growth or material deposition in which new crystalline layers are formed with one or more well-defined orientations with respect to the crystalline seed layer"; "homoepitaxy is a kind of epitaxy performed with only one material, in which a crystalline film is grown on a substrate or film of the same material" - see Wikipedia

The isotactic polypropylene crystallises according to four main types of phases, the monoclinic α-crystals, the triclinic β-crystals, the orthorhombic γ-crystals and the mesophase which components are condis crystals (see 2.3.1 for definition).

The chain conformation of iPP in the crystalline state is constituted by two enantiomers: right-handed and left-handed three fold helices with a periodicity of 6.5 angstrom as illustrated at figure 2.90. On figure 2.90(a), the triangle tops are approximately located at the vertices of methyl groups and the numbers refer to the height of the backbone carbons [11]. On figure 2.90(b) the right (R) and left (L) handed three-fold minimum energy conformations are illustrated and for each conformation, the orientation (up or down) is given. Numbers refer in this case to the height of the methyl groups in sixths of the c-axis with $[CH_3]$ groups in red, $[CH]$ in green and $[CH_2]$ in white [120].

Isotactic polypropylene exhibit different crystallographic structures and morphologies as a function of crystallisation conditions: cooling the melt at low or moderate rates results in monoclinic α-crystals. The 2*3/1 helix are aligned parallel to the cristallographic c-axis and left-handed and right-handed helices achieve closest packing as nearest neighbours.

2.3.3.2 The crystalline phases of iPP

The α-phase of iPP

The **α-crystals** are the most widely encountered structure of crystals of iPP. It is described as an alternation, in the b-axis direction, of layers parallel to the ac-plane and composed only of left-handed (L) or right-handed (R) helices. The position of the methyl groups for both enantiomers is "up" or "down". The terms "a", "b" and "c" refer to the dimensions of the unit cell. The figure 2.91 gives an illustration where each monoclinic cell has been highlighted by a rectangular grid.

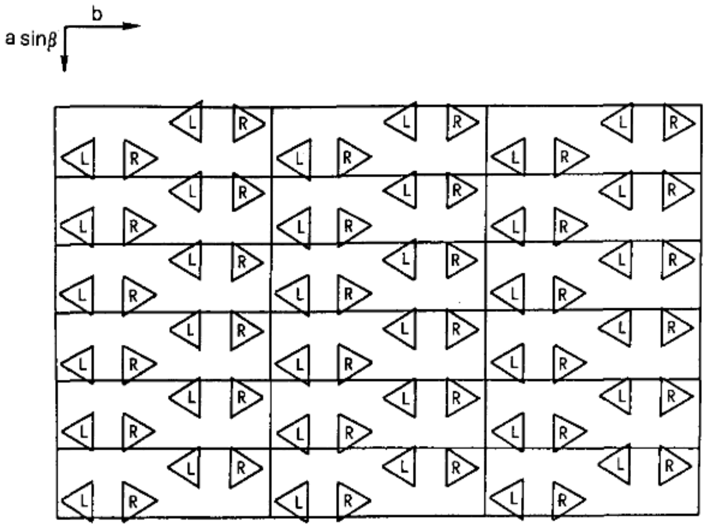

Figure 2.91: Mode of packing of right- and left- handed chains of iPP viewed along c-axis [120]

The characteristics of α-phase monoclinic cell are summarized in the table below taken from reference [18]. Figure 2.92 illustrates how lamellae are growing along the a* direction, where a* is aligned to the crystal and Wc holds for b-axis.

a (nm)	b (nm)	c (nm)	$\beta(°)$	T_m(°C)	ΔH(kJ/mol)	$\rho(g/cm3)$
0.665	2.096	0.65	99.62	187.5	8.7	0.946

Major defects are caused by helix segments of wrong handedness followed by up and/or down defects creating disorder in the inclination of the methyl groups of neighbouring chains. Two limiting phase exist, i.e. a metastable α_1-phase and a stable α_2-phase.

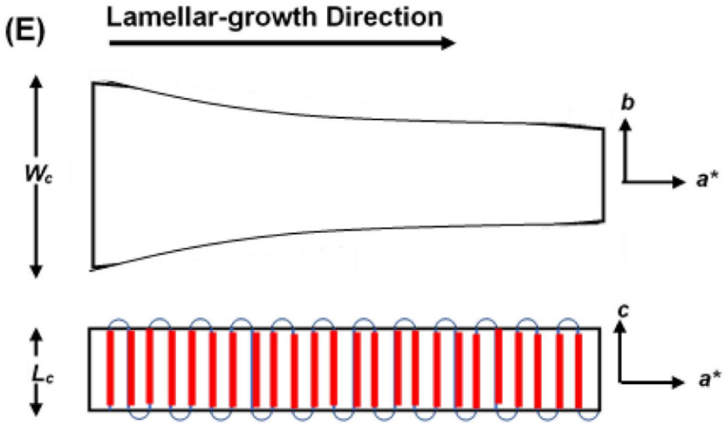

Figure 2.92: Lamellar-growth direction [124]

The superstructure of melt-grown monoclinic crystals is the spherulite with lamellae displaying unique branching. Epitaxial growth of daughter lamellae leads to the well known "cross-hatching" structure, where spherulites contain both radially and tangentially oriented lamellae [18], as illustrated at figure 2.93.

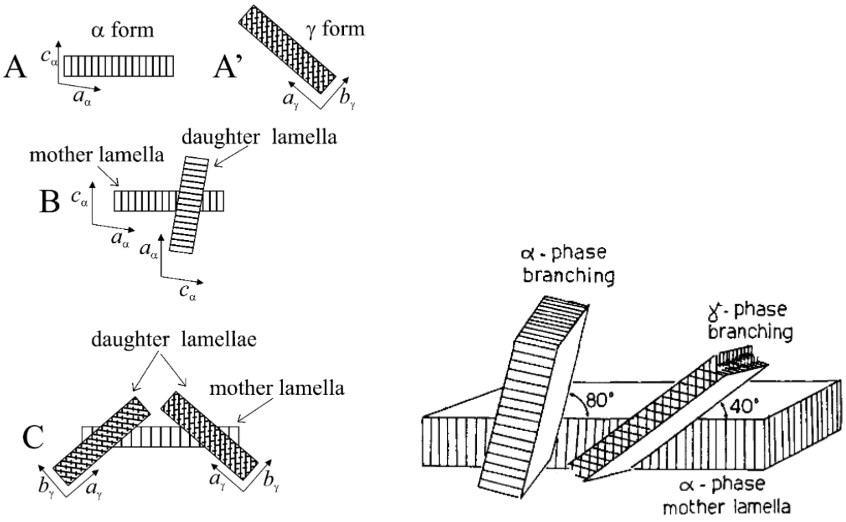

Figure 2.93: Lamellar branching and epitaxial relationship in iPP (left:[67] and right:[120])

More generally, Iijima and Ströbl [125] have demonstrated that iPP, when forming the α-phase under isothermal crystallisation, is governed by the same general laws for crystallisation and melting as syndiotactic polypropylene: there are two separate laws governing melting and crystallisation.

According to the Gibbs-Thomson theory, the thickness of lamellar crystallites l_c is inversely proportional to the supercooling below a temperature $T_c^\infty = 191°C \pm 3°C$. This temperature is located a few degrees above the equilibrium melting point T_m^∞ of the sample. This means that the formation of the lamellae occurs via the formation of a well-defined initial form which then becomes stabilized into the final lamellar crystallites. They identified three kinds of lamellae: 1°) the dominant crystallites growing in the radial direction , 2°) what they name "subsidiary" crystallites, also oriented along the radius of the spherulites, forming subsequently by insertion, and 3°) crystallites oriented with their surfaces in the transverse direction, producing ultimately the cross-hatched morphology. These transverse crystallites have the lowest stability, then the subsidiary lamellae then the primary ones. The two first categories are consistent with the proposal that lamellae are in reality constituted with "layers", as illustrated at figure 2.94.

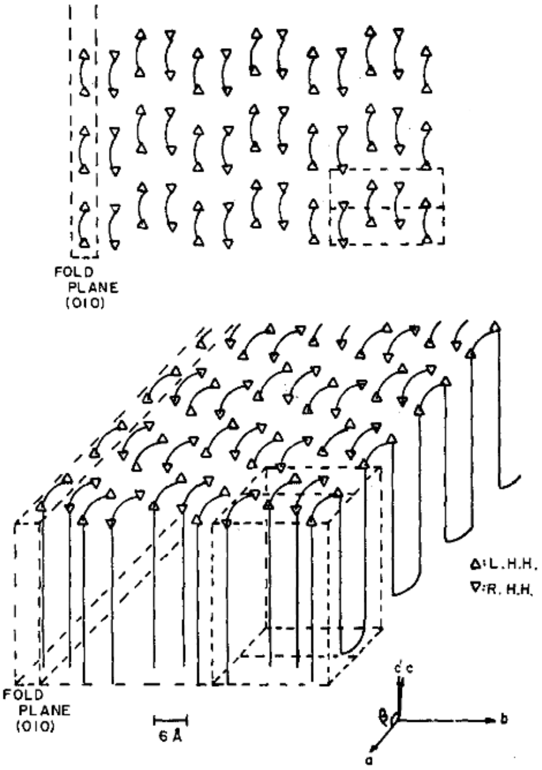

Figure 2.94: Schematic representation of a possible form of 010 fold packing [53]

Observing both subsidiary and primary lamellae (and likely transverse ones) have the same thickness, they found that the initial structure present there can be described as a planar array of crystal blocks, that stabilize during crystallisation by a fusion into continuous layers [126], yielding in some cases granular structures, as illustrated at figure 2.95.

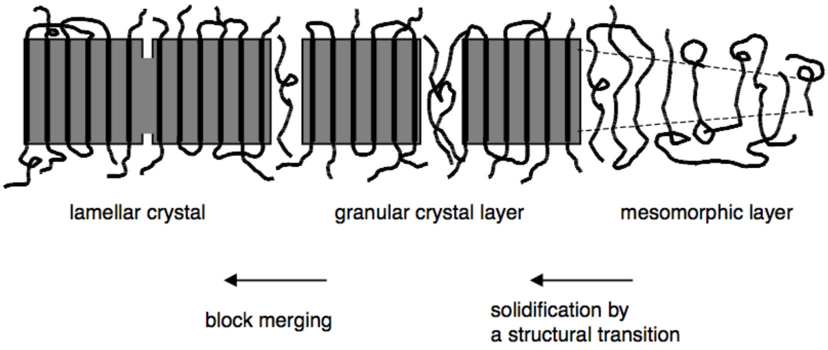

Figure 2.95: Pathway followed in the growth of polymer crystallites [127]

The figures 2.96 and 2.97 illustrate respectively how radial (R-) and tangential (T-) lamellae are built up and how it looks like in the microscope. Crystallisation begins thus from a melt that is already pre-ordered and has fixed achievable crystallinities. Observing that crystal thicknesses are not affected by the presence of co-units in stereodefects, they speculate on the possibility that this exclusion operates already in the pre-ordered layers present in the melt, because defects produce a bend and therefore cannot be part of a straightened chain sequence.

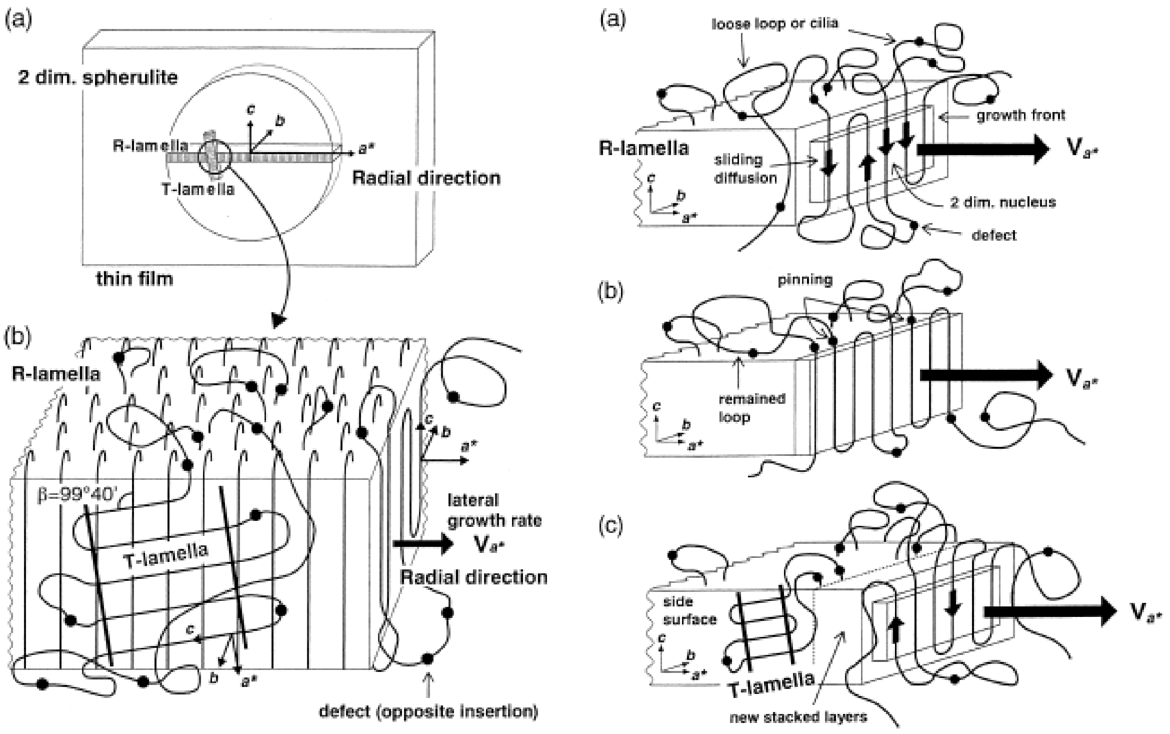

Figure 2.96: Left: (a) two-dimensional α-form spherulite showing an edge-on lamella; (b) onset of a T-lamella growing epitaxially on the side surface of an R-lamella. Right: formation process of a T-lamella; (a) a nucleus formed on the growth front of a lamella grows via a pulling-in of loose loops or cilia, (b) the pulling-in stops by pinning due to a defect in molecule or the stacking of layers on the nucleus, (c) epitaxial nucleation of the loop on the side surface (010) of an R-lamella which forms a T-lamella [128]

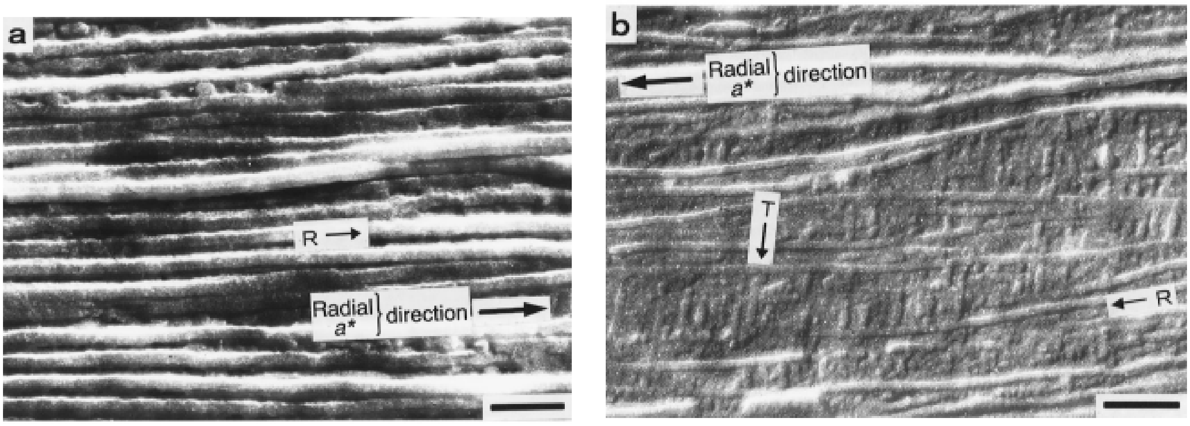

Figure 2.97: a) and b) Typical lamellar morphology in iPP spherulites observed by transmission electron microscopy. R and T indicate R-lamella and T-lamella, respectively. The radial direction corresponds to the a* direction of an α-form unit cell; the scale bar is 0.2 μm [128]

The β-phase of iPP

The β-phase is a rather cumbersome crystalline phase. The β-crystals of iPP are observed under specific crystallisation conditions such as orientation of the melt (shear), temperature gradient or nucleating agent. The growth rate of β-crystals is higher than the α-crystals in a wide range of temperatures between ca. 105 to 140°C. This is attributed to a lower surface free-energy penalty on the top of molecular stems at the (110) growth face, i.e. secondary nucleation sites. The primary nucleation rate of β-phase is lower than that of α-crystals and can be fostered only by addition of β-phase nucleating agents [19], though under above-mentioned undercooling[29]

---

[29] undercooling ΔT is defined as the difference $\Delta T = T_m - T_c$ between T_m the melting temperature and T_c the crystallisation temperature

temperatures, it can be triggered without any additive [48]. The β-phase has a trigonal unit-cell as illustrated at figure 2.98. In some cases, its packing can be pseudo-hexagonal. This phase may also re-crystallise to α-phase upon heating, and does not display cross-hatch structure [11], [19].

The main characteristics of β-crystals are presented in the table below [11].

a (nm)	b (nm)	c (nm)	$\beta(°)$	T_m(°C)	ΔH(kJ/mol)	$\rho(g/cm3)$
1.1	1.1	0.65	120	177	5	-

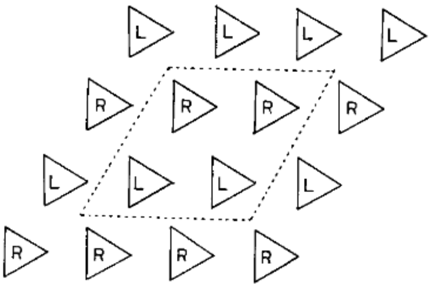

Figure 2.98: Trigonal packing of beta iPP [120]

The γ-phase of iPP

The orthorhombic γ-crystals are observed quite often in combination with the α-phase. This structure is obtained in samples crystallising under high pressure and in presence of degraded, low molecular weights. A high amount of γ-phase was obtained under atmospheric pressure in systems with a low level of tacticity or with metallocene catalysis [11]. This can be namely explained by the fact that these crystals develop preferentially in presence of defects which limit isotactic sequences. The unit cell has adjacent bilayers of chain segments with a very important relative tilt angle of 81°. Vis-à-vis the basal plane, chains are oriented with an angle of 40° normal to the plane of the lamella [18], [120]. This configuration is illustrated at figures 2.93 and 2.99.

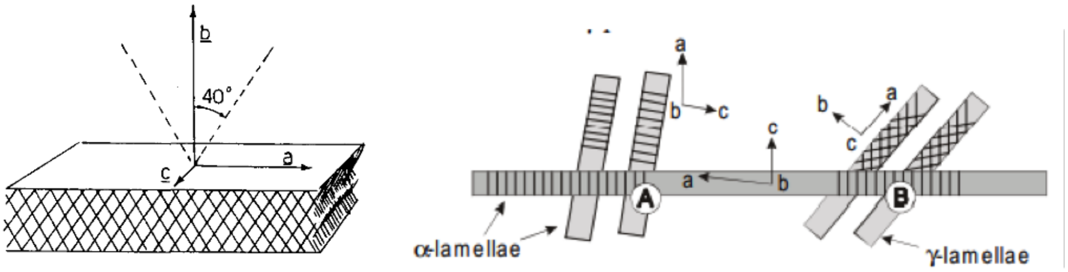

Figure 2.99: a) Sketch of gamma-crystal [120] and b) configuration of α and γ lamellae [11]

The main characteristics of γ-crystals are presented in the table below [11].

a (nm)	b (nm)	c (nm)	β (°)	T_m(°C)	ΔH(kJ/mol)	ρ (g/cm3)
0.85	0.993	4.241	-	187.2	6.1	-

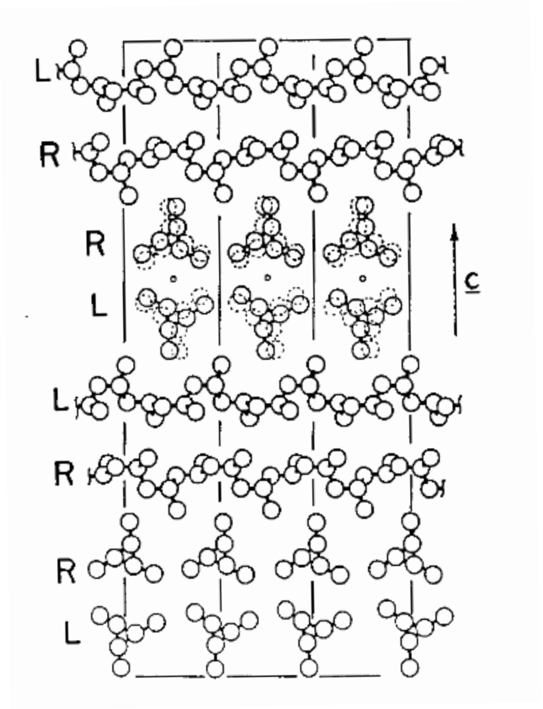

Figure 2.100: Packing of gamma orthorhombic cell along *ab* plane [120]

Before addressing the various aspects of the mesophase in iPP, it is useful to mention already some features related to the cristallographic analysis of the α and γ crystalline phases obtained from Wide Angle RX scattering (WAXS). Figure 2.101 illustrates the evolution of WAXS spectres (left) of different metallocene iPP with various amounts of α and γ crystalline phases together with (right) the crystallographic planes (dashed lines).

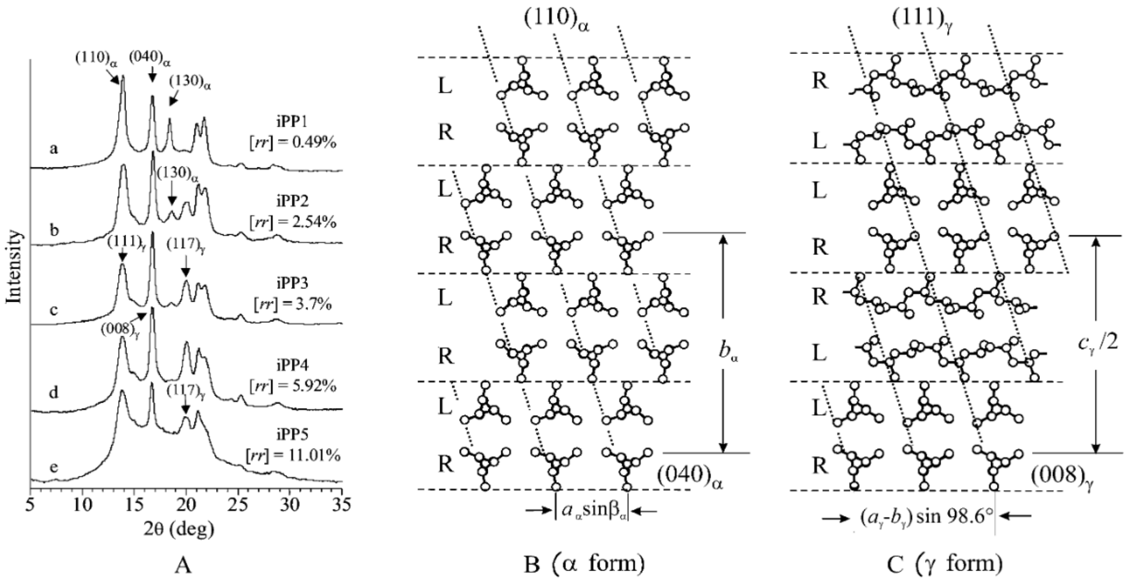

Figure 2.101: Cristallographic planes of α and γ phases for a series of metallocene iPP [67]

2.3.3.3 Morphology description of the mesophase in iPP

The morphology of the crystals in semi-crystalline polymers is controlled by the chemical architecture of the macromolecules and the conditions of crystallisation.

As explained in [19], there is nowadays a consensus on the fact that the mesophase of iPP is a condis glass that is hindered to convert into a fully ordered crystal according to Ostwald's step rule by cooling below its T_g during its formation. Ostwald's rule states that, during the formation of polymorphs, the less stable polymorph crystallises first. The mesophase contains bundles of $2{*}3_1$ helices that are parallel and terminated in direction of the chain axis by helix reversal and other conformational defects. However, despite this disordered configuration, long-range positional and orientational order exist between the helix segments and is metastable below its T_g about 70°C. Heating the mesophase above results in re-crystallisation into the α-phase. The mesophase -crystal conversion engages only intramolecular removal of local, non-equilibrium helix defects and small improvements in crystal symmetry. Its enthalpy is therefore very small. Its density ranges around 0.920 g/cm3, between the density of the crystal at 0.9405g/cm3 and of the amorphous phase at 0.8665g/cm3.

In order to understand the mesophase structure, two thermal routes starting from the melt can be taken and compared, as illustrated at figure 2.102. We will find this type of approaches on a regular basis along our review.

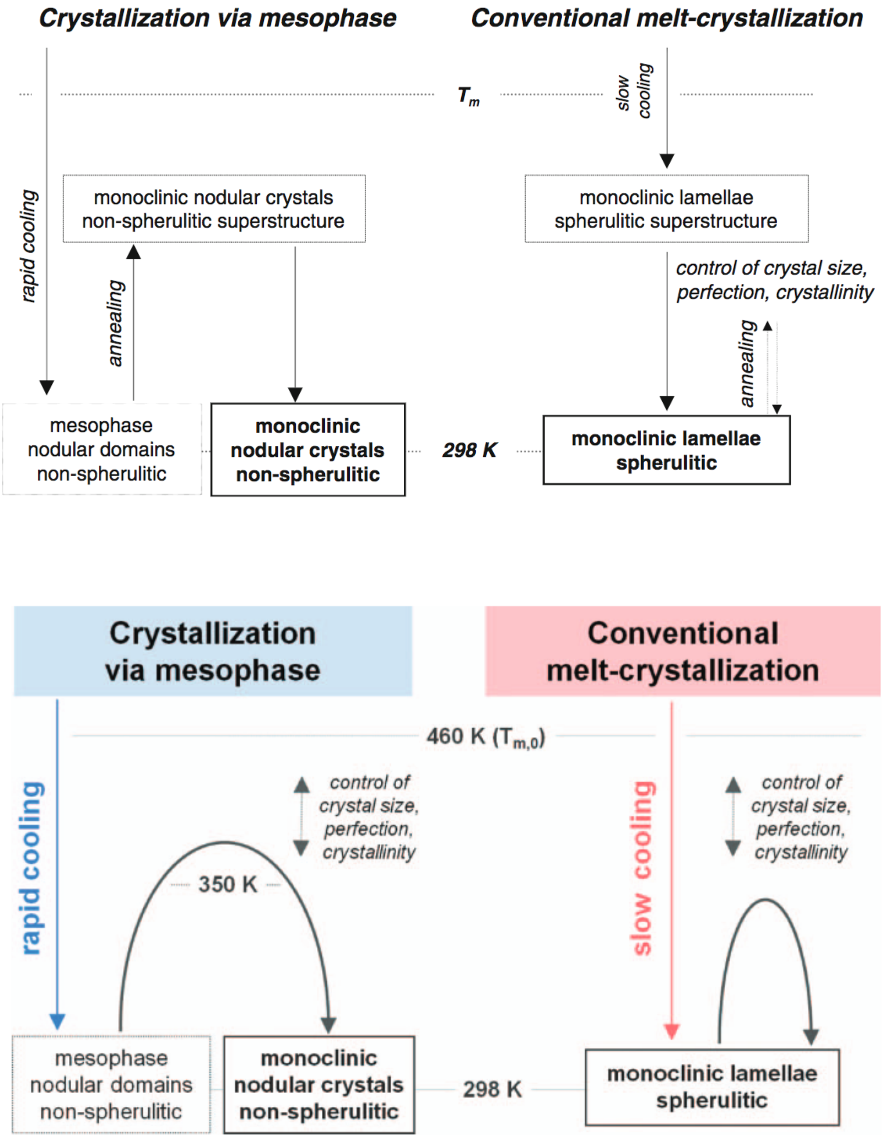

Figure 2.102: Two illustrations of the same pathway of crystallisation of iPP: crystallisation via the mesophase (left) results in formation of nodular crystals and non spherulitic structure; conventional melt-crystallisation (right) leads to the formation of lamellae and spherulites [20], [121]

The crystallisation can occur via rapid cooling (left) and result in nodular mesophase domains or nodular crystals or from the melt (right) and result in monoclinic lamellae.

Temperature ranges and cooling-rate ranges that host the conversion of melt to mesophase are presented schematically at figure 2.103.

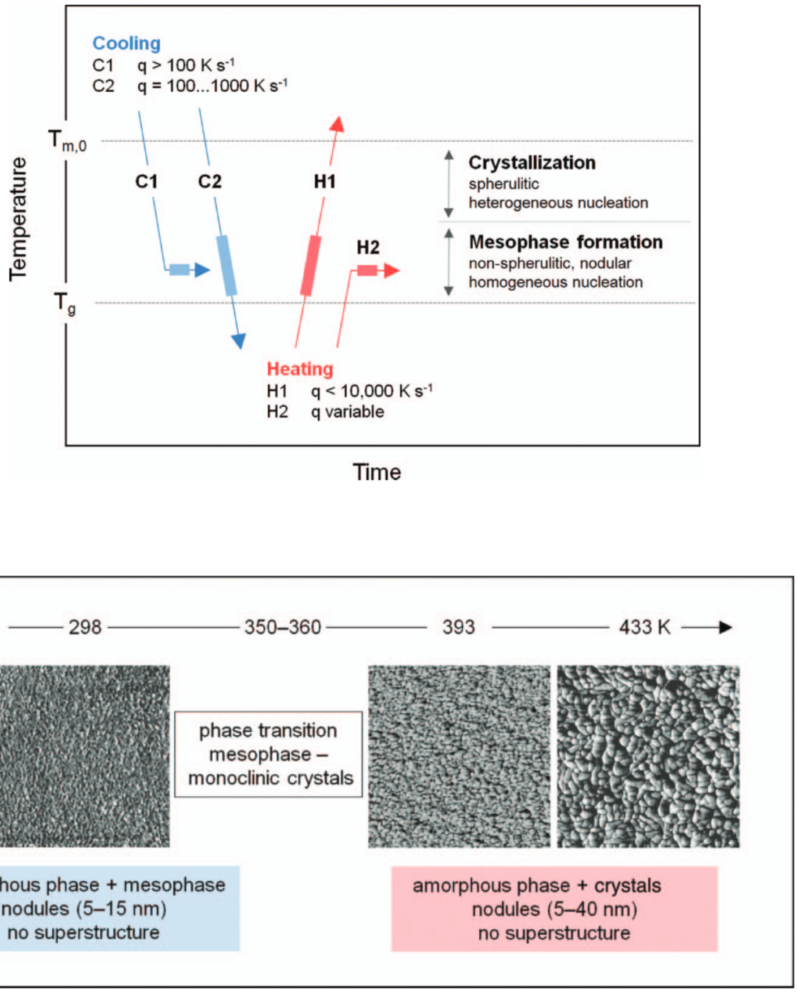

Figure 2.103: Thermal and time conditions of mesophase formation; the size of AFM images is 1μm x 1μm [20], [121]

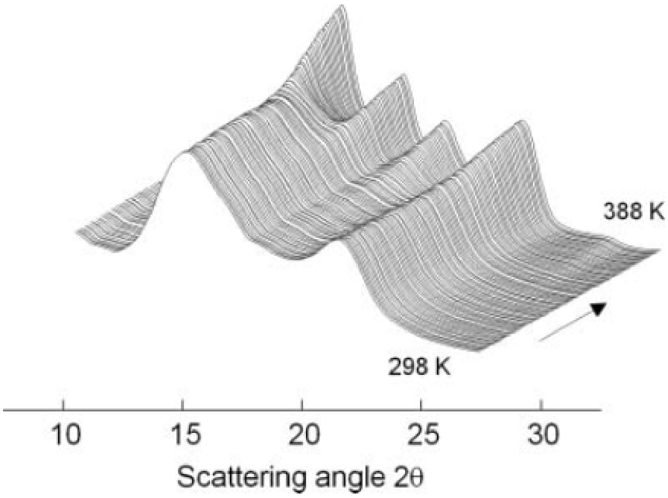

Figure 2.104: Temperature XR scattering for analysis of mesophase-crystal phase transition. The mesophase was heated from 25°C at 2°C/min and converted into α monoclinic crystals at about 80°C [121]

The AFM photographs illustrate the homogeneous nucleation process leading to the nodular structure as well as the heterogeneous nucleation range leading to the combination of lamellae and nodules in the intermediate range of temperatures. The WAXS spectrum of figure 2.104 present the evolution of the peaks between 25°C and 115°C.

Let us highlight that, in some cases, it seems that, even for high temperatures (above 130°C), some mesophase is still present and not all of it does transform into monoclinic crystals ([129], [123], [69]). To summarize, iPP has an incredible capacity to create networked structures thanks to the mobility of its helix and its groups. Thermal analysis shows that in a number of cases, a shoulder coexist with the main melting peak in the heat capacity curve. It has been attributed to two causes: either, when the microstructure is composed of mother and daughter lamellae, the shoulder is associated to the melting of thinner tangential daughter lamellae and the mean peak corresponds to the fusion of radial thicker crystalline lamellae. Or, the shoulder is related to a γ-phase that can convert into an α-phase, especially in presence of a large amount of regio and stereo-defects. In this case together with a decrease of crystallisation temperature, the number of tangential lamellae increases [130].

2.3.3.4 The mesophase in practice

Let us illustrate those phenomenon on the base of the data from Zia et al [109].

The figure 2.105 presents from left to right AFM images of (a) iPP melt-crystallised at 22°C/sec to 20°C and (b) annealed to 120°C; (c) the same iPP melt-crystallised at 1050°C/sec to 20°C and (d) annealed at 140°C (right).

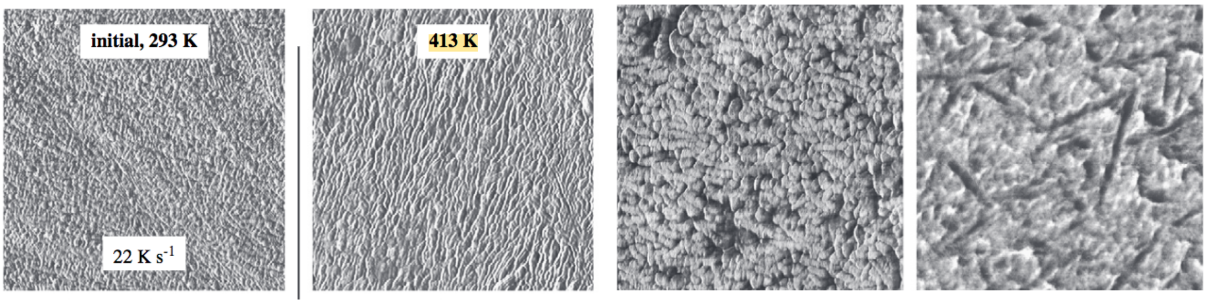

Figure 2.105: (a) iPP melt-crystallised at 22°C/sec to 20°C and (b) annealed to 120°C; (c) the same iPP melt-crystallised at 1050°C/sec to 20°C and (d) annealed at 140°C; the size of AFM images is 1μm x 1μm [109]

The associated evolution of nodular sizes as a function of annealing temperature for samples melt-crystallised at various speeds is presented in figure 2.106.

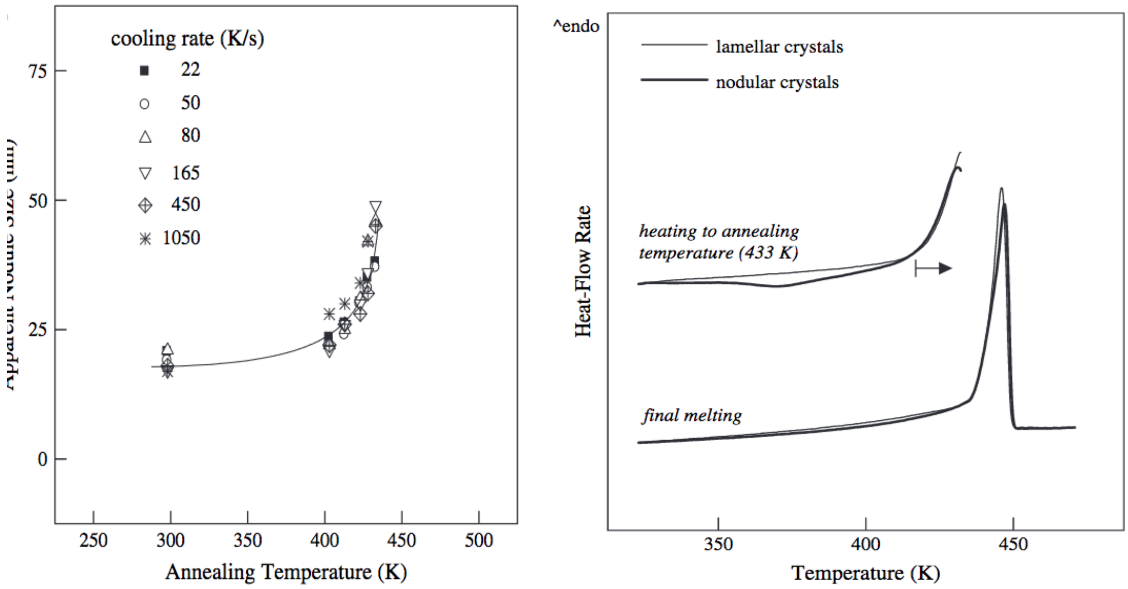

Figure 2.106: (a) Nodule size as a function of annealing temperature and (b) heat flow rate as a function of T on heating lamellae and nodular crystals. The upper two curves show the approach of the annealing temperature and the lower two curves represent the final melting after annealing and cooling to ambient temperature [109]

The melting/recrystallisation of mesophase nodules leads to a variety of lamellae on the genesis of the process illustrated at figure 2.107.

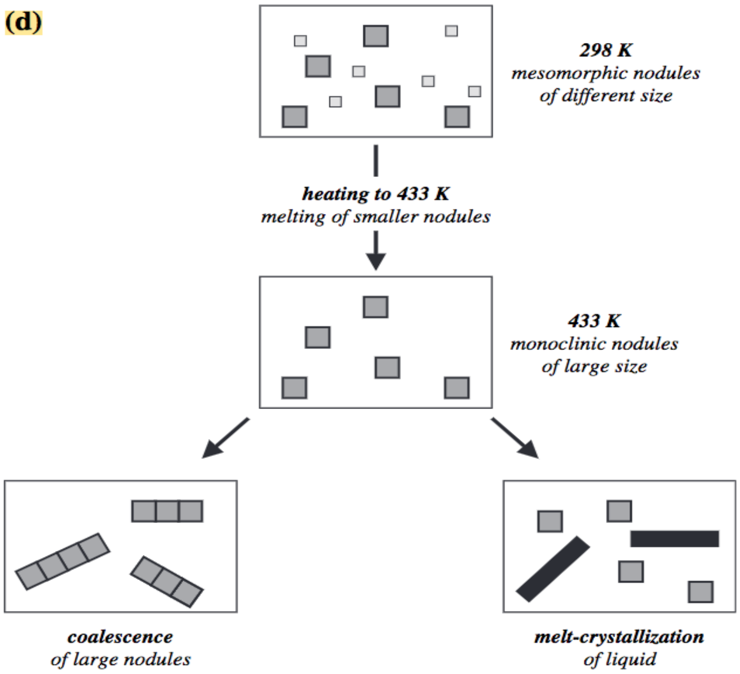

Figure 2.107: Temperature XR scattering for analysis of mesophase-crystal phase transition. The mesophase was heated from 25°C at 2°C/min and converted into α monoclinic crystals at about 80°C [109]

Finally, the table below displays the crystal shape, size, structure and superstructure of the same melt-crystallised iPP as a function of the rate of cooling.

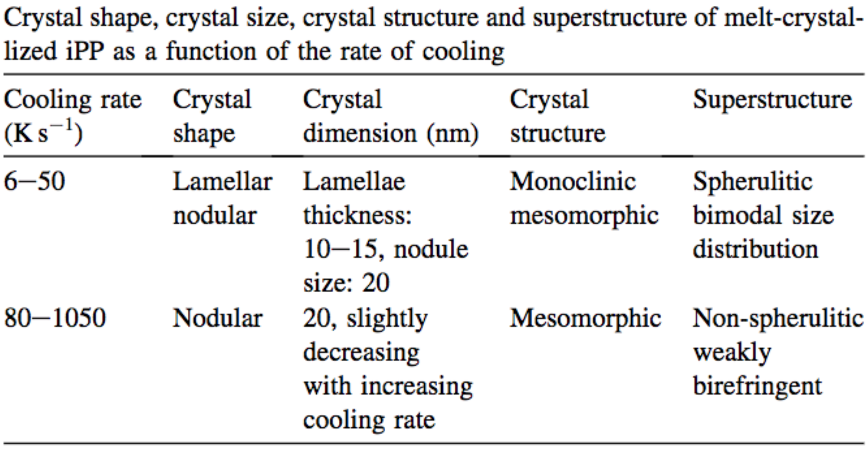

Crystal shape, crystal size, crystal structure and superstructure of melt-crystallized iPP as a function of the rate of cooling

Cooling rate ($K\,s^{-1}$)	Crystal shape	Crystal dimension (nm)	Crystal structure	Superstructure
6–50	Lamellar nodular	Lamellae thickness: 10–15, nodule size: 20	Monoclinic mesomorphic	Spherulitic bimodal size distribution
80–1050	Nodular	20, slightly decreasing with increasing cooling rate	Mesomorphic	Non-spherulitic weakly birefringent

Figure 2.108: Crystal shape, size, structure and superstructure of the same melt-crystallised iPP as a function of the rate of cooling [109]

The transformation of mesomorphic phase into monoclinic is also illustrated at figure 2.109.

To summarize, mesophase and especially conformationally disordered crystal structures exhibit long range positional and orientational order between the helix segments. These structures are metastable and transform spontaneously into stable crystalline structures upon annealing above a certain temperature, located around 80°C for the iPP. The different temperature ranges for the transitions should be linked to molecular mobility of the molecular chains, that trigger rearrangements of chain conformation and packing of the unit cell to a more energetically favorable state. In iPP, chain mobility is achieved within the mesophase when the glass transition of condis glass is reached around 70°C [19].

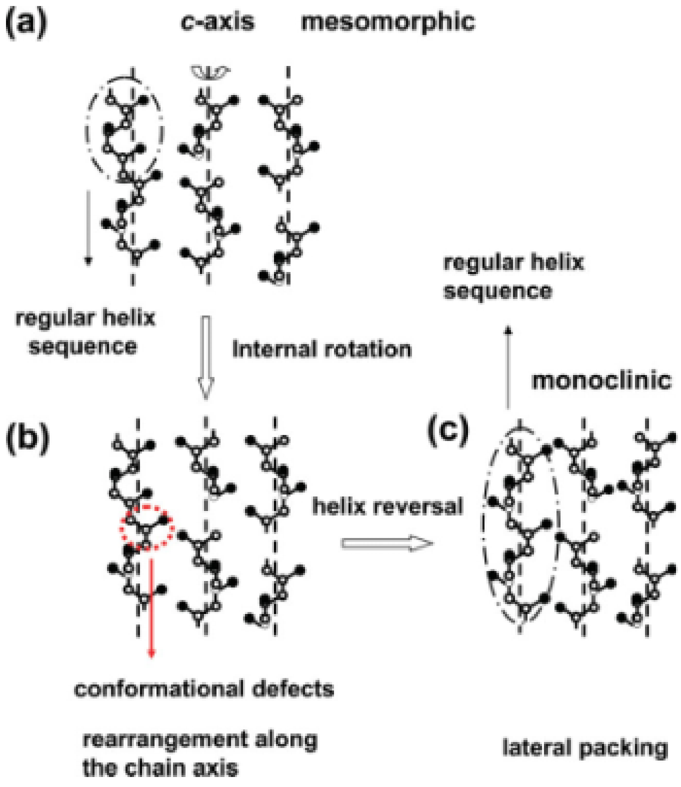

Figure 2.109: Phase transition from mesophase crystals to monoclinic crystals [131]

2.3.3.5 The amorphous phase

Since the pioneering studies of Wunderlich et al [106], [108], [107], presented at section 2.3.1, the amorphous phase has attracted less attention than the crystalline or the mesophase, though it is not yet fully understood [132]. The intrinsic properties of that phase in relation with the chain topology have nevertheless a big impact on the macroscopic properties. The way the amorphous phase is organised has an influence on the various phases of the material. Various types of chains are involved in the interlamellar amorphous regions, as already illustrated at figures 2.41, 2.88 or 2.96.

Figure 2.110 displays for instance the random coil crystallisation from the molten state in the case of two situations, where the assumption has been made that the chain topology is preserved.

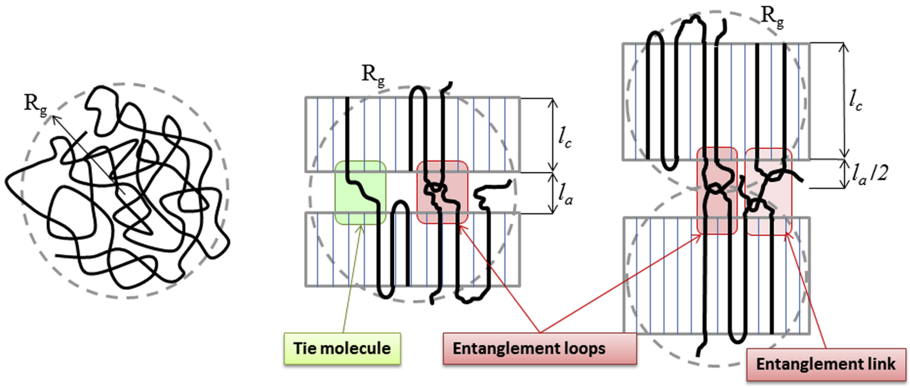

(a) (b) (c)

Figure 2.110: Chain random coil in the melt followed by two situations after crystallisation: (a) random coil and its gyration radius R_g, (b) model of Huang and Brown [73] where the gyration radius spans $2L_c + l_a$ and (c) model where the gyration radius spans $l_c + 1/2l_a$ [46]

A more detailed, though not exhaustive, explanation is displayed at figure 2.111 in the case of PE. The letters A to F refer to various components of the interlamellar molecular network: (A) tight fold, (B) statistical loop, (C) loose chain end, (D) free chain, (E) tie chain, (F) trapped entanglement involving two statistical loops [133] referred as "entanglement link" in the figure 2.110.

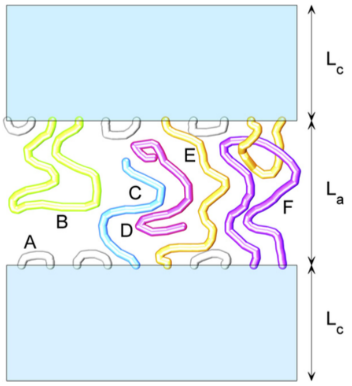

Figure 2.111: Possible shapes of polymer chains entering the amorphous region between two crystalline layers; for explanation on the letters, see text [133]

From a mechanical point of view, another description of the amorphous phase has also been attempted by Nikolov et al [34] in the frame of a micro-macro approach of small deformation in HDPE. In this case, this phase was modelled at room temperature assuming it was constituted by small domains of liquid crystal-like structures as represented at figure 2.112. Indeed, the polymer chains in the amorphous phase are subjected to severe constraints from the lamellae and are situated in extremely thin layers with thickness of the order of 8-10 nm, i.e only one order of magnitude of the persistence length that is evaluated to be 1 nm for PE and 2.38 nm for iPP [124]. As most of the molecules are anchored in lamellae, chain ends are situated mostly on the lamellae surfaces and entanglements are quite stable defects. In these conditions, the domains are assumed to slide on each other, resulting in the shearing of the amorphous phase. As a result, the viscoelastic stress in the amorphous layers is due to the resistance of polymer molecules to distortion during deformation rather than to their stretching and reptation as in the melt.

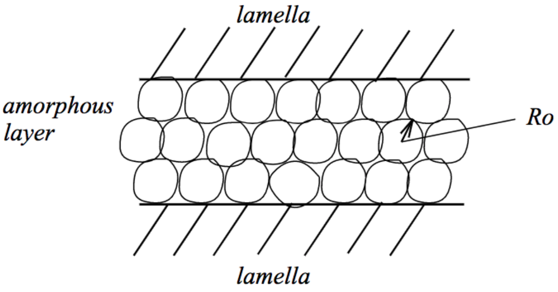

Figure 2.112: Microstructure of the amorphous layer with the domains for HDPE [34]

This approach could be supported by the research of Rungswang et al [124] that monitored by SAXS the evolution of crystalline lamellae of two isotactic polypropylenes during crystallisation. These authors identified that polymer chains aggregate into denser domains prior to crystallisation, and these can be considered as nucleation sites. These domains are induced by the parallel interaction of ordered chain segments and are formed when these segments length exceed the critical value of the persistence length. As time passes and as illustrated at figure 2.113, the chains fold and form stacks of lamellae, though one has to keep in mind that not all the domains will transform into lamellae and could then remain in the solidifying polymer as mesophase.

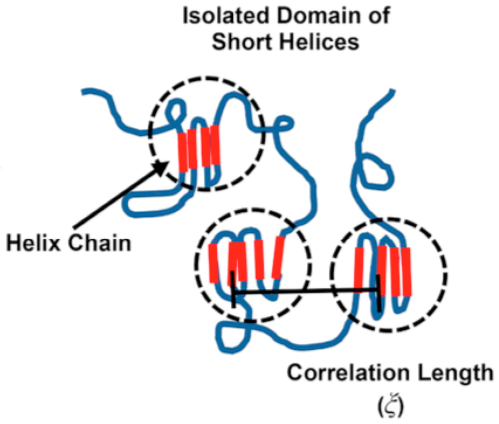

Figure 2.113: Steps of evolution from the random coil during crystallisation with the apparition of elusive dense isolated domains; the correlation length found from the SAXS measurement gives an idea of the average distance between neighbouring domains [124]

Nikolov et al proposed also that in semi-crystalline polymers, each crystalline lamella should be wrapped with a surface layer (membrane) of intermediate phase that ensures the link between the crystalline and amorphous phases. This scheme is in fact displayed at figure 2.114 where Rungswang speaks about a transition zone whereas referring to the section 2.3.1, this link has been ascribed to the RAF that is covalently bounded with the crystal lamellae. It is thus quite tempting to define the intermediate layer as the RAF, though the exact structure and location of this latter has still to be better understood [134].

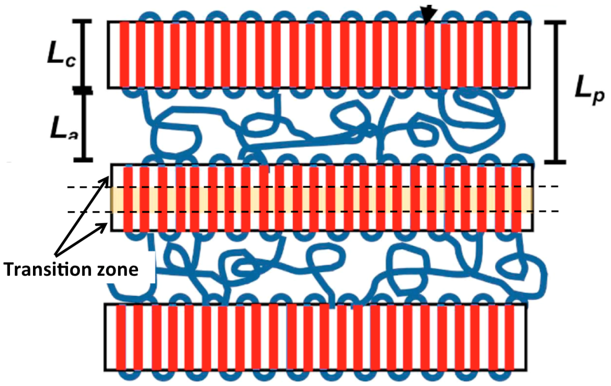

Figure 2.114: Crystalline lamellae with a transition zone between the crystalline and amorphous phase [124]

It is worth to highlight that the notions of mobile and rigid amorphous fractions have been developed by Wunderlich et al by adopting a thermodynamic approach [106], [108], [107], [18], meaning that thermal analysis was the main tool used. Since then, several authors have tried to identify by other complementary techniques such as modulated DSC, DMTA or various spectroscopies (FTIR, SAXS, WAXS, RAMAN) its real structure and topology and how it is influenced by the mesophase (see chapter 5 for more details and for instance [21], [135], [64]).

A scheme presenting the evolution of the mesophase and of the two amorphous phases is displayed at figure 2.115 where the crystalline and meso- phases are drawn in blue, the RAF in green and the MAF in yellow. Authors explain that [21] as RAF is covalently coupled with the mesophase and MAF, its conformation regularity is higher for the segments neighbouring the mesophase than those nearby the MAF. When the temperature ranges between 20°C and 60°C, the mesophase is preserved, the RAF segments close to the MAF undergo their glass transition and therefore transfer chains to the MAF. Meanwhile, the RAF segments that are more regular and close to the mesophase are also preserved. Via this mechanism, the RAF amount (thickness) decreases whereas the MAF amount (thickness) increases while the global amount of amorphous phase remain constant. Then, as temperature increases further (between 60°C and 120°C), the RAF segments close to the mesophase form α-nuclei by adjusting their chirality and/or moving their position, allowing the chains in the mesophase to form an α-crystal. When the temperature goes beyond 120°C, the number n of the helical sequences of consecutive monomers present in the crystal increase from $8 \leq n < 13$ to $n \geq 13$ and those ones in the amorphous phase decrease from $n \leq 4$ to shorter ones (see chapter 5 for detailed explanation).

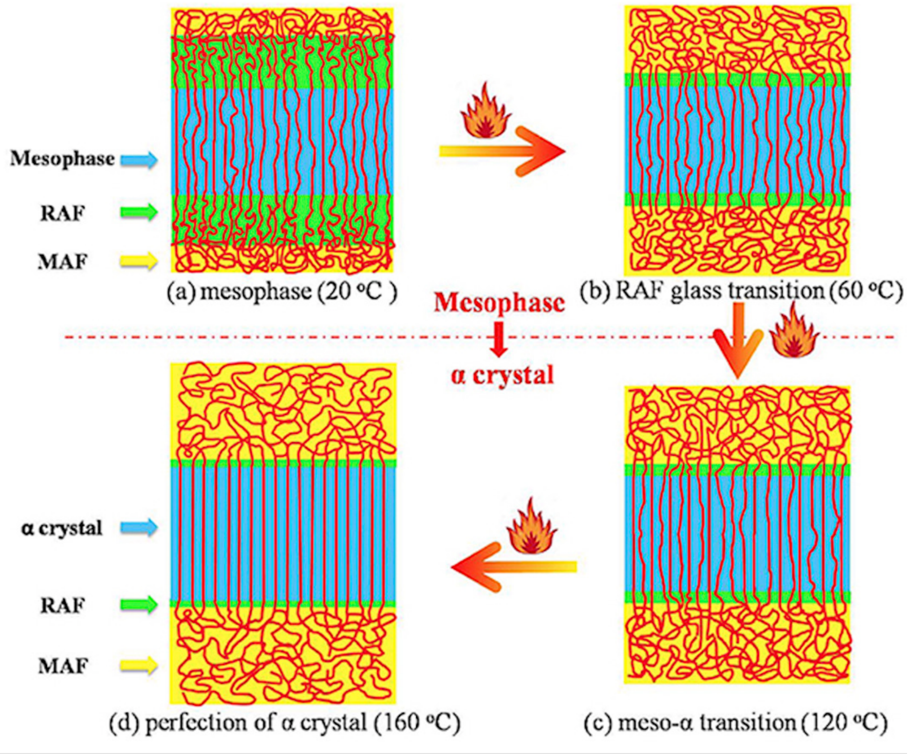

Figure 2.115: Microstructural changes in the meso- to α-crystal phase transformation process; the crystalline and meso- phases are drawn in blue, the RAF in green and the MAF in yellow [124]

Kida and Yamagushi [64] on their side prepared samples of iPP with various fractions of rigid amorphous phase. Using various spectroscopies as well as DSC, they found that the RAF increased, suggesting that it is not located at the interface with the crystalline lamellae. Rather, they observed that the RAF increased linearly with n for $12 \leq n \leq 14$. Therefore, they assigned the RAF to helical sequences ranging between 12 and 14 monomers mainly included as defects in the crystalline lamellae because $n = 12$ is the minimum number requested of monomer units for helical sequences to crystallise. These defects are excluded from the crystal above the visco-elastic α temperature. As a consequence, RAF exhibits the opposite behaviour of MAF during the annealing process, supporting the observations of Jiang et al [21] mentioned above.

All in all, and also referring to section 2.2.2.12, the analysis of the amorphous phase and of its coupling with the other phases shows that an important aspect to be considered for a further investigation of their visco-elastic and mechanical properties should be how far the confinement operated by primary crystalline lamellae and crystalline lamellae resulting from the transformation of the mesophase plays a role.

2.4 A specific type of chemical aging: the thermo-oxidation of isotactic polypropylene

The thermo-oxidation of polyolefins has been studied for a while by various techniques with the aim to understanding its kinetics, the mechanisms of reaction in relation with the microstructure and its impact on the properties [136], [137], [6], [14], [138], [139], [140], [94], [141]. The oxidation rate of these polymers is strongly dependent on the chemical structure, the thermo-mechanical history of the sample and the oxidation conditions. It is not the purpose to perform here a detailed review of the literature dealing with this topic, rather to mention some of the important and main characteristic features, as thermo-oxidation had to be taken into account in the experimental part of this research as we shall see later in chapter 3.

Polypropylene can undergo degradation under heat and light and in presence of oxygen, which has an impact on its usage properties. The stability of polypropylene depends on trace amounts of impurities such as hydroperoxides, carbonyl and contamination such as catalyst residues and metallic compounds [136], [6]. The oxidation of polyolefins is an heterogeneous phenomenon which kinetics is complex, because it is not only due to the semi-crystalline nature of the polymer and in the case of polypropylene, to its level of isotacticity, but also due its density as well as the geometry of the sample involved in the oxidation [142],[137].

For many years, the crystalline phase was considered not to be affected, because of the very low mobility of the chains that exclude oxygen from this phase. However it has also been demonstrated that oxidative degradation has an effect on crystal phase characteristics. The dramatic changes in the DSC curves have then been explained as an effect coming from the oxidation of crystal surface [138] while density and crystallinity increase at the beginning of degradation and this has been related to chain scission, which is the main driving force leading to rearrangement of chains formerly unable or prevented to move [14]. These slight variations in the iPP crystalline content have been found during oxidation induction time as well as first stages of oxidation. It has been evidenced that this deals not only with the apparition of an increase amount of "low-T_m crystals" formed by annealing and chain scission processes and subsequent disappearance at the beginning of auto-acceleration, "high-T_m crystals" are also involved [138]. The terms "low-T_m crystals" and "high-T_m crystals" refer respectively to crystals well below or close to the melting temperature (see also section 2.2.4).

To summarise, the initiation step seems to come from chain shortening in disordered regions of the crystalline interphase (or RAF) whereas the propagation step seems to be linked to the crystal phase itself and the problem is to understand if the ordered regions integrate chain segments from the amorphous phase or undergo a true modification of the crystalline phase because of physicochemical processes (annealing, oxygenated groups build-up and chain scission) [14].

The chain scission leading to degradation has been described in figure 2.116.

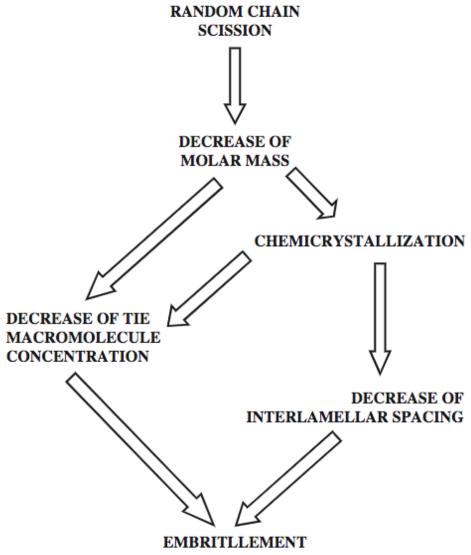

Figure 2.116: Scheme of possible causal chains for degradation-induced embrittlement due to chain scission [139]

The effect of content and quality of isotacticity defects together with the associated average isotactic length on the induction time t_{ind} and on the activation energy E_{act}^{th-ox} of the thermo-oxidation impact significantly at an average isotactic length of 30 propylene units. This is explained by the changes induced in the crystalline interphase, i.e. by the local dynamics of the (macro)molecules that are closely linked to the initial stage of the thermo-oxidation and can be characterized by the DMTA gamma relaxation. Above 30 units, the insertion of isotacticity defects decreases the thermal stability of the material. By contrast, below this number, the insertion of defects cause both the activation energy of the mechanism and the stability to increase. The relative intensity of the iPP sub-T_g relaxation can be used to identify the induction time of the degradation process, with the induction time measured at the moment at which the oxygen uptake reflects the ability of individual chains to accumulate hydroperoxydes [140].

In general, thermo-degradation processes are identified via a toolbox of techniques, among which DSC, DMTA and FTIR are the most popular. The figure 2.117 gives a good summary of the analyzed components. The detailed explanation of each peak is given hereunder.

The literature reports an increase of several peaks associated to the thermo-oxidation of iPP. This latter is characterized by hydroxyl [OH] groups, carbonyl [C=O] groups and unsaturated [C=C] groups, i.e. H-bonded hydroxyl (hydroperoxides) groups centered around $3400 cm^{-1}$, multiple carbonyl peaks centered around $1720 cm^{-1}$

or internal standard such as $1166 cm^{-1}$ or $2721 cm^{-1}$. The relative area between this latter and the carbonyl peak is used as carbonyl index to assess the degree of degradation.

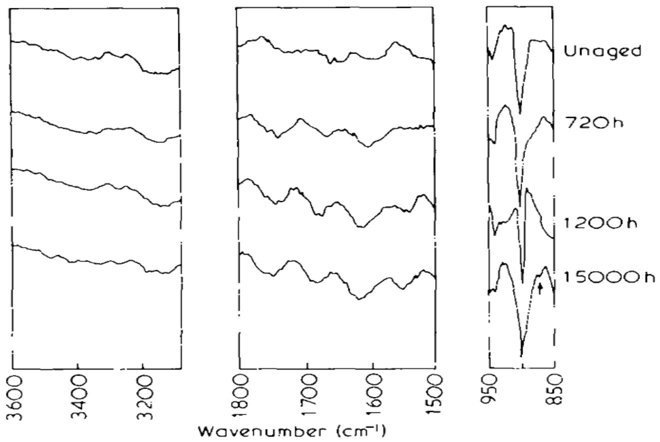

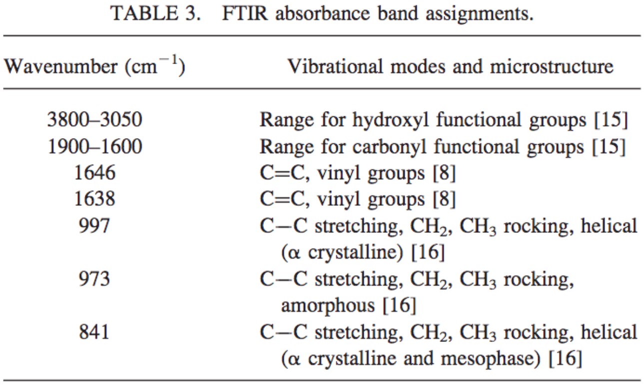

TABLE 3. FTIR absorbance band assignments.

Wavenumber (cm^{-1})	Vibrational modes and microstructure
3800–3050	Range for hydroxyl functional groups [15]
1900–1600	Range for carbonyl functional groups [15]
1646	C=C, vinyl groups [8]
1638	C=C, vinyl groups [8]
997	C−C stretching, CH_2, CH_3 rocking, helical (α crystalline) [16]
973	C−C stretching, CH_2, CH_3 rocking, amorphous [16]
841	C−C stretching, CH_2, CH_3 rocking, helical (α crystalline and mesophase) [16]

Figure 2.117: (a) FTIR peaks associated with thermo-oxydation of iPP (hydroxyl: $3800 - 3050 cm^{-1}$, carbonyl: $1900 - 1600 cm^{-1}$, unsaturated groups as of $1600 cm^{-1}$ and crystal region: $1000 - 850 cm^{-1}$ [136] and (b) table summarizing the related molecular motions [6]

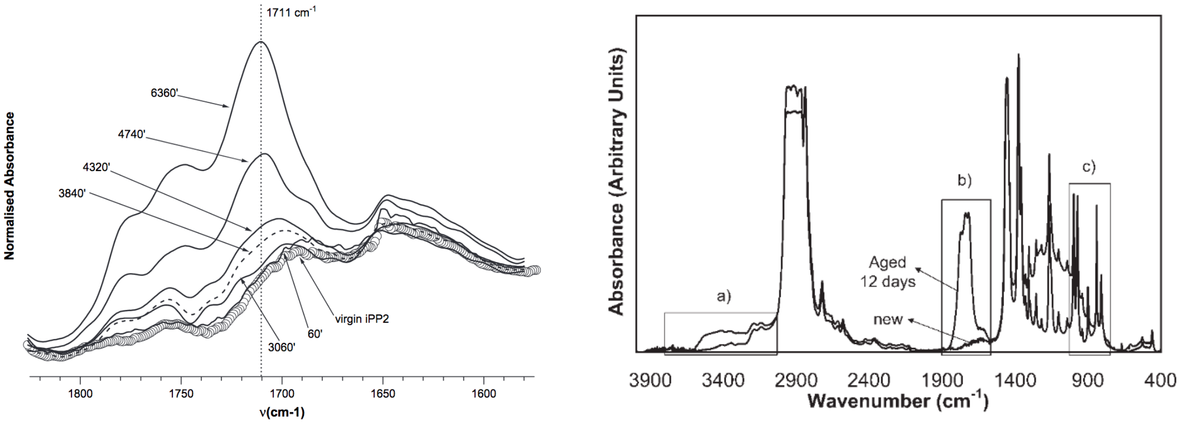

Figure 2.118: FTIR peak evolution as a function of annealing time of (left) carbonyl [138] and (right) a) region for hydroxyl groups, b) region for carbonyl groups and c) region for crystallinity [6]

Furthermore, the more the material is damaged, the more the peak increases, as illustrated for instance at figure 2.118 for the carbonyl, with an iPP virgin and then aged at various times.

2.5 Conclusion

Isotactic polypropylene is a very cumbersome material, being composed in its solid state of various phases themselves organised into hierarchical structures, and undergoing influences from time, temperature, deformation, physical and/or chemical ageing. These components depend themselves on the crystallisation conditions and thermo-mechanical history and on the chemical structure. In this state-of-the-art, we have reviewed the various models and theories tackling these various dimensions, emphasizing the link between the microscopic and the macroscopic scales via the various deformation and relaxation processes occurring at small deformation in relation with the type of catalysis technology used.

The main aspects are highlighted hereunder.

With regards to the molecular relaxations, the multiphasic composition of the iPP is translated into multi peak relaxations in the visco-elastic spectra. The molecular movements occurring in these various phases are strongly coupled to each other above the glass transition where two components have been identified: a lower and upper relaxation, named α_1 and α_2 assigned to the nucleation and propagation of dislocations in the crystalline phase and their subsequent strain transfer to the amorphous phase, making the interface between phases, i.e. the rigid amorphous fraction, a critical layer the role of which has to be understood. When there is only one α-peak, the influence of the molecular structure can be seen via the shift of T_α between the values of α_1 and α_2, i.e. $T_{\alpha 1} < T_\alpha < T_{\alpha 2}$. The same type of observation can be made by analysing the influence of frequency because depending on its magnitude the position of these vary as well and one or several peaks can appear.

The influence of the catalyst, namely the role of defects and defects distribution - with the molecular mass being otherwise equal - on the crystalline and the amorphous phase has been highlighted via the isotactic length n_{iso} that is a relevant parameter to describe what is happening at the interfaces. Ideally, this parameter should be put in relation to a certain extent to the stress transmitters. The crystalline phase is more prone to trap the stereo-defects which tend to be distributed over the higher masses in ZN catalyst. The regio-defects, evenly distributed on the chain in the metallocene catalysts, are likely to be rejected in the amorphous phase. These features have an impact on the crystalline thickness, the melting temperature, the number and quality of stress transmitters as well as the global visco-elastic behaviour of the amorphous phase.

At similar chemical structures, the influence of the thermo-mechanical history has been highlighted by the presence of various phases: a crystalline phase that is in the vast majority of cases an α-phase. These crystals are seen as nodes between the amorphous layers and have thus, depending on their geometry, a more less substantial impact on their global viscoelasticity and structure. The mesophase composed itself of nodules of condis crystals, MAF and RAF undergoes a glass transition and a solid/solid transformation into an α-phase above 80°C-100°C. Depending on the solidification/ageing or annealing conditions, the crystalline phase can be therefore constituted with parent, subsidiary and transverse lamellae, the two latters likely resulting from the mesophase transformation. In this case, the resulting solid state microstructure could be considered as a tri- or a quadri-phasic system, embedding various crystalline lamellae, RAF and MAF and more indirectly the stress transmitters. There is thus a real need to understand how far these various components are interacting mutually and transfer helical sequences to each other at their interfaces , and especially how their evolution with the annealing temperature and namely the apparition of subsidiary and/or transverse lamellae confines further the amorphous phase in general.

With regard to the deformation mechanisms of plasticity, the same type of molecular events than those found in the visco-elastic relaxations, i.e. the nucleation and propagation of dislocation, explain the presence of a double yield that has been proved to be associated to the two α-relaxations: the first yield around 5-15% associated to the homogeneous slip of crystalline lamellae and to the upper relaxation α_2, and the second yield around 20-30% associated to the heterogeneous slip or shear and the neck apparition as well as to the lower relaxation α_1. It is known that there is a competition between the plastic flow and the cavitation process, and that the heterogeneous slip mechanism is coupled at the microscopic level with the creation and coalescence of voids. From a statistical viewpoint, the influence of polydispersity on the global crystalline microstructure is maybe an element that should also be taken into account. In particular, it is possible that shorter chains and their chain ends play an important role in the creation of local inhomogeneities and defects promoting imperfect crystals more prone to be fragmented. One may also wonder about the possibility to get different dislocation kinetics in relation with different crystal thicknesses. The distribution of molecular weights would play here the same as strain rate or temperature. This competition has thus to be clarified in order to understand what are the respective kinetics and thermodynamics of the two processes.

One way to address this issue is to look at these mechanisms as activated ones. In order to do that, Ree-Eyring theory is a useful approach, having also its counterpart for mechanisms linked to fracture (Zhurkov theory) that we did not address in this review.

The Ree-Eyring theory allows to identify the various mechanisms of yielding at stake in the material, and to calculate activation parameters such as energy and volume. It makes also the link between the micro- and the macroscale via a term that reflects the frequency at which the order or disorder changes under the influence of the stress and of the temperature, and is directly related to the solid state of the considered material.

In the visco-elastic range, we have seen that the building of a master curve is one way to widen the access to a broad range of temperatures and times, as long as - and this is critical - we are comparing identical mechanisms. The procedure coming from methodologies used in rheology helping to make visible very small structural variations while ensuring to compare the same phenomena is an interesting tool to be considered to study a solid state where many phases and therefore many mechanisms are interacting together, and possibly overlapping.

Finally, the thermo-oxidation topic was also quickly overviewed because this process is important when working over long periods and at high temperatures. It is important to ensure that the microstructure remains the same and that no degradation occurs during the whole experiment.

In conclusion, thanks to the underlying common dislocation mechanisms, first, the two limits of the small deformation range can be put in relation with each other, and the various activation parameters identified and compared, and second those can be put in relation with the chemistry and the thermo-mechanical history behind, especially the role of defects, of condis and RAF and of stress transmitters.

Chapter 3 : Characterisation of the solid state microstructure

Table of contents

3.1 Introduction

As explained in chapter 2, iPP has a particularly complex solid state structure, that undergoes changes of its solid state microstructure under aging, thermo-oxidation or annealing [136], [137], [6], [14], [138], [139], [140], [94], [141]. There was thus a need to understand the evolution of our materials in order to find the most adapted stabilisation conditions.

Polypropylene can undergo degradation under heat and light and in presence of oxygen, which has an impact on its usage properties. The stability of polypropylene depends on trace amounts of impurities such as hydroperoxides, carbonyl and contamination such as catalyst residues and metallic compounds [136], [6]. The oxidation of polyolefins is an heterogeneous phenomenon which kinetics is complex, because it is not only due to the semi-crystalline nature of the polymer and in the case of polypropylene, to its level of isotacticity, but also to its density as well as the geometry of the sample involved in the oxidation [142],[137].

Oxidative degradation has an effect on both crystal and amorphous phases characteristics, as illustrated for instance by dramatic changes in the DSC curves [138]. Density and crystallinity increase also at the beginning of degradation and this has been related to chain scission, which is the main driving force leading to rearrangement of chains formerly unable or prevented to move [14]. The initiation step seems to come from chain shortening in disordered regions of the crystalline interphase (or RAF) whereas the propagation step seems to be linked to the crystal phase itself and the problem is to understand if the ordered regions integrate chain segments from the amorphous phase or undergo a true modification of the crystalline phase because of physicochemical processes (annealing, oxygenated groups build-up and chain scission) [14].

In general, thermo-degradation processes are identified via a toolbox of techniques, among which DSC, DMTA and FTIR are the most popular. In this latter case, the literature reports an increase with damage of several peaks, such as hydroxyl [OH], carbonyl [C=0] and unsaturated [C=C] groups, i.e. H-bonded hydroxyl (hydroperoxides) groups centered around $3400cm^{-1}$, multiple carbonyl peaks centered around $1720cm^{-1}$ or internal standard such as $1166cm^{-1}$ or $2721cm^{-1}$.

In this chapter, we will present the results obtained on the characterisation of the solid state microstructure for the two campaigns carried out on the materials. We have looked especially at the aging or annealing time and temperature conditions at which the various structures have stabilised without undergoing degradation. We have also checked their crystalline form and measured first mechanical properties at room temperature.

3.2 Materials and sample preparation

The use of industrial grades has allowed mitigating all possible variations due to the chemical structure and a very special care was taken to mitigate the irreducible scattering coming from cooling conditions and laboratory experiments by controlling at best its origin (film and possible degradation, test or signal). When, due to technical problems, two equipment's were used for one type of test, the alignment between the results was always checked and discrepancies analysed. We have also used the same samples to perform first non destructive tests such as FTIR or RX and then destructive tests such as DSC or tensile tests. When this was not possible, we have tried to set samples as close as possible of removal locations that were duly recorded.

3.2.1 Materials

The materials used in this research are grades of isotactic polypropylene provided by TotalEnergies. They are all pelletised homopolymers, without any additives but those required for stabilisation and process.

The characteristics of the materials are presented at table 3.7. The products were selected with a view to allowing easy comparison of the molecular structures, namely two different catalysis platforms with two types of non-uniformity (polydispersity) index, the metallocene catalysis displaying a narrow distribution of molecular weights M_n/M_w compared to Ziegler-Natta. Ziegler-Natta catalyst (ZN) is known to have only stereo-defects, whereas metallocenes (MET) have both stereo- and regio-defects [112], [115].

Table 3.7: Characteristics of the various homopolymers used in this study. "ZN" states for "Ziegler-Natta" catalyst and "MET" for "Metallocene" catalyst. The isotactic index is given by the percentage of pentads [mmmm]; * values coming from P_5 considered as similar to P_6

Product	P_1	P_2	P_3	P_4	P_5	P_6
Catalyst	ZN	ZN	ZN	ZN	MET	MET
$MFI(g/10min)$	4	12	25	25	25	15
$M_n(Da)$	54 100	42500	32 400	45 600	52 800	64 600
$M_w(Da)$	333 000	251000	185 000	186 000	157 000	187 000
$M_z(Da)$	1 130 000	1 210000	562 000	418 000	294 000	356 000
M_w/M_n	6.2	5.9	5.7	4.1	3	2.9
$T_m(°C)$	163	163	163	163	150,3	151
$[mmmm](\%)$	97,5	/	97	/	99.2	99.2*
$[mm](\%)$	98.5	/	98.1	/	99.5	99.5*
$[mr](\%)$	1.03	/	1.2	/	0.3	0.3*
$regio - irregular](\%)$	/	/	/	/	0.9	0.9*

3.2.2 Samples preparation

All the films have been moulded using two Carver presses and one mould. The average thickness of the films was around 300 μm though a range between 200μm and 400μm was observed. The details can be found in the supporting information - see section 3.6.1.
Two campaigns have been organised, one dedicated to the processing influence and a second to the molecular architecture influence. In the first campaign, the films of P_1 were prepared according to three cooling conditions: quenched (called "P_{11}"), quenched and annealed 8h at 130°C (called "P_{12}"), undercooled isothermally 8h at 130°C (called "P_{13}"). The cooling rate for the quench was estimated to be around 20°C/sec. The temperature for the annealing and undercooling was identified from isothermal crystallisation performed by DSC between 110°C and 150°C with either 10°C or 5°C steps. The second campaign tackled all the products with only the quenched conditions, from P_{11} to P_{61}.

3.3 Microstructure: characterisation methods

In this section, we describe the various characterisation methods of the microstructure used in general for this research. As will be explained later, DSC has been used mainly to establish the relevant time and temperature conditions to get a stabilised structure whereas FTIR and SEC have been used to analyse the degradation aspects. RX (SAXS, WAXS) methods have allowed to identify the crystalline structure of our materials. Finally, quasi-static tests have allowed to complete this overview of the solid microstructure characterisation.

3.3.1 DSC

The DSC traces were recorded with two different apparatus because of some technical issues, a TA Q200 and TA Q2000. All the tests were run at 10°C/min. The heating and cooling phases were ranging between 15°C and 230°C and the material was kept during 5 minutes at 230°C before cooling.

As primary tests used to identify stabilised microstructure, DSC traces were analysed by taking into account the thermomechanical history and the testing equipment (physical conditions and signal treatment).

3.3.2 FTIR

The FTIR measurements were performed with a Bruker Tensor 27 Standard equipment. Spectra were recorded using 64 scans at a resolution of $2cm^{-1}$ between 4000 and 600 cm^{-1} at ambient temperature under air. Spectra were then normalised thanks to the software Opus®.

3.3.3 RX

Wide-angle X-ray scattering (WAXS) experiments were carried out owing to a Xeuss (XENOCS) SAXS-WAXS equipment using the CuK_α radiation ($\lambda = 1.54$Å). The WAXS patterns were collected on a Pilatus 100k detector (Dectris). Intensity files were computed from the 2D WAXS patterns using the Foxtrot® software. Standard corrections (dark subtraction, empty beam correction...) were applied before performing any treatment to obtained patterns. Average diffractograms were calculated from the normalized intensity profiles .

SAXS measurements were performed on the same equipment with a different set-up.

3.3.4 SEC

Size exclusion chromatography (SEC) allows determining the molecular average weights in measuring their number average M_n, weight average M_w and z average M_z. Is is usually realised at high temperature (145°C). It was measured on P_1 in order to check the possible presence of some degradation due to annealing conditions, characterised by a shift of the high molecular weight tail towards the left due to macromolecular chains break.

3.3.5 Mechanical tests

A tensile machine Zwick-Roell Z 2.5 with a load cell of 500N was used to run tests at room temperature and measure the Young modulus and the yield stress on the films under standard conditions i.e. 1%/min for the Young modulus and 50%/min for the yield. No extensometer was used and the deformation was calculated from the crosshead displacement. The distance between clamps was 25.4mm. The Young modulus was calculated with a linear regression in the range (0.05%-0.25%) and the yield was taken at the maximum of the stress-strain curve. Both measures were made on the same sample by switching the strain rate/crosshead speed at 0.25%, at the end of the strain range for modulus calculation.

The samples were stamped with a dogbone ISO527 1BA/ASTM D638-V shape.

3.4 Results and discussion

The type of study run in this research constrained us to work with stabilised microstructures because isotactic polypropylene is known to undergo physical ageing and thermo-oxidation [138], [136], [139]. This phenomenon was indeed observed as the press used to manufacture the films was not running under inert atmosphere and the formulation of the products was not overstabilised. As the cooling conditions were providing films not entirely homogeneous and reproducible, the location at which the samples were removed was duly recorded.
The type of crystalline structure targeted was the α-crystal form. It was characterised in order to check the possible presence of other phases, namely due to catalytic support, annealing or degradation.

3.4.1 First campaign: analysis of P_{11}, P_{12} and P_{13} evolution

The films were aged and/or annealed at 100°C, 120°C and 140°C. The annealing temperatures were selected on the base of two main aspects: on the one side, the literature tackling the general phenomenon of physical aging and its kinetics in polypropylene [7], [8], [97], [25]; on the other side, the need to implement quasi-static tests at higher temperatures in order to accelerate the various physical processes occurring under those conditions and ensure that the test time would not go beyond 10% of the total annealing time.

At room temperature, the stay was lasting a few weeks. For the annealing conditions, the films were staying in the oven during up to 350hours. At these temperatures, the literature reports a structural transition of the metastable domains into a stable crystalline form. The crystalline phase can then be constituted by primary, subsidiary and transverse crystalline lamellae and a “low-T_m crystal content” is defined as the content involving subsidiary and transverse lamellae [39], [18], [107], [143], [144], [121], [145], [19]. This “low-T_m crystal content” or "secondary crystal population" is identified as a shoulder on DSC traces [83], [87], [138], [109] and has also a specific signature on WAXS spectra [11], [121], [69].

The degradation observed on the films has been assumed to come from thermo-oxidation processes: it starts from the film edges, challenging the processing conditions, because if the mould is not totally filled, thermo-oxidation can easily be triggered there. The literature reports that thermo-oxidative process starts in the amorphous phase, and/or when a γ-phase crystals is present [138], [136], [140], [94], [139].

3.4.1.1 DSC traces

The method developed to ensure the most robust calculation of thermal quantities (enthalpies, crystallinity) uses the temperature derivative of the heat flow and is based on local extrema, that are physical signatures of processes occurring during the sample heating, as represented at figure 3.119. Though derivative is a very old and traditional approach to signal treatment, we could not find any trace in the reviewed literature.

As we will see in the discussion, this method has allowed us 1°) detecting physical similarities in the DSC traces of all the products before the main melting peak, 2°) highlighting in the expected range of temperature the remaining presence of mesophase even after an annealing above 130 $°C$ [129], [123], [69] and/or α-crystals resulting from its transformation [18], [20], [121]. The figure 3.119 displays the first minimum at (a) 52$°C$ and

(b) 48 $^\circ C$ that corresponds to the onset of disordering of the condis and/or RAF reorganisation process. The second minimum at 81 $^\circ C$ (almost not visible on (b)) is characteristic of the achievement of this process and the beginning of the mesophase transformation into α-crystals that is completed around 120°C [19].

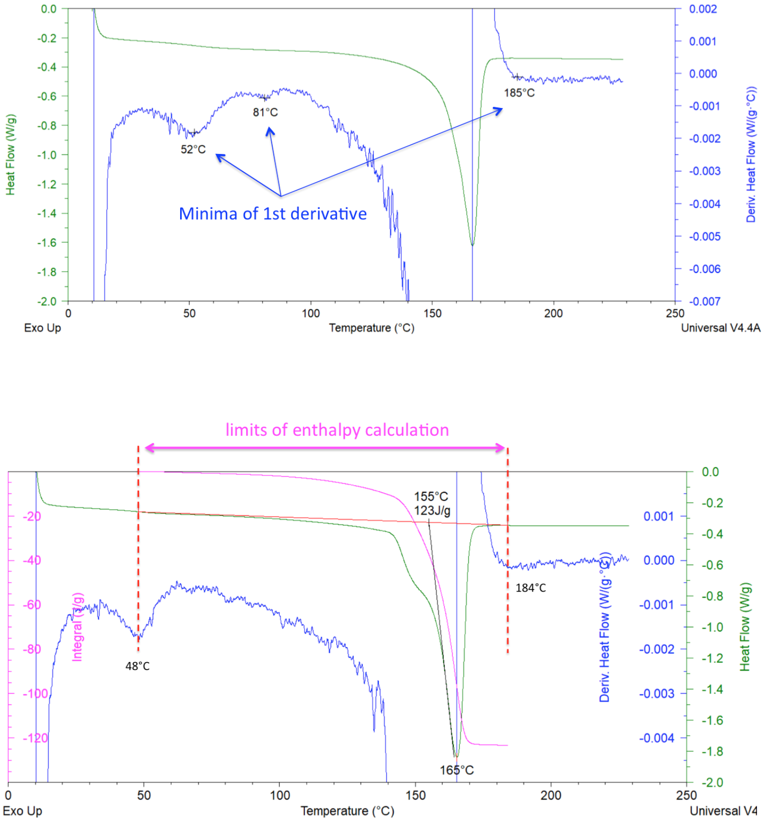

Figure 3.119: (a) Local minima of the temperature derivate of heat flow on P_{11} aged at room temperature; (b) limits identified for the calculation of the enthalpy on P_{11} annealed 4 days at 140°C. Colour code: heat flow in green, 1st derivative in blue, base line and calculation limits in red, enthalpy (integral of heat flow) in pink

According to [83], the typical double endotherm shown by DSC reflects the great complexity of iPP crystallization behaviour (see figure 3.119(b)). As it is composed with several endotherms, it should be deconvoluted in two or even three peaks corresponding to the successive melting of transverse, subsidiary and main parent lamella. In order to circumvent issues linked to deconvolution [10], [125], the low-T_m content was rather calculated in an empirical way [83] from the relative area spanning the beginning of DSC diagram and the temperature $T_m - 8°C$, i.e. the area under the low-temperature shoulder.

The enthalpies, crystallinities and low-T_m content have been computed for all the samples (aged or annealed). Only a few are presented below. Figure 3.120 displays examples of the trend for each quantity. The enthalpy of a perfect α-crystal has been taken as 207 J/g [125], [42].

The analysis of the whole set of data gives some global trends.

Regarding the melting temperature T_m, we have to discriminate between 140°C and the other ageing or annealing temperatures:

1. under ageing at 23°C and beyond 100h, P_{11} melting temperature stabilises around 166°C; under annealing at 100°C and 120°C and also beyond 100h, it stabilises around 165°C; as for P_{12}, beyond 100h and under both ageing and annealing at 100°C and 120°C, it stabilises around 165°C. P_{13} sees its melting temperature increase from 169°C under ageing at ambient temperature to 170°C under annealing at 100°C and 120°C
2. under annealing at 140°C, P_{11} and P_{12} are stabilised around 166°C below 150h; after they start degrading. P_{13} temperature increases slightly to reach 171°C.

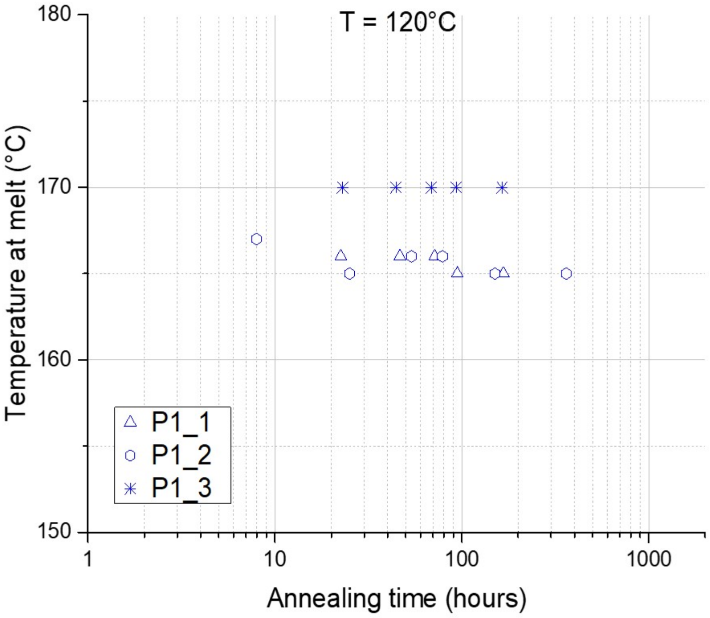

Regarding enthalpies of fusion:

1. under ageing at ambient temperature, P_{12} and P_{13} enthalpy of fusion around 115J/g behave quite similarly whereas P_{11} starts lower (below 100 J/g) but increases and seems to catch up asymptotically at ageing times higher than 1000 hours.
2. under annealing (100°C, 120°C and 140°C; only 140°C is displayed), P_{12} behaves more like P_{11} with an increasing enthalpy that reaches 120 J/g between 100h and 150h and converges towards the level of P_{13}. Beyond 150h, the samples are degraded.

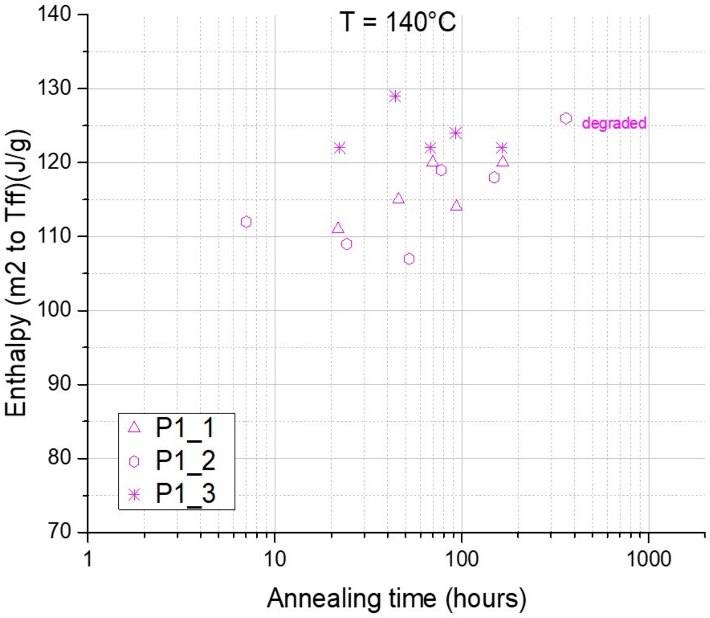

Regarding the fraction of low-T_m content:

1. under ageing at ambient temperature, P_{12} and P_{11} behave quite similarly around 0.35 whereas P_{13} is at 0.45. These values seem to remain constant, even beyond 1000h

2. under annealing (100°C, 120°C and 140°C; only 140°C is displayed), P_{12} and P_{11} behave also similarly, decreasing from 0.35 to 0.3 until degradation beyond 150h. The level of P_{13} remains constant at 0.45; there is thus no difference between ageing and annealing from that point of view.

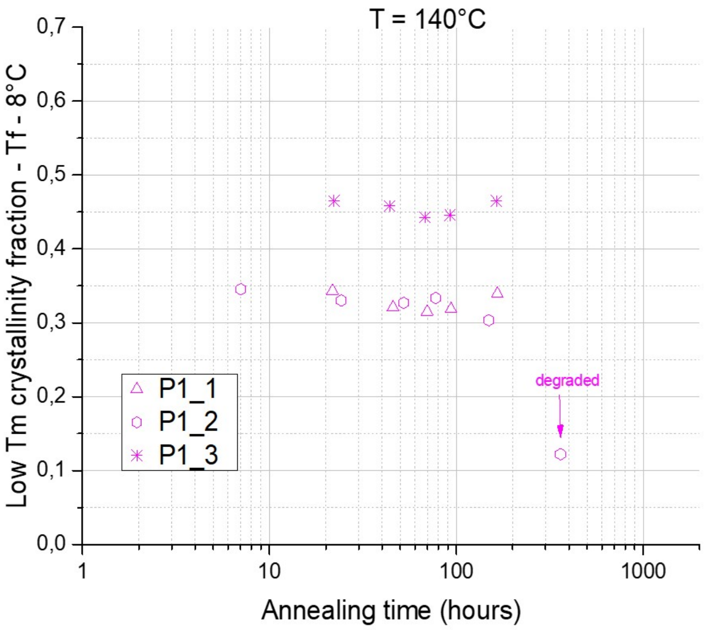

Figure 3.120: Evolution of the melting temperatures, enthalpies and low T_m-content with aging or annealing time of P_{11}, P_{12}, P_{13} at two different temperatures

The results and their trends obtained are summarised in the table 3.8 below.

Table 3.8: Summary of stabilisation conditions. All quantities are approximated values

Product	ageing T $°C$	time (hours)	annealing T $°C$	time (hours)	T_m $°C$	ΔH J/g	χ_c	low-T_m content
P_{11}	23	> 1000	/	/	166	> 100	> 0.48	0.35
P_{11}	/	/	140	100-150	166	120	0.58	0.3
P_{12}	23	> 1000	/	/	165	115	0.55	0.35
P_{12}	/	/	140	100-150	166	120	0.58	0.3
P_{13}	23	> 1000	/	/	169	115	0.55	0.45
P_{13}	/	/	140	< 150	171	120	0.58	0.45

It can be observed that regarding the global crystallinity, P_{12} behaves as P_{13} whereas for the low-T_m content, it is similar to P_{11}, indicating that the subsidiary and transverse lamellae could be similar between both products.

3.4.1.2 SAXS and WAXS measurements

SAXS and WAXS have been performed on samples aged at 23°C and various times. Two different manufactured films have been used in the case of the quenched sample P_{11} to check reproducibility. The crystallinities have been taken from the DSC results obtained on other samples.

Table 3.9: Summary of crystallinity χ_c, long period L_p, crystalline lamellae l_c and amorphous phase l_a thicknesses

Product (age at measure)	χ_c	L_p nm	ρ	l_c nm	l_a nm
P_{11}(576h)	0.47	13.4	0.89	6	7.4
P_{11}(672h)	0.47	13.1	0.89	5.9	7.2
P_{12}(408h)	0.53	17.9	0.90	9.1	8.8
P_{13}(960h)	0.56	21.6	0.90	11.6	10

In the case of the **SAXS** experiments, the long period L_p has been measured (see figure 3.121(a)), which allows finding the crystal thickness l_c by introducing in the calculation the respective crystalline and amorphous densities taken as $\rho_c = 0.95$ and $\rho_a = 0.85$ [42]. Some of the results are listed in the table 3.9 and figure 3.121 below. The way to compute these values is available in the supporting information section 3.6.2.

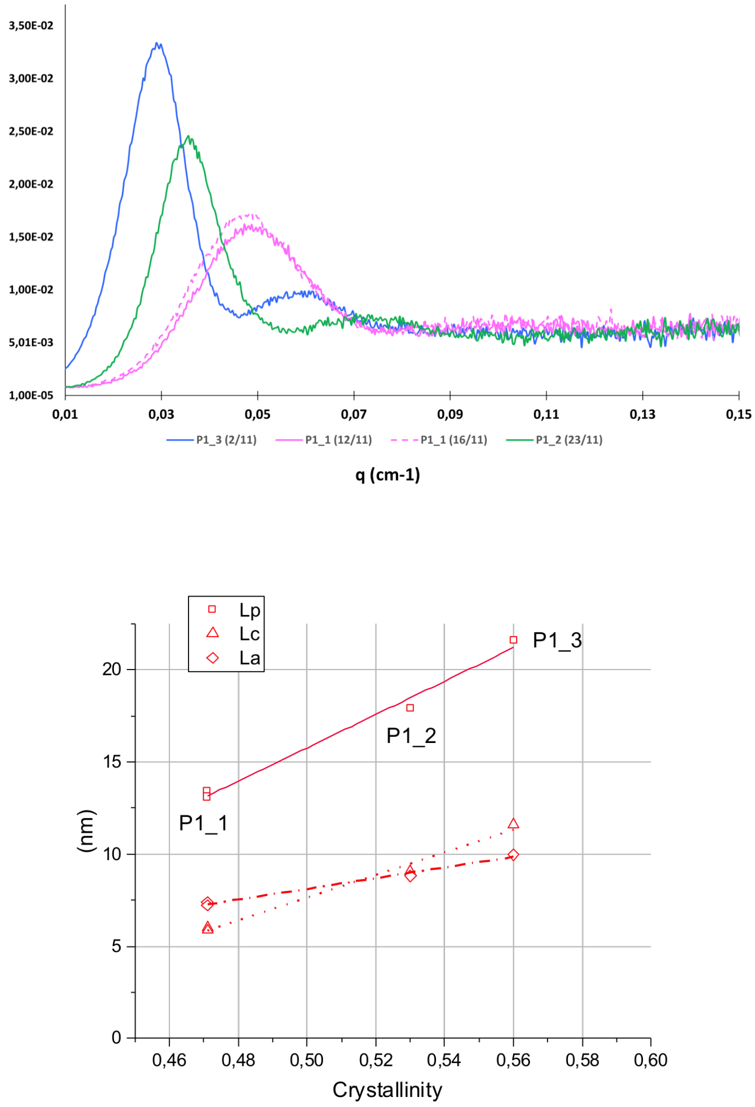

Figure 3.121: (a) SAXS intensity $Iq^2 = f(q)$ on P_{11} (pink), P_{12} (green) and P_{13} (blue) and (b) long period (solid line), amorphous (dashed-dotted line) and crystalline (dotted line) thickness as a function of crystallinity

The ranking of crystal thickness for the products aged at room temperature is as expected [11], [42], [146], [147] i.e. lower for quenched samples, in-between for quenched and annealed samples and higher for isothermally undercooled samples. For P_{12} and P_{13}, the thicknesses of both crystalline and amorphous phases increase with annealing, namely because of the thermal expansion [21], though not at the same rate.

In the case of **WAXS** experiments, the spectra have been compared with the literature standards of iPP (see supporting information for the three polymorphs 3.6.3).

WAXS experiments have been performed on the three products, P_{11}, P_{12} and P_{13}, on films kept at room temperature during several hundred of hours and on films annealed at 140°C.

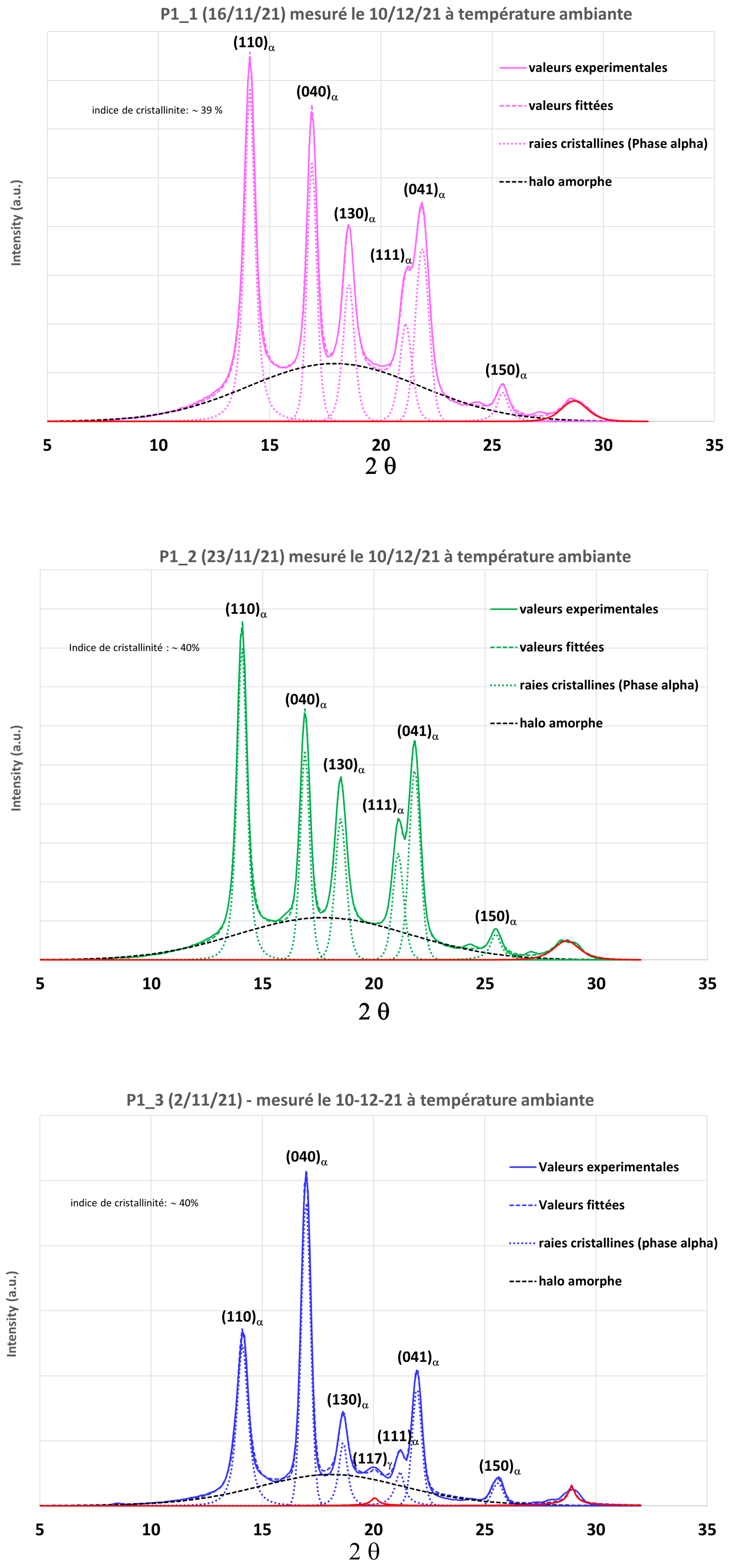
P1_1 (16/11/21) mesuré le 10/12/21 à température ambiante

P1_2 (23/11/21) mesuré le 10/12/21 à température ambiante

P1_3 (2/11/21) - mesuré le 10-12-21 à température ambiante

Figure 3.122: Deconvolution of WAXS-patterns of P_{11}, P_{12} and P_{13} after a stay at room temperature of several hundred of hours. Crystallographic planes have been indicated

According to the literature [18], [69], [148], [135] cooling below 100°C/sec or isothermal crystallisation at temperatures higher than 60°C typically leads to formation of the thermodynamically stable α form. As the quenching conditions adopted for P_{11} are around 20°C/sec, we expect thus to find either only α-form, or a mix of α- and γ- forms.

Figure 3.122 shows the three spectra of (a) P_{11}, (b) P_{12} and (c) P_{13} after a stay at room temperature of several hundred of hours with the deconvoluted peaks. P_{11} is in pink, P_{12} in green and P_{13} in blue.

Figure 3.123 presents the WAXS patterns of P_{11} and P_{13} after respectively a stay at room temperature during 17 days (solid line) and at 140°C during 4 days (dotted lines).

Whereas the spectra of P_{11} and P_{12} are quite similar and characteristic of an α-form, the spectrum of P_{13} displays an intense peak at $(040)_\alpha$ as well as a small peak at $(117)_\gamma$ leading to the conclusion that there is a mix of α- and γ-forms, the α-form being prevailing. The presence of a small β-peak for the P_{11} aged during 17 days and P_{13} annealed at 140°C during 4 days indicate that even under quite traditional cooling conditions, such a crystalline form can be found, though in quite small quantities.

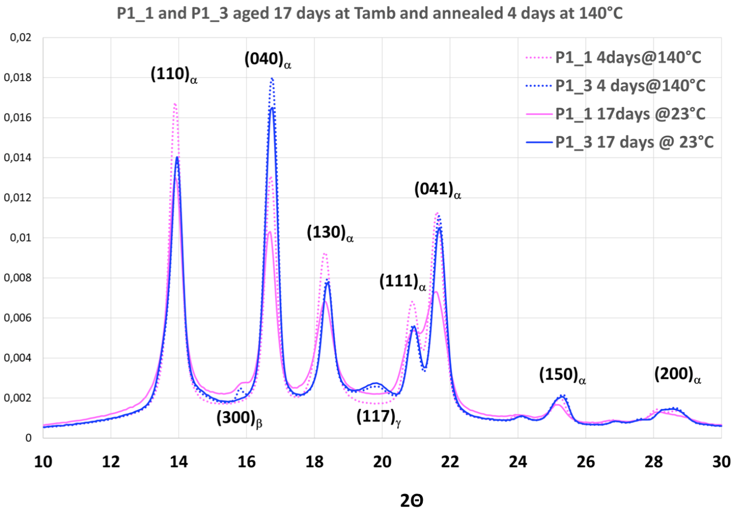

Figure 3.123: WAXS-patterns of P_{11} (in pink) and P_{13} (in blue). Solid lines for a stay at room temperature during 17 days and dotted lines for a stay at 140°C during 4 days; crystallographic planes have been indicated

We can conclude that:

1. the long period increases and the scattering peak sharpens as the crystallinity increases, which means that the distribution of crystals becomes narrow and the crystals more perfects;
2. the evolution of the amorphous and crystalline thicknesses is different. The crystalline thickness increases faster than the amorphous one; this latter remains constant or even decreases with crystallinity
3. due to thermal expansion, the amorphous phase is more significant for P_{13} than P_{11} but it is difficult at this stage to extrapolate on the ratio between its various components (MAF, RAF); the same holds for the mesophase
4. the crystalline form is mainly an α-form; a small portion of β- and γ-forms can be observed in some circumstances.

3.4.2 Controlling degradation

The degradation by thermo-oxidation can be highlighted via combined experiments of DSC, FTIR, RX and SEC. The picture of the figure 3.124 below displays such a phenomenon (left top corner) on a film of P_{11} annealed during four days at 140°C.

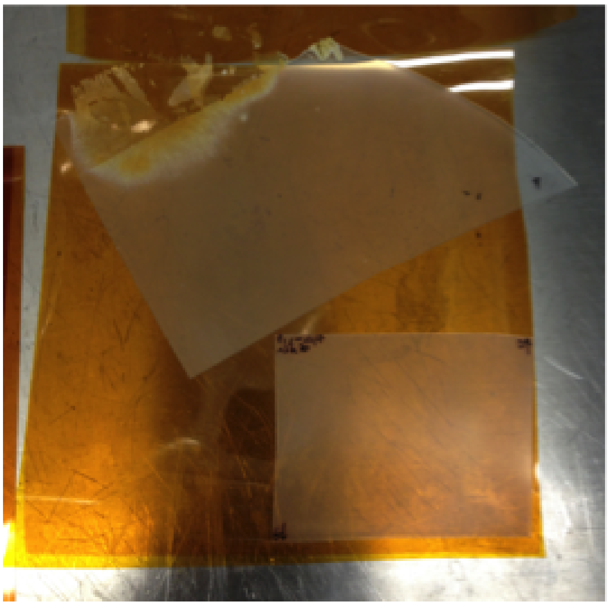

Figure 3.124: Film of P_{11} annealed during 4 days at 140°C. The top left corner of the film is degraded

3.4.2.1 Influence of degradation on DSC traces

The figure 3.125 displays a few tests where the differences between non degraded and degraded samples taken on P_{11} films are visible, according to their location. The samples aged during five days at ambient temperature are drawn with dashed lines and the ones annealed during four days at 140°C with solid lines. It can be clearly observed that the samples located at the edges have a broadened melting peak shifted to the lower temperatures. This is confirmed by other samples not presented here.

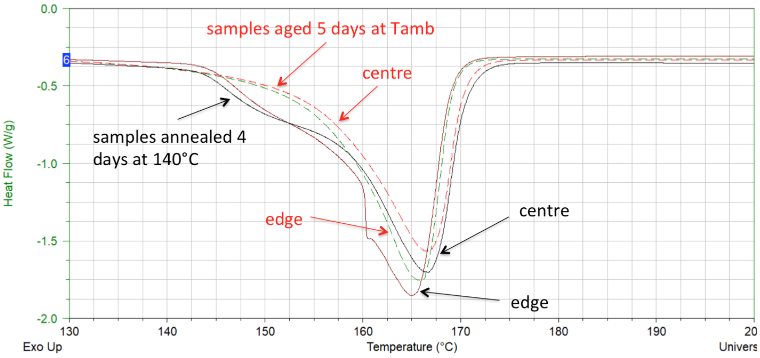

Figure 3.125: Samples of P_{11} aged during 5 days at room temperature (dashed lines) and annealed during 4 days at 140°C (solid lines). Edge and centre locations have been labelled

The heat flow of respectively aged and annealed samples of the isothermal cooled product P_{13} have been superimposed. Some of the annealed samples have been totally degraded, as they were located at the edge of the film and display even a second crystallisation at higher temperature - see figure 3.126.

SAXS measurements have allowed calculating the crystalline and amorphous thicknesses. At the figure 3.127, the damaged zone is visible because of having a lower melting enthalpy and therefore a lower crystallinity while constant long period.

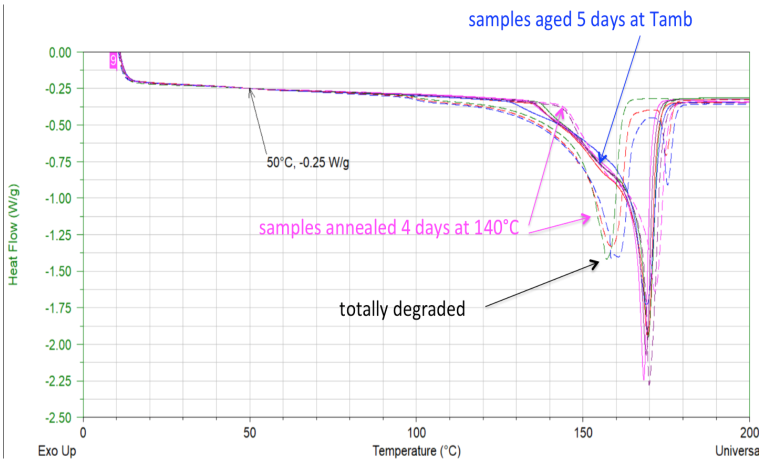

Figure 3.126: Heat flow of isothermal cooled P_{13} samples aged 5 days at room temperature and annealed 4 days at 140°C (some are totally degraded). Line code: samples aged in solid lines, samples annealed in dashed lines

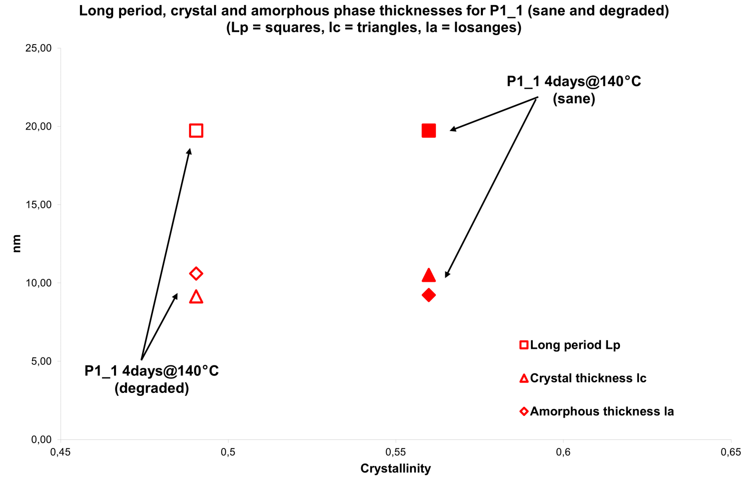

Figure 3.127: Long period L_p, amorphous l_a and crystalline l_c thickness as a function of crystallinity for annealed sane and degraded samples. The damaged sample has been identified as being the less crystalline. Only P_{11} is presented here for readability. Legend: square = L_p , losange = l_a and triangle = l_c. Empty marks hold for degraded sample

It is possible to conclude that:

1. the influence of the degradation on the melting peak temperature T_m (parent lamellae) depends on the aging or annealing temperature. At room temperature, the location of the sample on the film is a first order parameter compared to the cooling conditions whereas at 140°C, the cooling conditions are the first order parameter compared to the location;
2. degradation leads to lower T_m, more intense heat flow in the peak and even to the apparition of a second melting peak;
3. the hypothesis of higher degradation at the edges (trapped in the frame, free edges due to mould not totally filled) is confirmed.

3.4.2.2 FTIR

According to literature [138], [136], the thermo-oxidation of isotactic polypropylene can be monitored thanks to the same chemical species involved in degradation, i.e. hydroxyl groups OH, carbonyl C=O and unsaturated C=C groups as illustrated at figure 3.128.

Usually, the following peaks are considered for these species: the H-bonded hydroxyl groups are centred around a broad peak at $3400cm^{-1}$, the multiple carbonyl peaks centred around $1720cm^{-1}$ and the unsaturated peaks existing in the range $1650-850cm^{-1}$[149].

In the literature [136], [138], FTIR signals are normalised according to internal standards such as $1166cm^{-1}$ or $2721cm^{-1}$, in order to compare the curves. The evolution of the carbonyl peak as a function of the annealing/degradation time is presented at figure 3.128(a) and (b).

Rather than studying the evolution in time of FTIR peaks to monitor degradation as in the literature, we have preferred a different approach, looking at their evolution in the space in relation to the big or small distance with a degraded stain. We have selected the peak at $2721cm^{-1}$ as reference.

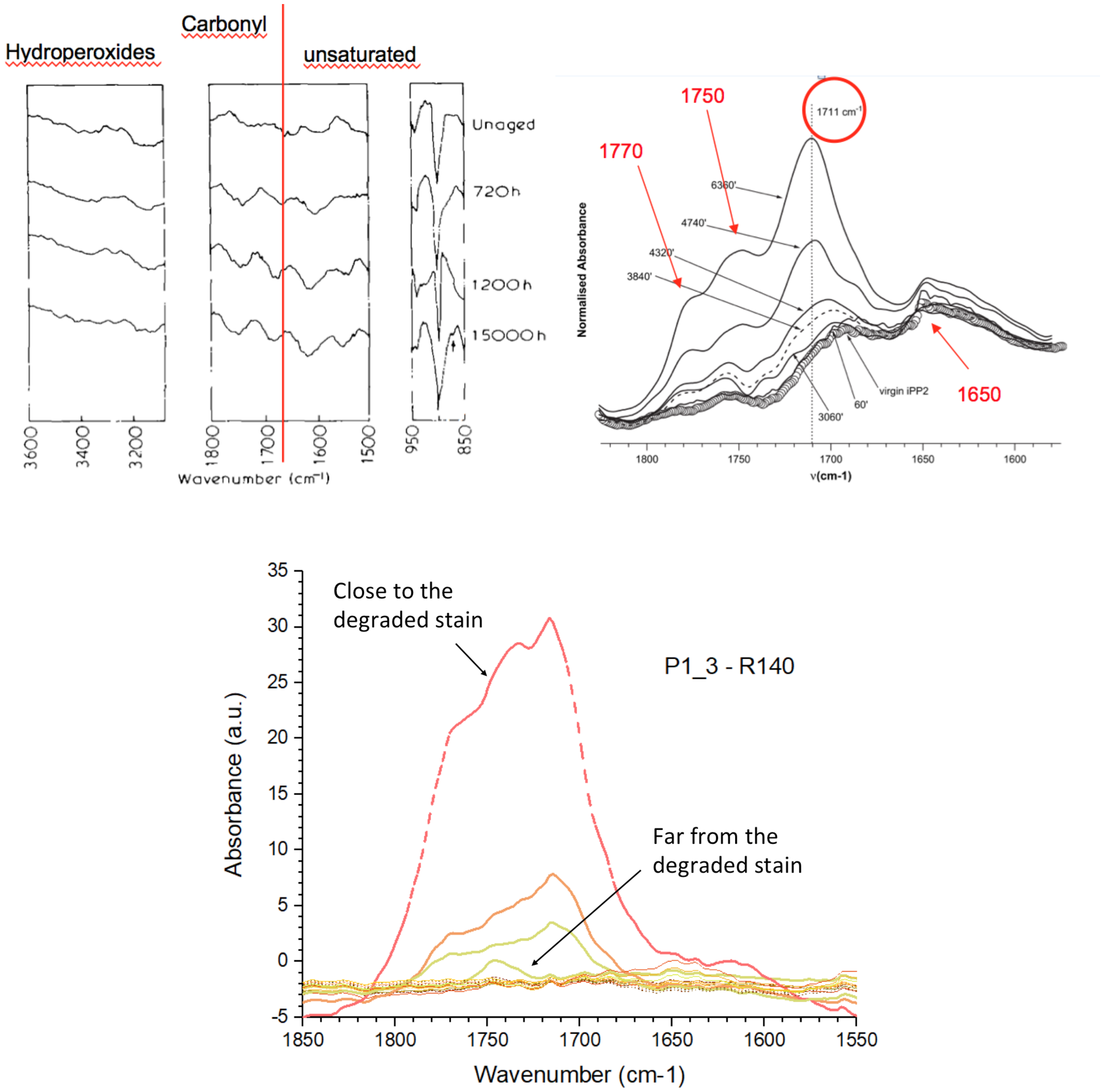

Figure 3.128: Time evolution of IR peaks under annealing: (a) peaks ranges according to the considered species and (b) time evolution of the peak at $1721cm^{-1}$ [136], [138]; the peak is indicated by the red circle; (c) spatial evolution of the peak at $1722cm^{-1}$ for the isothermally undercooled product P_{13} after a stay at 140°C and when approaching a degraded stain

The figure 3.128(c) displays the results for P_{13} after a stay at 140°C at locations closer and closer of a stain. The increase of the peak at $1722cm^{-1}$ is very visible as the distance decreases. On the stain, the intensity of the peak reaches 30 arbitrary units, confirming the literature (see figure 3.128(a) and (b), [136], [138]).

Having identified the peak's intensity levels characterising degradation, we carried out an arbitrary large number of measurements to test whether the film was sound, and used these results to guide moreless the sampling for the other characterisation methods.

3.4.2.3 SEC measurements

The SEC measurements were implemented via GPC on P_{11} and P_{13} purposely degraded samples (5 days at 140°C) with a view to identifying possible changes in the molecular weights distribution, especially in the range of high molecular weights. All the samples were taken close to IR measures. Table 3.10 hereunder displays the results where the ages are expressed in days and the samples aged at $23°C$ provide the reference.

In the low molecular weights, there is a slight difference $\Delta M_w \approx 1580 - 2510$. The difference is more pronounced in the higher molecular weights. More globally, in the case of P_{11}, there is 5 % variation of M_w, a 5 % variation of M_n/M_w, and a bigger variation of M_z. In the case of P_{13}, no variation was observed.

Table 3.10: Modification of the molecular weight distribution for severe annealing conditions. Aging at 23°C is the reference

	P_{11} 6d@$23°C$	P_{11} 5d@$140°C$	P_{13} 6d@$23°C$	P_{13} 5d@$140°C$	P_{13} 5d@$140°C$
M_n	52700	52600	52500	53200	52600
M_w	338000	322800	334300	337400	332200
M_z	1165500	1077900	1146200	1159900	1128000
M_w/M_n	6.4	6.1	6.4	6.3	6.3
M_z/M_w	3.4	3.3	3.4	3.4	3.4

The accuracy of M_w is the highest with 3 to 5 %, the accuracy of M_n/M_w is around 5 to 10 %. The PP degradation is radicalar and results in a decrease of high molecular weights, the probability to find radicals on long chains being higher due to the fact that there are more carbons per chain and that the probability to create a radical is basically the same for each carbon.

M_z will be the most impacted, though it is also the less accurate. The second parameter that signs the degradation (and is related to M_n and M_w) is the narrowing of the molecular weights distribution (M_w/M_n, M_z/M_w). We see that P_{11} is the most changed, though the amount is quite low. Ultimately, no significant impact could be detected.

3.4.3 Stabilisation conditions for the microstructure evolution

The balance between stabilisation and degradation resulted in final conditions of 3 days spent at 135°C, that we name "standard conditions".
These final conditions put ZN and MET iPP below respectively approximately 30°C and 20°C of their melting temperature. The mechanical tests to be implemented should not last beyond ideally 7h to 10h, in order to have a ratio between the test time and the annealing time of around 10-15%.

3.4.4 Second campaign: validation of the standard conditions for P_{11} to P_{61}

Another campaign has been performed to confirm those results on all the quenched products, P_{11} to P_{61}.

Some of the results are presented hereunder at figure 3.129, selected among the three main experimental techniques. As of here, the colour code for the products will remain the same throughout the whole thesis: P_{11} is red, P_{21} is yellow or blue cyan, P_{31} is magenta, P_{41} is black, P_{51} is green and P_{61} is blue.

The evolution of the melting temperature with the annealing time is presented at figure 3.129(a). As expected, the two levels of temperatures related to the catalyst used are visible. The melting temperature should be independent on the annealing time [7]. This is confirmed by their small variation between 164°C and 167°C for the ZN iPP and 154°C-155°C for the MET iPP, and by comparing the evolution of melting temperature for all products respectively annealed up to 4 days and aged up to 8 days.

The SAXS and WAXS patterns have also been recorded, in order to obtain the long period as well as check the type of crystalline phase, as displayed at 3.129(b) and (c) and table 5.22.

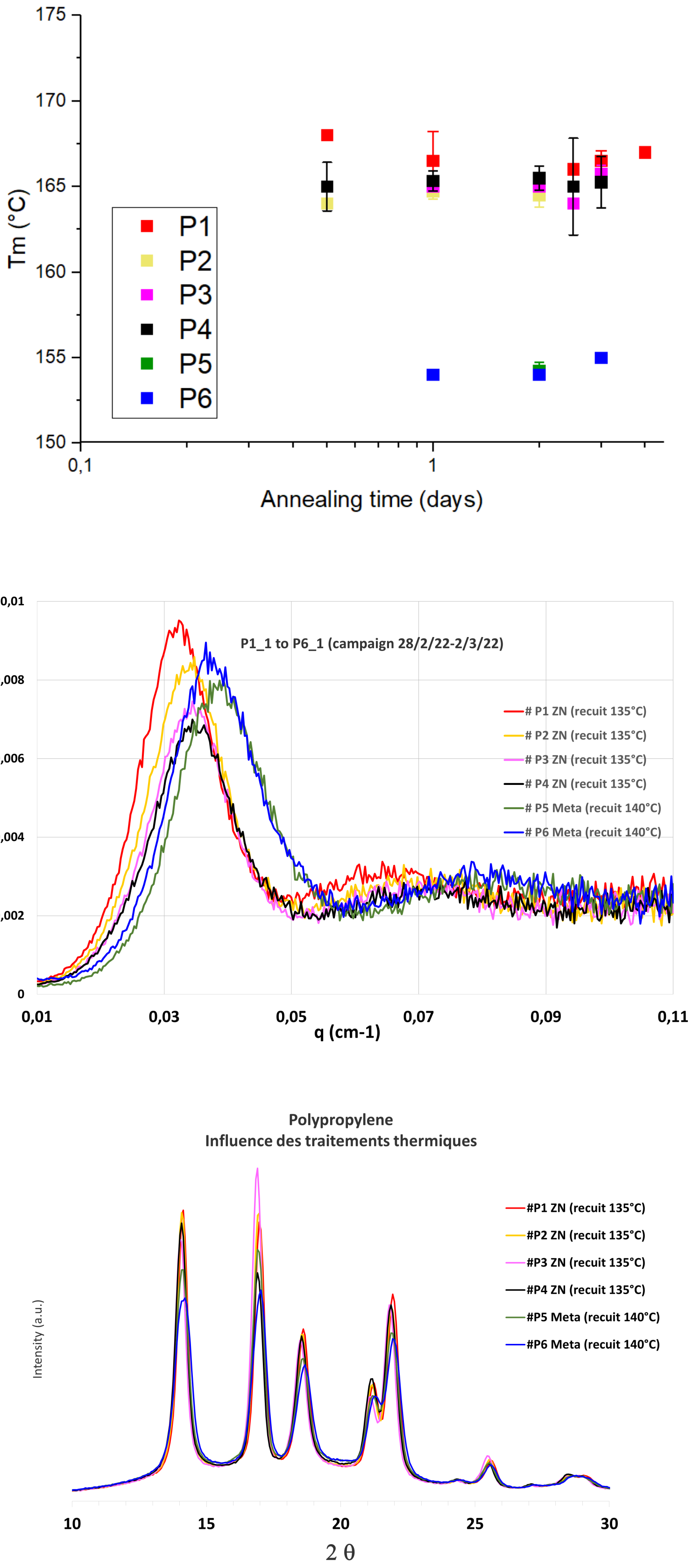

Figure 3.129: (a) Evolution with annealing time at 135°C of the melting temperatures of P_{11} to P_{61}, (b) SAXS spectrum for P_{11} to P_{61} annealed during 3 days at 135°C for ZN and 140°C for metallocenes and (c) WAXS pattern for the same products

Table 3.11: Crystalline and amorphous quantities for P_{11} to P_{61} annealed 3 days at 135°C (ZN) and 140°C (MET)

Product	χ_c	low-T_m	L_p nm	l_c nm	l_a nm	catalyst
P_{11}	0.54	0.36	19.45	9.84	9.61	ZN
P_{21}	0.55	0.39	18.25	9.43	8.82	ZN
P_{31}	0.54	0.36	18.41	9.27	9.14	ZN
P_{41}	0.52	0.37	18.41	8.94	9.47	ZN
P_{51}	0.51	0.35	17.04	8.11	8.93	MET
P_{61}	0.47	0.34	17.04	7.48	9.56	MET

From those results, it can be concluded that all the product display a crystalline α-phase and that the crystallinity and the long period L_p of metallocene resins is lower than the one of the Ziegler-Natta, with the presence of regio-defects that decrease the thickness of the crystalline lamellae but not that of the amorphous phase in the case of metallocenes.

3.4.5 Mechanical tests at T_{amb}: Young modulus and yield

The figure 133 of chapter 4 displays the tensile curves and some zooms on small deformations for all the products aged at room temperature (P_{11}) or annealed at 135°C (P_{11} to P_{61}) and gathered by catalytic support.

The evolution of the stress and tensile modulus with crystallinity and crystalline thickness is also displayed at figure 3.130 and table 3.12 below.

Table 3.12: Young modulus E at 1%/min ($1.6710^{-4} sec^{-1}$) and yield stress σ_y at 50%/min ($8.310^{-3} sec^{-1}$) measured at room temperature for P_{11} to P_{61} annealed 3 days at 135°C (ZN) and 140°C (MET)

Product	E (MPa)	s.d. (1σ) (MPa)	σ_y (MPa)	s.d. (1σ) (MPa)	catalyst
P_{11}	1985	± 288	37.4	± 0.5	ZN
P_{21}	1866	± 234	38.4	± 2	ZN
P_{31}	1942	± 473	37.9	± 0.7	ZN
P_{41}	1676	± 122	38.4	± 0.6	ZN
P_{51}	1764	± 156	37.7	± 0.5	MET
P_{61}	1556	± 16	37	± 1	MET

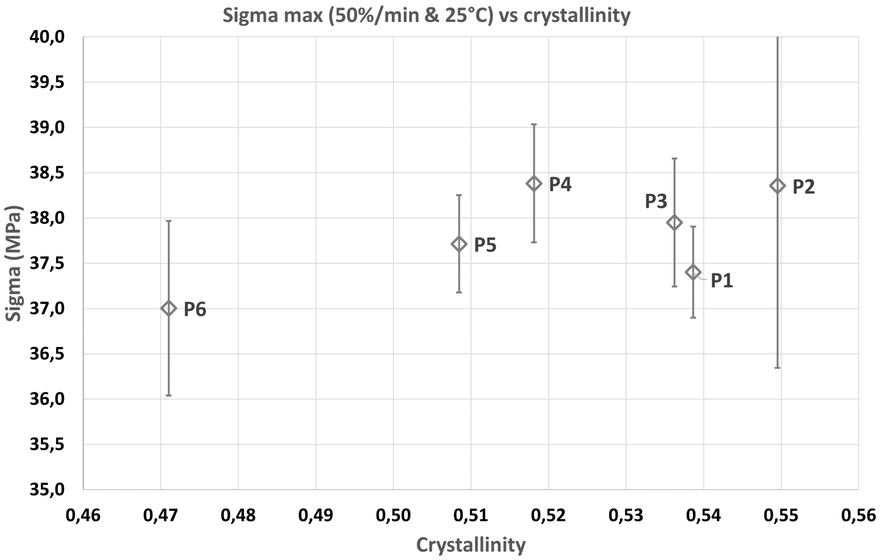

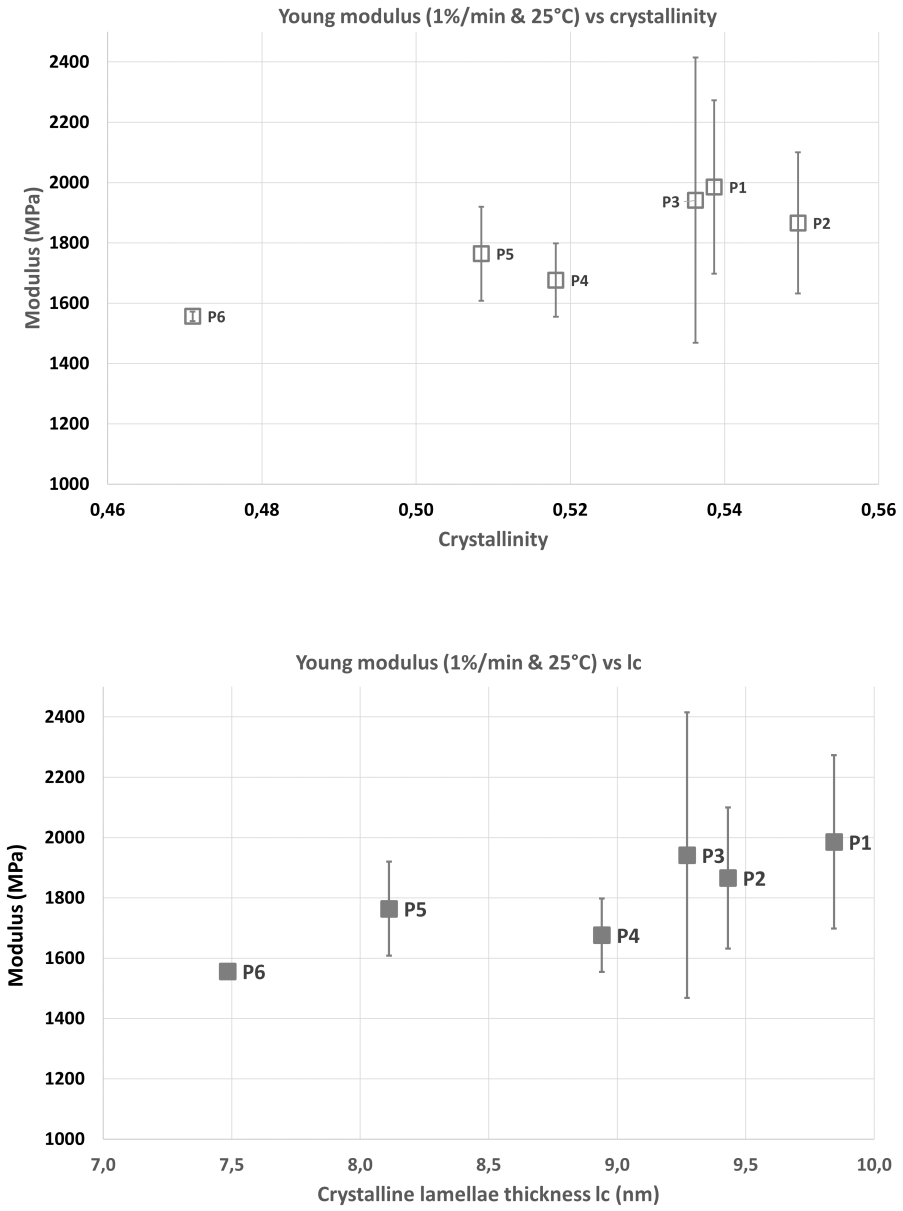

Figure 3.130: (a) Stress at max as a function of crystallinity of P_{11} to P_{61} at 25°C and $50\%min^{-1}$ $(8.310^{-3}sec^{-1})$, (b) Young modulus as a function of crystallinity at 25°C and $1\%min^{-1}$ $(1.6710^{-4}sec^{-1})$ and (c) Young modulus as a function of crystal thickness at 25°C and $1\%min^{-1}$ $(1.6710^{-4}sec^{-1})$

The table gives only a general trend, as the scattering was quite high especially on the module value. Whereas P_{11} and P_{31} behave in a similar way, P_{31} and P_{61} are definitely different. The link between the mechanical properties and the main microstructure parameters is discussed below.

3.4.6 Discussion

For the first campaign, the quenching conditions are supposed to ensure an α-phase accompanied by a metastable condis phase. The former crystallises in monoclinic lamellae of 10-15nm thick. The latter solidifies in lamellar "nodules" of around 20 nm that undergo large reorganisation into crystalline α-phase as temperature increases and under annealing above 80°C-100°C [39], [18], [107], [143], [144], [121], [145], [19]. In this case, the crystalline phase can be constituted, besides the primary lamellae, of subsidiary and transverse easily recognisable as a shoulder on DSC traces, the "low-T_m crystal content" or "secondary crystal population" [83], [87], [138], [109].

Such a shoulder is visible at figure 3.119(b) before the main melting peak for P_{11} annealed at 140°C. More generally, quenched samples P_{11} and quenched and annealed samples P_{12} displayed similar α-form crystalline content and similar secondary crystals, as their low-T_m content is in the range 0.3-0.35 for both, and does not depend on the annealing time spent at 140°C. Only the size of the crystalline lamellae increases under the different cooling conditions with the next ranking for l_c: $P_{11} < P_{12} < P_{13}$. In some cases, the crystalline nodules resulting from the mesophase transformation can coalesce into α lamellae of 40-50nm under annealing around 135°C-140°C [109], though this is not what was observed from the SAXS experiments.

The undercooling conditions at 130°C for P_{13} are supposed to ensure an α-phase constituted by conventional crystalline lamellae and spherolites, with a possible cross-hatched structure [20], [126], [19]. The significantly higher value of the low-T_m content at 0.45 for P_{13} advocates in that sense though this was not verified.

From the viewpoint of the crystalline forms composition, the undercooled sample P_{13} has a different crystallographic signature, and is composed of a mix of α- and γ- forms whereas P_{11} and P_{12} show pure α-phase form. In some circumstances linked to aging or annealing, a small β-peak can even be present. Small amounts of β- and γ-crystal forms could be related to the very tiny fraction of mesomorphic material that seem to be still present as displayed by the DSC derivative curves or by the presence of stereo-defects trapped in the crystalline lamellae [11], [87] as no clear chain scission was observed via SEC measurements. The literature shows that the presence of stereo-defects in the crystals could promote the apparition of these crystalline forms (regio-defects are usually rejected in the amorphous phase). This could be an explanation to such small phenomenon in a ZN product that does not exhibit regio-defects [150].

From the SAXS measurements, it was observed that the long period increases and the scattering peak sharpens as the crystallinity increases, which means that the distribution of crystals becomes narrow and the crystals more thicker and perfect. Moreover, the evolution of the amorphous and crystalline thicknesses is different, as can be seen at figure 3.121(b). The crystalline thickness increases faster than the amorphous one; this latter remains moreless constant or even decreases with crystallinity (not shown). This could come from the contribution of the mesophase transformation into α-crystals for P_{12} and from the thickening of the traditional lamellae together with their higher perfection for the undercooled P_{13} [18]. Due to thermal expansion [21], the amorphous phase is more significant for P_{13} than P_{11} but it is difficult at this stage to extrapolate on the ratio between its various components (MAF, RAF); the same holds for the mesophase. The long period does not seem to be impacted by the degradation, contrary to crystallinity.

The quasi-static tests performed on the three products show that their modulus are ranked according to their crystalline thickness and crystallinity. The shape of the tensile curve combined with the DSC curves where no shoulder is detected are characteristic of a substantial mesophase presence [54].

Finally, the thermo-oxidation phenomenon studied under different processing conditions and afterwards ageing and annealing times was demonstrated to occur at the edges, though not at the same intensity. A minimum in the enthalpy after 2 to 2,5 days was observed likely to result from the competition between reorganisation of the mesomorphic phase and degradation. A finer analysis of the DSC trace demonstrates that the melting peak becomes more intense, shift to lower temperatures and changes of shape with increasing degradation whereas the minimum around 50°C at which the metastable mesophase starts its transition is also impacted (not discussed here). This is confirmed by literature (see for example [14]).

The study on the first campaign resulted in defining a good balance between stabilisation and degradation and resulted in final conditions of 3 days spent at 135°C that was applied to all the six quenched products, P_{11} to P_{61}.
These final conditions put ZN and MET iPP below respectively approximately 30°C and 20°C their melting temperature.

The mechanical tests were implemented with the view to not lasting beyond ideally 7h to 10h, in order to have a ratio between the test time and the annealing time of around 10-15%.

Regarding the second campaign, the crystalline α-form was confirmed by WAXS for all the products (see figure 3.129) and the analysis of the DSC traces, namely the derivative of the heat flow led to the conclusion that some mesophase fraction could have subsisted after the thermal treatment, though the exact amount was not verified at this stage [129], [123], [69]. The presence of nodules was not checked either. The amount of amorphous phase remains substantial, looking at the crystallinity, and the RAF is likely to play a role [21].

For what concerns the link between the modulus, the yield and the microstructure, the literature shows that it is not trivial at all.

With the type of processing conditions adopted, and given that a rather narrow distribution of the nodules promote the apparition of neck and the increase of elongation at break [20], it is obvious that the deformation at yield and break is driven by other parameters than just crystallinity [68], [41]. Crystallinity in reality involves two aspects: on the one side and indirectly, the dislocations via the crystal lamellae thickness (see infra for detailed discussion) and, on the other side, the stress transmitters (ST) via the long period, the ST being viewed as the whole network linking two crystal lamellae (i.e. tie molecules, entanglements, loose loops, etc) [68]. As the modulus of the amorphous phase is much lower than that of the crystalline phase, the transfer of stress will strongly depend on the quality of the interlamellar space and on the thickness of the lamellae, especially the thinner ones [41]. The stress distribution on the crystals is greatly influenced by the number of tie molecules and more generally by stress transmitters. At equivalent crystalline lamellae thickness l_c, the yield stress value increases with the concentration of ST that is directly influenced by the molecular weight [60].

Several articles points also to the role played by the amorphous phase behaviour under increasing strain rate and below or above its glass transition to explain the increase of the yield stress and the Young modulus [69], [60].

Our own results are coherent with this analysis, as we can observe a global increase of the modulus with the crystallinity and with the crystalline thickness. The same holds for the yield stress - see figure 3.130(a). It is difficult to push further the comparison, as the type and number of defects are quite different between ZN and MET, and whereas the literature shows such an influence [67], we have not a sufficient base of products for relevant comparison.

The microstructural data of P_{11}, P_{31} and P_{61} have been summarised at table 3.13. The microstructure has been characterised with DSC, SAXS, NMR and quasi-static tensile measurements. More especially, the Young modulus E has been measured at $1\%min^{-1}$ ($1.67\ 10^{-4}sec^{-1}$) and the yield stress at $50\%min^{-1}$ ($8.3\ 10^{-3}sec^{-1}$), both at T_{amb}. The isotactic length n_{iso} was calculated from NMR data according to [87], [151] and expressed in monomeric moeities C_3H_6 and in nm in order to assess the number of stacks $2l_c + l_a$ spanned by n_{iso}. All these calculations are available in the supporting information 3.6.4. The NMR values for P_{61} have been taken from P_{51} data, both being considered as similar from that viewpoint.

Table 3.13: Summary of the results obtained on samples of P_{11}, P_{31} and P_{61} annealed at 135°C during 3 days; the values marked with * come from P_{51} considered as similar to P_{61} - see text for detailed explanations

Product - Catalyst	P_{11}	-	ZN	P_{31}	-	ZN	P_{61}	-	MET
$T_m(°C), \chi_c, low - T_m$	166.5	0.54	0.36	165.7	0.54	0.36	155.5	0.47	0.34
$L_p, l_c, l_a(nm)$	19.4	9.8	9.6	18.4	9.3	9.1	17	7.5	9.6
$n_{iso}(\#C_3H_6), n_{iso}(nm)$	190		124	164		106	178*		116*
$2l_c + l_a(nm)$, $\#(2l_c + l_a)$ in n_{iso}	29.3		4.23	27.7		3.85	24.5*		4.72*
E (MPa), σ_y (MPa)	1985		37.4	1942		37.9	1556		37

The analysis of the microstructural parameters shows that ZN and MET behave in a different way, as consequence of the difference in molecular weights but also in type, amount and distribution of defects.

Regarding the comparison between the ZN products, tables 3.7 and 3.13 show that P_{11} and P_{31} have approximately the same level of isotacticity (table 3.7), crystallinity, and low-T_m crystal content (table 3.13.

On the contrary, the distribution of molecular weight is narrower for P_{31} and it has more shorter chains. Its long period is smaller than that of P_{11}, with smaller crystalline and amorphous thicknesses and a higher global amount of stereo-defects (not shown) resulting in smaller isotactic length. As a consequence of these different observations, one isotactic length will span a smaller number of $2l_c + l_a$ for P_{31} than for P_{11}. Furthermore, as the crystallinity and the low-T_m content are the same, this means that there are more thinner crystalline lamellae.

We know also that there is a direct influence of the molecular weight on the crystal thickness and amorphous phase via the scaling relationship between the random coil dimension R_g in the molten state and the crystallite thickness in the solid state [77]. We can thus expect for P_{31} that lower M_w will lead to a smaller amount of ST under the same thermo-mechanical history.

When comparing ZN and MET, we see that despite a molecular weight quite close of each other, P_{31} and P_{61} do not behave in the same way. P_{61} has the lowest crystalline thickness and crystallinity among the three products, but an amorphous layer equal to that one of P_{11}. This is likely to be due to the narrower polydispersity index that, compared to P_{31}, promotes higher molecular weights less prone to crystallise, and to the presence of homogeneously distributed regio-defects that are hardly incorporated into the crystal phase, as already mentioned earlier [150].

Both facts could explain the intermediary level of MET compared to ZN for the isotactic length. The lower amount of low-T_m content of P_{61} is hard to explain as it means that there are less subsidiary and transverse lamellae proportionally in this material than in the two other products. We could assign this observation among other to the very high isotacticity level that promotes on the average more perfect primary crystalline lamellae combined with a proportionally more important amorphous phase, as the crystallinity of MET is lower and the ratio between l_c and l_a is also smaller than for ZN. In any case, the possible co-existence of an initial structure after quenching composed of crystalline nodules and conventional monoclinic lamellae the size of which would increase after annealing has to be checked, as well as the existence of cross-hatched texture and spherulites [109], [19]. Complementary to that, a small fraction of mesomorphic phase not transformed into the monoclinic α-phase crystalline nodules could persist despite the annealing treatment. The presence of defects could also prevent the mesophase or the RAF to transform into subsidiary lamellae.

A smaller value of the stack length $2l_c + l_a$ combined with a lower amount of shorter chains could result, at a given molecular mass, in a higher probability to create stress transmitters and a higher probability to tie several stacks. This latter hypothesis being confirmed by the larger number of these stacks in the isotactic length n_{iso} as seen at table 3.13. This explanation seems to be relevant, as highlighted by the shape of the tensile yield drop, narrower than for the ZN products, and the pronounced neck without any whitening (see chapter 4).

3.5 Conclusion

In this study, we have first analysed the influence of cooling conditions on one chemical structure, P_1, with the view to establishing appropriate conditions for the stabilisation of the microstructure of our products, while avoiding degradation and ensuring that the time spent under mechanical tests in temperature would not exceed 10-15% of the annealing time.
Due to not that big differences between the products, at least for standard thermal and mechanical tests, we have taken into account all possible causes for scattering coming from the equipments, the materials, the process and the tests.

A special method has been developed to handle DSC traces that uses the temperature derivative of the heat flow and is based on local extrema, that are physical signatures of processes occurring during the sample heating. It has allowed us first detecting similarities in the DSC traces of all the products before the main melting peak, and secondly highlighting in the expected range of temperature the remaining presence of mesophase and/or α-crystals resulting from its transformation even after an annealing above 130 $°C$.

The analysis has shown that the evolution of microstructural parameters of these materials evolves according to the literature: the long period increases with a decreasing temperature ramp, the crystalline thickness evolving very rapidly compared to the amorphous phase, meaning that the ratio between l_c/l_a increases accordingly despite thermal expansion. The quenched and annealed product P_{12} presents similarities with the quenched product P_{11} and with the undercooled product P_{13}: its low-T_m content is similar to P_{11} and does not depend on the annealing time spent at 140°C, its crystallinity is similar to P_{13} and its WAXS crystallographic signature has characteristics from both.

In all cases, degradation is prevailing at the edges, and occurs at any of the temperatures considered. Under promoted degradation conditions, it appears that the crystallinity decreases, but the long period of the samples remains constant.

The balance between stabilisation and degradation resulted in final conditions of 3 days spent at 135°C that were validated on the second campaign.

Regarding the second campaign, it was shown that the Young modulus and, to somewhat less extent yield stress, were evolving with the crystallinity and the crystalline thickness according to literature, and this can be assigned respectively to the stress transmitters and to the dislocations: the Young modulus decreases with decreasing crystallinity, crystalline thickness and long period, or similarly, it decreases with a decreasing ratio between the crystalline and amorphous phase.

The isotactic length was also computed and put in relation with the stacks $2l_c + l_a$ of the literature on tie molecules and stress transmitters. It was shown that the difference between ZN products came mainly from the molecular weights and molecular weight distribution, acting on the thickness of amorphous and crystalline phases. The difference between ZN and MET was ascribed to the MET ability producing a smaller lamellae thickness combined with a important amorphous layer, i.e. a smaller ratio between the crystalline phase and the amorphous phase likely coming from the presence of defects at similar molecular weight. This resulted in the highest amount of $2l_c + l_a$ stacks spanned by the MET isotactic length.

3.6 Supporting information

We want to highlight that, whenever possible and because of the need to mitigate all possible causes of scattering in the results, we have used the same samples to perform first non destructive tests such as FTIR or RX and then destructive tests such as DSC or tensile tests. When this was not possible, we have tried to draw samples as close as possible of removal locations that were duly recorded.

3.6.1 Samples preparation

For the first campaign, the mould was constituted of two stainless steel blades each coated with a PTFE film, one aluminium $500\mu m$ thick A4 format frame, two PTFE sheets and two PI films. The frame was sandwiched between first the PI films, then the PTFE sheets and finally the stainless steel blades. For the second type of films, the PTFE was removed and the PI was put in direct contact with the blades. The moulding conditions were modified because of presence of large ripples in the films provoked by the sudden immersion in the cold water and subsequent shrinking of the hot steel.

The quenched films were the most difficult to fabricate in a reproducible way with the available equipment. The pellets were molten at 230°C and maintained at 0.5bars during three minutes after their complete melt. After that, degassing was carried out as quick as possible by applying successively 3, 5 and 9 bars. The film was then maintained during one minute at 10 bars and then removed from the press.

1. for the quenched films P_{11}: after removal, the mould was placed on a support kept at ambient temperature allowing four clamps to be placed at each corner. It was then immersed in a water bath at 10°C where a temperature gauge had been put in order to monitor the time needed for solidification. Due to the time needed to fix the clamps, the temperature of the mould when dropped in the water was estimated to be around 200°C; the complete solidification was reached after maximum 10 sec. The cooling rate was around 20 °C/sec. After solidification, the film was removed from the mould, gently dried and kept in the lab at room temperature in the darkness. Quenching in the water presented a lot of issues and several procedures have been tried, none of them being totally satisfactory as will be explained later
2. for the quenched and annealed films P_{12}: the procedure to quench the film was the same than P_{11}; once solidified, the film was then placed again in the press and remained at 130°C during eight hours under five bars
3. for the film undercooled isothermally at 130°C P_{13}: the procedure was slightly different. After three minutes maintain, it was removed from the first press and put in a second press at 130°C under five bars during eight hours. The mould was then removed from this second equipment and the film quenched in the air. At the moment of the mould opening, the film was undergoing a rapid final crystallisation process.

3.6.2 Calculation of crystalline and amorphous thicknesses from density, DSC traces and SAXS measurements

It is possible to calculate the density of the material and the thicknesses of the crystalline lamellae and of the amorphous layer with the data and models presented hereunder.

Calculation of the material density

The literature indicates [42] values for the density of a pure monoclinic crystal and a pure amorphous phase. These are obtained usually by extrapolating the data to a crystallinity of 1 or 0.

Density of pure crystalline phase: $\rho_c = 0.95$
Density of amorphous phase: $\rho_a = 0.85$

DSC measurements provide the values of the crystallinity percentage χ_c and the enthalpy of the perfect crystal, 207J/g [125], [42]. Combined with the densities of the amorphous and crystalline phase, and with the long period, it is possible to calculate the material density ρ with the equations below.

$$\chi_c = \frac{\Delta H}{207} \tag{3.43}$$

$$\frac{1}{\rho} = \frac{\chi_c}{\rho_c} + \frac{1-\chi_c}{\rho_a} \tag{3.44}$$

Calculation of crystalline thickness from SAXS

Small angle scattering X-ray allows measuring a scattering angle 2θ with a wavelength λ in order to obtain a scattering vector q. Thanks to the value of the scattering vector at its maximal intensity q_{max}, it is possible to obtain the long period L_p, the thickness of the amorphous layer l_a and the thickness of the crystalline phase l_c.

$$q = \frac{2}{\lambda} sin\theta \tag{3.45}$$

$$L_p = \frac{2\pi}{q_{max}} = l_c + l_a \tag{3.46}$$

$$l_c = L_p \frac{\rho}{\rho_c} \chi_c \tag{3.47}$$

3.6.3 Crystallographic planes of iPP obtained by WAXS spectra

The crystallographic planes of the main crystalline form of iPP are presented at figure 3.131 hereunder.

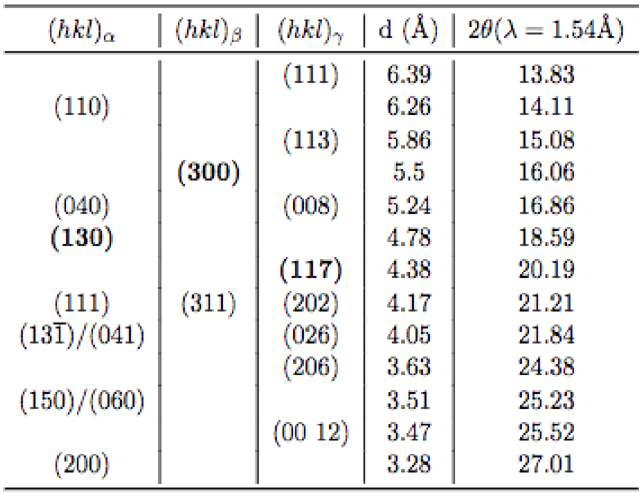

$(hkl)_\alpha$	$(hkl)_\beta$	$(hkl)_\gamma$	d (Å)	$2\theta(\lambda = 1.54$Å$)$
		(111)	6.39	13.83
(110)			6.26	14.11
		(113)	5.86	15.08
	(300)		5.5	16.06
(040)		(008)	5.24	16.86
(130)			4.78	18.59
		(117)	4.38	20.19
(111)	(311)	(202)	4.17	21.21
(13$\bar{1}$)/(041)		(026)	4.05	21.84
		(206)	3.63	24.38
(150)/(060)			3.51	25.23
		(00 12)	3.47	25.52
(200)			3.28	27.01

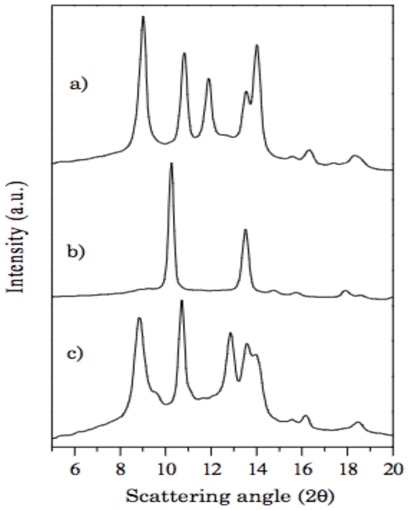

Figure 3.131: (a) Crystallographic planes for iPP polymorphs as measured by WAXS at $\lambda = 1$ and recalculated at $\lambda = 1.54$ from [11]. Main planes are in bold; (b) WAXS-patterns of pure α, β and γ-phase, indicated by a, b, and c, respectively (in this graph, $\lambda = 1$) [11]

3.6.4 Calculation of microstructure parameters

Calculation of the volume of the iPP α-crystalline monoclinic unit cell

The dimensions of the α-crystalline monoclinic unit cell are the following [11]: a=0.665nm, b=2.096nm, c=0.65nm, β=99.62°

The volume of the unit cell is therefore:

$$V = a.b.c.sin\beta = 0.89 \ \ nm^3 \tag{3.48}$$

Calculation of the volume occupied by one group CH_2

The α-crystalline monoclinic unit cell is composed of 3 monomers along the c-axis i.e. 9 CH_2 entities. There are 4 chains in the *ab*-plane. The unit cell is composed of 9 x 4 = 36 C + 72 H. The weight of the unit cell is equal to the weight of $36CH_2$ i.e. 504 Daltons

Combining the result of equation (3.48) with the number of CH_2 in one unit cell, the volume occupied by a CH_2 becomes:

$$0.89/36 = 0.0248 \ \ nm^3 \tag{3.49}$$

Calculation of the amount of CH_2 groups in the activation volume

It is quite easy, from equation (3.49) to get the amount of CH_2 in the activation volume. For instance, for P_{11}, V_0=3.58 nm^3

$$3.58/0.0248 = 144\ \ CH_2 \tag{3.50}$$

Let us remark that we have not taken into account the tie molecules and other stress transmitters in these calculations.

Calculation of the amount of CH_2 groups in $L_p, l_c, l_a, 2l_c + l_a$

Having the value of $L_p, l_c, l_a, 2l_c + l_a$, these quantities are divided by the value of the c-axis. For instance, for P_{11}, L_p=19.4nm, l_c=9.84nm, l_a=9.61 nm, $2l_c + l_a$ = 29.29nm

$$L_p/0.65 = 19.4/0.65 = 29.8\ \ CH_2 \tag{3.51}$$

$$l_c/0.65 = 9.84/0.65 = 15.1\ \ CH_2 \tag{3.52}$$

$$l_a/0.65 = 9.61/0.65 = 14.8\ \ CH_2 \tag{3.53}$$

$$2l_c + l_a = 29.29/0.65 = 45\ \ CH_2 \tag{3.54}$$

Calculation of the isotactic length n_{iso} in amount of C_3H_6 monomeric units, in nm and in amount of $2l_c + l_a$

n_{iso} is the isotactic length i.e. the average distance between two interruptions (defaults) and depends on the catalytic system. It is obtained from NMR measures according to the following equation [83], [87], [151]:

$$n_{iso} = \frac{[mm] + 0.5[mr\ \ +\ \ mx]}{0.5[mx]} \tag{3.55}$$

$$[mx] = [mr]\ \ for\ \ ZN \tag{3.56}$$

$$[mx] = [mr] + [regio - irregular\ \ PPP]\ \ for\ \ MET \tag{3.57}$$

It is easy to convert this length into nm and number of C_3H_6 monomeric units as they are aligned with the c-axis.

For instance, for P_{11},

$$[mr] = 1.03,\ \ [mm] = 98.5\ \ and\ \ n_{iso} = 190\ \ C_3H_6\ \ units \tag{3.58}$$

$$190\ \ C_3H_6\ \ .\ \ 0.65\ \ nm = 124\ \ nm \tag{3.59}$$

$$124\ \ nm/29.29\ \ nm = 4.23\ \ 2l_c + l_a\ \ in\ \ n_{iso} \tag{3.60}$$

For instance, for P_{51} (in place of P_{61}),

$$[mr] = 0.3,\ \ [mm] = 99.5, [mx] = [mm] + 0.9,\ \ and\ \ n_{iso} = 178\ \ C_3H_6\ \ units \tag{3.61}$$

$$178\ \ C_3H_6\ \ .\ \ 0.65\ \ nm = 116\ \ nm \tag{3.62}$$

$$116\ \ nm/24.52\ \ nm = 4.72\ \ 2l_c + l_a\ \ in\ \ n_{iso} \tag{3.63}$$

Chapter 4 : Impact of the chemical structure and the thermo-mechanical history on the Deformation mechanisms in Ziegler-Natta and Metallocene catalyst-based iPP

Table of contents

4.1 Introduction

Polypropylene is a very widely used commodity polymer. Its global market size is evaluated to be around EUR 113.30 billion in 2022 and is expected to expand at a compound annual growth rate (CAGR) of 4.7% from 2023 to 2030. The growth of the market is mainly driven by end-use industries such as automotive, packaging, and building & construction. In these markets, homopolymer is the largest segment and accounted for a market share of over 80% [4], [5]. The main applications find themselves in injection moulding, film extrusion, fiber production or thermoplastic elastomers [1] where the requested properties are in the range of short to mid-term characteristic times.

Due to the applications needs, some of them have been extensively studied: crystallization, stiffness, short term impact resistance (with adiabic heating) or brittle/ductile transition, fracture, aging or degradation to name just a few [6], [7], [8], [9], [10], [11], [12], [13], [14].

In the field of long term properties and viscoelastic analysis [115], [112], polypropylene has suffered from its close relation with polyethylene as the results obtained for this latter were usually simply transposed in a traditional scheme of analogy though without comprehensive verification.
The result is that not that many papers have tackled the existence of two yielding processes (also called double yield phenomenon) for iPP during mechanical tests [39], [57], [152] and scarcely investigated their longer term evolution and their link with the underlying microstructure.

Understanding therefore the underlying deformation mechanisms occurring with time ranging between hours and a few months would be an interesting way to support the development of new structures for long-term applications.

Regarding its microstructure in the solid state, isotactic polypropylene is one of the most complex semi-crystalline polymers, due to the flexibility of its helix macromolecular chain, the presence of several types of defects and the influence of the solidification circumstances [107], [18], [67]. It exhibits different crystallographic structures and morphologies depending on processing and crystallisation conditions[30]. The most common form is the monoclinic α-crystals. The β-phase is a rather cumbersome crystalline phase and is observed under specific crystallisation conditions such as orientation of the melt (shear), temperature gradient or nucleating agent. The orthorhombic γ-crystals are observed quite often in combination with the α-phase. This phase is obtained in samples crystallising under high pressure and in presence of degraded, low molecular weights, at atmospheric pressure with metallocene catalysis or by introducing comonomers such as ethylene [7], [11], [120].

The mesophase of iPP is a conformationaly disordered glass or crystal (condis glass or crystal) that is hindered to convert into a fully ordered crystal by cooling it below its T_g [18]. The amorphous phase is also reported to be constituted by a mobile amorphous fraction (MAF) and a rigid amorphous fraction (RAF) [135], [18] that play a critical role in terms of mobility [21].

The molecular architecture and synthesis technology have both an important influence. Two routes exist currently to synthetise this polymer, Ziegler-Natta and metallocene catalysts. Defects in the backbone break the regularity of the chain in the similar way as the addition of a comonomer [112], which obviously has an impact on the crystallisation parameters. They influence directly the average pure isotactic length, *i.e.* the crystallizable sequence between two distinct configurations. Single-site catalysts such as metallocene typically distribute their defects in a homogeneous way all along the polymeric chain, whereas multi-sites Ziegler-Natta catalysis rather gather them in blocks with very long isotactic segments in between. The consequence is that single-site catalysts have rather short isotactic segments and tend to crystallise in the γ-crystal form [1].

In the solid state, isotactic polypropylene, as thermoplastic polymers in general, is known to be far from thermodynamic equilibrium and to undergo an evolution of its (micro)structure with time and temperature, such as under physical ageing or annealing, or with strain. Its microstructure is particularly sensitive to these factors due to its metastable mesophase constituted mainly of condis [107], [108], able to undergo a transition above a certain temperature towards an α-crystalline monoclinic form and/or different co-existing crystalline polymorphs [67], [18], [117], [121], [69], [122], [16], [19], [10], [123], [20]. The different temperature ranges for these transitions should be linked to the mobility of the macromolecules that triggers rearrangements of chain conformation and packing of the unit cell to a more energetically favorable state, generating long range positional and orientational order between the helix segments. In iPP, chain mobility is achieved within the mesophase when the glass transition of condis glass is reached at 70°C-80°C [19].

iPP is also sensitive to degradation by thermo-oxidation. As a consequence, establishing a good compromise between the stabilisation of the microstructure and its degradation due to process influence and thermo-mechanical history is a key pillar for a study investigating the long-term properties via accelerated tests.

---

[30] We mention here only the most usual ones. For further information, see f.i. [7], [11] or see chapter 2

Regarding micro-macro approaches and numeric models in general, a set of predictive models, covering the whole range of deformation has been developed for product design and development, in order to answer more rapid cycles or replace traditional materials such as metals in an increasing number of applications. Because there is no unified theory encompassing the whole material's behaviour, predicting in a robust way the response of polymeric parts of a complex structure until their macroscopic and/or massive failure remains still a challenge that results in a situation where the local failure criteria, the damaging and the behaviour laws are not integrated and their choice remains somehow arbitrary [153], [154], [27], [23]. Understanding the respective influences of each scale in a micro-macro approach means to integrate the material behaviour at each scale, from nanometric constituents (mobile and rigid amorphous phase, metastable mesomorphic phase and crystalline polymorphs) and under increasing strains to macroscopic design scales, from small deformation to large ones, from visco-elasticity to microscopic or macroscopic failure [15], [154], [155], [156], [157].

We would also like to draw the attention to an important vocabulary aspect: the very term ***failure*** itself can encompass in this context various situations and have different meanings if it is used at the macroscopic or the microscopic level: the *ultimate* failure refers clearly to the massive though nanoscopic rupture of the material covalent bonds whereas the macroscopic "*ductile*" failure refers to moment where a more or less complex part is no more usable because it has locally crossed the yield and shifted to irreversible plastic deformations. The meaning of the word "failure" will thus be clarified later in this text by the context in which it is introduced [23], [27], [24], [25], [26].

On this global scene, and despite tremendous progresses performed since last decades in computing methodologies and applications, as well as in nanotechnology-based equipments and analytical theories [154], the understanding of plasticity processes of iPP's complex multi-scale multi-hierarchical micro-structure is far from being completed [17], [153].

Establishing thus a good understanding of the processes occurring at the nano- to microscopic scale from a physical viewpoint and in relation with the molecular architecture is critical to feed models and develop new chemical structures with predicted and controlled properties.

We have therefore analysed the impact of various molecular structures and thermo-mechanical histories on their quasi-static behaviour under small deformation using various Ziegler-Natta and Metallocene catalyst-based iPP. We have especially zoomed in on their drop shape at various temperatures and low strain rates, and made the link with the macroscopic deformation mechanisms with a special care to the competition between plasticising and cavitation phenomena.

In order to do so, we have assumed that the cavitation phenomena were triggered beyond the first yield, i.e. the maximum of the stress-strain curves, and used the very well known Ree-Eyring theory to model plastic flow and its dependence to long characteristic times.

4.2 Materials, samples preparation and characterisation

The materials and samples preparation have been detailed at chapter 3, as well as the characterisation methods of the microstructure.

Regarding mechanical tests, two tensile machines were used to confirm the presence of the double yield at room temperature, the second one being used also for the tests in temperature with an oven and a camera. Samples with a dogbones ISO527 1BA/ASTM D638-V shape were stamped and distance between clamps was fixed at 25.4mm.

A comparison between the results of the two equipment's was carried out. The whole set-up and the procedure to remove films' samples are provided in the supporting information 4.6.1.

A series of Matlab® home made programs have been written and implemented on the experimental set-up to treat the relevant signals. Some details are available in the supporting information at section 4.6.2.

4.3 Results and discussion

As explained in the introduction, the objective of the mechanical tensile tests is to demonstrate the presence of two deformation mechanisms in the long-term plasticising behaviour of isotactic polypropylene on a series of different molecular homopolymer structures coming from two catalysts.

Regarding the microstructure, standard conditions (see chapter 3), i.e. 3 days spent at 135°C, have been applied to all the six quenched products, P_{11} to P_{61}. The crystalline α-form has been confirmed by WAXS for all of them and the analysis of the DSC traces, namely the derivative of the heat flow has led to the conclusion that some mesophase fraction could have subsisted after the thermal treatment, though the exact amount was not verified at this stage [129], [123], [69]. The presence of nodules was not checked either. The amount of amorphous phase remains substantial, looking at the crystallinity, and the RAF is likely to play a role [21].

Mid- to long-term characteristic times means, from the viewpoint of mechanical properties and Ree-Eyring model (that we will discuss later), to carry out quasi-static and possibly creep tests. Fortunately, it is possible to exploit both by working with some remarkable points such as ϵ_y and σ_y taken at the maximum of the quasi-static stress-strain curve or such as the inflexion point $\epsilon_y(t_y)$ and its strain rate $\dot{\epsilon}_y(t_y)$ measured in a creep test. Deformation processes are indeed the same ones, as was demonstrated by Bauwens et al [158], [159]. In our case, it was possible to go down to quite low strain rates with quasi-static tests only, and there was therefore no need to implement creep tests[31].

The signature of two plastic deformation mechanisms in the stress-strain curve is the presence of a double yield that is characterised in the quasi-static tests by the presence in the yield drop of a convex shaped shoulder, where the neck or plastic instability is triggered, and in the creep tests by the stabilisation of the deformation during the time evolution. The necking is triggered just before failure in this case. Such a drop shape can be put in relation with the presence of mesophase or RAF [54] as we will see later.

We would like to draw the attention that the subscript "y" has been replaced in our graphs by the subscript "max". Though the presence of a pure plasticising process is our hypothesis, these subscripts will remain by precaution as long as we have not confirmed that the first local maximum is associated only to that mechanism, without involving cavitation. In the remaining part of this study, we will use σ_{max}, ϵ_{max} and $\dot{\epsilon}_{max}$.

4.3.1 Preliminary mechanical tests experiments

Before installing the set-up with the camera, a preliminary round of tests was carried out at room temperature on samples of the two campaigns, respectively aged at T_{amb} and annealed under standard conditions. The strain was obtained from the crosshead displacement.

Tests were performed at T_{amb} and $50\% min^{-1}$ ($8.3\ 10^{-3} sec^{-1}$) on P_{11} to P_{61} samples in order to confirm the presence of a double yield in the stress-strain curves. All products displayed a shoulder in the yield drop and differed from each other vis-à-vis the presence or not of a neck propagation plateau and a strain hardening, as well as the way the failure occurred.

Figure 4.132 displays the double yield for all the products aged at room temperature (P_{11}) or annealed at 135°C (P_{11} to P_{61}) and gathered by catalytic support.

As of now, the colour code remains the same for all the products throughout the whole study: P_{11} in red, P_{21} in yellow or cyan blue, P_{31} in magenta, P_{41} in black, P_{51} in green and P_{61} in blue.

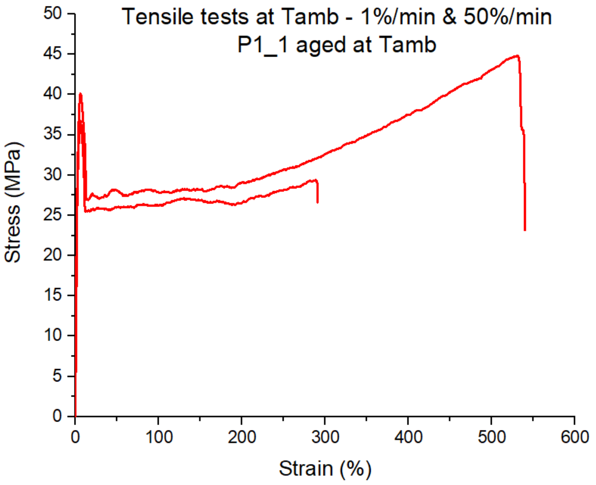

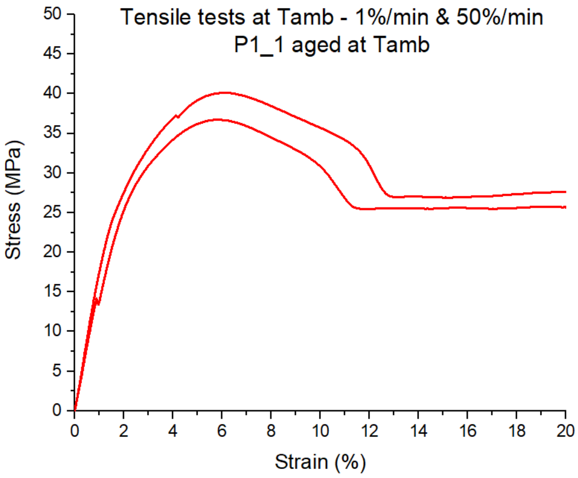

---

[31] it appears that many traditional weighted creep equipments have been dismantled for many years in academics.

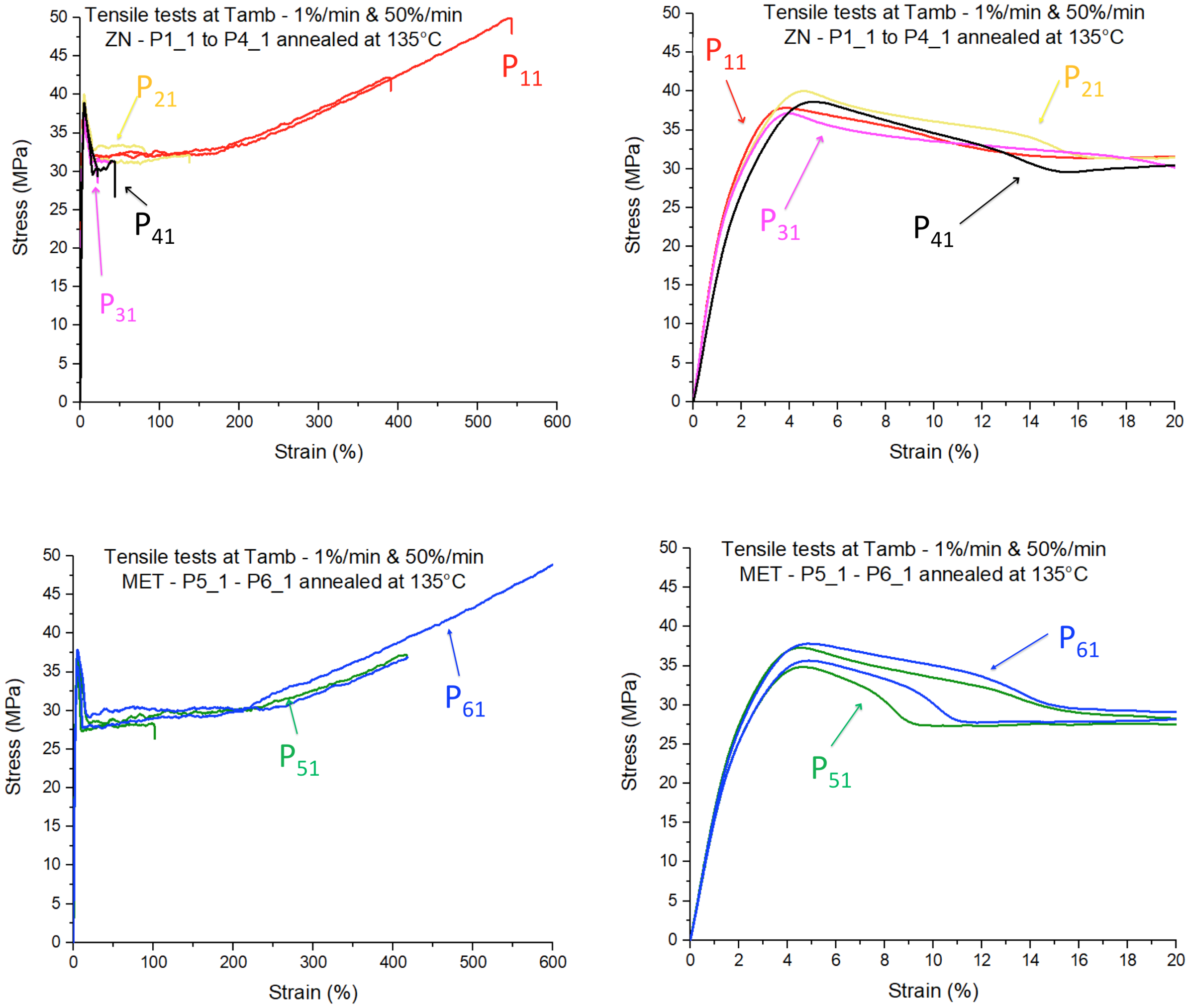

Figure 4.132: From left to right and top to bottom: stress-strain curves taken at 23°C and $50\% min^{-1}$ $(8.310^{-3} sec^{-1})$ of (a) P_{11} aged at room temperature (whole curve) and (b) zoom; (c) ZN products P_{11} to P_{41} annealed at 135°C (whole curve) and (d) zoom; (e) MET products P_{51} and P_{61} annealed at 135°C (zoom) and (f) zoom. The strain was measured with the crosshead displacement; the gauge length was 25.4mm. Colour code: see text

For almost all the products, the shape of the yield drop was convex. This shape is of fundamental importance to identify the existence of a double yield (and more generally the shape of the whole curve up to the plateau though this will not be discussed). The presence of convex or concave curvature in the drop will be examined at section 4.3.2.

4.3.2 Quasi-static tensile tests at 25°C, 69°C and 128°C at 5 different strain rates

The isotactic polypropylene is known to have its α-relaxation starting around 40°C-50°C and ending between 80°C and 120°C depending on its structure [71], [94], [36]. As the hypothesis is that the α-relaxation is responsible of the yielding processes, this means that the presence of a double yielding mechanism could be detected in that temperature range if the strain rates are selected in a relevant frame [69], [39]. In order to emphasize each mechanism, it was decided to make tensile tests on P_{11}, P_{31} and P_{61} at temperatures lower than-, in the middle of- and above this crystalline transition temperature i.e. at 25°C, 69°C and 128°C, as illustrated at figure 4.133.

Five different strain rates were applied as test conditions, as illustrated at table 4.14. The strain rates of the central and right columns are the same in two different units.

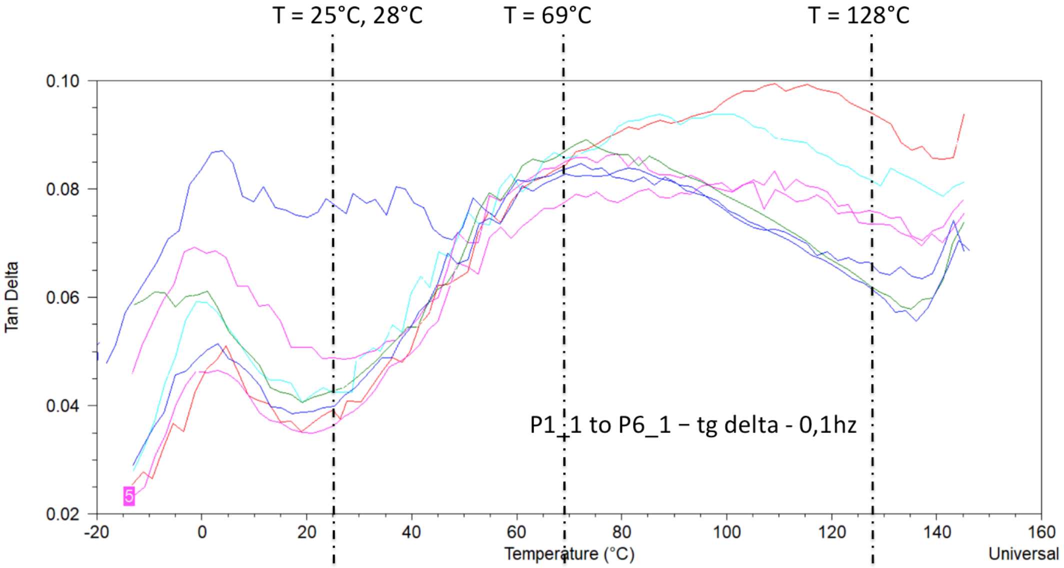

Figure 4.133: Evolution with the temperature of tgδ curves of P_{11} to P_{61} annealed at 135°C and tested at $0.1 sec^{-1}$; the colour code has been explained; the vertical dotted lines at 25°C or 28°C, 69°C and 128°C allow to identify on the viscoelastic spectra if the tensile tests carried out at these temperatures are located before, in the middle or after the crystalline relaxation

Table 4.14: Quasi-static tensile test strain rates at 25°C, 69°C and 128°C; the strain rates are shown in two different units

Temperature $°C$	Strain rate $\%min^{-1}$	Strain rate $10^{-5}sec^{-1}$
25	0.1, 0.5, 1, 5, 10	1.67, 8.35, 16.7, 83.5 , 167
69	0.1, 0.5, 1, 5, 10	1.67, 8.35, 16.7, 83.5 , 167
128	0.1, 1	1.67, 16.7

The nominal strain, strain rate and width were measured directly by the camera which allowed to monitor the various changes undergone by the sample response while taking photos. The machine was piloted with the constant speed of the crosshead and the sample gauge length was 9.5mm. Figure 4.134 illustrates the changes occurring during the test, with three different regimes (take care of the different scales).

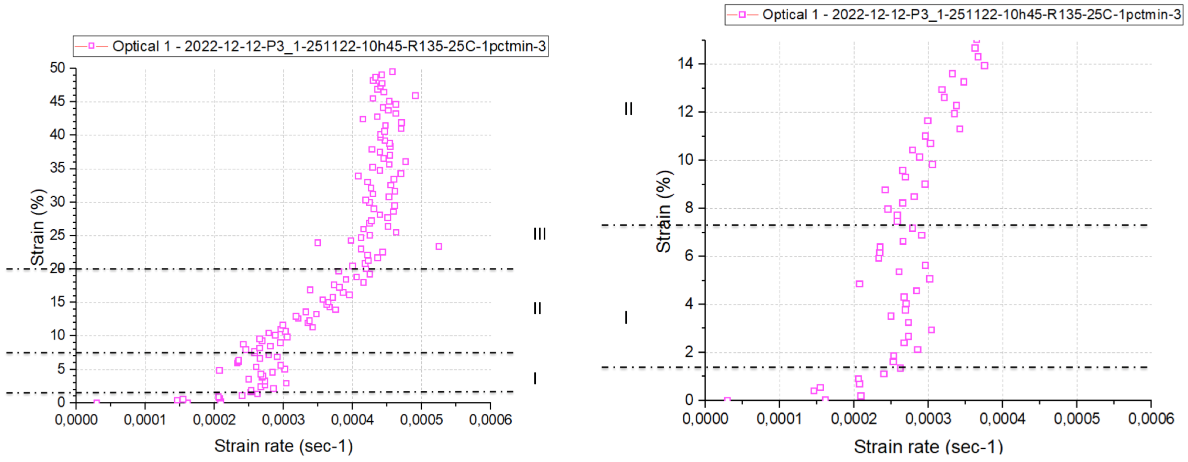

Figure 4.134: Strain as measured by the camera versus strain rate for P_{31} sample n°3. Regime I = "elastic", regime II= accelerated (including max of stress-strain curve), regime III = stabilised ("plateau")

The three regimes can be identified by sudden changes in the curve "strain as a function of strain rate". The first regime (I) is characteristic of a small (though not infinitesimal) deformation portion, where the strain increases as strain rate remain constant; in regime II strain increases with strain rate and the maximum of the stress-strain curve is found in that portion; the regime (III) corresponds to the stabilisation of the strain rate as the strain increases further. This can be linked to the presence of a necking as will be explained at the next paragraph. Not all the three regimes are always present. Figure 4.134(b) is a zoom of figure 4.134(a).

The presence of a double yield was confirmed. The arrows highlight it on some of the stress-strain curves displayed at figure 4.135 where we have gathered the results obtained on P_{61} at one of the five strain rates ($1\% min^{-1}$ ($1.67\ 10^{-4} sec^{-1}$)) and at the three temperatures considered (25°C, 69°C and 128°C). Two samples have been tested for each temperature. The position of the second yield can be obtained by calculating the minimum of the first derivative of the stress-strain curve in that range, i.e the inflexion point.

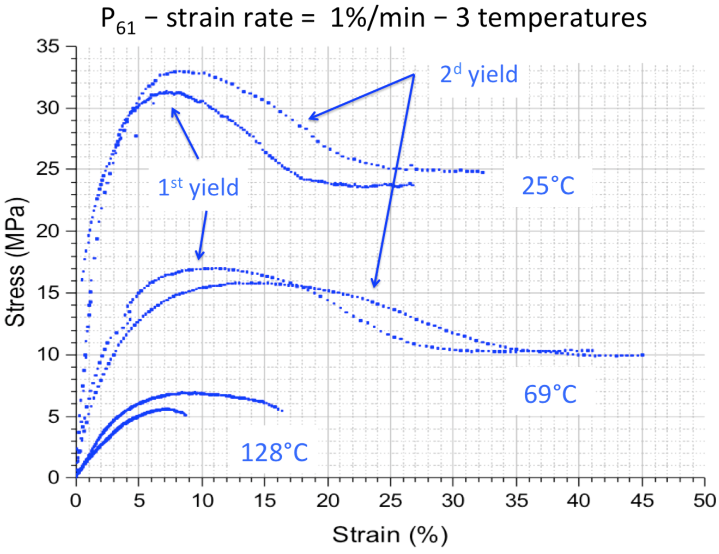

Figure 4.135: Stress-strain curves at 25°C, 69°C and 128°C and $1\% min^{-1}$ ($1.67\ 10^{-4} sec^{-1}$) of P_{61} annealed at 135°C during 3 days; two samples have been tested at each temperature; the first (maximum) and second (shoulder) yield are approximately indicated with arrows on the curves at 25°C and 69°C; the second yield can be obtained with good precision by taking the inflexion point

As the scattering of the curves was sometimes important, reduced stress-strain curves were drawn, that are presented in figure 4.136. The reduction was obtained by dividing respectively the strain and the stress by their value at the maximum of the stress-strain curve, ϵ_{max} and σ_{max}.

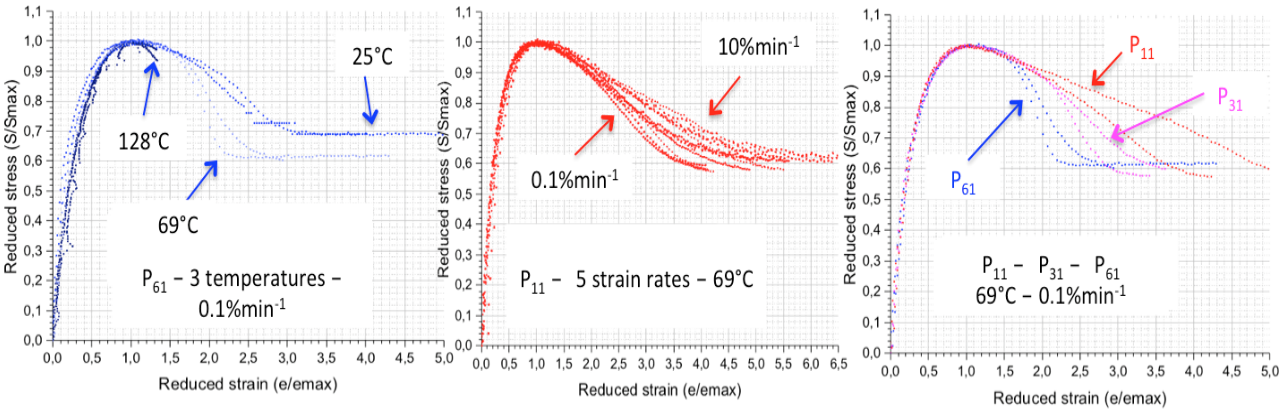

Figure 4.136: Reduced stress-strain curves of annealed samples: (a) P_{61} measured at 25°C, 69°C and 128°C and $0.1\% min^{-1}$ ($1.67\ 10^{-5} sec^{-1}$), (b) P_{11} measured at 69°C and the 5 strain rates of table 4.14 and (c) P_{11} , P_{31} and P_{61} measured at 69°C and $0.1\% min^{-1}$ ($1.67\ 10^{-5} sec^{-1}$)

Figure 4.136 allows to compare the behaviour under (a) varying temperatures at one strain rate, (b) varying strain rates at one temperature and (c) different products at one temperature and one strain rate. In figure 4.136(a) and (b), two different levels can be observed for the neck propagation plateau. The temperature (figure 4.136(a)) is clearly a first order factor compared to the strain rate (figure 4.136(b)). As the lower plateau is related to higher temperature (or lower strain rates), a deepening of the yield drop is consequently observed.

When comparing the products together on figure 4.136(c), we see that P_{61} and P_{11} have respectively the most narrow and broad drop[32]. This phenomenon can be related to the type of plasticising undergone by each product. The curvature of all the samples displayed at figure 4.136 is convex, but not all the testing conditions resulted in such type of shape.

4.3.3 Observed macroscopic deformation mechanisms

In this section, we comment on the macroscopic deformation mechanisms observed during the tests. We somehow make the link with the microscopic mechanisms presented in the introduction, reminding that the macroscopic process can be the result of microscopic competitions. We also would like to draw attention, and we will remind it in the explanations, to the fact that our comments relate to the observations made well beyond the maximum of the curve and very often after the necking.

Several macroscopic deformation mechanisms have been observed at the macroscopic level during the tests, diffuse and pronounced necking, microcracking, themselves associated or not with shear banding, stress whitening or microcracking [17], [48], [160] and leading to various macroscopic failure modes. We remind here that the term "failure" can have different significations, as explained in the introduction. In this case, we consider that the failure corresponds to the end of the test i.e. the sample failure, which is what we observe optically here.

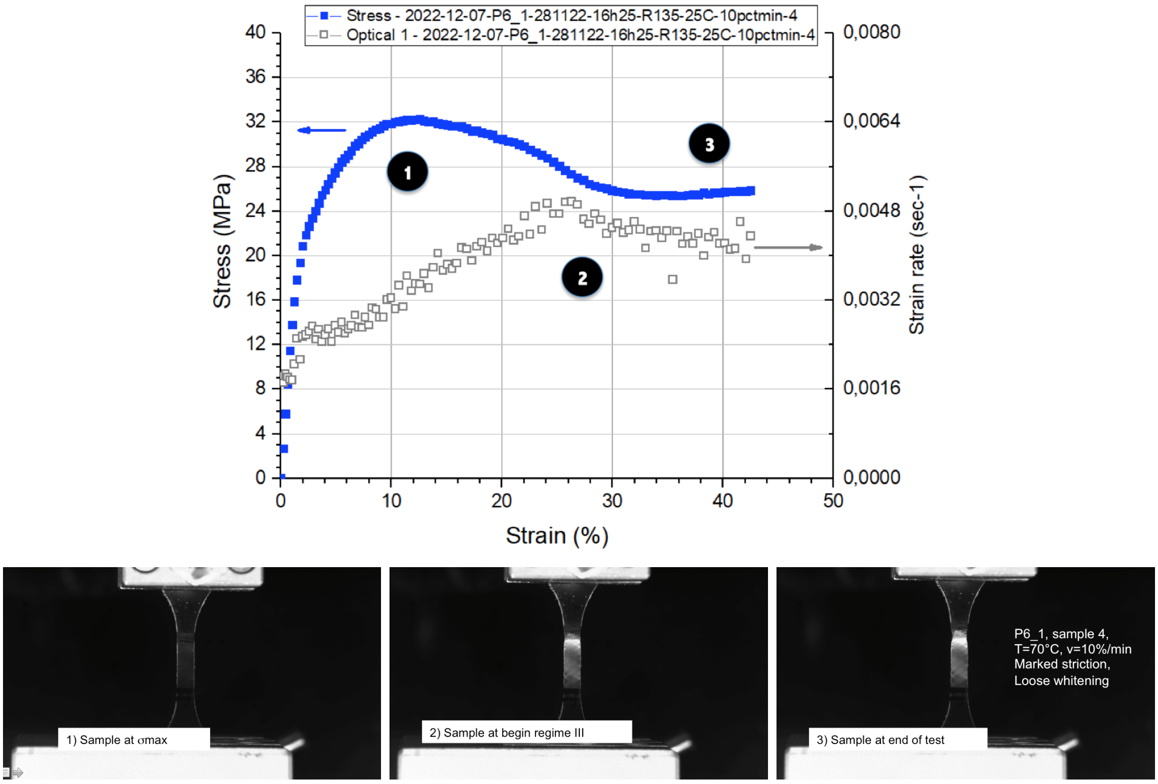

Figure 4.137: Top: Stress-strain curve (in blue) of annealed P_{61} measured at 69°C and 10%/min (1.67 $10^{-3} sec^{-1}$); from left to right, the left-Y axis corresponds to the stress (in blue) and the right-Y axis corresponds to the strain rate (in grey); the numbers 1, 2 and 3 correspond to the same number on each picture. Bottom: pictures taken respectively (1) at the maximum of the stress-strain curve, (2) at the beginning of regime III, (3) at the end of the test; the two latters have been identified manually

At figure 4.137, we have displayed the remarkable points of the stress-strain curve (in blue) that were linked to the picture taken at that very moment with the camera during the test. The principle was to identify (1)

---

[32] we refer to the definition of the drop height and width given at section 2.2.1 though the measurement of the width is not trivial as explained in [68]

the maximum of the stress-strain curve (1^{st} yield), (2) the beginning of the regime III (see figure 4.134) where the strain rate has stabilised just after necking (2^{d} yield) and (3) the plateau, considered as the end of the test. While the first yield has been obtained by calculating the maximum of the curve, the two other quantities have been assessed manually from the graphs, as they do not intervene from a quantitative viewpoint at this stage in our approach.

The figure 4.138 below summarises the macroscopic failure modes observed during the whole campaign of tests. From left to right: (a) pronounced or heterogeneous necking, (b) diffused or homogeneous necking with tedious whitening (c) pronounced necking with stress whitening, (d) microcracks (at low T/high speed) and cracks (at high T/low speed), (e) heterogeneous necking with shear banding, (f) necking with microcracks and whitening. Usually, whitening is associated to cavitation, though not always [161].

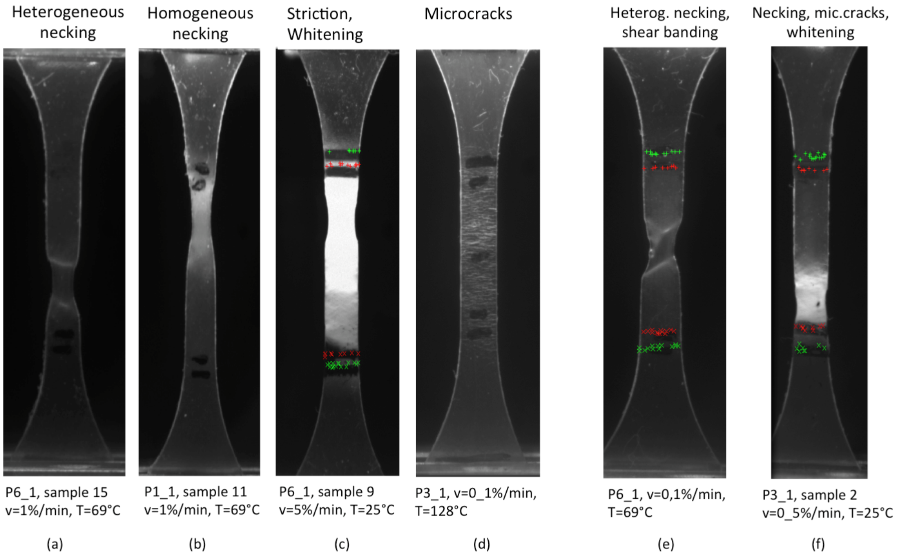

Figure 4.138: A summary of macroscopic failure modes observed during the whole campaign of tests. The small black spot in the right middle of the stretched white zone on picture (f) is a hole

Some of these mechanisms can be related to *plasticity processes* such as (a) pronounced or (b) diffused necking eventually (e) accompanied by shear banding triggered by small defects created at the sample edges during its removal. This type of mechanism corresponds to different shapes of the stress-strain curves that display always convex curvature in the whole or partial zone of drop. When cavitation/whitening is present, and depending on its magnitude, parts of the curve can be concave in the zone beyond the maximum of the stress-strain curve and the plateau (if any).

The pronounced necking is directly related to a very visible shoulder in the drop, as illustrated by figure 4.135, that appears after the diffuse neck.

The question of the diffused necking is more tricky because an homogeneous yield at the macroscopic level can hide a set of various processes at the microscopic scale. In our case, it can be accompanied or not by very light whitening, such as in figure 4.138(b), and it has a very smooth and broad drop as illustrated at figure 4.136(b). These shapes are related in the literature to the double yield, therefore we name them first (homogeneous) and second (heterogeneous) yield [17], [153], [34], [162], [163], [164], [78], [55], [54], [68], [160], letting open the question of the coherence between microscopic and macroscopic observations.

On the other side, when *whitening* occurs, and this can happen quite early in the test, it generally means that a *cavitation phenomenon* has been triggered, with cavities tall enough to cross the light wavelength [48], [54], [70], [47], [51], [50].

The question is now to understand when does plasticity be triggered. At this stage, it is not clear for some materials if the maximum of the stress-strain curve is only linked to plasticity or to the competing processes of yielding and cavitation and a finer analysis should be performed. In this research, we assume that only plasticity occurs at the very maximum, and that cavitation processes are triggered beyond, at least at 25°C and 69°C.

Intermediary results obtained via SAXS and WAXS on samples deformed respectively beyond the first and second yield - not presented here - have shown that, between the two yields, cavities oriented perpendicularly to the drawing direction (depending on the product) can be present, and that their size can reach around 1μm. At that moment, the long period still exists, which is no more the case beyond the second yield. On the contrary, WAXS reveal the same α-pattern for deformed and not deformed samples.

We'll have a final look at microcracking considered as a competition between yielding and cavitation. At 128°C, microcracking mechanism is activated in all cases in competition with a moreless pronounced yielding depending on product.

4.3.4 Deformation mechanisms as activated processes

The results of the tensile tests realised at the three temperatures are presented at figures 4.139 and 4.140. The evolution of σ_{max}/T (figure 4.139) and of ϵ_{max} (figure 4.140) with $log\dot{\epsilon}_{max}$ is shown. The strain rate has been taken at the maximum of the stress-strain curve as it is not constant during the test. The black lines highlighting the areas of the different processes have been drawn to support visually the eye. The empty symbols have different meanings: in the case of P_{11}, the symbols with inside crosses refer to tests carried out at room temperature on the Zwick (see section 4.2 and supporting information); in the case of P_{31}, the empty squares refer to samples tested at 28°C; in the case of P_{61}, the solid squares and empty diamonds refer respectively to films manufactured at two different moments (under the same standard conditions).

When we look at the graphical representations for each product, we can see where the various deformation processes are located. We need to keep in mind that these mechanisms are observed beyond the second yield point (if any). Whereas P_{11} displays either a competition between plasticising and cavitation or only smooth necking excepted at high strain rates where the pronounced necking becomes predominant, P_{61} displays a very broad domain where only necking occurs without any whitening, which is a characteristic of pure plastic behaviour.

From the curves of figure 4.139, and reminding that we are currently discussing the processes occurring at the maximum of the tensile curve (and not at the end of the test), it can be seen that on the one side, at 25°C and 69°C, there is one mechanism for P_{11} and P_{61} and two for P_{31} as they display respectively one and two slopes in their Ree-Eyring diagram. On the other side, at 128°C, the mechanism is clearly different for the three products.

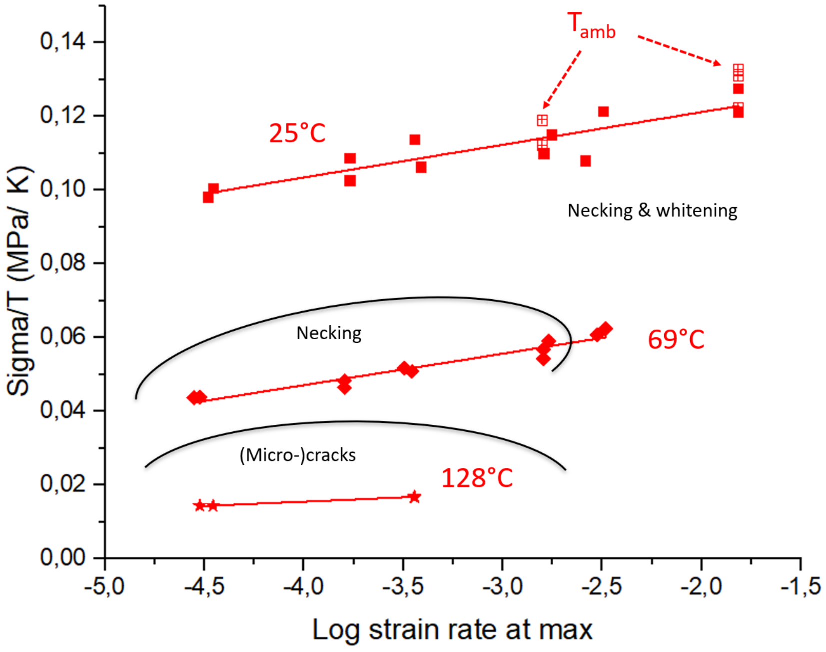

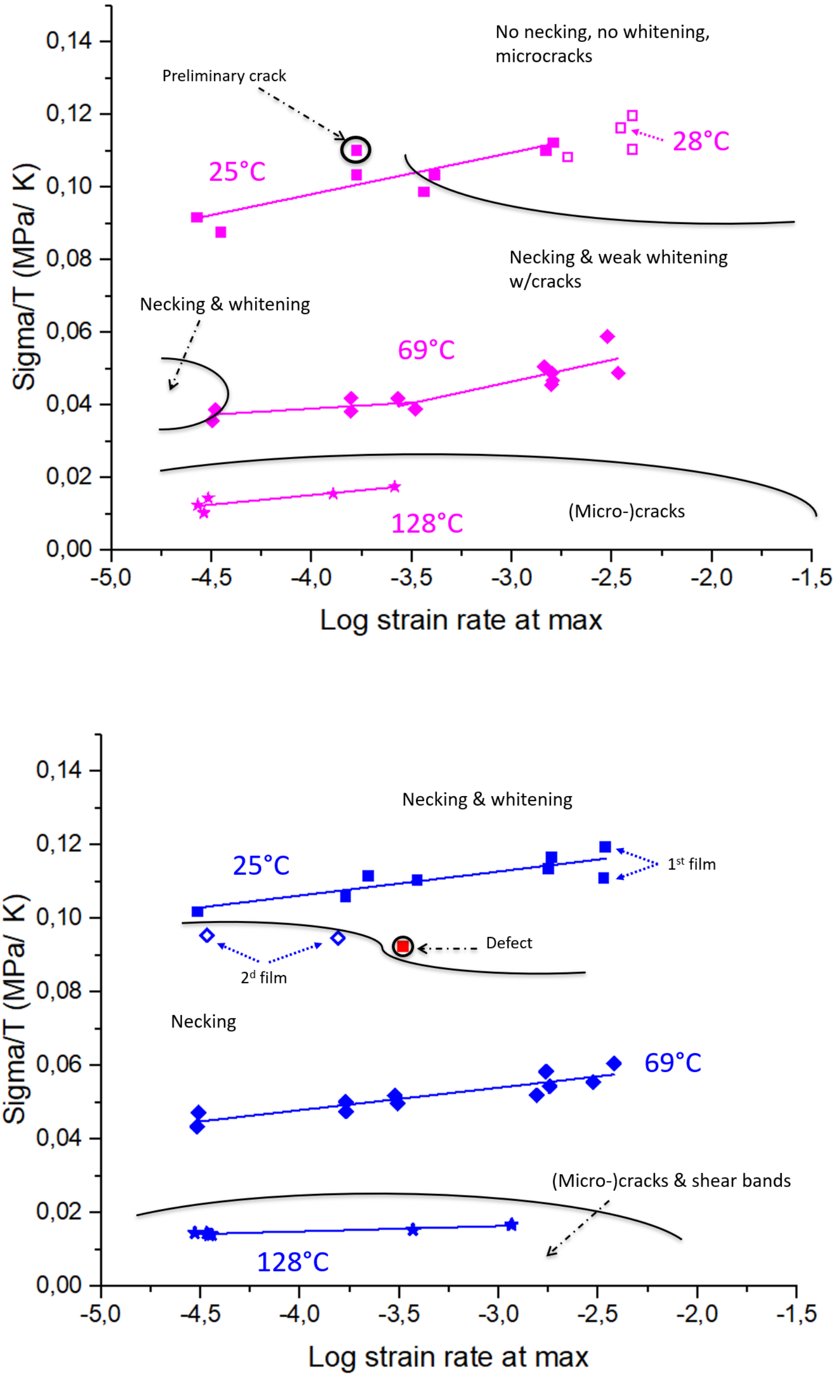

Figure 4.139: Evolution in a semi-logarithmic representation of $\sigma_{\mathbf{max}}/T$ as a function of $log\dot{\epsilon}_{max}$ presented for (a) P_{11}, (b) P_{31} and (c) P_{61} at three temperatures each, together with the type of deformation mechanism observed at the ***end*** of the test, so beyond the second yield; black lines delineating the different areas for failure mechanisms are a visual support for the eye; see text for the explanation of the different symbols

This is confirmed when looking at the trends of ϵ_{max} presented at figure 4.140 and table 4.15. If there was only plastic flow, ϵ_{max} would increase with increasing temperature and/or decreasing strain rate. The strain at 128°C for P_{61} increases with the decreasing strain rate (see figure 4.140(c)) and, given the type of deformation mechanism observed, is likely due to a strong competition between a dominant yielding and cavitation. As expected, at this temperature, the strain at maximum of the P_{11} and P_{31} decreases as microcracking is dominant (see section 4.3.3).

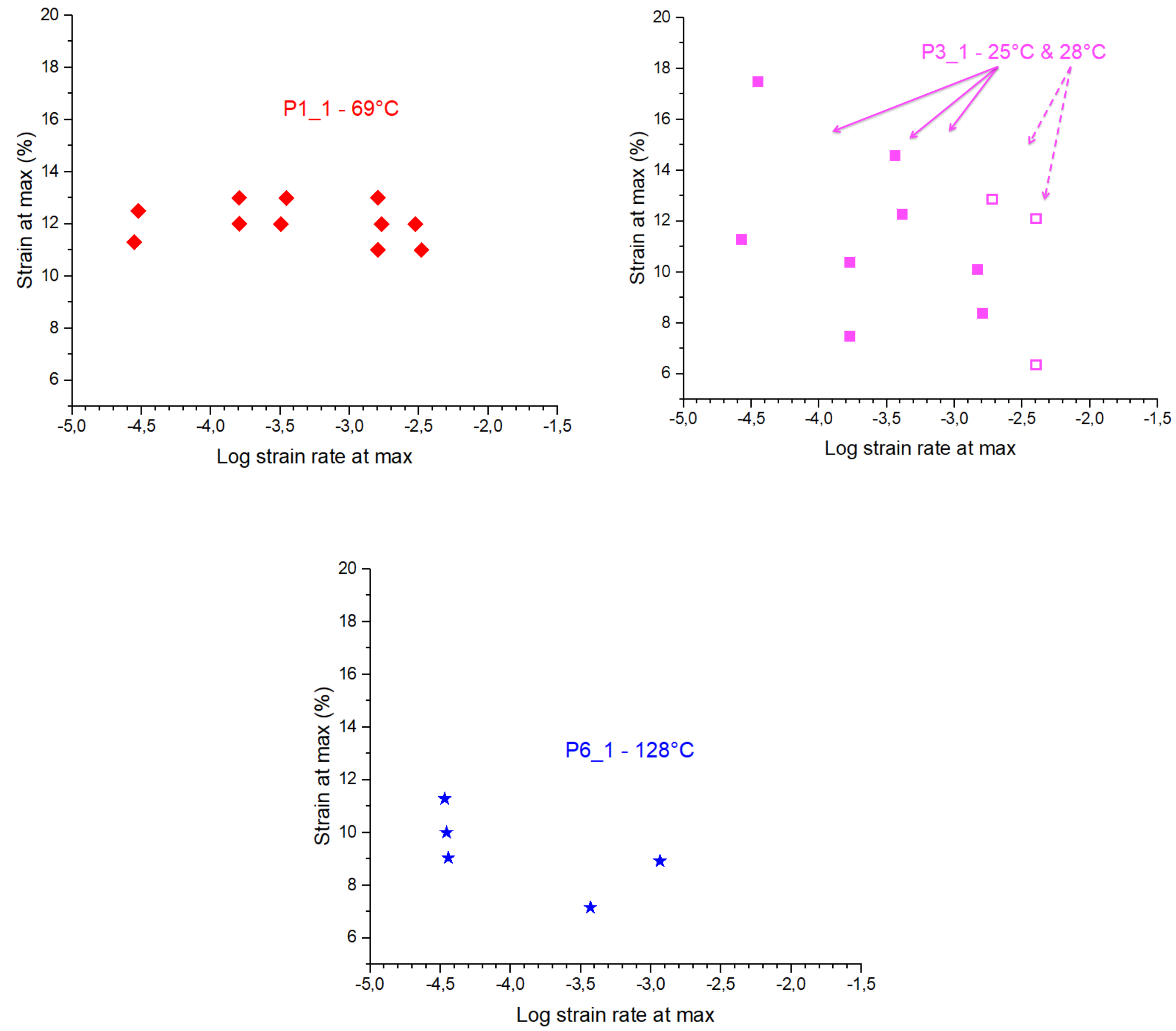

Figure 4.140: Evolution in a semi-logarithmic representation of ϵ_{max} as a function of $log\dot{\epsilon}_{max}$; (a) P_{11} at 69°C, (b) P_{31} at 25°C (full squares) and 28°C (empty squares), (c) P_{61} at 128°C

At figure 4.141, the non-linear evolution of σ_{max} and ϵ_{max} as a function of the temperature and for two strain rates confirms this observation.

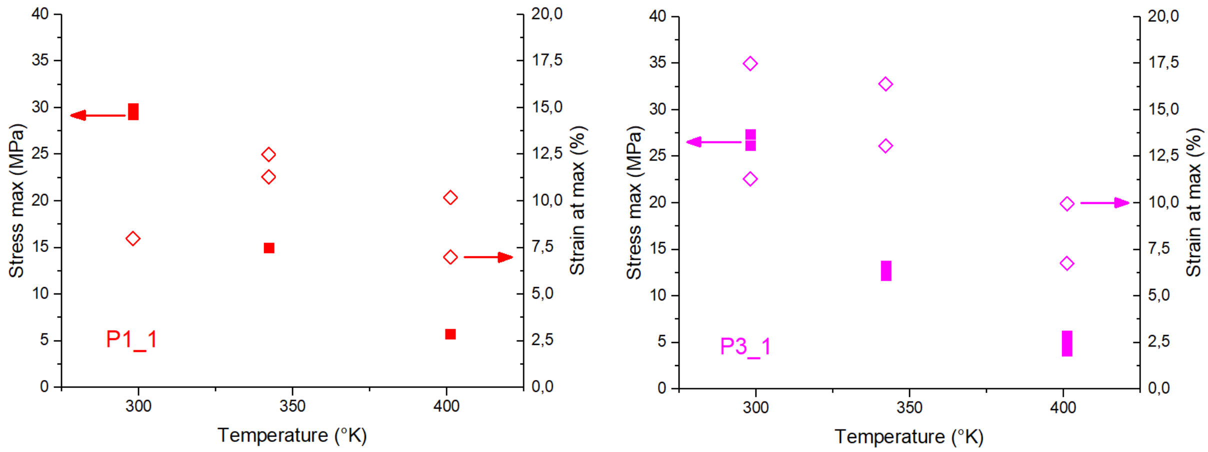

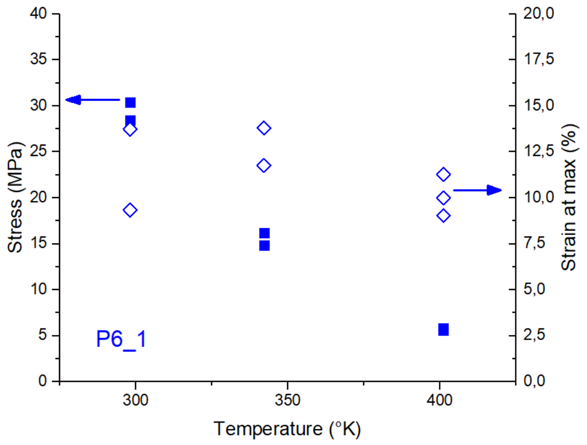

Figure 4.141: Evolution of σ_{max} (left Y-axis) and ϵ_{max} (right Y-axis) as a function of temperature for $\dot{\epsilon} = 1.67$ $10^{-5} sec^{-1}$ (0.1%/min) and 1.67 $10^{-4} sec^{-1}$ (1%/min) for the three products (a) P_{11}, (b) P_{31}, (c) P_{61}; the solid and empty symbols refer respectively to the stress and the strain at the maximum, as indicated with the arrows

Table 4.15: Evolution of ϵ_{max} as a function of $log\dot{\epsilon}_{max}$ for the three products. The trend is indicated for each temperature and increasing strain rates. The sign "+" means that ϵ_{max} increases with increasing strain rate, "=" means that ϵ_{max} remains constant with increasing strain rates and "-" means that ϵ_{max} decreases with increasing strain rates

Product	T (°C)	trend	T (°C)	trend	T (°C)	trend
P_{11}	25	+	69	=	128	-
P_{31}	25	+	69	-	128	-
P_{61}	25	+	69	=	128	+

The interpretation of the second slope of P_{31} visible on figure 4.139(b) is unclear for the moment. Indeed, we have assumed that at the maximum of the stress-strain curve, which is the location where the data are taken, only plasticity is active and not (yet) cavitation that occurs afterwards. From that viewpoint, the second slope could be considered as a second mechanism. However, it does not say if this latter is an homogeneous one, and on the contrary, it seems it is not the case. Indeed, the careful examination of the evolution of the strain beyond ϵ_{max}, the shape of the stress-strain curve in the yield drop and the subsequent pictures advocate rather for a competition between yield and cavitation; the sample also displays a pronounced neck together with an intense whitening. A more in-depth analysis of the microstructure during an in-situ test should ideally be performed in order to understand the kinetics of each mechanism.

The microscopic mechanism behind the macroscopic necking phenomenon is known to be due to the nucleation and propagation of screw dislocations in the crystalline lamellae in response to the applied stress [17], [163], [164]. First, when the temperature is high (i.e. above α-relaxation) or the strain rate low, the local kinetics of the propagation accommodate the macroscopic strain rate allowing the stems to tilt though not modifying the global crystal structure, leading ultimately to microscopic fine slipping and macroscopic homogeneous yield. This mechanism is characterised by a high activation volume. Second, when the temperature is low (below the α-relaxation) or the strain rate high, the macroscopic strain rate become too high for the dislocations nucleate and propagate, the lamellae are fragmented into crystalline mosaïc blocks leading to microscopic heterogeneous (coarse) and localised slipping, through defective interfaces within the lamellae or through the occurrence of partial dislocations involving the build-up of stacking faults. This results into a macroscopic heterogeneous yield with pronounced neck. The activation volume is then low, characterising a reduced ability for thermal nucleation of dislocations. Microcracks are then likely to occur [39], [152].

This phenomenon is exactly what can be observed at figure 4.137 where the strain rate increases with the strain and stabilise when the necking appears, around 22%, at the shoulder of the stress-strain curve for that example.

According to equation (4.65) - see section 4.3.5 -, it is then possible to calculate the different activated process constants. The mathematical procedure to calculate these quantities is illustrated at figure 4.142 for P_{11} and detailed in the annex (see section 4.5) together with their values (see table 4.19). In figure 4.142(a) the slope and intercept of product P_{11} measured in this example at 69°C are calculated with a linear regression; the respective values obtained and their link with the activation constants are given on the graph itself together with the regression coefficient r^2 with $r^2 = 0.94$. Figure 4.142(b) displays the two slope calculated at the two temperatures (25°C and 69°C) for P_{11}. Given the values of their error bars, these slopes are considered to be similar enough and their average is calculated. Let us remind here indeed that the activation energy can only be calculated for the same mechanism, this feature being translated by the fact that the slopes are identical.

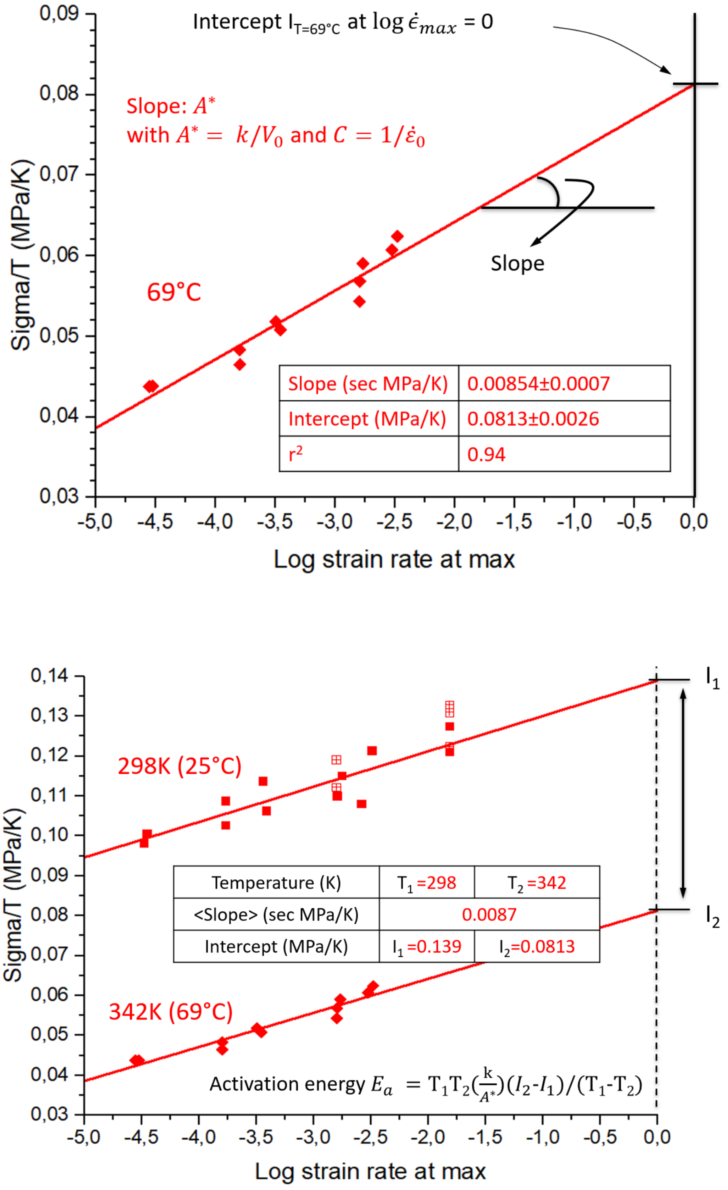

Figure 4.142: (a) Calculation by linear regression of the slope and intercept of product P_{11} measured at 69°C; (b) illustration of how the activation energy can be obtained from two series of tests carried out at 25°C and 69°C for P_{11} if the deformation mechanisms are considered as identical; I_1 and I_2 are the intercepts at respectively T_1= 25°C and T_2=69°C; the formula to calculate the activation energy E_a is also indicated - see text for detailed explanation

All the activation quantities are presented at table 4.16 where error bars have been removed because their magnitude is considered as small enough and it improves the readability of the table.

Table 4.16: Activation energy, volumes and time constant for the three products between 25°C and 69°C. The type of catalysis is indicated (ZN= Ziegler-Natta, MET=Metallocene) together with the molecular weight and non-uniformity (or polydispersity) index I; error bars have not been displayed for readability

Product	E_a kJ/mole	V_0 nm^3	C sec	$log_{10}C$	M_w kDa	$I = M_w/M_n$	Catalyst
P_{11}	128	3.6	$1.5\ e^{-36}$	-15.5	333	6.2	ZN
P_{31}	101	2.7	$1.23\ e^{-29}$	-12.5	185	5.7	ZN
P_{61}	183	5.0	$8.24\ e^{-54}$	-22.5	187	2.9	MET

These results show several features:

1. the activation volumes and energy are in the range of the literature [39], [80], [165]
2. the values for ZN products are clearly, according to the few articles mentioning such calculations, associated to heterogeneous yielding mechanism
3. the two ZN resins activation quantities rank according to their molecular masses
4. the activation volume and energy of MET product is bigger than the ones of ZN products
5. the comparison between the two ZN and MET products with almost identical molecular masses shows that the activation volume and energy of MET P_{61} is almost twice the one of product ZN P_{31}
6. from equation (4.65), the values associated to C give an idea of the vibration time of the molecular units involved in the process. Values of such parameters, hard to find in the literature, seem to be in its range [80].

We get therefore the following ranking of mechanism activation quantities.

$$P_{61} > P_{11} > P_{31} \tag{4.64}$$

4.3.5 Discussion

During the presentation of the results, we have adopted a macroscopic perspective to make the link between the the yield drop, the deformation mechanisms and the activation quantities of the Ree-Eyring model. We review now the most common deformation mechanisms in semi-crystalline polymers under increasing strain from the viewpoint of the micro-macro approach [161], [17] or see chapter 2.

When considering a tensile curve, the whole deformation process consists of several stages with different micro-mechanisms involved in each stage. Generally speaking, the plastic deformation initiates at yield point where the crystal lamellae experience crystallographic events like slips and interlamellar shear, then the crystallites fragment into lamellae blocks connected by oriented amorphous chains with the strain increasing. Finally, at large strain, the lamellar crystals change into fibrillar ones, allowing a significant hardening effect if chain disentanglement is not involved. In tensile deformation mode, the polymer may also cavitate during the whole stretching process.

The most current deformation mechanisms are [161]: cavitation, homogeneous and heterogeneous shear, thermally activated dislocations, solid/solid transformations (crystal/crystal, disordered/ordered), crystallisation under tension.

It is possible to look at these deformation mechanisms by hierarchical spatial scale, looking first at the crystal and defects, then at amorphous phase, then at the lamellae, then at the spherulite level. We refer to chapter 2 for such a review. We mention here just a few [161].

The crystalline phase can be the locus of shear, crystal twin, phase transformation, fragmentation, melting/ recrystallisation.

The amorphous phase, made of a mobile amorphous fraction (MAF) and a rigid amorphous fraction (RAF), can be the region where lamellae slip or separation takes place. Generally, slip occurs under compression or shear and separation under tension [22]. Cavitation also takes place in the amorphous phase under tensile solicitation because of the negative hydrostatic pressure or, on the long term, by coalescence of microvoiding under for example chain disentanglement or relaxation.

The rigid amorphous phase at the interface of the amorphous and crystalline phase, and the mesophase, so critical in iPP, can both undergo a solid/solid transformation either via a glass transition, or via the transformation of mesophase into α-monoclinic crystals. These mechanisms occur via nucleation and diffusion of screw dislocations that proceed by helical jumps of polymer chains and lead to the relaxation of the constrained chains and helical sequences transfer between the phases. Usually [36], [92], the viscoelastic α-relaxation is considered as two-folded, with a lower- and upper-temperature component related to the jumps of polymer chains neighbouring respectively the amorphous phase and the crystals, and allowing crystal viscous slip for the second.

The glass transition of the isotactic polypropylene is considered to be the glass transition of the MAF.

All these mechanisms can compete together. All in all, the critical deformation mechanisms may depend on a set of variables and factors linked to the material microstructure and test conditions, and follow irreversible or reversible paths, leading to changes in conformations or packing, when the stress is released.

Let us focus more specifically on the viscous flow and plasticity processes.

In this case, one of the most widely known and used is the Ree-Eyring theory of chain segment displacement. This theory considers the stress σ, the strain rate $\dot{\epsilon}$ and the temperature T to be linked via an activation process. It has been widely used for amorphous and semi-crystalline polymers [96], [166], [100], [80]. It describes the viscous flow by considering the way each segment of macromolecules has the freedom to move whereas each is prevented to do so because of the binding forces with other macromolecular segments [98], [99]. In presence of several deformation mechanisms, each one is associated with one relaxation time and the link between the different quantities is expressed as [100]:

$$\frac{\sigma}{T} = \sum_{n=1}^{N} A_i^* (ln 2 C_i \dot{\epsilon} + \frac{E_a^i}{kT}) \tag{4.65}$$

with $A_i^* = k/V_0^i$ and $C_i = 1/\dot{\epsilon}_0^i$ the constants of the yield process i and $\sigma >> A_i^* T$.

V_0^i is the activation volume of the mechanism i and C_i is the vibration time of the i^{th} molecular stem involved in the displacement and located at the bottom of its potential well of height E_a^i.

In the theory, $\dot{\epsilon}_0^i$ is proportional to the rate of jump of the segment considered between two equilibrium positions in the absence of a stress and under thermal activity. The jump rate can be written as:

$$Jump\ rate = \dot{\epsilon}_0^i exp(-\frac{E_a^i}{kT}) \tag{4.66}$$

At equilibrium, $\dot{\epsilon}_0^i \approx$ forward jump $\approx$ backwards jump. This diffusion process gives rise to a macroscopically permanent deformation when some directions are favored, for example under the action of a stress.

However, the Ree-Eyring model is unable, as such, to account for the polymer structure, and there is a need to rewrite equation (4.65) as a function of the Gibbs function $\Delta G^i = \Delta H^i - T\Delta S^i$ of the yield process i instead of the activation energy, with $\Delta H^i \equiv E_a^i$. This allows to introduce an entropy term ΔS^i that is a measure of the change in structural disorder of the molecular segment taking place when it jumps over the barrier E_a^i. The parameter $\dot{\epsilon}_0^i$ can be then expressed by the equation (4.67) below ([165], J.C. Bauwens in [25]), where ν_0^i is the vibration frequency of the segment at the bottom of its potential well.

This approach has been applied to analyse the physical aging process, and it was assumed that the aging has an impact on the flexibility of the macromolecules.

$$\dot{\epsilon}_0^i = \frac{\nu_0^i}{2} exp(\frac{\Delta S^i}{k}) \tag{4.67}$$

We suggest to transpose it to the case where, rather than analysing various annealing times of the same chemical structure, we analyse various chemical structures at one annealing time. This assumption can be supported by the fact that the same molecular motions seem to be involved in the yield behaviour and physical aging in amorphous polymers (J.C. Bauwens in [25]).

In this case, we can develop the equation (4.65) for a set of different molecular architectures P_{n1} where $n = 1\ to\ 6$:

$$\frac{\sigma_n}{T} = A^*_{i,n}(ln2C_{i,n}\dot{\epsilon} + \frac{E^i_{a,n}}{kT}) \tag{4.68}$$

where $C_{i,n} = 1/\dot{\epsilon}^i_{0,n}$ contains the information on the structural disorder of the product.

This equation allows thus binding semi-empirically the microstructural quantities to the macroscopic mechanical properties. This model has not been so often studied for isotactic polypropylene [62], [42], [39], [79], [71].

To dig in deeper in the plasticising phenomena, in presence of a double yielding process two types of mechanisms have been identified. First, an interlamellar fine slip that results via crystal slip into the tilting of the chain axis and preserve the lamellae integrity; this leads to a homogeneous shear. Secondly, an intralamellar coarse slip with unchanged chain axis orientation that leads to the fragmentation of the lamellae into mosaïc blocks and to heterogeneous shear. Both are accompanied by interlamellar shear of the amorphous (RAF, MAF) phase. The heterogeneous slip is ascribed to the lower visco-elastic α-relaxation and the homogeneous to the upper one [163], [164].

As mentioned earlier, the yield process is interpreted as a mechanism of nucleation and propagation of the dislocations in the crystalline lamellae, and as such, as an activated process, (contrary to the melting/recrystallisation explanation). The free energy barrier for the nucleation from the lateral crystal face of a pure screw dislocation parallel to the chain axis is directly proportional to the lamellar thickness as demonstrated by Darras et al [167]. The lower the crystalline thickness, the lower the barrier. These researchers remark that the corollary to thermal activation of dislocation is the fact that the activation volume should be very large because a great number of cooperating atoms is required and that the sole role of the amorphous phase is to transfer the stress to the crystal, whatever its proportion.

We think however that, even if the energy requested to trigger dislocation nucleation does not depend on the proportion of amorphous phase, it does not say anything about its local stiffness and the resulting stress (or strain) transfer.

Lefebvre and Escaig [78] calculated the dislocation density in various semi-crystalline polymers and highlighted the role of the entangled intercrystal amorphous phase. As it is related to the chain stiffness, and more specifically to the chain stem or to the chain persistence length, they concluded that the chain flexibility controls the activation volume. Other authors came to a similar conclusion, though from a very different viewpoint: they looked at the isotactic length influence on α-viscoelastic relaxation [83] or modeled the diffusion of dislocations on the base of the chains stiffness [38].
We think also that, as the mechanism at stake in the yielding process will approach the glass transition temperature, the free volume will become an important parameter that could modify the global flexibility of the macromolecular chains involved in the process and therefore its activation volume.

To our knowledge, the literature does not display a lot of information about the activation energies. This is still more the case for the activation volumes and the vibration frequency of the considered molecular segments undergoing the deformation is only mentioned in a couple of papers. We could not find any papers carrying out tests at strain rates or frequencies lower than $10^{-5} sec^{-1}$ (see [168] for a partial review).

The scarce levels of activation energy and volumes mentioned in the literature are respectively ranging between 2 nm^3 - 4.7 nm^3 and 100 kJ/mol - 160 kJ/mol [80], [39] to 7 nm^3 - 20 nm^3 and 200 kJ/mol - 500 kJ/mol [165] far beyond the energy of rupture of a C-C bond that is prohibited in plasticity [79], [62].

These authors consider that small activation volume and energy are associated with the mechanism of heterogeneous shear occurring at low temperatures, high strain rates and large deformations whereas large activation volumes and energy are associated with the mechanism of homogeneous shear occurring at higher temperature and lower strain rates or small strains.

In order to proceed to relevant comparisons, it is important to consider behaviours under *identical* deformation or failure *mechanisms*. We will discuss first the results obtained at 25°C and 69°C assuming that plasticisation mechanisms dominates and neglecting cavitation phenomenon that has a statistically significant effect only beyond $(\epsilon_{max}, \sigma_{max})$, as already mentioned earlier; we will tackle afterwards the results obtained at 128°C when microcracking dominates - see figure 4.139.

The tables 4.17 and 4.18 summarise the results obtained on the microstructure and on the activation parameters. The microstructure has been characterised with DSC, SAXS, NMR and quasi-static tensile measurements.

More especially, the Young modulus E has been measured at $1\% min^{-1}$ ($1.67\ 10^{-4} sec^{-1}$) and the yield stress at $50\% min^{-1}$ ($8.3\ 10^{-3} sec^{-1}$), both at T_{amb}. The isotactic length n_{iso} was calculated from NMR data according to [87], [151] and expressed in monomeric moieties C_3H_6 and in nm in order to assess the number of stacks $2l_c + l_a$ spanned by n_{iso}. The calculation of the number of CH_2 in the activated volume V_0 is available, together with the other quantities, at chapter 3 and in the supporting information 3.6.4; this calculation does not take into account neither the stress transmitters nor the microcavities. The NMR values for P_{61} have been taken from P_{51} data, both being considered as similar from that viewpoint.

Table 4.17: Summary of the results obtained on samples of P_{11}, P_{31} and P_{61} annealed at 135°C during 3 days; the values marked with * come from P_{51} considered as similar to P_{61} - see text for detailed explanations

Product	P_{11}			P_{31}			P_{61}		
$T_m(°C), \chi_c, low - T_m$	166.5	0.54	0.36	165.7	0.54	0.36	155.5	0.47	0.34
$L_p, l_c, l_a (nm)$	19.4	9.8	9.6	18.4	9.3	9.1	17	7.5	9.6
$n_{iso}(\#C_3H_6), n_{iso}(nm)$	190		124	164		106	178*		116*
$2l_c + l_a(nm)$, $\#(2l_c + l_a)$ in n_{iso}	29.3		4.23	27.7		3.85	24.5*		4.72*
E (MPa), σ_y (MPa)	1985		37.4	1942		37.9	1556		37

Table 4.18: Summary of the results obtained on samples of P_{11}, P_{31} and P_{61} annealed at 135°C during 3 days. Data from Eyring theory obtained (top) in the range 25°C to 69°C and (bottom) at 128°C; (**) activation volume for P_{31} second mechanism; (***) these values have been converted in base 10 logarithm - see table 4.16

$25°C - 69°C$ - dominant deformation mechanism: plastic flow									
$E_a(kJ/mole), V_0(nm^3)$, $C(sec)^{***}$	128	3.6	$10^{-15.5}$	101	2.7 9.51**	$10^{-12.5}$	183	5.0	$10^{-22.5}$
$\#CH_2$, #monomer units in V_0	144		48	111		37	195		65
$128°C$ - dominant deformation mechanism: micro-cracking									
$V_0(nm^3)$		13.6			6.0			21.9	
$\#CH_2$, #monomer units in V_0	548		183	242		81	883		294

Between 25°C and 69°C and in the range of strain rates investigated, where the plastic flow dominates, our own results could be ascribed to the heterogeneous yield for the ZN products and MET.

The activation volumes of ZN products are totally aligned with the values found in the literature whereas the value for MET is somewhat higher. However, all the deformation mechanisms visually observed during the tests were advocating for an heterogeneous mechanism. The activation volume and activation energy follow the same ranking: MET P_{61} is larger than ZN P_{11} itself larger than ZN P_{31}. If we assume that mesophase is well present and/or that the more important amount of amorphous phase, especially the RAF, plays a role, the activation volume should be larger when the amorphous phase amount is larger [39]. Another complementary explanation is the fact that a larger molecular weight leads to the high molecular weights having a higher probability to span more than two lamellae in one stack $2l_c + l_a$. Both arguments can explain the ranking between P_{11} and P_{31} and between P_{31} and P_{61}, whatever the role played by the defects. Especially in the case of P_{61}, we suspect that a higher amount of stress transmitters associated to a more entangled network coming from the defect presence could explain the larger activation volume, and that the quality of these connections could be also playing a role. In other words, a larger amount of ST result in a lower local stress on the crystal, but a higher or lower intrinsic chain or stem stiffness would act on the type of stress or strain transfer able to trigger the dislocation. Finally, resulting from the higher activation volumes and lower isotactic length, we can see that P_{61} displays more CH_2 and therefore more monomeric units implied in the process than the two other products.

The lower molecular weight of P_{31} could also be at the origin of the massive presence of microvoiding and cavitation that compete with the plastic flow. P_{31} is the only product to present microcracking or cracking as well as whitening phenomena on almost the whole domain of strain rates and temperatures analysed. A more careful analysis of the reduced curves at 25°C shows that for lower strain rates, the second yield is present but for strain rates around 10%/min, the curvature of the drop has become concave, indicating a pronounced softening of the material, likely to be due to a cavitation process triggered just after the maximum of the stress-strain curve. The same type of phenomenon is observed at 69°C, with a broader and very smooth drop at the highest strain rates.

Besides activation volumes and energies, the time constants $C_{i,n}$ provide useful information on the behaviour of the microstructure and the kinetics of dislocations therein.

We remind here that $C_{i,n} = 1/\dot{\epsilon}^{i}_{0,n}$. Disregarding the process i, let us have a look at $\dot{\epsilon}_{0,n}$ expressed in sec^{-1} and let us take its logarithm[33]; the literature provides a range going from[34] 16 [168] to 32 [7] to 39 [80] to 47 [165]. Our own results fall in this interval, between 12.5 (P_{31}) to 15.5 (P_{11}) to 22.5 (P_{61}).

Let us remind first that 69°C is in the middle of the α-relaxation (see figure 4.133) and close to the glass transition of the condis crystals that ranges between 50°C and 85°C when cooperative motions are triggered that will free mobilities and enable the transformation of these defective crystals into the monoclinic α-phase at higher temperatures.

A few comments can be first done on $\dot{\epsilon}^{i}_{0,n}$ itself. Let us remind that [166], from equations (4.65) and (4.67) it is proportional to the jump rate and reflects, via the entropy term, the changes occurring in the structural disorder of the molecular segment taking place when it jumps over the barrier E^{i}_{a}. In other words, this quantity translates somehow the kinetics of the disorder changes occurring during the i^{th} process of the P_{n1} product because it is also related to the nucleation and propagation of chain twists for the mechanism at stake [79].

The table 4.18 provides us with the following ranking:

$$\dot{\epsilon}_{0,3}/2 \ < \ \dot{\epsilon}_{0,1}/2 < \ \dot{\epsilon}_{0,6}/2 \tag{4.69}$$

The inequality (4.69) means that the kinetics of the disorder change, the "disorder change frequency" is larger for P_{61} than for P_{31} and P_{11}. The difference between the ZN products is smaller than the difference between ZN and MET. This ranking is in agreement with the considerations developed in this discussion - see supra - that the amount of mesomorphic phase and/or of rigid amorphous phase is larger for the MET than for the ZN. A more detailed analysis should therefore appeal for a better description of these materials.

Another consequence of inequality (4.69) is directly related to the number of processes observed for our different products in the Ree-Eyring diagrams, at figure 4.139, whatever these processes could be.

If we develop equation (4.68) considering only one single mechanism, replacing the stress σ by σ_{max} and the activation constants by their physical expression, we can write for P_{n1} where $n = 1 \ to \ 6$:

$$\frac{\sigma_{max,n}}{T} = \frac{k}{V_{0,n}}(ln2 + \frac{E_{a,n}}{kT}) + \frac{k}{V_{0,n}}(ln\dot{\epsilon} - ln\dot{\epsilon}_{0,n}) \tag{4.70}$$

This means that when the test is performed at a certain temperature T and a certain strain rate $ln\dot{\epsilon}$, the ranking of the difference $ln\Delta\dot{\epsilon} = ln\dot{\epsilon} - ln\dot{\epsilon}_{0,n}$ is

$$ln\Delta\dot{\epsilon}_{31} < ln\Delta\dot{\epsilon}_{11} < ln\Delta\dot{\epsilon}_{61} \tag{4.71}$$

This means also that the disorder change characteric time, linked to the rate of jumps, can be reached more easily by the macroscopic strain rate for P_{31} than for the two other products and that a larger portion of its whole ($log\dot{\epsilon}$ - σ_{max}/T) curve - with all its mechanisms - has become experimentally accessible compared to the two others.

The lower isotactic length and lower span of $(2l_c + l_a)$ stacks resulting from a lower molecular weight together with a higher number of stereodefects possibly encapsulated in thinner crystalline lamellae [11] could accelerate this phenomenon; especially as the requested energy to exceed the potential barrier is lower due to the direct link with the crystal thickness (see table 4.18 but also [78]).

In order to confirm this hypothesis and make appear the second process for P_{11} and P_{61}, we should target strain rates $log\dot{\epsilon} \ < \ 10^{-5} \ sec^{-1}$ in the standard experimental range of temperature. However if it happens that we

---

[33] i.e. we look at a frequency and no more at a time

[34] all the values have been normalised according to log_{10}

come very close to the glass transition domain, it is likely that the influence of its large cooperative movements on the free volume would not be taken into account by the Ree-Eyring model and that another type of theory such as WLF should be used.

A final consequence of equation (4.70) is that, when the macroscopic strain rate approaches the "disorder change frequency", i.e. when $\dot{\epsilon} = \dot{\epsilon}_{0,n}/2$ it could be possible to reach a threshold for the considered mechanism [100], expressed by the equation (4.72).

$$\sigma_{max,n} V_{0,n} = E_{a,n} \tag{4.72}$$

In this case, $\sigma_{max,n}$ would have become independent of the strain rate and would be proportional on the sole ratio of the energy barrier $E_{a,n}$ and the activation volume $V_{0,n}$. At this stage, other mechanisms such as stress cracking and disentanglement, active at more longer terms than these processes, could appear.

Let us conclude this discussion with the results at 128°C. Compared to the plastic flow dominated regime, the microcracking regime shows an increase of the activation volumes for P_{11} and P_{61} and a decrease for P_{31}. This latter is likely to highlight the dominant role played by cavitation because all the failures observed during the tests carried out at this temperature display microcracks associated to almost constant width beyond the maximum of the stress-strain curve (see figure 4.138(d)). Whitening accompanied by 45° shear band and holes appear at a very late stage, close to final rupture of the sample. This is coherent with the assumption of a second heterogeneous yield promoted by the competition with cavitation.

We think that this is a direct influence of the molecular weight or of the number of ST, compared to P_{11}.

We computed an equivalent number of monomers or CH_2 groups for the three activation volumes, though it is somewhat challenging to make such analogy. Indeed, the creation of cavities means that no molecule is involved in the void volume and no stress is transmitted. In the same way, the stress transmitters are not taken into account.

The larger activation volumes of P_{11} and P_{61} could reflect a mixed situation, with still a large amount of molecules undergoing yield and strain hardening at the microscopic level competing with the coalescence of voids. This could be analysed namely by looking at the coupling between cavitation and plastic instability as well as the amount of stress transmitters [68].

4.4 Conclusion

We have demonstrated, via the analysis of the stress-strain curves, their shape in the yield drop and the pictures taken at remarkable points that a double yield was indeed existing, especially in the case of the metallocene product. However, this was not translated into a change of slope in the Ree-Eyring diagrams for two out of the three products. As whitening was also present in a specific range of temperature and strain rates, we have tried to clarify at the macroscopic level how the competition between associated cavitation and yielding was operating. We have come to the conclusion that the different long term/low strain rates behaviours of ZN resins can be explained by the critical influence of their molecular weight and that the differences between ZN and MET behaviours have to imply not only the molecular weight but also the regio-defects typical of the metallocene catalysis. Indeed, the (rigid) amorphous phase plays a key role in the local stress transfer but the activation of dislocation propagation is itself linked to the crystal thickness and to the number of stress transmitters as well as to the glass transition of the condis crystals occurring around 50°C-60°C. These features are at the base of the moreless entangled and flexible network of the amorphous and mesophase and have as consequence that the activation volume is controlled by the flexibility of the macromolecular chains and that this is translated by the increased disorder change of the helical jumps. We think also that the second mechanism is not necessarily an homogeneous one. Furthermore, if it is identified in a zone close to, or partially overlapping the glass transition, another type of physical model, such as WLF ([7], [102], [96] should be used to take into account the evolution of the free volume under the thermal action.

To our knowledge, it is the first time that such a detailed explanation is provided on the quality of the activation constants in relation with both the chemical structure and the thermo-mechanical history.

The next step will be to confirm that the type of molecular relaxation at stake in the mechanisms observed during the tensile tests is indeed linked to a double yield phenomenon. To that purpose, we will make the link with visco-elastic relaxations occurring in the crystalline phase.

4.5 Annex

4.5.1 Mathematical procedure to calculate the activation energy of one yielding process

We remind that the Ree-Eyring equation is expressed as:

$$\frac{\sigma}{T} = \sum_{n=1}^{N} A_i^*(ln2C_i\dot{\epsilon} + \frac{E_a^i}{kT}) \tag{4.73}$$

with $A_i^* = k/V_0^i$ and $C_i = 1/\dot{\epsilon}_0^i$ the constants of the yield process i and $\sigma >> A_i^*T$. V_0^i is the activation volume of the mechanism i and C_i is the vibration time of the i^{th} molecular stem involved in the displacement and located at the bottom of its potential well of height E_a^i.

Let us consider here only one process. The equation (4.73) simplifies in:

$$\frac{\sigma}{T} = A^*(ln2C\dot{\epsilon} + \frac{E_a}{kT}) \tag{4.74}$$

with $A^* = k/V_0$ and $C = 1/\dot{\epsilon}_0$. The graphs of figures 4.140 and 4.142 give us the values of the respective slopes and intercepts that are thus known quantities calculated in a log_{10} base.

It is possible to deduce the activation energy by considering either two temperatures T_1 and T_2 at constant strain rate or two strain rates at constant σ/T as long as the slope of both series of test is identical. The activation energy of the considered process can then be found by resolving a set of two equations with two unknowns, taking care of the conversion of the neperian logarithm:

$$\frac{\sigma}{T_1} = A^*(ln2C\dot{\epsilon} + \frac{E_a}{kT_1}) = \frac{A^*}{2.302}ln2C + \frac{A^*}{2.302}ln\dot{\epsilon} + A^*\frac{E_a}{kT_1} = A^*log\dot{\epsilon} + I_{T_1} \tag{4.75}$$

$$\frac{\sigma}{T_2} = A^*(ln2C\dot{\epsilon} + \frac{E_a}{kT_2}) = \frac{A^*}{2.302}ln2C + \frac{A^*}{2.302}ln\dot{\epsilon} + A^*\frac{E_a}{kT_2} = A^*log\dot{\epsilon} + I_{T_2} \tag{4.76}$$

where $I_{T_1}(\equiv I_1)$ and $I_{T_2}(\equiv I_2)$ are the known intercepts and A^* the known slope of graphs 4.142. As the intercepts I_{T_1} and I_{T_2} are calculated when $log\dot{\epsilon} = 0$, equations (4.75) and (4.76) can then be written as:

$$I_{T_1} = A^*log2C + A^*\frac{E_a}{kT_1} \tag{4.77}$$

$$I_{T_2} = A^*log2C + A^*\frac{E_a}{kT_2} \tag{4.78}$$

and the activation energy E_a is found to be:

$$E_a = \frac{T_1T_2}{T_1 - T_2}\frac{k}{A^*}(I_{T_2} - I_{T_1}) \tag{4.79}$$

4.5.2 Values of slopes and intercepts

The table 4.19 displays the various constants of the processes calculated for each product and at each temperature, according to equations (4.74) and its practical implementation (4.75) and (4.76) for the three temperatures considered. The error bars are calculated with one standard deviation.

Table 4.19: Table of processes constants $A_i^* = \frac{k}{V_0^i}$ for each product and at the three temperatures; the error bar is calculated with one standard deviation

Product	T °K (°C)	Slope (= A^*) sec MPa/°K	Intercept MPa/°K	V_0 nm^3	Catalyst
P_{11}	298 (25)	0.0089 ± 0.0014	0.1390 ± 0.0046	3.6	ZN
	342 (69)	0.0085 ± 0.0007	0.0813 ± 0.0026	3.7	
	401 (128)	0.0023 ± 0.0002	0.0248 ± 0.0007	13.6	
P_{31}	298 (25)	0.0115 ± 0.0030	0.1440 ± 0.0109	2.8	ZN
	342 (69)	0.0119 ± 0.0036	0.0824 ± 0.0105	2.7	
	342 (69)	0.0033 ± 0.0021	0.0524 ± 0.0082	9.5	
	401 (128)	0.0053 ± 0.0018	0.0364 ± 0.0078	6.0	
P_{61}	298 (25)	0.0065 ± 0.0016	0.1324 ± 0.0052	4.9	MET
	342 (69)	0.0061 ± 0.0009	0.0724 ± 0.0032	5.2	
	401 (128)	0.0014 ± 0.0002	0.0207 ± 0.0010	21.9	

4.6 Supporting information

4.6.1 Tensile machines and samples

A tensile machine Zwick-Roell Z 2.5 with a load cell of 500N was used to confirm the presence of the double yield at room temperature.

A tensile machine Lloyd LS1E with a load cell of 250N was used with its oven for the tests at controlled room and higher temperatures. The temperature in the oven was controlled during the tests with a standard thermocouple. The camera Nikon used to record the pictures was using the Vimba 6.0 software to acquire images. The complete set-up is displayed at figure 4.143. Several difficulties linked to the set-up were solved, such as finding the appropriate oven background to have a good contrast, oscillating lightening, fog on the door window or silent blocks as support for the equipment.

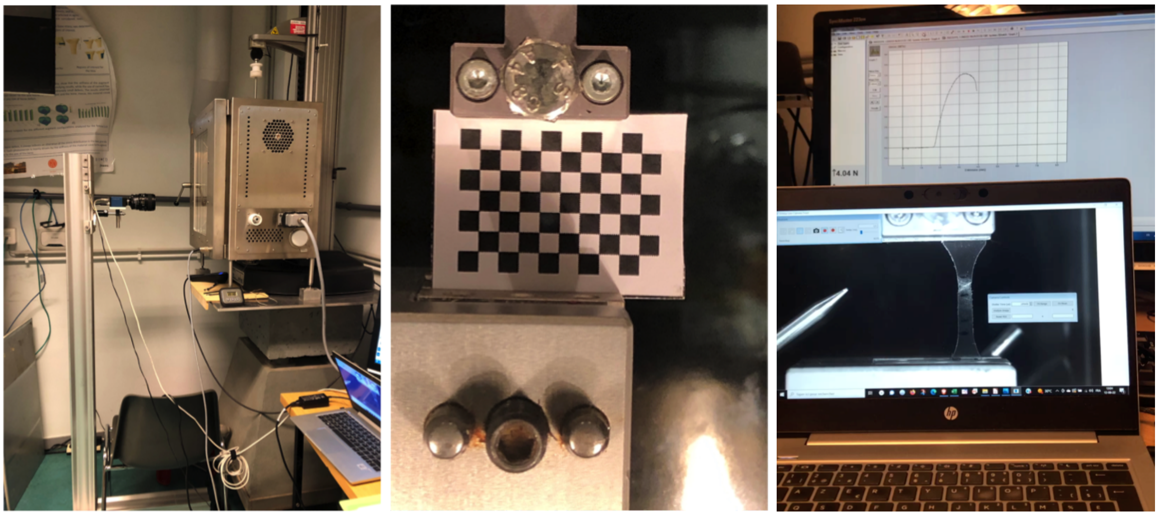

Figure 4.143: (a) Set-up with camera, oven and tensile machine (b) checkerboard for the alignment of the image capture and (c) sample monitored together with load signal

The samples used were manually removed with an ISO527 1BA/ASTM 638-V shape die. The length between clamps was 25.4mm. Due to the low thickness of the samples, a small procedure was set-up in order to get the most accurate and clean edges after the removal of the samples.

For the tests implemented on the Zwick and in absence of extensometer, the crosshead displacement was used in order to compute the nominal strain. For the tests carried out on the Lloyd, several marks were put on the samples, as presented at figure 4.144. In order to ensure a constant gauge length between the marks, steel gauges of respectively 5.1mm, 7.6mm and 9.5mm were machined and used when drawing the marks on the sample. The nominal strain rate was obtained from the image analysis and it was cross-checked with the crosshead constant speed.

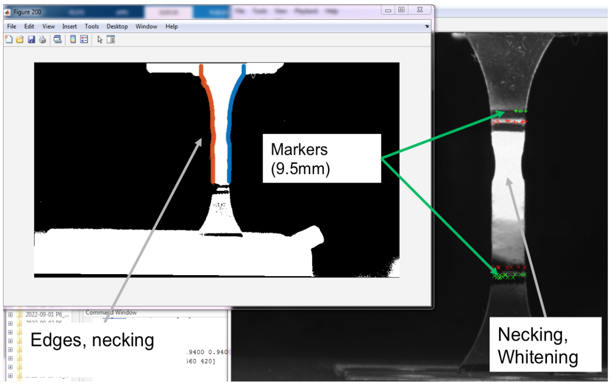

Figure 4.144: Monitoring of deformation and width on a P_{61} sample tested at 25°C and $5\%min^{-1}$ (or 8.3 $10^{-4}sec^{-1}$). Red marks span a gauge length of 7.6mm; green marks span a gauge length of 9.5mm

The samples' age and position on the film were duly recorded just after their removal. Because of the importance of edges quality on the yield apparition in that type of material, the duration between the removal and the test was mitigated as far as possible, with a view to avoiding thermo-oxidation (see chapter 3). The samples dimensions were taken on a graph paper in order to get the most reproducible measure (three measures for width and thickness taken in the gauge length).

4.6.2 Matlab® program to measure longitudinal and lateral strains

A series of Matlab® 2022b and 2023b home made programs have been set-up and implemented in order to

1. get the quantitative measure of longitudinal and lateral strains from the image analysis
2. synchronise the load cell and crosshead signals with the camera
3. access the time evolution of the nominal strain rate

Chapter 5 : Comparison between viscoelastic relaxations and yielding behaviour

Table of contents

5.1 Introduction

The literature dealing with the viscoelastic behaviour of iPP is, to our best knowledge, not very extensive, and when papers investigate this field, they are rarely interested by the lower frequencies or the longer term properties, - which is our case - because on the one hand, the vast majority of iPP applications are falling in the range of smaller characteristic times (such as quasi-static or impact tests) and on the other hand, these tests are difficult to be implemented on usual equipment or just take too much time.

5.1.1 The viscoelastic relaxations

According to [7], [81], isotactic polypropylene is known to have a series of six transitions among which the main ones are the γ-, β- and the α-relaxations. The reality of basic relaxations processes and their general trends are known. However, despite the amount of studies dedicated to them, the exact molecular origin and the morphological assignment of notably the α-relaxation are still a mater of discussion because of the complexity of the material and the variety of results and interpretations proposed by various authors.

The γ- relaxation is located between -120°C and -40°C and is associated to local crankshaft motions of C-CH3 groups of the backbone chain in the amorphous phase [82].

The β-relaxation, located around 0°C is related to the glass-rubber transition of the (mobile) amorphous fraction. It is very broad compared to amorphous polymers.

The α-relaxation is located between around 40°C and 120°C. Its position varies with many factors (structure, density, thermal history, frequency, etc.). The origin of this process is controversial in the literature, but it undoubtedly requires the presence of a crystalline phase [81], [71], [36].

Even without considering superstructures such as spherulites, the polymer is considered as a multiphasic composite material where the exchanges of segments of molecular chains between the various phases play a crucial role, depending on the range of time, temperature or strain considered. The consequence is that the mechanisms triggered by local deformation at the interface of these various components are critical because they will determine the manner the transfer of strain will happen [69], [20], [16], [78], [92].

This is particularly true in the linear visco-elastic domain where the number and quality of phases are generally translated into relaxations. These phases are obviously strongly dependent on the thermo-mechanical history and on the chemical structure of the material. The evolution in time and temperature of their viscoelastic properties will vary accordingly, making sometimes their interpretation quite difficult.

Several models are proposed in the literature for the α viscoelastic relaxation and for the microstructure of isotactic polypropylene, going from biphasic amorphous/crystalline to continuum. We try to summarise them here, keeping in mind that these descriptions are not restricted to such a semi-crystalline polymer.

The main components considered are the amorphous phase, the crystalline phase and the metastable mesophase [69], constituted by conformationaly disordered crystals or condis [20], [18]. The amorphous phase itself is said to be composed by a mobile amorphous fraction (MAF) and a rigid amorphous fraction (RAF) [20], [109], [135], this latter we understand as the equivalent of so called the intermediary layer because it is covalently bounded to the crystal or to the mesophase. Some other authors consider rather a continuum between the mobile amorphous fraction and the crystalline phase [16]. In any case, RAF plays a critical role in the α-relaxation of monoclinic iPP.

Let us have a look at the models proposed for the microstructure. In the biphasic model [69], [71],[79], [37] the crystalline phase plays the role of physical crosslinking nodes of the amorphous phase.

The glass transition or β-relaxation behaves then in a way similar to that of a wholly amorphous polymer, with two characteristics: a high rubbery plateau, indicating the cross-linking effect by the crystalline phase, and a very high dependence of the strain on correlation effects, i.e. that the interface between the crystalline and amorphous phases plays an important role in the deformation of the latter. The levels found for the apparent activation energy of this relaxation are in the range of 380-450kJ/mol which is a typical value for the glass transition of amorphous polymers. The microstructure does change during the glass transition that triggers a change in the chains' free volume and long distance cooperative effects, the order of magnitude of which is very large.

Regarding the α-relaxation, it exists only when there is a crystalline phase and occurs at a higher temperature and a lower activation energy than the glass transition. The processes occurring during the α-relaxation are due to simpler mechanisms than those occurring during the glass transition and therefore have not the same order of magnitude in terms of cooperative movements and long distance effects.

These long distance effects take place via the stress-assisted diffusion of defects in the crystals that trigger rearrangements in the non-crystalline phase. This mechanism is activated by the temperature and obeys an Arrhenius law on a broad range of temperatures, indicating a constant microstructure, unlike the glass rubber transition. It is characterised by a few sharp relaxations times that depend on the mechanical history: when the defect arrive at the interface of the crystallite from its original position, a needed arrangement has to occur in the amorphous phase to accommodate the deformation.

The nature of the alpha relaxation was studied by several authors, namely by Pluta and Kryszewski [92].

In this very comprehensive study, two components of the mechanical α-relaxation were found for non-spherulitic samples, crystallised from the glassy state. The low-temperature component was attributed to the stress relaxation of the non-crystalline phase, especially the part containing strained molecules and segments of molecules belonging to the specific (irregular) arrangement of the surface layer of the crystallites. The high-temperature component of the α-relaxation was connected with the viscous slip of the crystalline elements within the non-crystalline phase. Other studies mention that [16] α-relaxation at lower temperature, named α_1, could be ascribed to the diffusion of helical jumps of polymer chains neighbouring the amorphous phase and α-relaxation at high temperature, named α_2, originates from the diffusion of helical jumps of the polymer chains close to the crystalline phase.

Regarding the methodological approach that we have taken, the way to identify the behaviour and number of the various phases and their translation into characteristics of the thermal and viscoelastic properties is on the one hand, to produce different types of microstructures obtained with different thermo-mechanical histories, i.e. quenched samples, with a large amount of metastable mesophase, quenched and annealed samples, where the annealing temperature T_a is varied, and isothermally undercooled samples at the same temperature than T_a; on the other hand, to test the obtained structure in a range of temperatures with a specific temperature scanning rate.

There has been a lot of controversies on the α-relaxation because of the nature of relaxations occurring at the temperatures at stake, i.e. between 40°C and 120°C.

The role played by the various phases has been refined namely by Chang et al [16], Kida et al[64] and Jiang et al [21] with a focus on the rigid amorphous phase fraction (RAF) (or intermediate phase) measured by different techniques such as FTIR, WAXS/SAXS or modulated DSC.

However, the main challenge in reality, not yet solved, comes from the question of knowing if each process observed is an enthalpic reversible or entropic irreversible one and if the superposition $t - T$ can be applied. From that viewpoint, the dependence on temperature and temperature scanning rate of the associated thermal and viscoelastic quantities are critical. So is the evolution of the microstructure. We review this hereunder.

Let us have a look first at the influence of annealing and testing temperature. The influence of temperature can be summarised as follows [16], [64], [21], [17]:

1. the mesophase is itself a tri-phasic system constituted by mesophase, RAF and MAF. The T_g of the MAF is the glass transition of the material, i.e. the β-relaxation
2. the α-relaxation depends strongly on the annealing temperature not only because of the thickening of the lamellae but also because of the stronger confinement force exerted by the polymer chains in the RAF
3. in non annealed samples and under the glass transition temperature of the condis crystals, the RAF is constrained by crystallites with a broad size distribution, leading to one α-relaxation peak
4. The contents of different helical sequences exhibit different variation trends in the triphasic mesophase system. As temperature raises, a four-steps mechanism is proposed for the evolution of the mesophase where the RAF plays a critical role: 1°) the onset of condis arrangement formed and annealed at slightly lower temperature, because of the glass transition of the RAF; this is characterised by an endotherm between 40°C and 80°C on the DSC curve and associated to the low-temperature α_1-relaxation; 2°) the solid-solid meso-α crystal transition; this phase is thermodynamically irreversible, i.e. on cooling, the formed α-crystal phase will not transform back into a mesophase; this is characterised by an exotherm between 80°C and 120°C and is usually assigned to the upper-temperature α_2-relaxation; 3°) the perfection of the crystalline lamellae and their thickening between 120°C and 160°C and 4°) the melting of crystals resulting from the initial mesophase reorganisation, characterised by the final and deep DSC endotherm beyond 120°C [19] or the melting of the primary lamellae [83] beyond 160°C [21]

5. during the heating process, the helical sequences in the crystalline and amorphous phase vary and helical sequence with 12 monomer units was found to exist in RAF, suggesting that RAF chains are attributable to defects in the crystals as n=12 monomer units is the minimum for consecutive helical chains to crystallise. Between 120°C and 160°C, the sequences of the crystal phase have become long (n>13). The isothermal crystallization results showed that the meso-α-crystal transformation is a nucleation and growth process from α-nuclei.

Secondly, we analyse the influence of the molecular architecture and the critical role of the isotactic length.

The influence of the molecular architecture has been studied by Hoyos et al [94], [87]. Recognizing that helical jumps through the RAF and chain-diffusion within the crystals are responsible for the α-relaxation, they found that the combination of the processing conditions and of the molecular architecture determine the fraction of low-T_m crystals, the surface exposed by parent lamellae to amorphous phase, the trapping degree in the inter-lamellae region and then, the availability of isotactic chains to be exchanged between the amorphous and crystalline phases. They studied a large set of molecular structures obtained under the relative same solidification conditions. From DSC traces characterising the various lamellae regimes (parent, subsidiary and transverse), they could calculate empirically the content of subsidiary and transverse crystalline lamellae, called low-T_m crystal content. This latter is strongly coupled with the crystallisation temperature.

Their main results are summarised hereunder where T_α is the temperature of the α-relaxation at which the tgδ is at its maximum and I_α is the relative intensity of the α-relaxation, measured by the ratio of $E''(T_\alpha)$ on the area under the glass transition peak:

1. T_α is determined by the isotactic length n_{iso} or the total content of isotacticity interruptions
2. I_α is determined mainly by the crystalline distribution, itself depending on the molecular weights, broadening results obtained on PE [163]
3. a general correlation exists between the low-T_m crystal content and I_α dynamics that is coherent with motions involving an exchange of isotactic chain segments between the amorphous and the crystalline phase
4. only one mechanism was present in their visco-elastic measurements.

Finally, we look at the influence of the solicitation frequency. The α- and β-relaxations depend on frequency. The influence of frequency on T_α will be discussed later, but the literature [36], [71], [16] mentions usually a shift towards lower temperatures when the frequency decreases. This is a very traditional observation [169].

In the case of iPP, both temperatures do not behave in the same way. When frequency decreases, T_α undergoes a larger shift than its equivalent T_β. This means that the apparent activation energy is larger for β than for α. Consequently, the shape of the β-relaxation curve is very much influenced by the presence of the α-relaxation, highlighting a lack of time-temperature superposition [71].

5.1.2 The crystallographic approach of underlying mechanisms: nucleation and diffusion of screw dislocations

Let us first have a look at the *physical meaning* of the α-relaxation.

It has been proved both in PE [39] and in iPP [94], [83] that the peak temperature T_α depends on the crystal thickness. When the lamella thickness l_c increases, the time required for dislocations to pass through it at constant diffusion speed increases; inversely, when a constant straining frequency is imposed, such as in a visco-elastic test, the migration rate of the defects should increase with the thickness in order for them to move throughout the whole thickness in a time scale that is compatible with the period of a strain cycle. This requirement is fulfilled by a rise in temperature, i.e. a higher α-relaxation temperature. Dislocation glide and α-relaxation can be thus activated at lower temperatures as the crystal thickness decreases [163], [79], [41], [39].

Assuming the presence of two mechanisms, the lower and upper α-relaxations are related respectively to the coarse or heterogeneous slip and fine or homogeneous slip in the crystalline lamellae, as illustrated in the figure 5.145 below and explained hereunder from [17].

The fine and coarse slips concern solely the deformation of crystal lamellae, while the interlamellar slip involves mainly the parallel shear of amorphous layer together with lamellae. Precisely, the fine slip is an homogeneous slip process that causes a change of angle between the normal direction to crystal surface **n** and the chain axis **c**. Such deformation leads to a progressive tilting of chains in crystallites, which results eventually in a gradual thinning of crystal lamellae. For coarse slip, the shear process is proceeded by sliding a crystal block one past another, with no divergence between **n** with respect to **c**. Unlike fine slip, the deformation by coarse slip can be highly heterogeneous and may lead to lamellae fragmentation.

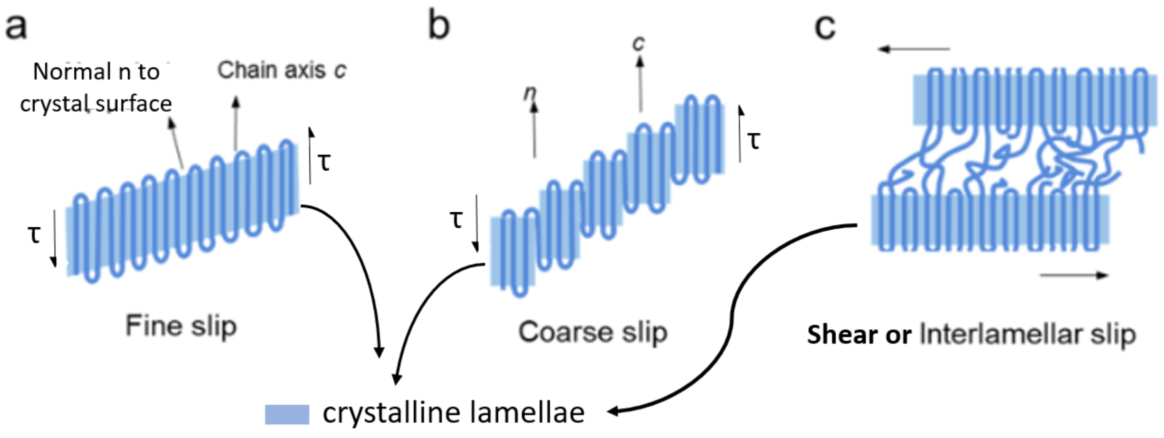

Figure 5.145: Main processes of slip propagation: (a) fine slip; (b) coarse slip; (c) interlamellar slip or shear. **n** and **c** represents the normal to crystal surface and chain axis, respectively [17]

Let us then have a look at the *activation energy* of the α-viscoelastic relaxation.

According to Jourdan et al, [71], the range found for the apparent activation energy of the α-relaxation is around 150kJ/mol.

However, considering that the process occurs in two steps, the diffusion of the defect inside the crystallite and the resulting rearrangement in the amorphous phase, they assume that these motions are more less correlated. The experimental apparent activation energy includes then this correlation effect that can be calculated to obtain the true activation energy of the sole defects migration in the crystal.

This latter was estimated to be around $E_a \simeq 33.5kJ/mol$, close to the value obtained by other authors in PE [79] or via dielectric measurements [90]. On their side, Jiang et al found an activation energy of 33.8kJ/mol for the meso-to-α transformation and Chang et al [16] found an activation energy of the α-relaxation in the range $14kJ/mol \leq E_a \leq 38kJ/mol$ for a RAF thickness ranging between 3nm to 2 nm[35]. One cannot be not struck by the fact that the levels of these activation energies are very similar, reinforcing the interpretation of mechanisms occurring at the interface of the RAF and the crystal.

Finally, let us examine the *double yield process and its link* with the α-viscoelastic relaxation.

Our research tries to establish a link between the viscoelastic properties and the yield behaviour via the nucleation and propagation of dislocations.

In semi-crystalline polymers, the yield process and the visco-elastic relaxations are linked to nucleation and propagation of screw dislocations in the crystalline phase [chapter 4], [160], [162], [163], [164], [62], [100], [80], [70], [143], [144] and are strongly coupled with the rigid amorphous fraction close to the lamellae composed of condis crystals frozen in the system during the crystallisation step [16], [18], [135], [19].

The first yield on the quasi-static stress-strain curve is related to the fine slip of segments that the dislocation propagation lets integer, whereas the second yield at larger deformations refers to their fragmentation into mosaïc blocks, due to the inability of dislocations to propagate at the rhythm of the imposed macroscopic strain rate and their subsequent accumulation in stack faults [17], [81], [152].

The great accommodation of slipping mechanism to various deformation modes illustrates well the generality of activated dislocations model and more importantly, the associated critical crystallographic events (like sliding of crystal blocks and tilting of lamellae) can also be fundamental molecular processes [17].

---

[35] we have some doubt about the validity of the time-temperature superposition used to obtain E_a, due to the overlapping of the two mechanisms.

5.1.3 The master curve and its mathematical treatment

The master or composite curve is an approach that assumes that the distribution of relaxation times is well represented by a Boltzmann statistics [102]. It takes benefits of the dependence of polymers on time and temperature. It allows to extend in a practical way the experimental realm by superposing curves obtained in a range of frequencies at a specific temperature to a shifted range at another temperature. By doing so, a shift factor a_T can be calculated that gives a new frequency value corresponding to the used temperature. This is the so called Arrhenius equation [69], [105], [103]:

$$a_T(T) = exp(\frac{E_a}{R}(\frac{1}{T} - \frac{1}{T_0})) = \frac{f(T_0)}{f(T)} \tag{5.80}$$

with E_a the activation energy of the mechanism, R the gas constant and the shift factor being the ratio between the frequency $f(T_0)$ at the reference temperature T_0 and the frequency $f(T)$ at the considered temperature T.

This equation allows scanning how the visco-elastic property considered (compliance, modulus or loss factor) evolves on a large range of temperatures in order to detect the transitions. Each visco-elastic transition is associated with one relaxation time.

The main issue, for this type of methodology, is when relaxations are overlapping. In this case, the construction of the time-temperature master curve is really at stake because it is quite easy to compare mechanisms that are in reality different and that should not be compared. It could be argued that the viscoelastic curve should be deconvoluted. However, in order to do so, one has to be sure about the number and location of transitions to be identified, which is not our case.

We have therefore selected a thermorheological approach usually implemented in the melt because, as it was demonstrated in the case of time-temperature superposition in the molten state [105], it is particularly relevant to highlight variations of activation energy in the framework of a study focusing on transitions between various mechanisms.

According to [105], "*in order to determine reliable and comparable activation energies, the evaluation method is crucial*" because the shift factor is the link with the microstructure. Some literature has used and still does, besides the shift factor along the frequencies, a shift factor along the moduli. This has been quite controversial and in order to circumvent this pitfall, the authors have decided to work with tan$\delta(\omega, T_0)$ or rather $\delta(\omega, T_0)$:

$$tan\delta(\omega, T_0) = tan\delta(a_T\omega, T_0) \tag{5.81}$$

Equation (5.81) leads directly to a similar result as equation (5.80) were ω is the circular rheological equivalent of f in the solid state:

$$\frac{\omega(T_0)}{\omega(T)} = exp(\frac{E_a}{RT}) = a_T \tag{5.82}$$

$$Rln(a_T) = \frac{E_a}{T} \tag{5.83}$$

The activation energy E_a can be determined as the slope of $ln(a_T)$ as a function of $\frac{1}{T}$ where a_T is determined between two temperatures from the curves $\delta = \delta(log\omega)$.

Once the activation energies have been calculated, it is possible to plot E_a as a function of δ. When it is constant, it means that the mechanism at stake is "pure", as illustrated at the figure 5.146 coming from preliminary calculations on one of our product[36].

According to the authors, this method is very powerful and sensitive to small differences, and its sensitivity can be exploited in the case of thermorheological complex polymers, if the range of frequencies ([and temperatures]) matches the internal time scales of the mechanisms at stake. We have assumed that we could find the relevant time and temperature frames thanks to this method.

---

[36] we draw the attention on the scale covered by δ on this figure. It covers only two degrees because there are few relaxation times whereas in the melt the range of δ involves several decades.

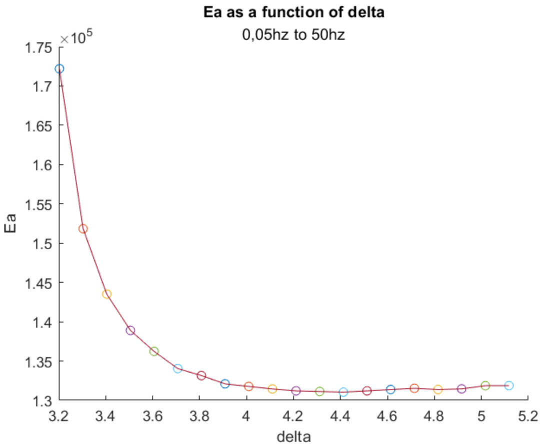

Figure 5.146: Activation energy E_a as a function of the loss factor δ

5.1.4 The scientific strategy

We will focus here on the link between the deformation mechanisms at yield, the visco-elastic relaxations of the crystalline phase and the microstructure of isotactic polypropylene.

We will investigate the visco-elastic behaviour in the solid state of a series of iPP from two different catalysis technologies under a large range of frequencies and temperatures and under their monoclinic α-crystalline form. We will focus on the link between the yield process at longer term and the α-relaxation measured by dynamic mechanical and thermal analysis (DMTA), both considered as activated processes. A special attention has been brought to lower frequencies and low strain rates.

5.2 Materials, samples and methods

The study of the behaviour at yield of iPP under various low strain rates and room to high temperatures has been presented in chapter 4 where we have compared two catalytic systems. It was concluded that the stress-strain curves, combined with the imaging of the macroscopic deformation mechanisms, provide evidence for a double yielding phenomenon though this process could not be clearly identified in the Ree-Eyring diagrams for two of the three products investigated. It was also concluded that the metallocene catalyst was rated better than its Ziegler-Natta equivalents in the investigated time and temperature realms.

Thanks to DMTA tests, we have identified the visco-elastic relaxations in a range of frequencies going from 0.01hz to 50hz and upper, and of temperatures going from room temperature to 140°C and we have calculated their activation energy.

In order to do so, we have applied the approach described above [105] to analyse the visco-elastic evolutions, overall tgδ and δ to build a master curve. The procedure used is extremely strict as to whether or not a certain number of results are kept.

Finally, we have compared the results with the activation energies obtained from the Ree-Eyring theory and tensile quasi-static measurements [chapter 4].

5.2.1 Materials and samples preparation

The materials and film preparation have been detailed at chapter 3. The samples were 5 mm-wide strips and at least 50mm long. More information is available in the supporting information.

5.2.2 Characterisation methods

The films have been tested under dynamic mechanical and thermal conditions on an equipment TA DMTA Q800 mounted with a tensile set-up. More information is available in the supporting information.

Different testing conditions were applied, covering all together a range of temperature comprised between -130°C and 140°C and a range of frequencies comprised between 0.01hz and 180hz, though an upper limit of 50hz was imposed for the data exploitation. The particular conditions will be specified on a case-by-case basis.

The other characterisation methods have been described in chapters 3 and 4.

5.2.3 The Matlab® program for the mathematical treatment of the master curve

We did not know exactly upfront what would be the small or large overlapping present in our tgδ curves measured isothermally on a wide range of frequencies, neither how many mechanisms we would get, neither in what (T, f) range one single mechanism would be observed. Given these uncertainties combined with average quality of data in the low frequency, we have built a Matlab® program able to fit a curve through the experimental data $(logf, \delta)$, calculate the shift factor a_T and, as consequence, deduce the (δ, E_a) curves by "sliding" along the whole range of temperatures (25°C-140°C).

More explanations can be found on the master curve in chapter 2 and in the supporting information together with the detailed procedure used to build the software.

5.3 Analysis of viscoelastic relaxations

We have discussed in the literature review the existence of two components of the α-relaxation and their link with the number of phases of the microstructure. In this section, we try to identify how many components our spectra involve.

The table 5.20 summarises the testing conditions applied during the two campaigns.

Table 5.20: Table summarising the test conditions for the two campaigns. In the first column, "#" refers to the numeral of the test conditions and "§" to the paragraph where it is tackled; "l.z." means "linear zone" that is different for each product

#, §	Product	aged (days)	annealed (days, $°C$)	type	test conditions
① 5.3.1	P_{11}, P_{12}, P_{13}	12		ramp	$1.5°C/min$, 1hz, 0.125%
② 5.3.1	P_{11}, P_{13}		4, 140	ramp	$2°C/min$, 10hz, 0.045%
③ 5.3.2	P_{11} to P_{51}		3, 135	ramp	$2°C/min$, 10hz, % l.z.
④ 5.3.2	P_{11} to P_{61}		3, 135	isotherm	0.01hz-10hz, $\Delta T = 2°C$, 5min, % l.z.
⑤ 5.3.2	P_{11} to P_{31}, P_{51}, P_{61}		3, 135	isotherm	0.05hz-200hz, $\Delta T = 2.5°C$, 5min, % l.z.

The ranges of temperature were -40°C to 145°C for testing conditions ①, ② and ④, -130°C to 145°C for ③ and 25°C to 120°C for ⑤.

The colour code for the first campaign is the following: pink/magenta for P_{11}, green for P_{12} and blue for P_{13}. The colour code for the second campaign is: P_{11} in red, P_{21} in blue cyan, P_{31} in pink, P_{41} in black, P_{51} in green and P_{61} in blue.
Let us remark that we have focused on the loss factor, δ, because this quantity was needed to compute the activation energies, as we will see at section 5.5 and also because it is a convenient way to eliminate problems of varying section dimensions from sample to sample.

5.3.1 First campaign: analysis of the viscoelastic peaks

Figure 5.147(a) displays P_{11}, P_{12} and P_{13} tested after 12 days aged at ambient temperature. Two samples have been measured for P_{13}. Various peaks appear that call for some comments:

1. P_{11} shows a maximum around 85°C, P_{12} and P_{13} have respectively a swallow maximum around 100°C and 105°C
2. P_{12} presents a peak around 57°C and P_{13} displays two peaks around 57°C and 67°C (1st curve) and only one peak around 67°C (2d curve)

3. on the left hand side of the glass transition, P_{11} and P_{13} are quite similar whereas on its right hand side, P_{11} and P_{12} do; this confirms the results obtained in chapter 3 where some microstructural aspects of P_{12} look like P_{11} or P_{13}, depending on the tests conditions.

These behaviours can be put in relation with the DSC traces and their derivatives measured on un-annealed/as-received samples, as illustrated at figure 5.148. It can be seen on figure 5.148(a) that three zones are identified on the derivative, that have been reproduced on the flow itself (figure 5.148(b)). These zones have to be put in relation with the various states of the microstructure, depending on the temperature: glass transition of the RAF, transformation of the mesophase into α monoclinic crystals, perfection of the crystalline phase (see supra and [21]).

The SAXS (not shown) and WAXS patterns have also been recorded, in order to obtain the long period as well as check the type of crystalline phase, as displayed at 5.149(a). The break down on four well known peaks reveal the typical signature of monoclinic α-crystals structure with an amount of mesophase and amorphous phase to be evaluated [117], [150], [120], [69].

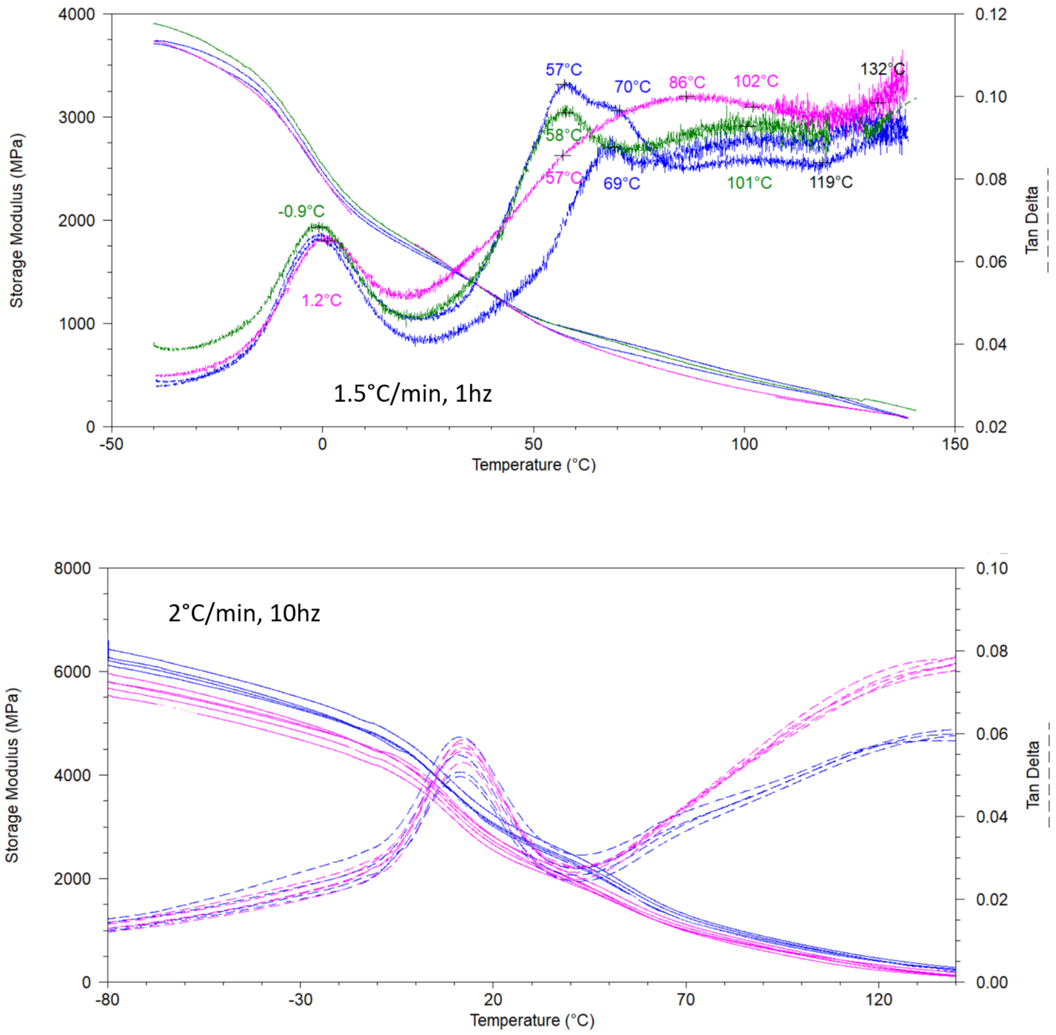

Figure 5.147: Storage modulus and tg δ of (a) P_{11}, P_{12} and P_{13} aged of 12 days tested under conditions ①; (b)P_{11} and P_{13} annealed during 4 days and tested under ②; numbers correspond to local extrema; pay attention to the different scales - see discussion for more information

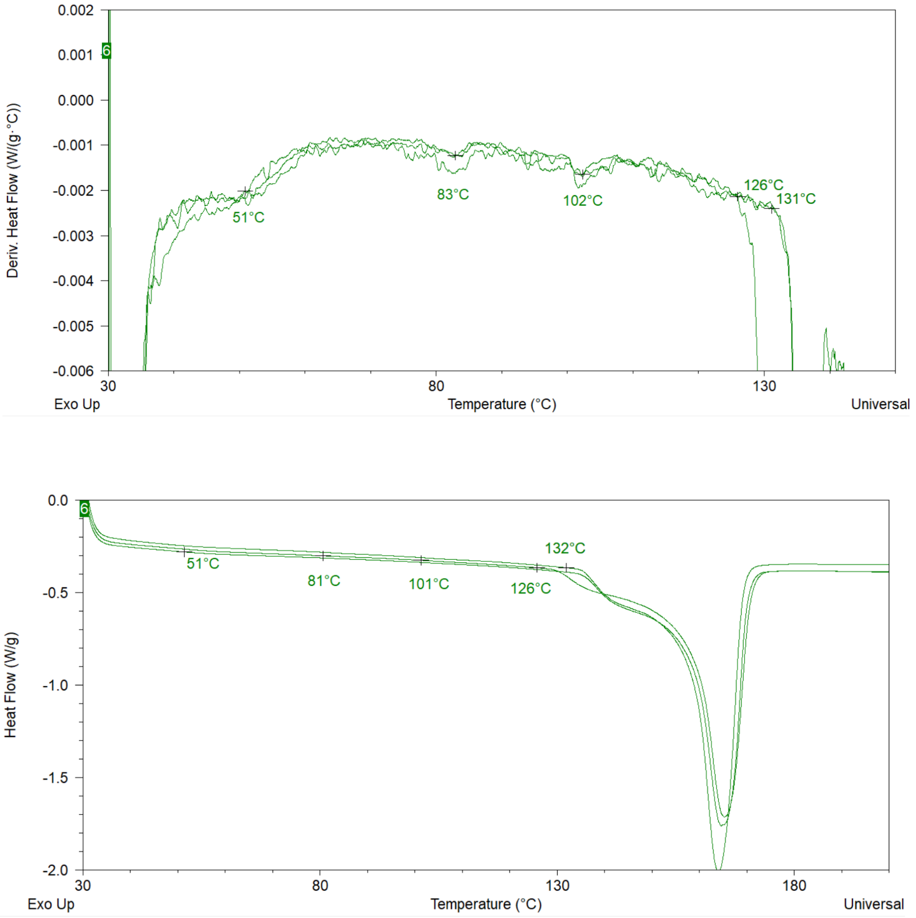

Figure 5.148: DSC traces of P_{12} aged 48 days at ambient temperature: (a) derivate of the heat flow and (b) heat flow. Numbers indicate local minima, which we call "remarkable points"

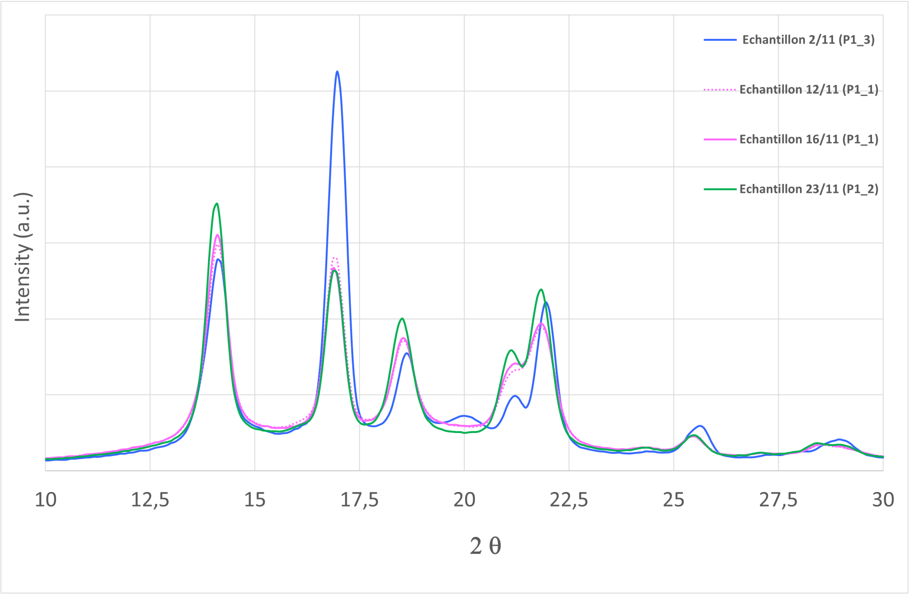

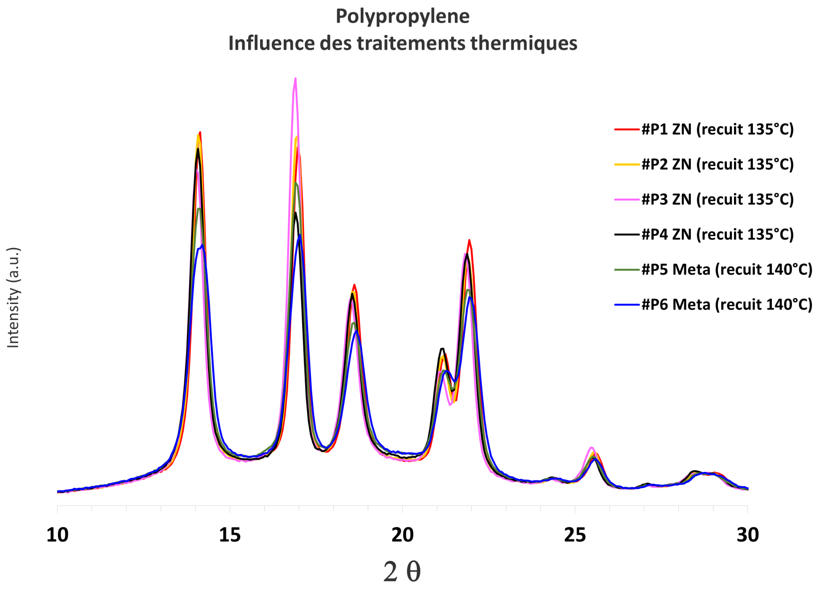

Figure 5.149: (a) WAXS spectrum of P_{11}, P_{12} and P_{13} aged at ambient temperature; (b) WAXS spectrum of P_{11} to P_{61} annealed during 3 days at 135°C.

Finally, figure 5.147(b) compares a series of P_{11} and P_{13} samples annealed 4 days at 140°C and tested under ⑤. One observes that:

1. the curves of the two products are diverging as of around 50°C-55°C with a increasing difference between the tangents of the loss factor, the quenched product having the highest value
2. the maximum of the curves are located around 130°C
3. tgδ of P_{11} is larger than P_{13} in this temperature range
4. the T_g at 10hz is located around 7-8°C for both.

All the results have been summarised in the table 5.21 below. Let us remark that the melting temperatures T_m displayed in this table do not refer to these samples and come from the same data as table 3.6, chapter 3: the values entered for the samples aged at ambient temperature have been averaged on 4 or 5 measures taken between 144h to 1896h whereas the values at 140°C refer to one sample measured at 93h for each product.

For a question of vocabulary consistency, we refer in the rest of the text to $T_{\alpha i}$ as the temperature assigned to the i^{th} peak, starting from the lower temperatures and from the left to the right.

Table 5.21: Average crystallinity χ_c, low-T_m, long period L_p, crystalline lamellae thickness l_c and amorphous phase thickness l_a of (top) P_{11} to P_{13} samples aged at ambient temperature during a few hundred to one thousand hours and (bottom) P_{11} and P_{13} samples annealed 4 days at 140°C. The enthalpy of a perfect α-crystal has been taken as 207 J/g [125], [42]; (*) data from other samples - see text. The three T_α temperatures come from figure 5.147 and are identified with the symbol "†" as these values come from other samples

Product (age at measure)	T_m $°C$	ΔH J/g	χ_c	low-T_m	L_p nm	ρ	l_c nm	l_a nm	$T_{\alpha 1}$ (1hz,	$T_{\alpha 2}$ $°C$,	$T_{\alpha 3}$ †)
P_{11}(576h)	166*	97.3	0.47	0.33	13.4	0.89	6	7.4	57	86	102
P_{11}(672h)	166*	97.3	0.47	0.32	13.1	0.89	5.9	7.2			
P_{12}(408h)	165*	109.7	0.53	0.34	17.9	0.90	9.1	8.8	58	69	101
P_{13}(960h)	169*	115.9	0.56	0.44	21.6	0.90	11.6	10	57	70	101
4days@140$°C$									(10hz,	$°C$,	†)
P_{11}	166*	118	0.57	0.33	19.7	0.90	10.5	9.2		90	>130
P_{13}	171*	128.3	0.62	0.46	22.3	0.91	13.2	9.1	70		120

5.3.2 Second campaign: analysis of the visco-elastic curves

We carried out the same analysis on the other quenched products, P_{21} to P_{61}, that have been all annealed at 135°C during 3 days. Figures 5.150, 5.151 and 5.152 present a series of experiments carried out under various conditions. Figure 5.150 presents one product of each catalyst. Figure 5.151 displays only the curves obtained at the lowest frequency on a series of P_{31} and P_{61} samples and figure 5.152 the superposition of all the products at (a) 10hz and (b) 0.1hz.

From figure 5.150, it can be seen that P_{51} displays large differences between the two samples on the left hand side of their glass transition, tgδ overlaps after the glass transition on a more less wide range between 50°C and 100°C. P_{21} samples have quite similar curves.

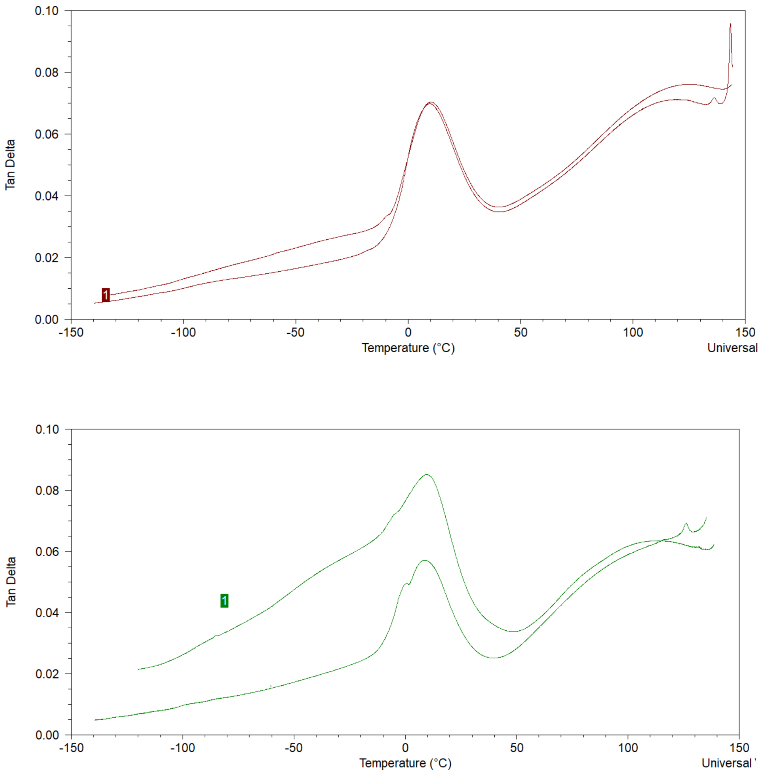

Figure 5.150: (a) tgδ as a function of T for P_{21} and (b) P_{51} tested under conditions ③

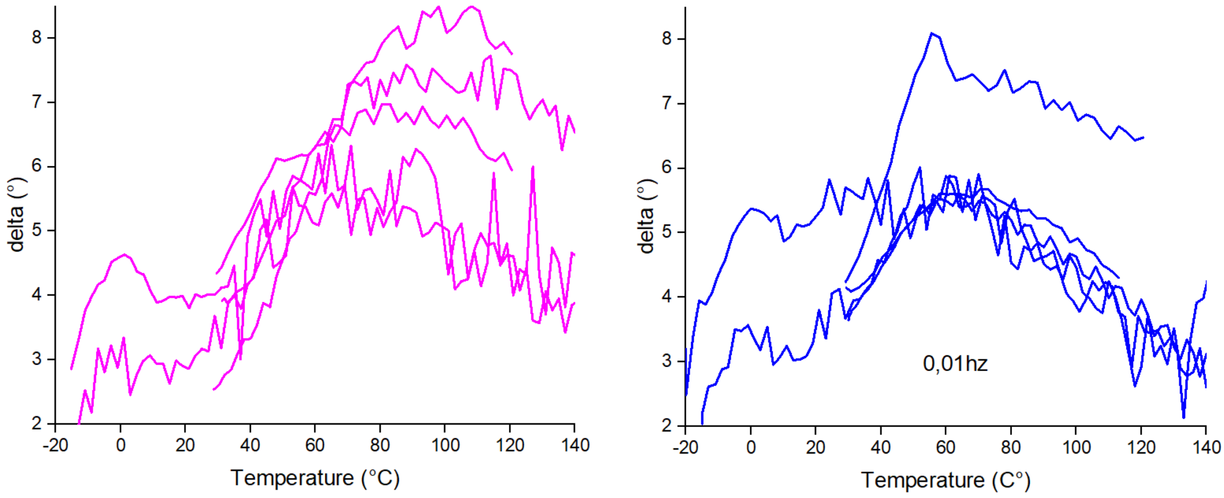

Figure 5.151: δ as a function of T for (a) P_{31} and (b) P_{61} measured at low frequencies - see also tests conditions ④ and ⑤

On figure 5.151, the range 40°C-60°C is very important because, despite their scattering, all the curves overlap in this zone and several curves on both graphs display a moreless important peak at 60°C, with a decreasing intensity of the signal afterwards. The significant discrepancy of some samples in the behaviour of tgδ have been highlighted with arrows at figure 5.152. We think that they come from the manufacturing uncontrolled variations. We have named them "out-of-average" curves and the other ones "average" curves. We draw also attention to the quantity used in the graphs, tgδ or δ.

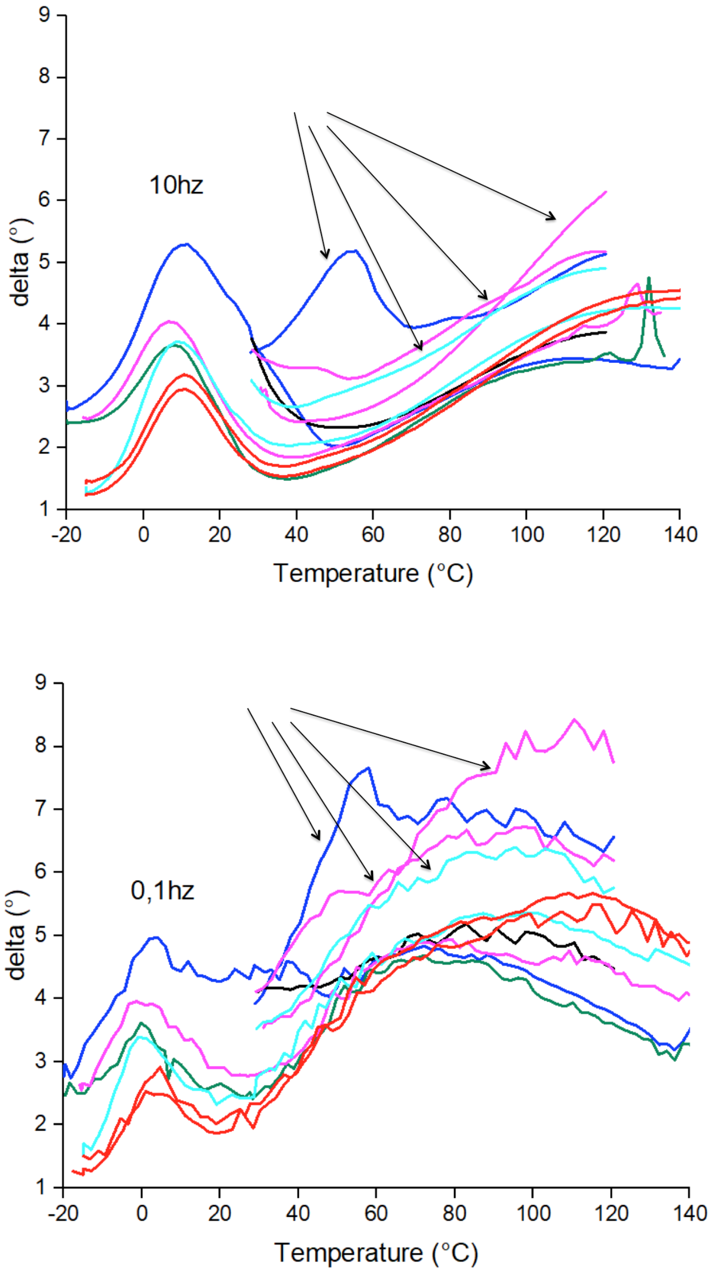

Figure 5.152: δ as a function of T for P_{11} to P_{61} measured at (a) 10hz and (b) 0.1hz; the arrow indicate the samples behaving in a quite different way - see also tests conditions ④ and ⑤

The SAXS and WAXS patterns have also been recorded, in order to obtain the long period as well as check the type of crystalline phase. Figure 5.149(b) displays the characteristic structure of the monoclinic α-phase. Compared to the figure 5.149(a) for P_{11}, it shows a narrowing of the same peaks. All the results related to the microstructure have been gathered at table 5.22 as a support for the discussion, as they have already been commented in chapters 3 and 4.

Table 5.22: Characteristics of microstructure of P_{11} to P_{61} annealed 3 days at 135°C (ZN) and 140°C (MET); * values coming from P_{51} considered as similar to P_{61}. The values for n_{iso} have been computed in chapter 3

Product	ΔH J/g	χ_c	low-T_m	L_p nm	ρ	l_c nm	l_a nm	n_{iso}	catalyst
P_{11}	111.8	0.54	0.36	19.45	0.90	9.84	9.61	190	ZN
P_{21}	113.8	0.55	0.39	18.25	0.90	9.43	8.82		ZN
P_{31}	111.8	0.54	0.36	18.41	0.90	9.27	9.14	164	ZN
P_{41}	107.6	0.52	0.37	18.41	0.90	8.94	9.47		ZN
P_{51}	105.6	0.51	0.35	17.04	0.90	8.11	8.93	178	MET
P_{61}	97.3	0.47	0.34	17.04	0.89	7.48	9.56	178*	MET

5.4 Influence of molecular architecture on viscoelastic relaxations

In this section, we will first compare all the products together, then within each catalysis type and between catalysis technologies.

5.4.1 Comparison of all DMTA spectra

Figure 5.153 shows (a) the curves of tgδ as a function of T measured under ramp temperature for P_{11} to P_{51} between -130°C and 145°C and the curves of δ - rather than tgδ - as a function of T for all the products, measured at (b) 10hz and (c) 0.1hz during isothermal tests.

Figures 5.153(b) and (c) are the same than figure 5.152(b) and (c) but we have removed the samples behaving very differently for the easiness of the analysis.

As of now, we have selected the samples the most relevant to illustrate the results. We will name them "average samples" whereas we will name the other ones displaying a different behaviour "out of average"(essentially, those indicated by the arrows on the figure 5.151).

At the left hand side of the glass transition (figure 5.153(a)), the evolution of the curves is similar for the ZN products P_{11} to P_{41} whereas the shape of MET P_{51} is quite different, indicating different types of molecular movements and amorphous phases between these two kinds of products [7], [36], [87]. At 10hz, T_g is approximately the same for all the products, around 10°C. It shifts slightly as expected to lower temperatures when the frequency decreases (figure 5.153(b) and (c))[16], [71].

At the right hand side of the glass transition and for increasing temperatures, the two spectra measured at 10hz (figure 5.153(a) and (b)) display the same behaviour, with an overlapping of all the curves between around 50°C and 90°C. The overlapping of the α-relaxation on the β-relaxation due to the large broadening of the former is very visible at low frequency for P_{51}[71].

Beyond 90°C, the curves start to differentiate and reach a maximum at different temperatures comprised between 110°C and 140°C. Notwithstanding the different kinds of relaxation behind the various peaks, the curves reach their maximum at decreasing temperatures for P_{11} to P_{61}, with identical temperatures for P_{51} and P_{61}. As expected, the curves shape changes with the frequency and several peaks appear, located f.i. at 60°C-70°C, 80°C-90°C and 110°C-120°C.

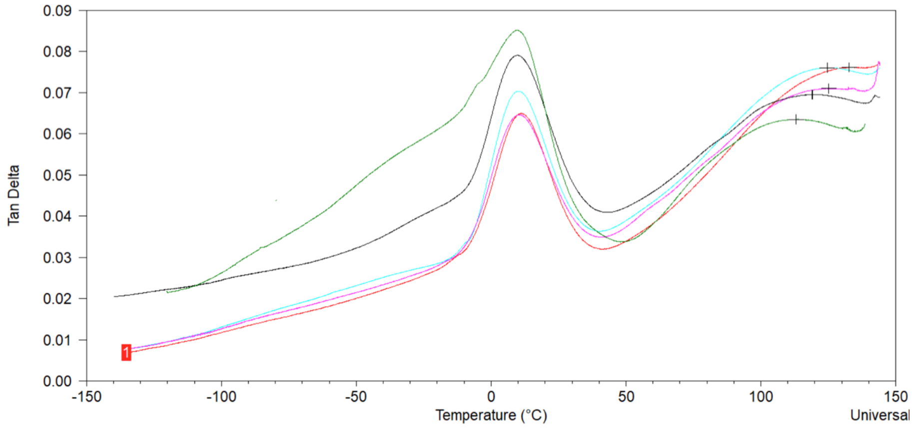

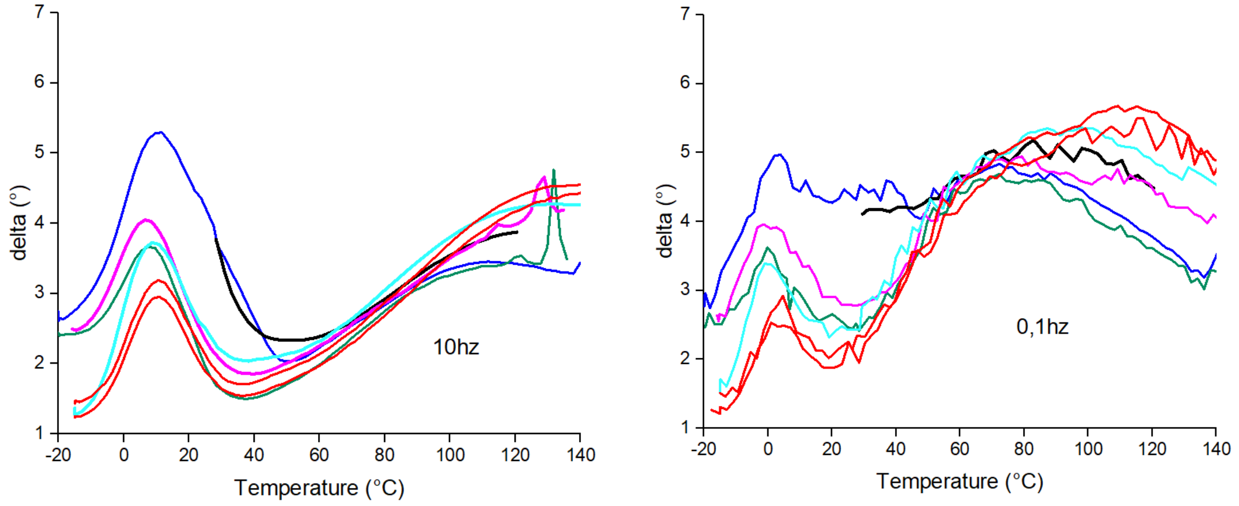

Figure 5.153: (a) tgδ as a function of T for P_{11} to P_{51} measured between -130°C and 145°C - see conditions ③; δ as a function of T for P_{11} to P_{61} measured at (b) 10hz and (c) 0.1hz - see conditions ④ and ⑤ (take care of the different Y-axis for (a) and (b) - (c))

5.4.2 Separate comparison of ZN and MET DMTA spectra

Figure 5.154 compares the different products respectively inside (a) ZN (P_{11} to P_{41}) and (b) MET (P_{51} and P_{61}) catalysis technologies at 0.1hz.

The comparison of ZN products (figure 5.154(a)) reveals after the glass transition zone that the converging point of all the curves remains located around 50°C. P_{11} and P_{21} start to split from P_{31} and P_{41} around 80°C. P_{41} displays a quite flat broadening.

Looking at MET products, and disregarding the out-of-average curves, it can be seen that, as of 50°C, P_{51} and P_{61} are quite similar. The out-of-average curve shows a significant peak around 55°C, at the same temperature than the connection of all the other curves.

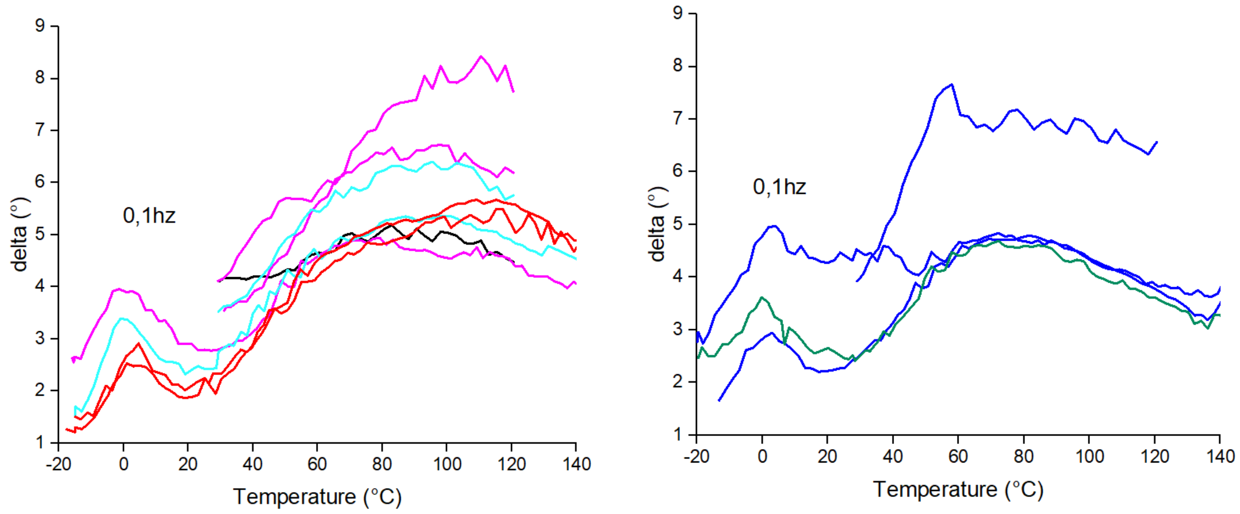

Figure 5.154: Comparison of the curves (temperature, δ) for (a) ZN P_{11} to P_{41} and (b) MET P_{51} to P_{61} products measured at 0.1hz - see conditions ⑧ and ⑨

5.4.3 Comparison of ZN with MET DMTA spectra

We can now compare P_{31} to P_{61}, looking at figure 5.155, where the most representative curves have been drawn at three different frequencies. We observe that (see also table 5.23)

1. both products behave in a quite similar manner, with large variation in the value of the loss factor, δ, and with a large broadening of the α-transition just after the glass transition in both cases (see for example

figure 5.155(c) with the blue and pink curves located between -20°C and 25°C)

2. for what concerns the average (A.) curves, the range of temperature where δ overlaps seems to shift to lower temperatures when the frequency decreases
3. for what concerns the out-of-average (O.A) curves, this is the reverse trend, as it seems to shift to higher temperatures when the frequency decreases.

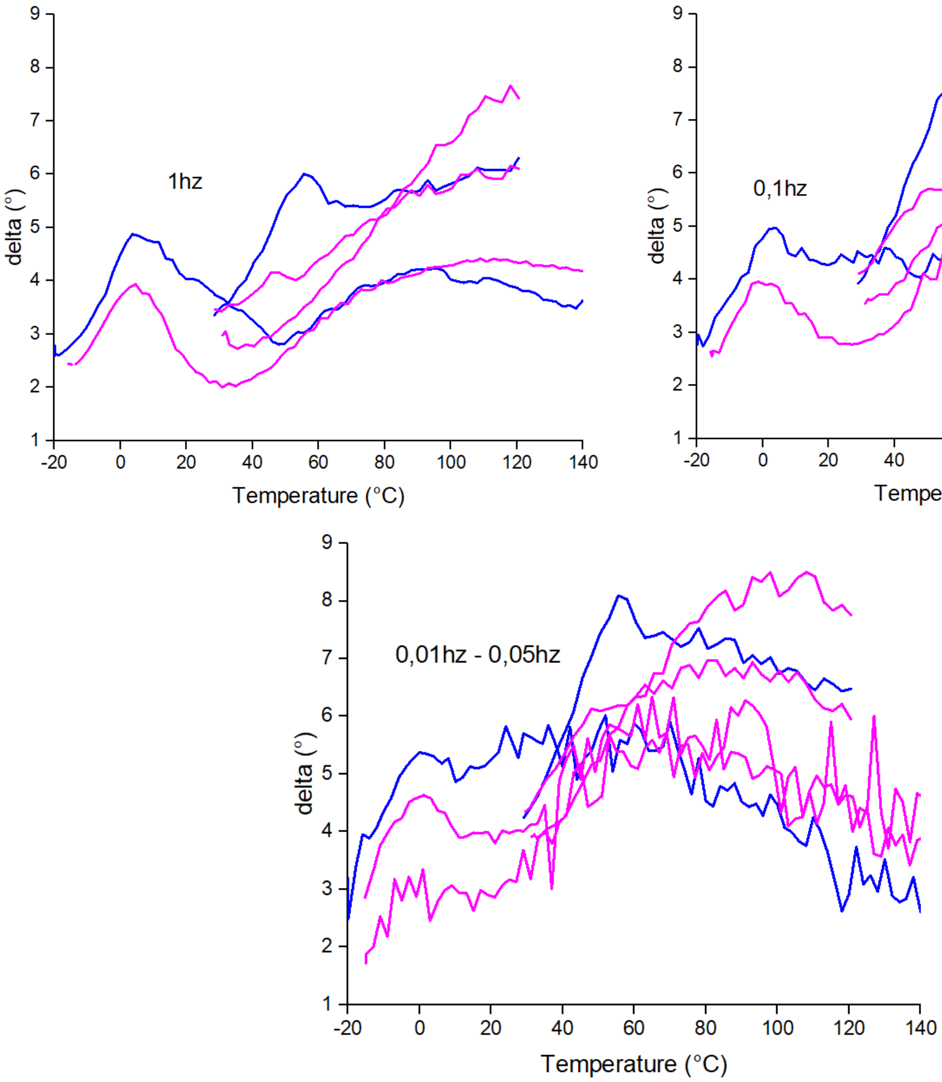

Figure 5.155: Comparison of the ZN-MET (temperature, δ) curves: P_{31} and P_{61} measured (a) 1hz, (b) 0.1hz and (c) 0.01hz - see conditions ④ and ⑤

We have summarised these findings at table 5.23.

Table 5.23: Ranges of temperature where the average (A.) and out-of-average (O.A.) δ curves overlap

Type A/O.A	freq hz	ΔT_1 °C	ΔT_2 °C	freq hz	ΔT_1 °C	ΔT_2 °C	freq hz	ΔT_1 °C	ΔT_2 °C
A	1	50-95		0.1	50 - 85		0.01	45-50 to 80	
O.A	1		80-120	0.1		80-120	0.01		90-110

This means that the average curves overlap in the range of the RAF/condis glass transition and the out-of-average curves overlap in the range of transformation of the mesophase to α-crystals. This means also that, for the average curves, the difference between ZN and MET should be related to the mesophase and that for the out-of-average curves, they are related to the RAF/condis phase[37]. These trends highlight the presence of various dependencies of the different mechanisms to the frequency i.e. different kinetics of the RAF glass transition or of the mesophase-to-α-transformation.

5.5 Activation energies of α viscoelastic relaxation

In this section, we present the results obtained for the activation energy calculated on the viscoelastic spectra of three products, two ZN, P_{11} and P_{31}, and one MET P_{61}, with the method proposed by Kessner et al [105] to build the master curve.

5.5.1 Implementation of mathematical procedure

As the mathematical procedure is somewhat cumbersome, we will now illustrate on P_{11} its main steps leading to graphs $E_a = E_a(\delta)$ similar to figure 5.146 (see table 5.20 for experimental conditions). When there is only one "pure" mechanism, i.e. that do not overlap, $E_a = E_a(\delta)$ is constant, meaning that the activation energy is independent of δ in that range of temperatures (see [71] and also introduction).

As said, this approach is severe, being very sensitive to small differences and matches our difficulty to, first, separate the various components of the relaxation and, second, identify how many components are present. Given the type of data dealt with in this study, we had also to make several hypothesis and impose some constraints.

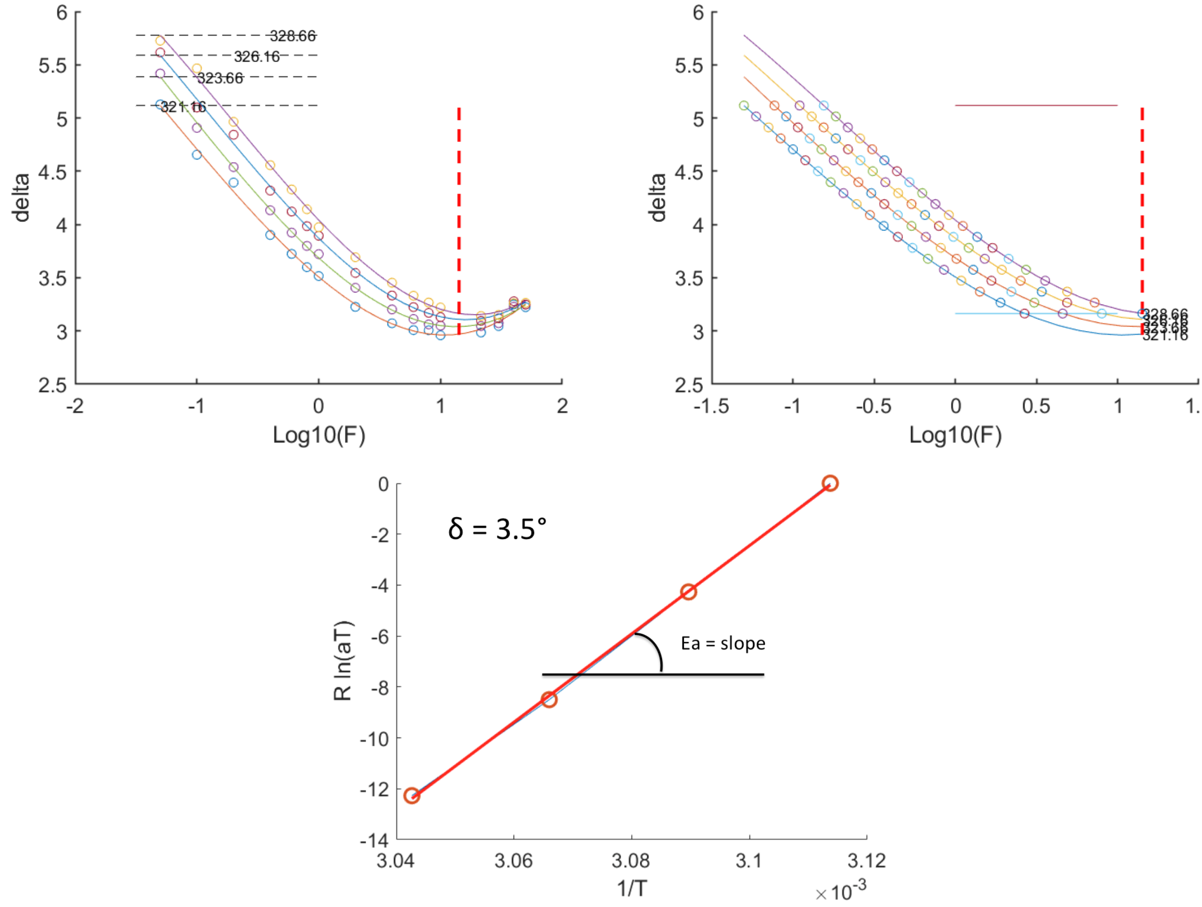

Figure 5.156: : (a) Four curves $\delta = \delta(log f)$ corresponding to four successive temperatures are selected and fitted with a polynomial order 4^{th} within the experimental frequency range; the reference temperature is at the left; (b) the Y-axis δ is divided on a series of equal segments (20 in this example) and for each segment, the shift factor is calculated (c) the slope of the shift factor a_T as a function of $1/T$ is then obtained for each of the 20 values of δ; $\delta = 3.5°$ in this example

---

[37] when an overlap is observed obviously, depending on the quality of the film manufacturing.

Regarding the *Hypothesis*:

1. the curve $\delta = \delta(log f)$ is modelled with a polynomial (2^d to 4^{th} order). Depending on the test conditions (mainly the range and number of selected frequencies), it has to be adapted
2. the range of frequencies and of temperatures can vary depending on the product considered, meaning that the transition can be restricted to a narrower or allowed to a broader range of temperatures in a certain range of δ
3. due to the moderate quality of the data, a good equilibrium between the polynomial order and the temperature range has to be obtained, leading to calculate shift factor on three or four consecutive temperatures ($4°C < \Delta T < 7.5°C$).

Regarding the *Constraints*:

1. the reference temperature is always the lowest, due to the Matlab® program used - see figure 5.156(a) where 4 temperatures have been selected for the time-temperature superposition and a polynomial order $4th$ has been used; the circles are experimental points and the reference (lowest) temperature is at the left of the graph
2. no extrapolations of δ are done on the $\delta = \delta(log f)$ curves - see figure 5.156(b) where the modelled curves are used within the frequency range and the circles are the calculated values
3. the correlation coefficient r^2 of the regression curve has to be $r^2 > 0.989$ for the calculation of the activation energy E_a; E_a is the slope of the $a_T = a_T(1/T)$ curve according to equation (5.80) - see figure 5.156(c) where each circle corresponds to the value of the shift factor multiplied by R, the constant of perfect gas, at the selected temperature.

In order to extract the relevant values of the activation energy and identify in which temperature range it is constant i.e. it becomes independent on δ, we came to and followed some *recommendations* after the completion of the sensitivity analysis performed in the frame of the hypothesis mentioned above. We list the most important ones hereunder (more information is available in the supporting information):

1. the range of δ considered should be larger than 0.5; this value could appear quite small but is adapted to the solid state where the overall range of δ is narrow compared to the molten one
2. the activation energy is considered as constant when $\Delta E_a < 5kJ/mol$
3. in case several levels of activation energy are found corresponding to several ranges of temperature, (almost) no overlap of the temperature ranges should be accepted.

The result obtained on P_{11} is presented at figure 5.157 where fig 5.157(a) is the result of the calculation carried out in this example with an activation energy of 122kJ/mol, fig 5.157(b) and (c) display the original tgδ experimental curves respectively as a function of temperature for the frequency range considered (0.05hz-50hz) and of the logarithm of the frequency for the temperature range considered (48°C-53°C).

Figure 5.156(a) and fig 5.157(c) are identical except that their Y-axis is respectively δ and tgδ. For the clarity of the reading, we have added some curves (dotted lines) corresponding to adjacent temperatures to make the relaxation appear. Let us also highlight the shape of the curves on figure 5.157(b) that resemble the curves of P_{31} and P_{61} already commented at section 5.3.1 and 5.3.2 and display a peak around 65°C.

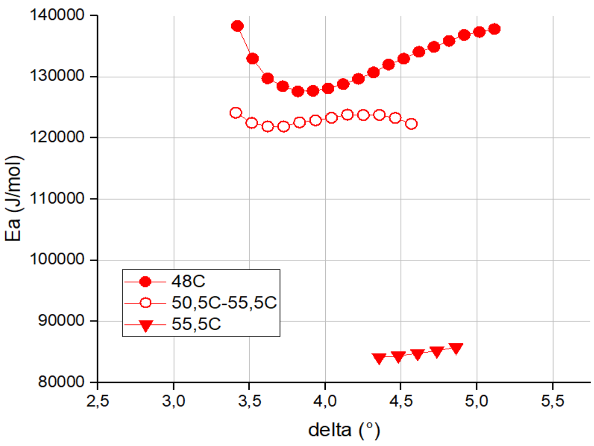

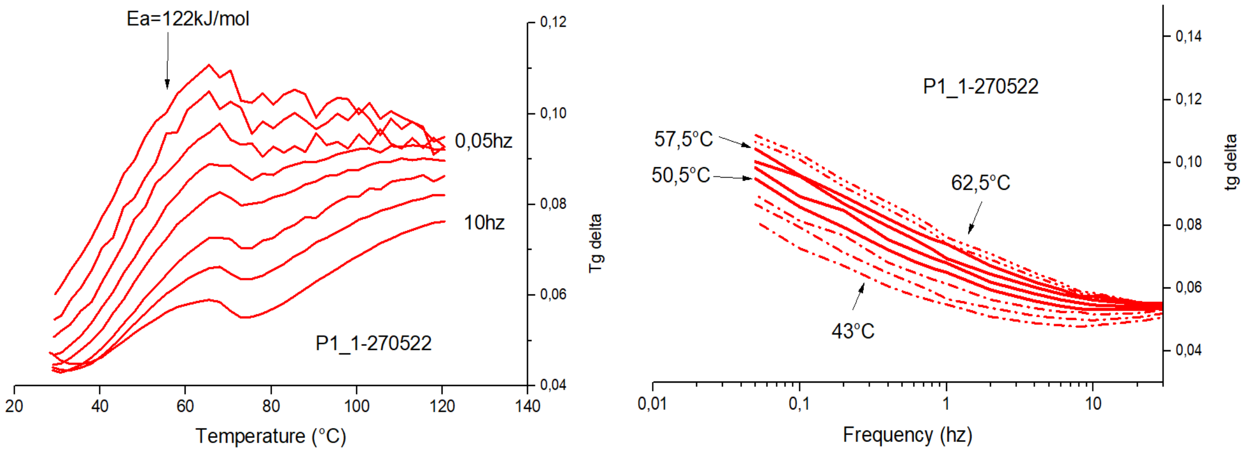

Figure 5.157: P_{11}: (a) for the curve at 122kJ/mol (empty circles), $E_a = E_a(\delta)$ is moreless constant on an interval ranging from around 3.2° to 4.6°; (b) tgδ as a function of temperature in a range of frequencies and (c) $tg\delta = tg\delta(log f)$ in the temperature range where the relaxation is identified - see test conditions ⑤

5.5.2 Activation energies of P_{11}, P_{31} and P_{61}

The graphs of figure 5.158 present the main results for P_{31}: (a) the values of E_a obtained for one specimen which displays two levels at 80kJ/mol and 100kJ/mol, (b) $\delta = \delta(T)$ curves measured at 0.05hz on two different specimens that display, each, one level of activation energy, (c) $\delta = \delta(T)$ curve for the sample at 100kJ/mol for a range of frequencies. It can be seen from fig 5.158(b) that the largest value of E_a corresponds to the curve with a very flat peak starting around 60°C. The $\delta = \delta(T)$ curves of this latter are very similar to the ones shown for P_{11} and P_{61}.

The graphs of figure 5.159 present the main results for P_{61}: (a) the values of E_a obtained for one specimen which displays two levels at 70kJ/mol and 200kJ/mol, (b) $\delta = \delta(T)$ curves measured between 0.05hz and 10hz for this specimen where the temperature ranges corresponding to the relaxations have been identified, (c) and (d) are the corresponding $\delta = \delta(log f)$ presented in the two ranges of the two relaxations, the dotted curves surround those affected by relaxation. It can be seen from fig 5.159(b) that this sample exhibit two relaxations, and that the curve peak is located around 55°C.

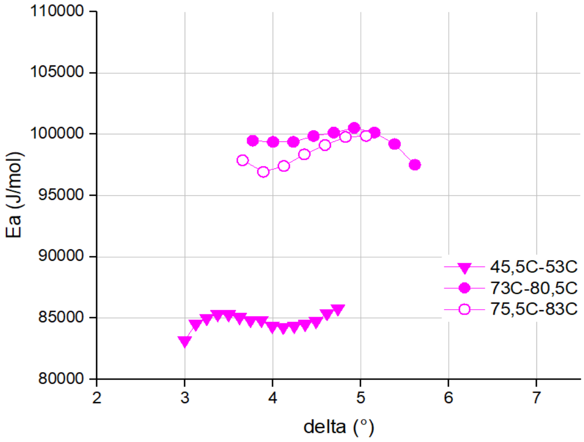

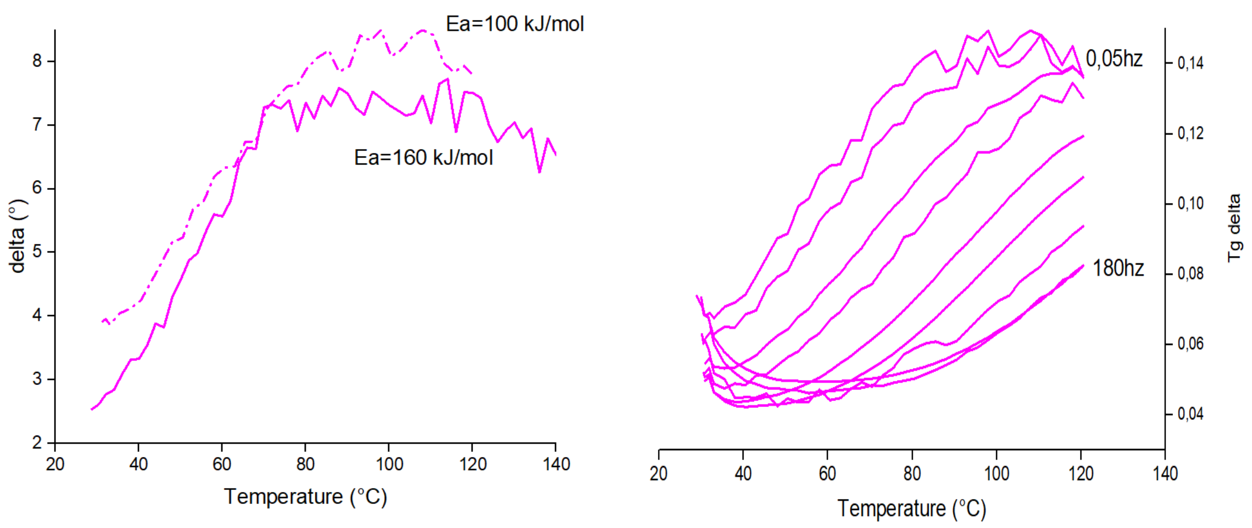

Figure 5.158: P_{31}: (a) values of E_a as a function of δ; (b) two $\delta = \delta(T)$ curves measured at 0.05hz on two different samples; (c) $tg\delta = tg\delta(T)$ curves measured on the whole spectrum of frequencies for $E_a = 100kJ/mol$ - see test conditions ⑤

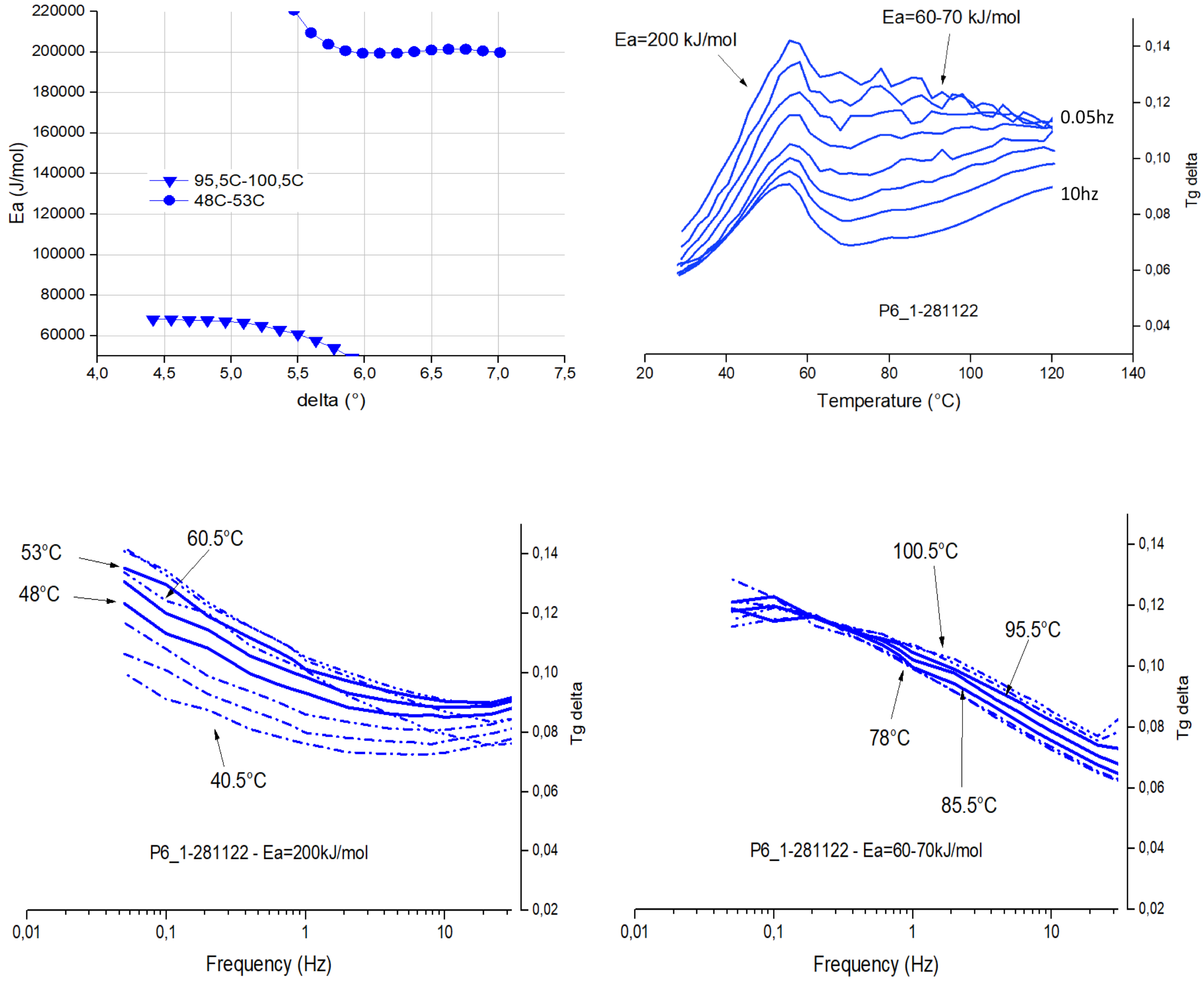

Figure 5.159: P_{61}: (a) values of E_a as a function of δ; (b) $tg\delta = tg\delta(T)$ curves measured between 0.05hz and 10hz; (c) and (d) $tg\delta = tg\delta(log f)$ for the two relaxations of each sample; the dotted curves surround those affected by relaxation - see test conditions ⑤

Table 5.24 displays a synthesis of all the activation levels obtained for the three products. Two or three levels of activation energy have been identified (column "E_a") and the corresponding temperature range is indicated (column "T"). One specimen could supply one or more than one level.

The upper values of the activation energy that we name E_a^{max} are in the range $150kJ/mol < E_a^{max} < 200kJ/mol$ and are consistent with what can be found in the literature [71], [21], [69] (see also Introduction and chapter 2). It is less clear for the lower values. At this stage, a few comments can be elaborated, keeping in mind that these values come from samples that could have undergo different uncontrolled thermo-mechanical history during their processing:

1. P_{61} shows the largest value of the activation energy
2. the levels for E_a^{max} correspond to the lowest temperature ranges and to shapes of (T, tgδ) curves with a very visible peak located in the range 55°C-65°C
3. P_{31} is the only one to present three levels of activation energy E_a though we cannot exclude that such a phenomenon could occur for the two other products
4. P_{61} displays for its two E_a levels well discriminated ranges of temperatures; for P_{11}, these are more close to each other and for P_{31}, they are partially overlapping, indicating mechanisms intimately intertwined.

5.5.3 Comparison of activation energies obtained from quasi-static and dynamic tests

In this section, we will compare the activation energies obtained from the quasi-static tensile tests and from the dynamic mechanical and thermal analysis tests. We compare thus the yield process occurring in the upper limit of the small deformations range with viscoelastic relaxations occurring at the lower limit of that domain.

In order to proceed to such a comparison, we should keep in mind that, as long as we remain in the range of small deformation, it is possible to express a quantity measured with one type of test, for example the elastic or Young modulus E_y of quasi-static tensile tests, with another quantity measured by another type of test, for example the storage modulus, $E'(f)$, of the viscoelastic test [169], [102]. Each measuring technique has its own limits, in terms of strain rate and characteristic time, and using various experimental techniques allow to considerably enhance the range of frequencies or strain rates investigated. This is illustrated in our case for the quasi-static (QS) and the DMTA tests at figure 5.160.

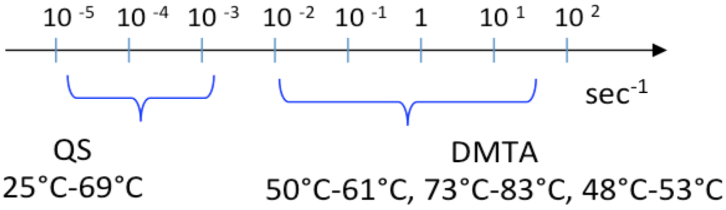

Figure 5.160: Summary of the characteristic times associated to quasi-static (QS) and dynamic (DMTA) tests carried out in this research, together with the temperature ranges where the activation energies were calculated

Reminding the results obtained in chapter 4 (namely table 4.15), we can now proceed to the comparison between the results obtained separately for the activation energies with both kinds of experiments. They are presented at table 5.24.

We see that there is a good agreement between the activation energy levels obtained in the linear viscoelastic range and at yield. We see also that P_{31} shows three levels in DMTA and two mechanisms in quasi-static tests. P_{11} and P_{61} on their side display two levels in DMTA and one mechanism in QS.

Table 5.24: Summary of the activation energies obtained from the yield stress evolution (QS) and the visco-elastic loss factor (DMTA); similar levels are assigned to their colour, the other ones are in black; one sample can provide one or several values, depending on the case; (*)activated volume obtained for measures at 69°C for the second mechanism

Product	Quasi-static(QS)				Dynamic(DMTA)			Cat.
	$\Delta\dot{\epsilon}$ sec^{-1}	ΔT $°C$	E_a $kJ/mole$	V_0 nm^3	$freq$ sec^{-1}	ΔT $°C$	E_a $kJ/mole$	
P_{11}	1.67 10^{-5}- 1.67 10^{-3}	25-69	**128**	3.65	1 10^{-2}- 1 10^{1}	50-61 60-87	**122-125** 65-95	ZN
P_{31}	1.67 10^{-5}- 1.67 10^{-3}	25-69 (69)*	**101** /	2.71 (9.5)*	1 10^{-2}- 1 10^{1}	40-54 45-63 73-83	155-165 75-85 **90-100**	ZN
P_{61}	1.67 10^{-5}- 1.67 10^{-3}	25-69	**183**	5.03	1 10^{-2}- 1 10^{1}	48-53 65.5-105.5	**200** 60-72	MET

5.6 Discussion

In this discussion, we will first examine the general shape of the curves, in order to define how many peaks are observed, and how far they are or not overlapping. We will make only general comments on the link with the microstructure of the materials.

We will *first* look at the relaxations in quenched, quenched and annealed and undercooled P_1.

Our systems have been obtained by following the traditional method of comparison of quenched, quenched and annealed and undercooled samples (see table 5.21). We assume that the solid microstructure of the quenched state P_{11} is a multi-phasic system composed as described above.

We assume also that a small portion of mesophase remains in the system after the treatment at 130°C (P_{12}) together with a larger amount of RAF and/or condis-crystals, and in the same way, in the undercooled product (P_{13}).

We think that our materials undergo four transitions, though maybe not in the exact ranges mentioned by the literature. This is what we would like to demonstrate below, taking benefit of the four steps of microstructure transformation upon heating described in our literature review.

In order to detect more easily the transitions in our curves, we use the derivate of the heat flow and identify local extrema [chapter 3] that correspond to inflexion points on the heat curve. The analysis of DSC thermograms and their derivates such as those of figure 5.148 on P_{12} or figure 5.161 on P_{11} and P_{13} displays for each product clear events as temperature increases. Four zones are visible, respectively comprised between 51°C-56°C to 83°C, 83°C to 102°C, 102°C to 126°C -134°C and the last part of the trace to the well of the melting peak at 165.5-166°C to 169°C. Associated with the shoulder present in DSC, the 4-peaks WAXS pattern and the DMTA, we assume the presence of quite small, though non null mesophase

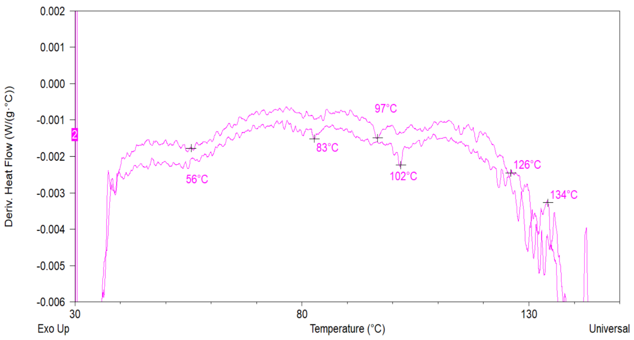

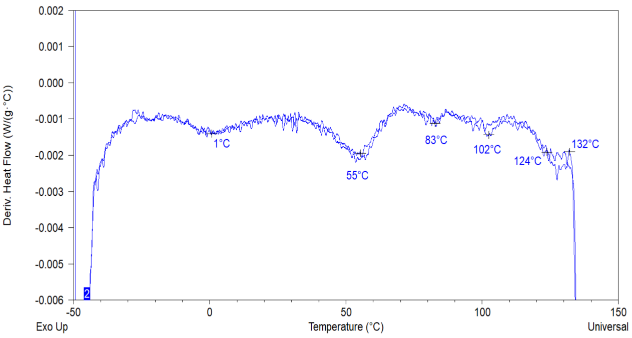

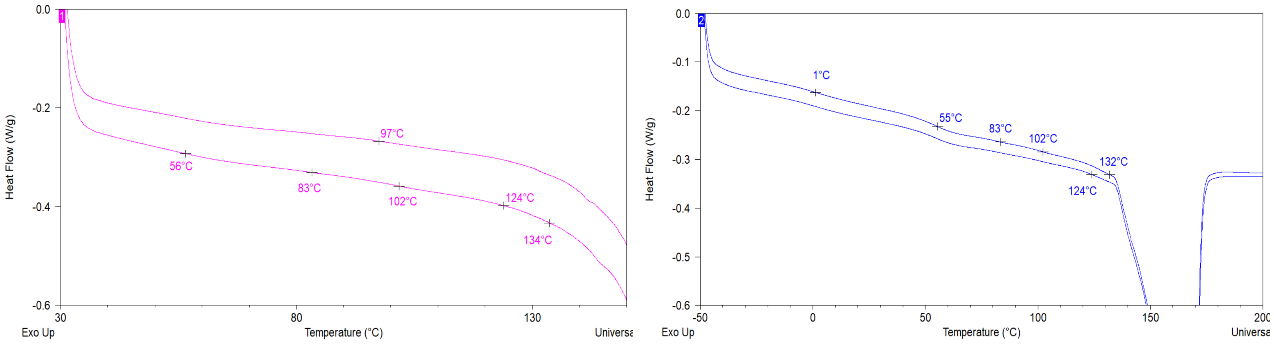

Figure 5.161: From top to bottom and left to right: (a) derivates of DSC traces of P_{11} and P_{13} aged 48 days at ambient temperature; numbers indicated the local minima (remarkable points - (see chapter 3) for more information on the method); (b) zoom of related heat flow; local extrema have been reproduced on the heat flow

At table 5.25, we compare DSC and DMTA curves and their local extrema[38]. We think that, in this case, we compare identical types of phenomena, i.e. the moment at which the transition is said to occur. The intensities I_T of these events can also be calculated via the area under the peak.

Table 5.25: Comparison of main zones identified for the α relaxation in DSC and DMTA; T_β is the glass transition temperature of the MAF measured respectively at 1hz for the as-received samples and 10hz for the annealed ones; $I_{T\beta}$ is its intensity evaluated thanks to the area under the peak

Product	$T^{\alpha}_{DSC}(^{\circ}C)$	$T^{\alpha}_{DMTA}(^{\circ}C)$	$T^{\circ}_{\beta}C)$	$I_{T\beta}$(min)
as received		1hz	1hz	1hz
P_{11}	56, 83, 102, 124-134	57, 86, 102, 120	0.7	0.27
P_{12}	51, 83, 102, 126-131	58, 69, 101, 120	-0.9	0.36
P_{13}	55, 83, 102, 126-132	57, 70, 101, 120	-0.5	0.38
annealed 4 days at 140 $^{\circ}C$		10hz	10hz	10hz
P_{11}	52-54, 86, 101, 137-139	70, 130	11.8	0.38
P_{13}	47-54, 93-97, 139	60, $\simeq$ 130	11.6	0.3

For the as-received samples, we understand that there could be four transitions in the α-relaxation, with two mechanisms triggered in the range of temperature usually ascribed in the literature to the glass transition of the RAF/condis crystals. This latter is quite narrow in the case of P_{12} to P_{13}. For the annealed samples, we understand that the evolution of the glass transition translates the decreased mobility of the amorphous chains between P_{11} and P_{13}; the evolution of T^{α}_{DSC} and $T^{\alpha 4}_{DMTA}$ towards higher temperatures with the annealing is compatible with more perfect and thicker lamellae; the four transitions are visible in DSC but not in DMTA probably because of the too high frequency that promotes the elastic behaviour and makes the temperatures shift to the right.

Secondly, we have analysed the influence of the molecular architecture on the α-relaxation and shown that the comparison of T^{α}_{DSC}, $T^{\beta}_{DMTA}(\equiv T_\beta)$ with $T^{\alpha}_{DMTA}(\equiv T_\alpha)$ for the various molecular structures reveal the same type of conclusion than at the previous section.

Thirdly, we will confirme the presence of more than two transitions in the α-relaxation of P_{11} annealed 3 days at 135°C.

Before going to the analysis of the influence of the molecular structure, we would like to comment on the issue related to the number of transitions/relaxations. In DSC, the literature, as widely explained in the introduction, delineates generally three transitions, if we do not take into account the melting of the primary crystals. This is, to our understanding, very much linked to the way the base line is calculated in the thermograms. However, different schemes exist in the literature and it is unclear to us how the endo- and exotherms are identified. The influence of the frequency and of the thermo-mechanical history induce variations. We think that there are,

---

[38] Local extrema have different meanings in DSC and DMTA: the minima read on the derivate of the heat flow correspond to inflexion points on the curve itself and the maxima read on the tgδ refer to the temperature at which the transition occurs.

as demonstrated by the presence of two peaks in the range 50°C-80°C, at least three mechanisms of relaxation though we cannot assign them exactly

We have clues of this complex structure by looking at two different measurements carried out on P_{11} annealed in standard conditions (3 days at 135°C), and measured with a Mettler equipment at 0.1hz , as seen at 5.162 below. It displays also the temperature derivative of a separate DSC trace measured under normal conditions (10°C/min) that has been added on the same graph in order to compare DSC and DMTA spectra.

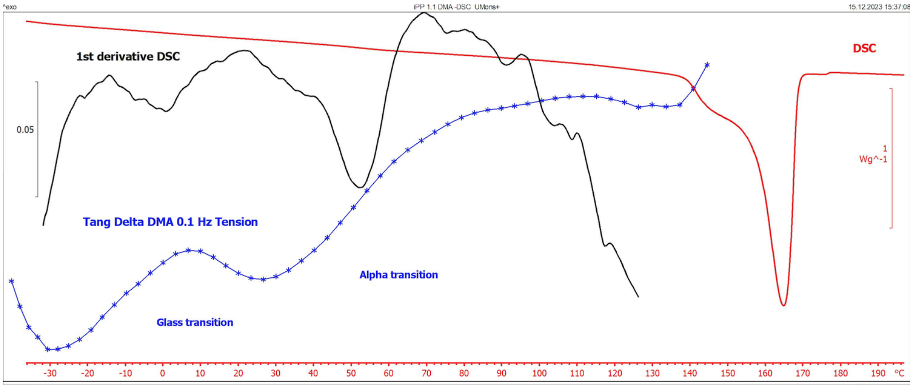

Figure 5.162: P_{11} measured at 0.1hz with a ramp temperature of 3°C per min complemented with the derivative of a separate DSC trace

Three transitions stand out for the α-relaxation, at respectively 55°C, 85°C and 110°C. The T_g is at 5°C.

We assume that we have four processes at stake that we would assign to: the first one to the RAF and/or condis glass transition via a nucleation/diffusion process of dislocations leading to coarse and heterogeneous slip of the crystals; the third process around 100°C to the solid/solid transformation of the mesophase into alpha-monoclinic crystals via a nucleation/diffusion process of dislocations leading to fine slip and tilting of the chains (translation and rotation); and the fourth one to the perfection and thickening of the lamellae via a mechanism to be determined.

Then, the question remains about the second transition, and we wonder if it could be assigned either to the subsidiary crystals, i.e. radial crystalline entities which show small size and/or low degree of perfection, constituted from the mesophase transformation and formed by insertion between the primary lamellae; or to the glass transition of a second RAF close to them. From those two options, the following considerations can be drawn:

1. if there is a broad distribution of crystalline lamellae f.i. centred around two average thicknesses l_c, and especially a difference between those coming from the nodules and the ones coming from the primary radial lamellae, then, there should be for those two thicknesses l_c two different migration rate of the defects to accommodate one macroscopic frequency. At a same frequency, the only way to increase the diffusion of defects/dislocations is to increase the temperature

2. if there is one average crystalline lamellae thickness l_c but two different types of RAF, one at the interface of primary lamellae and at the interface of "nodular" lamellae, their features such as thickness, stiffness or number of defects could be different and therefore the temperature at which mobilities are activated also.

Finally, we will discuss the activation energies of the α viscoelastic relaxation.

As explained at section 5.2.3, the calculation of the activation energies requests to scan the whole (T, $\delta = \delta(f)$) curve at each temperature and to calculate the shift factor on a set of three or four successive temperatures.

In the literature that we have reviewed to analyse the influence of temperature, the vast majority overlooks the issues of peaks overlaps or does not face them. For instance, the structures analysed by Hoyos et al [83] display only one α-relaxation peak, and in the comprehensive study performed by Chang et al [16], there are overlappings between the mechanisms and it is not clear if such an approach of the activation energy can be applied. In our mind, one should first calculate the deconvolution of the peaks at each frequency in order to check the relevance of such an approach but this requests the knowledge of the relaxation peak composition.

The approach taken by Kessner et al [105] has, to our best knowledge, helped us to avoid these pitfalls. Table 5.24 display a remarkable proximity of the energy levels obtained by both techniques in their solicitation domain and, consequently, the same ranking.

More particularly:

1. one sample can undergo two different processes, as is illustrated at figure 5.159
2. in all the cases where $E_a > 100kJ/mol$, the first peak around 55°C-65°C is very much pronounced, whatever the frequency and the other peaks disappear
3. P_{31} is the only one to show a second mechanism in quasi-static tests and the only one displaying three levels for its activation energy corresponding to three mechanisms; the temperature ranges of the two first ones are partially overlapping, indicating that the range of temperature at which the process is triggered is really narrow
4. the range of T_α where the various E_a are found is comprised between 40°C and 87°C for P_{11} and P_{31}, and between 65.5-105.5°C P_{61}. We think that they can be ascribed to the two first relaxations linked to either the RAF/condis glass transition or to the presence of the two different thicknesses of primary and secondary crystal population; in both cases to the heterogeneous slip, i.e. to the dislocations active close to the amorphous phase
5. whithin a same product, the lower the temperature T_α, the higher the activation energy E_a. Let us call E_a^{max} the maximal value of the activation energy corresponding to the lowest T_α.

Table 5.26 is a summary displaying two parts: on the left, the influence of the amorphous phase and of the isotactic length and on the right, the influence of the crystalline phase. Take care that the ranking of the products is not the same in each part. The activation energies are the E_a^{max} for each product.

Table 5.26: Summary of β- and α-relaxations: (*) for β-relaxation, the glass transition and its intensity have been measured at 0.1hz; for α-relaxation, maximal activation energy $E_a^{max}$and related transition temperatures T_α, isotactic length, crystalline and amorphous layer thickness of P_{11}, P_{31}, P_{61}

Product	T_β*	$I_{T\beta}$*	T_α	l_a	n_{iso}	Product	E_a^{max}	l_c	V_0
	$°C$	min	$°C$	nm	$\#C_3H_6$		kJ/mol	nm	nm^3
P_{31}	0	4.5	$40-54$	9.14	164	P_{11}	122-125	9.84	3.65
P_{61}	3.36	3.3	$48-53$	9.56	178	P_{31}	155-165	9.27	/
P_{11}	4.6	3.1	$50-61$	9.61	190	P_{61}	200	7.48	5.03

All in all, it highlights

1. regarding the global amorphous phase, the link between shorter n_{iso}, lower l_a, lower T_α and T_β and higher intensity $I_{T\beta}$ of the glass transition
2. regarding the crystalline phase, a dependence of E_a^{max} to the crystal thickness and to crystallinity, with E_a^{max} increasing when l_c and χ_c decrease
3. the need to understand more in-depth the role played by the various phases in relation with the distribution of defects and the number and distribution of stress transmitters.

Let us compare finally tables 5.24 and 5.26. We see that the highest activation energy in DMTA E_a^{max} corresponds to the same value in QS for P_{11} and P_{61}. This is not the case for P_{31}, where the equivalent activation energy is related to a range of temperature comprised between 73°C and 93°C. We had already observed that this product was the only one to show a second mechanism during the quasi-static tests.

It is of utmost importance to compare together mechanisms of the same type:

1. it seems that the processes at stake for P_{11} and P_{61} are the same and are related to the lower α-transition and to the heterogeneous shear; if this is the case, then the activation volumes can also be compared
2. the process at 100kJ/mol for P_{31} seems to call for another mechanism
3. the question now is to what extent cavitation plays a role in the analysis, since it is known that the plastic instability characteristic of the heterogeneous yield is linked to cavitation [47].

5.7 Conclusion

The purpose of this chapter was to compare the behaviour of isotactic polypropylene at yield and in the viscoelastic region in order to highlight the common underlying mechanisms.

We have analysed two types of structures based on Ziegler-Natta and metallocene catalysis, and carried out two types of dynamic mechanical thermal analysis tests in order to understand the influence of, on the one side, various thermo-mechanical histories on one chemical structure of isotactic polypropylene and, on the other side, of various molecular architectures produced with one thermal history.

By working at low to very low frequencies, we could demonstrate that four relaxations are at work when the thermal histories are varied, the various mechanisms of which having still to be elucidated.

By applying the thermorheological approach of Kessner et al coming from the melt to varying molecular structures, we found evidences of the same. Kessner's approach seemed relevant to us as it has allowed us to identify the narrow regions where relaxations occur while ensuring the comparison of identical phenomena. We could also show that when ZN and MET viscoelastic curves overlap, it can be due to similar relaxation behaviour either of the RAF/condis phase or of the mesophase.

Finally, we have compared the results of our calculations with those obtained in chapter 4. It appears that for the three products analysed under that way, equivalent levels of activation energy were found. The analysis of the temperature range where the corresponding mechanisms are active in both tests has shown that one ZN and one MET undergo the same relaxation, i.e. an heterogeneous slip while the other ZN undergoes another type of heterogeneous slip. These mechanisms are likely not the same ones, which explains why the second ZN is the only one to demonstrate two mechanisms in the tensile tests.

We could also emphasize some general trends among our structures: the global (MAF, RAF) amorphous phase influences not only the temperature at which the glass transition happens but also those associated to the heterogeneous shear of the α-relaxation; the crystalline phase influences the maximal activation energy and related volumes.

The question is to understand what are, besides the general conception about nucleation and propagation of dislocation, the true mechanisms occurring at the interface of the crystals and of the amorphous phase, especially the role of the rigid amorphous fraction, assuming a multiphasic system composed at least of three or four components.

If the RAF close to the possible mesophase or at least close to the MAF is indeed responsible for the two first relaxations and the coarse slip leading to fragmentation, what should be understood is

1. what is its status (frozen or relaxed) according to the domain of time-temperature considered, and how the diffusion kinetics of the conformational defects between the different phases would be able to lead to the fragmentation of the lamellae in mosaïc blocks
2. how far the meso or amorphous domains would be sheared, and interlamellar shear would occur
3. how a microstructure composed of crystalline alpha nodules finding their origin in the mesophase-to alpha transformation would help [135], [20].

If the RAF close to the possible mesophase or at least close to the lamellae surfaces is indeed responsible for the third relaxation, and the fine slip leading to crystal chains tilting, what should be understood is

1. what is its status (frozen or relaxed) according to the domain of time-temperature considered, and how the stress or deformation transfer would help the chain axis tilting
2. how a microstructure composed of crystalline alpha nodules finding their origin in the mesophase-to alpha transformation would help [135], [20].

More generally, two aspects should be further investigated, i.e. the link of, first, the various regio- and stereo-defects with the RAF and the crystalline structure and, second, the RAF with the distribution of crystalline lamellae and the amount of stress transmitters.

In order to concretise these perspectives, spectroscopies and other in-situ methodologies should be implemented, in order to see what is occurring in the material at the considered scales. These measurements should ideally be associated with relevant modelling tools as a compass, without forgetting approaches coming from the community of the confined systems (see for instance the researchs of Napolitano et al such as "Irreversible adsorption of polymer melts and nanoconfinement effects" published in Soft Matter, DOI: 10.1039/d0sm00361a).

5.8 Supporting information

5.8.1 Complement to characterisation methods

In order to remove the samples in a reproducible way, the film was laid on grid paper and its edges secured with adhesive paper. Samples were then cut with a dye cutter into 5 mm-wide strips with enough length so as to obtain an accurate alignment on the device, with an homogeneous distribution of the stress across the whole sample. The length between the clamps was kept between 15 and 20mm. The viscoelastic range revealed the early non linear character of these polymers and resulted in values for the imposed cyclic deformation lower than 0.1%. Due to the type of samples combined with the special testing conditions, the equipment was working very close to its lower limits and, combined with low frequencies, a lot of efforts have been devoted to get acceptable results. Due to the non conditioned laboratory and the big size and inertia of the oven, the samples were conditioned during 30 minutes before starting the test, at all temperatures.

5.8.2 Influence of the molecular architecture on the α-relaxation

Let us compare now T^{α}_{DSC}, $T^{\beta}_{DMTA}(\equiv T_\beta)$ and $T^{\alpha}_{DMTA}(\equiv T_\alpha)$ when the molecular structure varies.

The table 5.27 displays the peaks identified on the six products in a manual way. In this table and for the DMTA results, we have put in bold and in colour the maxima coming from the scans at 0.1hz, 1hz and 10hz. We have added also the shoulders and inflexion points, as well as the global trend (increasing or decreasing, represented by arrows) of the $\delta(T)$ curves.

Table 5.27: Comparison of main zones identified for the α relaxation in 1°) DSC on the heat flow and 2°) in DMTA, on tgδ for T_β and δ for T_α; T_β is the glass transition temperature of the MAF measured respectively at 0.1hz; $I_{T\beta}$ is its intensity evaluated thanks to the area under the peak. Legend and colours: the **maxima** of the curves are in **bold and coloured according to the code applied in section 5.3**; the *shoulders are in italic* and the inflexion points are underlined; the arrow indicate the general trend of the curve. $(^*)T^{\alpha}_{DMTA} \equiv T_\alpha$

Product	$T^{\alpha}_{DSC}(°C)$	$I_{T\beta}$(min)	$T_\beta(°C)$	$T^*_\alpha(°C)$	$T^*_\alpha(°C)$	$T^*_\alpha(°C)$
3 d.@135 $°C$		0.1hz	0.1hz	0.1hz	1hz	10hz
P_{11}	51, 84, 99, 132	3.1	4.6	*60*, *80*, **115**	*75*, *100*, **130**	80, **140**
P_{21}	50, 84, 98, 133	5.15	-0.1	*60*, **100**, ↘	*75*, *80*, **100-120**	80, **130**
P_{31}	48, 83, 98, 134	4.5	0	*60*, **80**, *100*	*75*, *90*, **110**	90, ↗
P_{41}	49, 98, 131	/	/	*60*, **80**, *100*	*80*, *90*, **110**	*100*, **120**
P_{51}	50, 87, 136	3.8	0	**70**, *90*	*70*, **95**, *110*	*80*, **110**
P_{61}	51, 84, 99, 131	3.3	3.36	**70**, *90*	*70*, **95**, *110*	*80*, **110**

5.8.3 The mathematical method for the time-temperature master curve: sensitivity analysis

In the introduction and overall in section 5.5.1, we have explained the main principles to build the master curve according to Kessner approach.

We give here complements on the question of the right balance between the polynomial order of the curve and the number of successive temperatures used to calculate the activation energies. A sensitivity analysis has been applied to various samples, that we explain here, reminding some of the steps already explained in the main text.

5.8.3.1 Hypothesis and constraints

The hypothesis are the following ones:

1. the curve $\delta = \delta(logf)$ is modellised with a polynomial (order between 2 to 4). Depending on the test conditions (mainly the range and number of selected frequencies), it has to be adapted
2. the range of frequencies and of temperatures can vary depending on the product considered, meaning that the transition can be restricted to a narrower or allowed to a broader range of temperatures in a certain range of delta

3. due to the moderate quality of the data, a good equilibrium between the polynomial order and the temperature range has to be obtained

The constraints are the following ones:

1. the correlation coefficient r^2 of the regression curve should be higher than $r^2 > 0.989$ for activation energy (slope) calculation
2. no extrapolations are done on the $\delta = \delta(logf)$ curves
3. the reference temperature is always the lowest.

5.8.3.2 Quality of the $\delta = \delta(logf)$ data curves

Two different types of issues can be raised by the data, one related to resonances of the equipment and one to the variations of the controlling variables such as temperature during the test.

We give examples of both hereunder. Figure 5.163(a) is the $\delta = \delta(logf)$ curve of a P_{11} sample tested in the range of temperature 50.5°C to 58°C and of frequency 0.05hz to 200hz where several resonance can be identified namely around 120hz. The figure 5.163(b) shows the influence on the curve of jumps due to less good control of some equipment signals on the data and (c) shows the same data as a function of temperature between 30 and 50hz.

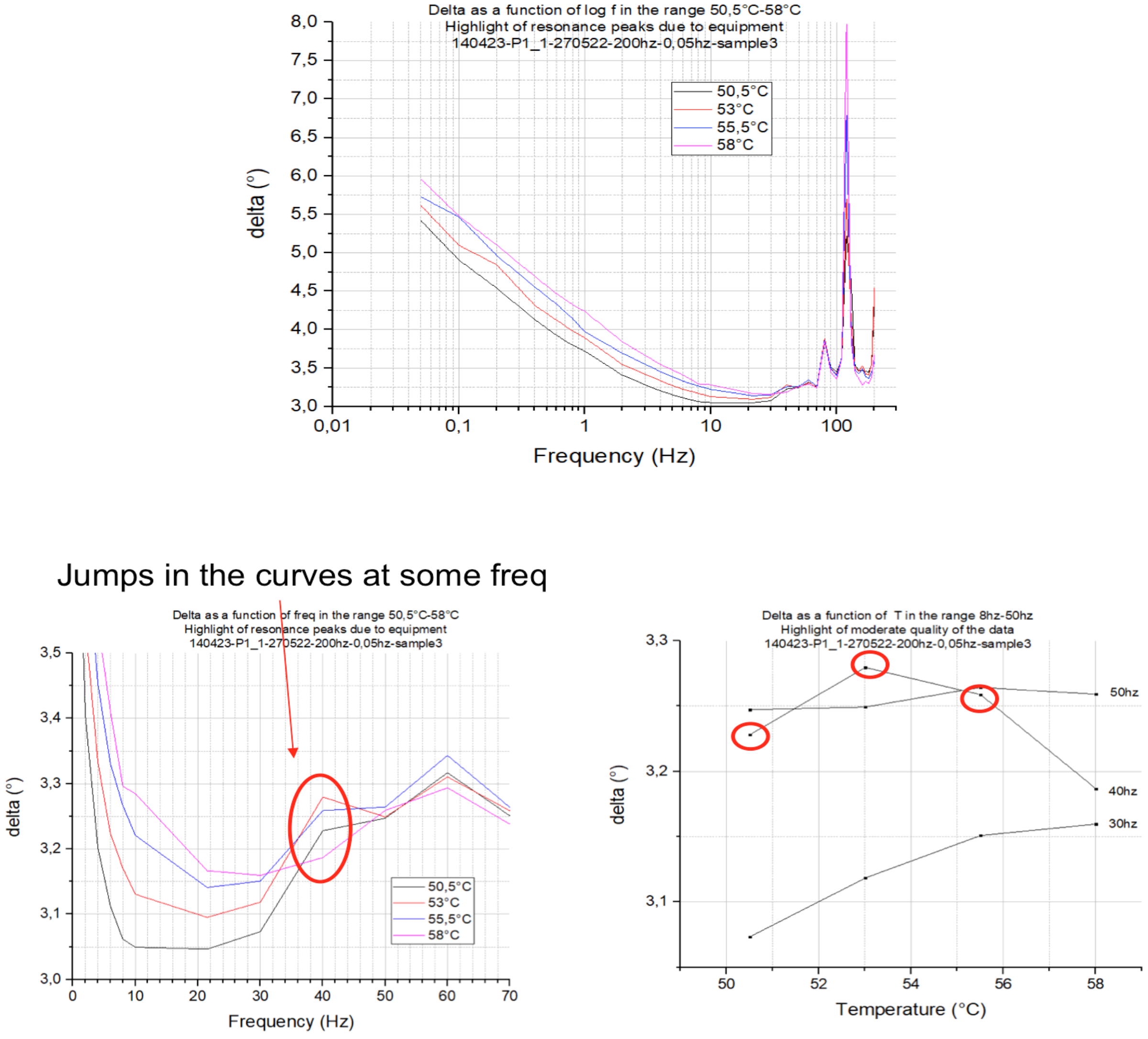

Figure 5.163: Highlight of resonance peaks due to the equipment: (a) whole frequency spectrum, (b) zoom on the range 0.05hz-70hz to show the jumps in the curve $\delta = \delta(logf)$ and (c) jumps in the curve $\delta = \delta(T)$ in the range 30hz to 50hz

5.8.3.3 Influence of the polynomial order

The influence of the polynomial order n on the sum of residues of mean-squares is then analysed, by taking $2 \leq n \leq 4$. It is presented at figures 5.164 and 5.165 according to two representations:

1. a calculation at 2 temperatures (50.5°C and 58°C) on 3 ranges of frequencies: 0.05hz - 50hz (blue squares), 0.05hz - 2hz (red losanges) and 0.05hz - 1hz (yellow triangles) - see figure 5.164
2. a calculation in 2 ranges of frequencies (0.005hz-50hz and 0.05hz-1hz) and at 4 temperatures: 50.5°C, 53°C, 55.5°C and 58°C.

This influence is then analysed by calculating the values of the activation energy E_a as a function of δ. The figure 5.164, figure 5.165 and figure 5.166 below show such a calculation at 43°C and 48°C for the same sample. Figure 5.164 displays the sum of the residues at two temperatures in three ranges of frequencies. It can be seen that n=2 calculated on the largest interval of frequency (0.05hz-50hz) displays also the highest value for the sum, which eliminates this order, unless it is not possible to make in another way. Figure 5.165 shows for four temperatures and in the range 0.05hz-50hz the calculation of the sum of the residues and the modelled corresponding $\delta = \delta(log f)$ curves.

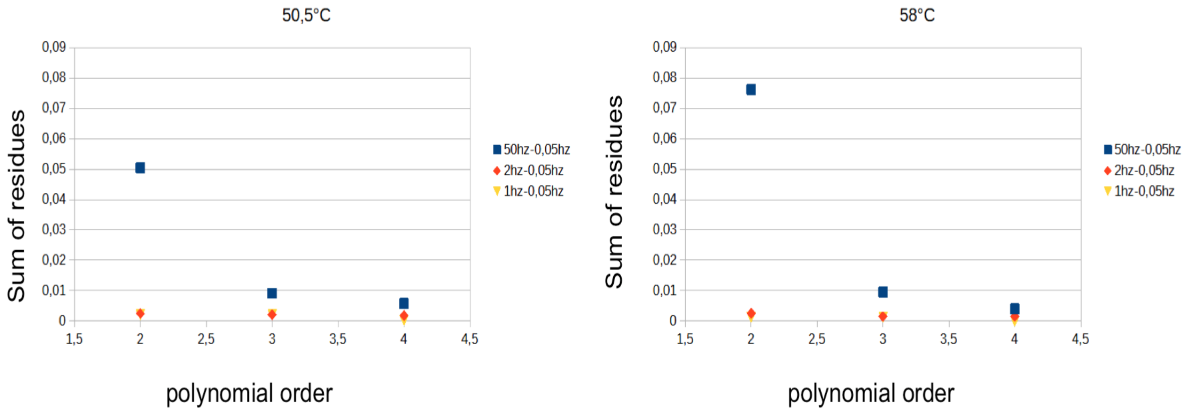

Figure 5.164: Influence of the polynomial order on the calculation of the activation energy at 43°C and 48°C

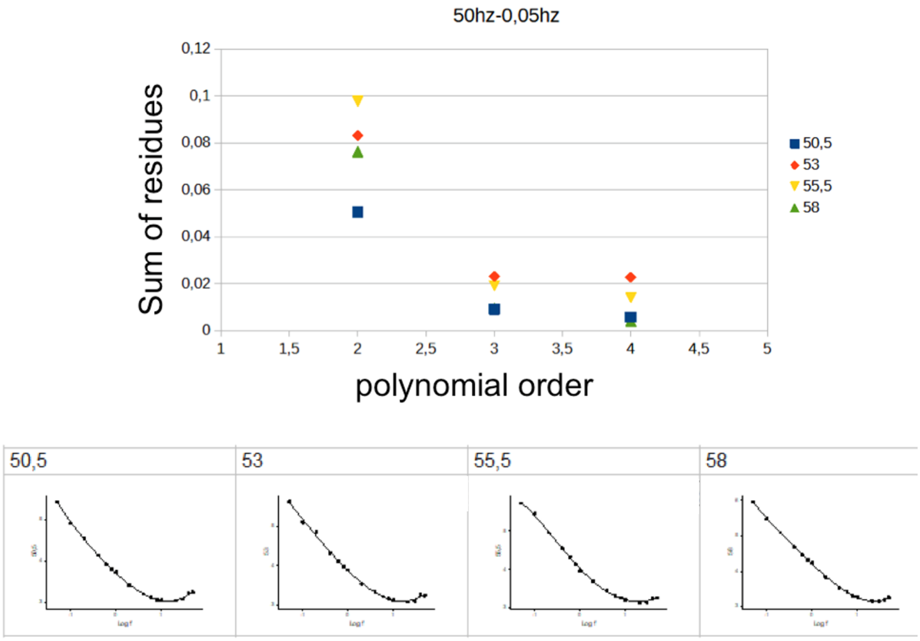

Figure 5.165: Influence of the polynomial order on the calculation of the sum of residues for a range of frequencies between 0.05hz and 50hz and 4 temperatures. The lower graphs display the $\delta = \delta(log f)$ data and their fitted curves on the frequency range considered

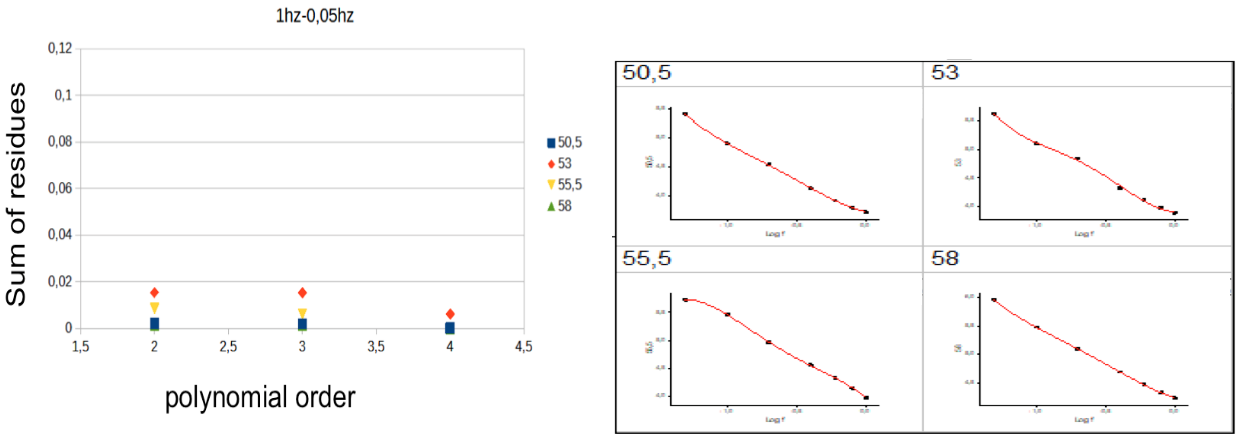

Figure 5.166: Influence of the polynomial order on the calculation of the sum of residues for a range of frequencies between 0.05hz and 1hz and 4 temperatures. The graphs at the right display the $\delta = \delta(log f)$ data and their fitted curves on the frequency range considered

It is observed on figure 5.167 that higher orders are better for the sum of residues and higher freq ranges are better for the stability of activation energy: (a) the energy is calculated on the base of a polynomial of order 2 between 0.05hz and 50hz (brown curve) and between 0.05hz and 1hz (dark green curve); (b) the same calculation than (a) with a polynomila of order 4. Large oscillations appear as can be seen on figure 5.168(a). The corresponding modelled curves are shown on the right (figure 5.168(b)). The oscillations come from a too best fit of the modelled curve with data presenting an average quality.

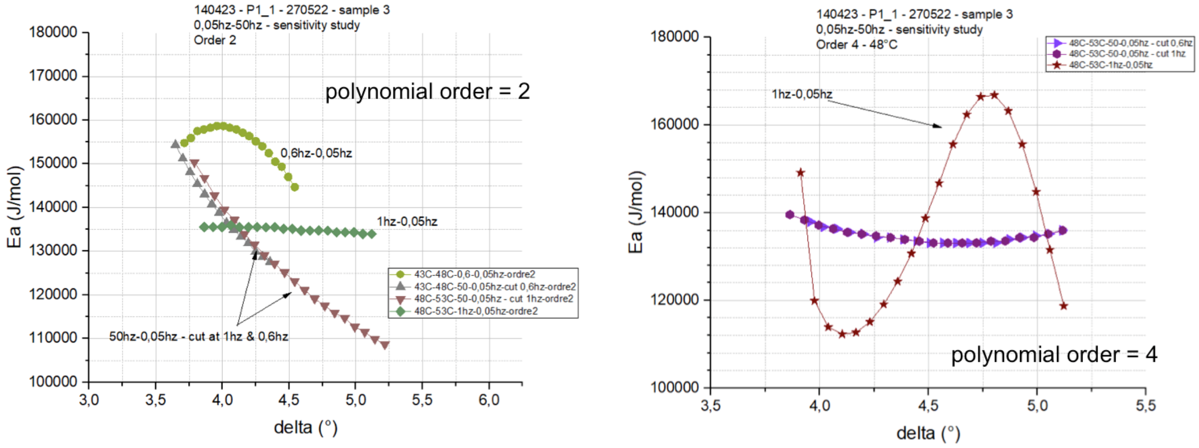

Figure 5.167: Influence of the range of frequency on the calculation of the activation energy at 48°C

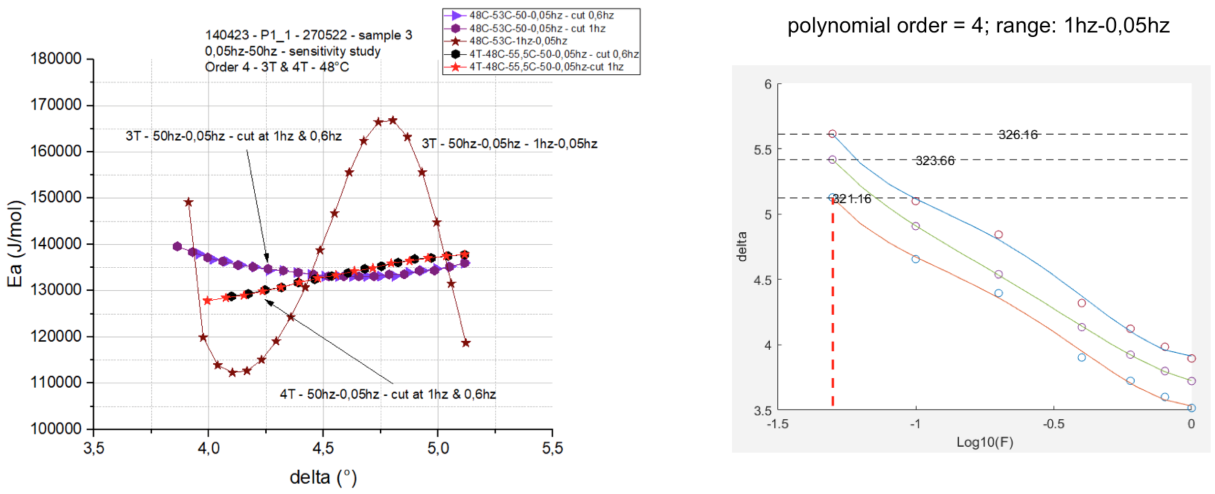

Figure 5.168: Identification of the causes for the oscillations: (a) combined calculation on 3 or 4 successive temperatures on 2 different frequency ranges; (b) waves are visible in the fitted curves

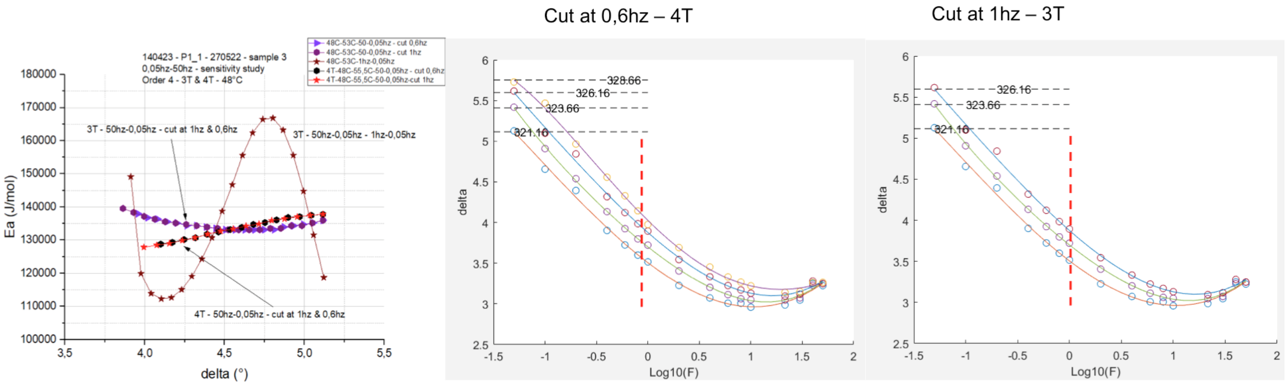

Figure 5.169: (a) Influence of the number of temperatures considered to calculate the shift factor and the activation energy, (b) and (c) are the corresponding $\delta = \delta(log f)$ for respectively 4 and 3 successive temperatures where the cut in frequency is identified with the dotted line to indicate where the claculation start

From the analysis of the curves shown at figure 5.169, one can conclude that:

1. it is important to model the whole curve and not only a small part
2. once modelled, the frequency where the calculation starts does not matter.

5.8.3.4 Summary and recommendations

We issue some recommendations hereunder:

1. consider carefully the raw data
2. use the highest polynomial order whenever possible (enough data for the selected range of frequencies)
3. model the whole curve
4. locate the cut to start computing the shift factors where it is relevant for the calculation as it doesn't matter
5. Use 3 temperatures (Delta T = 4°C or 5°) or 4 (Delta T = 6°C or 7,5°C) will depend on the polymer considered and an appropriate balance should be found with the polynomial order
6. accept oscillations of the $E_a = E_a(\delta)$ when $\Delta E_a \leq 5kJ/mol$
7. use a δ range that is larger than 0.5: $\Delta\delta \geq 0.5°$

8. check that in presence of 2 transitions, their temperature ranges should not overlap (too much).

Trying to find the «pure» mechanism between two transition is an art.

5.8.4 The mathematical method for the time-temperature master curve: Matlab® program

The main steps of the Matlab® ® program are presented hereunder.

5.8.4.1 Purpose of the program

The purpose of the program is to obtain the curve of the activation energy $E_a^n = E_a^n(\delta_n^0)$ as a function of δ_n^0.

Let us consider in a generic way: τ the relaxation time, T_0 and T_i the respective reference temperature and temperature considered, f the frequency, a_T the shift factor, δ the loss factor and E_a the activation energy.

$$\tau(T) = a_T(T, T_0)\ \tau(T_0) \tag{SI.1}$$

$$\frac{1}{f}(T) = a_T(T, T_0)\ \frac{1}{f}(T_0) \tag{SI.2}$$

Consequently,

$$a_T(T, T_0) = \frac{f(T_0)}{f(T)}(T) = \frac{f^0}{f^i} \tag{SI.3}$$

For $T_i >> T_g$, a Boltzmann statistics is applied and the shift factor follows an Arrhenius law:

$$a_{Ti} = exp(\frac{E_a}{R}(\frac{1}{T_i} - \frac{1}{T_0})) \tag{SI.4}$$

$$ln(a_{Ti}) = ln(\frac{f^0}{f^i}) = (\frac{E_a}{R}(\frac{1}{T_i} - \frac{1}{T_0})) \tag{SI.5}$$

$$E_a^i = R\ ln(a_{Ti})\ \ \frac{1}{(1/T_i - 1/T_0)} \tag{SI.6}$$

with

$$a_{Ti} = \frac{f^0}{f^i} \tag{SI.7}$$

For a given f^0, if a_{Ti} increases, then f^i decreases For the easiness of the treatment, the neperian logarithm ln is replaced by its equivalent value in base 10 log_{10} by incorporating the conversion factor whenever needed.

5.8.4.2 Step 1 : reading of the data

From the original data tgδ as a function of $logf$ at a given temperature, the values of δ are extracted and recorded in a file, the graph of which is found at figure 5.171(a). The resulting file is read by the software:

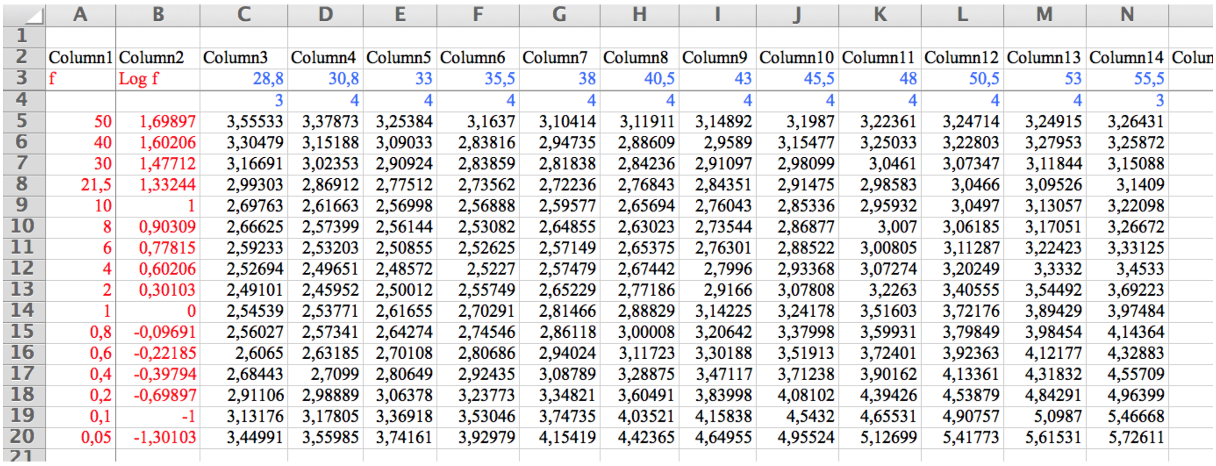

	A	B	C	D	E	F	G	H	I	J	K	L	M	N	
1															
2	Column1	Column2	Column3	Column4	Column5	Column6	Column7	Column8	Column9	Column10	Column11	Column12	Column13	Column14	Colun
3	f	Log f	28,8	30,8	33	35,5	38	40,5	43	45,5	48	50,5	53	55,5	
4			3	4	4	4	4	4	4	4	4	4	4	3	
5	50	1,69897	3,55533	3,37873	3,25384	3,1637	3,10414	3,11911	3,14892	3,1987	3,22361	3,24714	3,24915	3,26431	
6	40	1,60206	3,30479	3,15188	3,09033	2,83816	2,94735	2,88609	2,9589	3,15477	3,25033	3,22803	3,27953	3,25872	
7	30	1,47712	3,16691	3,02353	2,90924	2,83859	2,81838	2,84236	2,91097	2,98099	3,0461	3,07347	3,11844	3,15088	
8	21,5	1,33244	2,99303	2,86912	2,77512	2,73562	2,72236	2,76843	2,84351	2,91475	2,98583	3,0466	3,09526	3,1409	
9	10	1	2,69763	2,61663	2,56998	2,56888	2,59577	2,65694	2,76043	2,85336	2,95932	3,0497	3,13057	3,22098	
10	8	0,90309	2,66625	2,57399	2,56144	2,53082	2,64855	2,63023	2,73544	2,86877	3,007	3,06185	3,17051	3,26672	
11	6	0,77815	2,59233	2,53203	2,50855	2,52625	2,57149	2,65375	2,76301	2,88522	3,00805	3,11287	3,22423	3,33125	
12	4	0,60206	2,52694	2,49651	2,48572	2,5227	2,57479	2,67442	2,7996	2,93368	3,07274	3,20249	3,3332	3,4533	
13	2	0,30103	2,49101	2,45952	2,50012	2,55749	2,65229	2,77186	2,9166	3,07808	3,2263	3,40555	3,54492	3,69223	
14	1	0	2,54539	2,53771	2,61655	2,70291	2,81466	2,88829	3,14225	3,24178	3,51603	3,72176	3,89429	3,97484	
15	0,8	-0,09691	2,56027	2,57341	2,64274	2,74546	2,86118	3,00008	3,20642	3,37998	3,59931	3,79849	3,98454	4,14364	
16	0,6	-0,22185	2,6065	2,63185	2,70108	2,80686	2,94024	3,11723	3,30188	3,51913	3,72401	3,92363	4,12177	4,32883	
17	0,4	-0,39794	2,68443	2,7099	2,80649	2,92435	3,08789	3,28875	3,47117	3,71238	3,90162	4,13361	4,31832	4,55709	
18	0,2	-0,69897	2,91106	2,98889	3,06378	3,23773	3,34821	3,60491	3,83998	4,08102	4,39426	4,53879	4,84291	4,96399	
19	0,1	-1	3,13176	3,17805	3,36918	3,53046	3,74735	4,03521	4,15838	4,5432	4,65531	4,90757	5,0987	5,46668	
20	0,05	-1,30103	3,44991	3,55985	3,74161	3,92979	4,15419	4,42365	4,64955	4,95524	5,12699	5,41773	5,61531	5,72611	
21															

Figure 5.170: Reading of the data

5.8.4.3 Step 2 : fit $\delta^i = \delta^i(logf_n)$ at each temperature T^i with a polynomial

The curves δ as a function of $logf$ are then modelled:

$$\delta^i_{fit} = \delta^i(log_{10}f) \tag{SI.8}$$

where δ^i is a polynomial of order 3 or 4 the coefficients a_0 to a_4 of which are searched for each T^i as presented at figure 5.171(b).

The program then proposes to select the frequency at which the calculation will start, as illustrated by the dotted red line on figure 5.171(b), where the calculation is carried on the left side of the line.

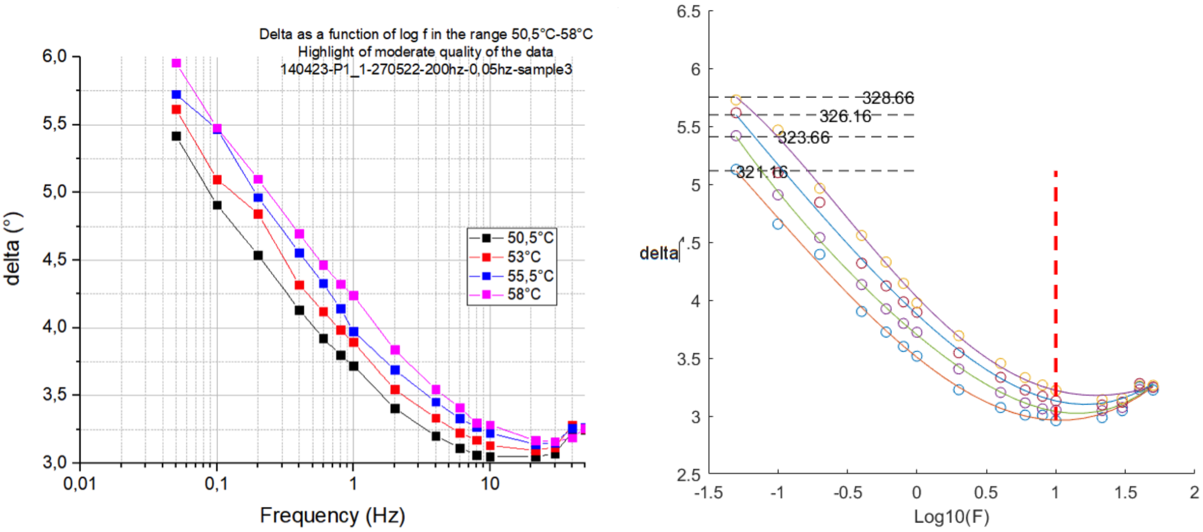

Figure 5.171: Graph of the raw data δ vs $logf$ (a) without fitted curve and (b) with fitted curve

5.8.4.4 Step 3: minimise the distance between delta at T^i and T^0 and find related frequencies

Each fitted curve is then divided in the same number of equal segments, f.i. 20 as illustrated at figure 5.172(a). According to the number of temperatures selected (3 or 4), let us define $i = 0 \ to \ 2 \ or \ 3$ with 0 as reference.

The distance between the fitted loss factor at the reference temperature and at the temperature T^i should be minimised for each of the 1 to n frequency f included in the raw data file:

$$d = \sqrt[2]{|\delta^0_n - \delta^i_n|^2} = 0 \tag{SI.9}$$

The ratio

$$log(\frac{f_n^0}{f_n^i}) \tag{SI.10}$$

is then found and the shift factor a_{Ti}^n can be computed within the defined range of δ as explained hereunder and illustrated at figure 5.172(b). The searched X-axis frequencies defining the shift factor are therefore only interpolated within the range of δ values, never extrapolated as illustrated at figure 5.172(a) by the horizontal lines framing the range (in this case, $3.2 \leq \delta \leq 5.2$).

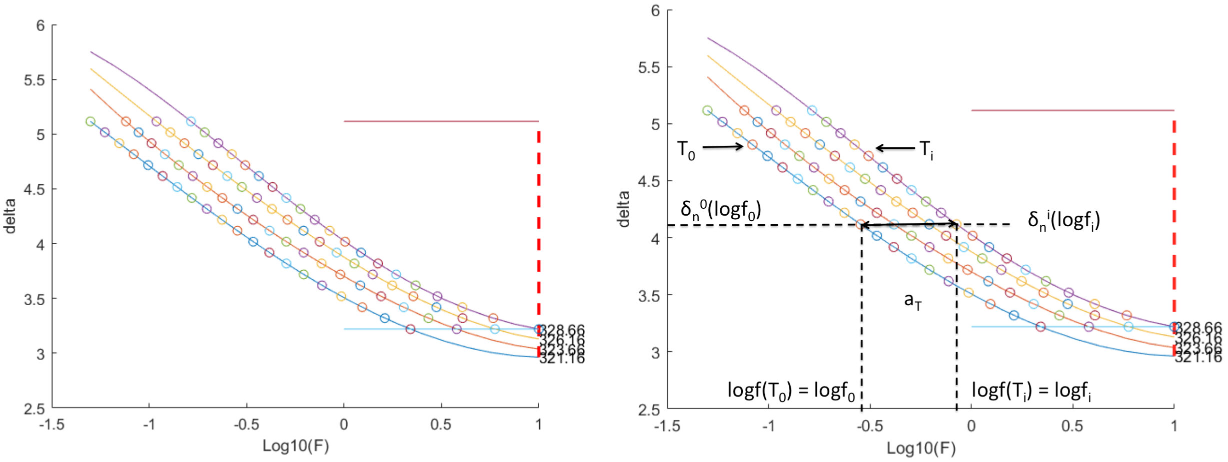

Figure 5.172: Graph of the raw data: δ vs $logf$

5.8.4.5 Step 4: Calculate corresponding shift factors a_T and activation energies

A matrix is obtained that calculates for each row and column "T, δ" the value f_n^0/f_n^1 :

$$\begin{array}{cccccc} & T^0 & T^1 & . & . & T^i \\ \delta_1^0 & f_1^0/f_1^1 & . & . & . & f_1^0/f_1^i \\ \delta_2^0 & f_2^0/f_2^1 & . & . & . & f_2^0/f_2^i \\ . & . & . & . & . & . \\ . & . & . & . & . & . \\ \delta_n^0 & f_n^0/f_n^1 & . & . & . & f_n^0/f_n^i \end{array} \tag{SI:M1}$$

From the matrix (SI:M1), the shift factors are found:

$$\begin{array}{cccccc} 1/T^0 & 1/T^1 & . & . & 1/T^i & \\ \delta_1^0 & R\ lna_{T1}^1 & . & . & R\ lna_{Ti}^1 & \rightarrow E_a^1 \\ \delta_2^0 & R\ lna_{T1}^2 & . & . & R\ lna_{Ti}^2 & \rightarrow E_a^2 \\ . & . & . & . & . & . \\ . & . & . & . & . & . \\ \delta_n^0 & R\ lna_{T1}^n & . & . & R\ lna_{Ti}^n & \rightarrow E_a^n \end{array} \tag{SI:M2}$$

and each column $(1/T_i, R\ lna_{Ti}^n)$ allows to find the slope E_a^n as illustrated at figure 5.173. If the correlation coefficient r^2 is $r^2 < 0.989$, its value is rejected.

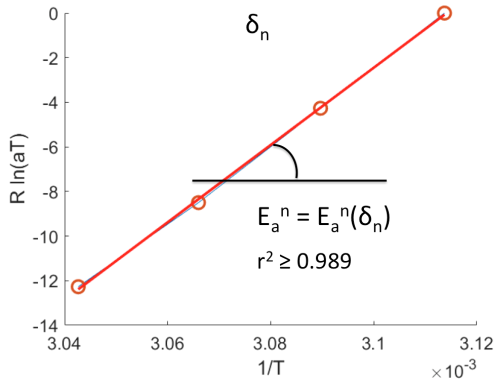

Figure 5.173: Calculation of activation energy E_a^n corresponding to δ_n

5.8.4.6 Step 5: draw the activation energy as a function of δ

Each couple of data (δ_n, E_a^n) is then reproduced on a graph, as illustrated at figure 5.174.

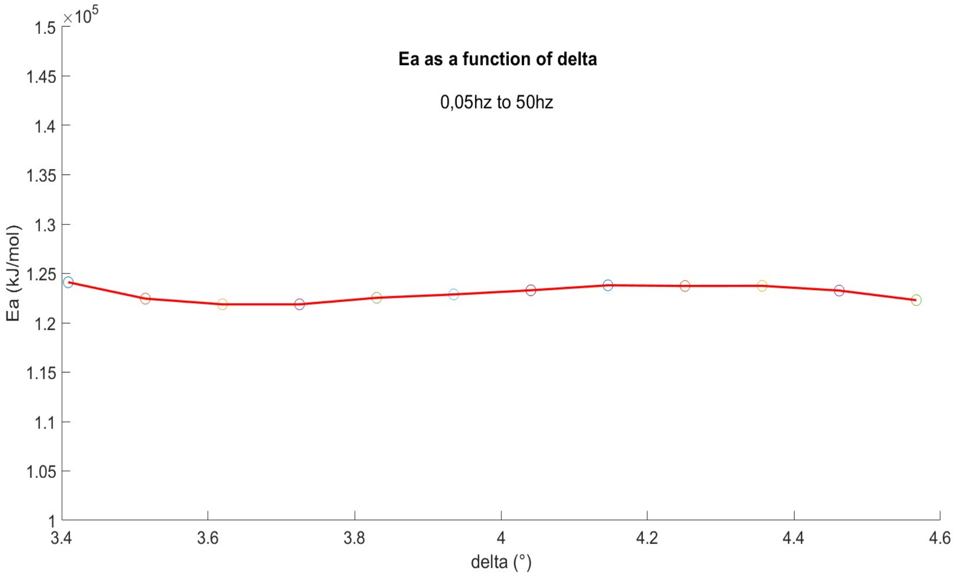

Figure 5.174: Activation energy E_a as a function of δ

5.8.5 How does it work in practice?

From a practical viewpoint, in order to understand the real nature of the phenomenon occurring in the temperature range of the α-relaxation, various aspects have to be considered:

1. the type of thermo-mechanical history undergone by the material, i.e. mainly the analysis of the microstructure behaviour under temperature of quenched product, quenched and annealed products and products undercooled isothermally from the melt
2. the dependence on temperature and temperature scanning rate of the microstructure in thermal experiments such as DSC
3. the dependence on temperature and temperature scanning rate of the microstructure in dynamic mechanical and thermal experiments such as DMTA where the time-temperature master curve can be built only if the changes undergone by the microstructure and translated into tgδ evolution are exactly the same when the frequency is changed; in other words, when the maximum of tgδ does not change with varying frequency. This is why the master curve has to be built in an isothermal way and not isochronous one, in order to keep a constant microstructure
4. these findings explains though why in all the publications dealing with this topic, a simple Arrhenius law has been used to obtain the activation energy, leading to the controversial use of combined horizontal and

vertical shifts mentionned previously. Taking these precautions, [69] and [71] frame the fact that when the temperature range is not too broad and the transitions do not overlap, neither E_a nor the shift factor a_T depend on the temperature and it is then possible to apply this methodology.

Chapter 6 : Conclusion

Table of contents

6.1 Conclusion

Isotactic polypropylene is one of the most complex semi-crystalline polymers, organised in its usual solid state as a multiphase, multi-scale and multi-hierarchical material. In this study, we have tried to unveil the subtle links existing between its various components such as crystalline phase resulting from mesophase solid/solid transition, rigid amorphous fraction and/or condis phase, its molecular relaxations and its behaviour at yield. In order to do so, we have assumed the existence of a common molecular mechanism spanning these events, the nucleation and propagation of dislocations, that sheds a special light on the interface between the crystalline phase and the other phases, especially on the rigid amorphous fraction.

More explicitly, we have investigated six structures belonging to two different catalytic systems under their α-crystalline form.

After having characterised the solid state microstructure and established the appropriate thermal conditions and thermal history allowing to not degrade our materials during the tests while keeping them stable, we have studied two aspects: first, their behaviour during quasi-static tensile tests at low to very low strain rates and second their visco-elastic relaxations. We have then analysed the influence of the catalytic system on the yield behaviour and established the link between the two limits of the small deformation range, i.e. the linear viscoelastic and the yield domain. We have also analysed the role of screw dislocation diffusion by helical jumps as the common underlying mechanism of both domains, in relation with the multiphasic structure of the material.

In the first part of the research, we have demonstrated, via the analysis of the stress-strain curves, their shape in the yield drop and the pictures taken at remarkable points that a double yield was indeed existing, especially in the case of the metallocene product, though its interpretation had to be nuanced by the possible presence of a competition between yielding and cavitation. We have suggested that the second mechanism could eventually be a second heterogeneous yield rather than an homogeneous one. We have found the activation energies and volumes resulting from the application of the Ree-Eyring model for plastic flow, and tried to identify the type of mechanism at work. A special attention was devoted to establishing the link between these parameters and the solid state microstructure for each catalysis. We have also commented, for the first time, the possible signification of the vibration frequency, the sole parameter of the model embedding the information on the microstructure itself because it reflects the disorder change in the helical jumps that the microstructure undergoes when the yield is achieved. The associated varying flexibility of the amorphous and mesophase network was highlighted.

We have come to the conclusion that the different long term/low strain rates behaviours of ZN resins can be explained by the critical influence of their molecular weight and that the differences between ZN and MET behaviours have to imply not only the molecular weight but also the regio-defects typical of the metallocene catalysis.

In the second part of the research, we have confirmed that the type of molecular relaxation at stake in the mechanisms observed during the tensile tests were linked to a double yield phenomenon. As the time-temperature superposition principle was difficult to apply because of the overlapping visco-elastic curves, we have used an approach coming from the melt, sensitive to small variations, to identify the number of relaxations in relation with the different structural phases and how temperature and frequency influence them. We have highlighted the existence of three to four mechanisms, among which two were assumed to be related to the heterogeneous slip of crystalline lamellae. We have established the link between the activation energies obtained for the yield behaviour and those obtained from the analysis of the relaxations. We have highlighted the role of structural quantities such as crystalline thickness known to be dependent on the molecular weight, of the rigid amorphous thickness known to depend on the crystallisation conditions and of the isotactic length - embedding the defects - known to depend on the chemical synthesis.

All in all, we have focused on the development of a new methodological approach combining the bottom-up perspective of the chemist with the top-down one of the physicist, and, in this latter case, bringing some rheology tools into the solid state.

This has allowed us drawing a first possible sketch for the undeformed structure of our two types of isotactic polypropylene, displayed at figure 6.175(a) for the Ziegler-Natta P_{11} and 6.175(b) for the metallocene P_{61}.

In order to make the drawing readible, we have neither represented the mobile amorphous fraction, nor the global molecular entangled network of the amorphous phase in general but a few chains. We refer to the sections 2.3.3.3 to 2.3.3.5 for more details.

Both polymers display a crystalline phase, an amorphous phase made of RAF and MAF and a mesophase which constituents are condis crystals, RAF and MAF. The RAF, drawn in green, bounds covalently the mesophase with the MAF or the crystal with the MAF. Thanks to the diffusion process of helical jumps and therefore dislocations, it can be located outside, partially inside or totally inside the crystal lamellae though at this stage, we do not take any option on the direction of the diffusion (from the amorphous phase to the crystal or vice-versa), both being possible. This process has been represented at figure 6.176 where two cases have been proposed: on the left hand side, the RAF is outside of the crystalline lamellae and on the right hand side, it is partially inside.

In order to emphasize the difference between the two catalytic systems and based on our data, we have drawn larger crystalline and amorphous thicknesses for the ZN product than for MET. As MET can display both kinds of defects (stereo- and regio-) distributed quite homogeneously on the chains, resulting in a shorter isotactic length, we have highlighted them with the solid circles coloured in dark grey. It can be seen that the regio-defects have been excluded from the crystalline lamellae. For what concerns the ZN, the stereo-defects, highlighted here by green solid circles and maybe constitutive of some RAF, are present in all the phases though spread inhomogeneously as they tend to be concentrated overall on the longer chains. We have also highlighted the mesophase with dotted circles, coloured in blue for the fringed micelles and in red for the small stacks of folded chains.

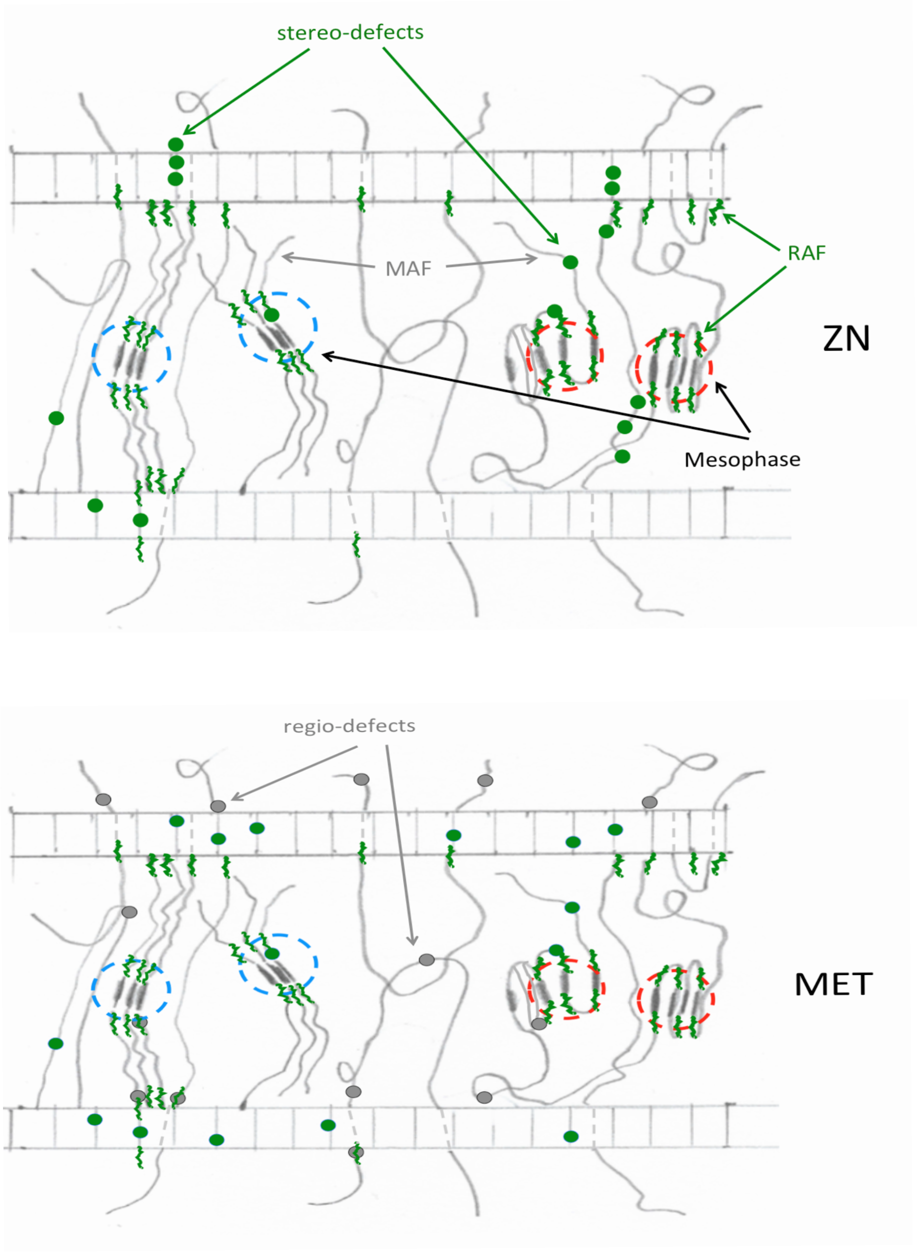

Figure 6.175: Two possible structures of undeformed polymer (a) for ZN and (b) for MET, with a focus on mesophase and RAF; only a few chains of MAF have been drawn and not all the stress transmitters and more globally the entangled molecular network have been displayed; the various scales are not respected, the amorphous and crystalline thickness of ZN (f.i. P_{11}) is larger than the one of MET (P_{61}) - see text for more details (credit: Luc Mathieu 2024)

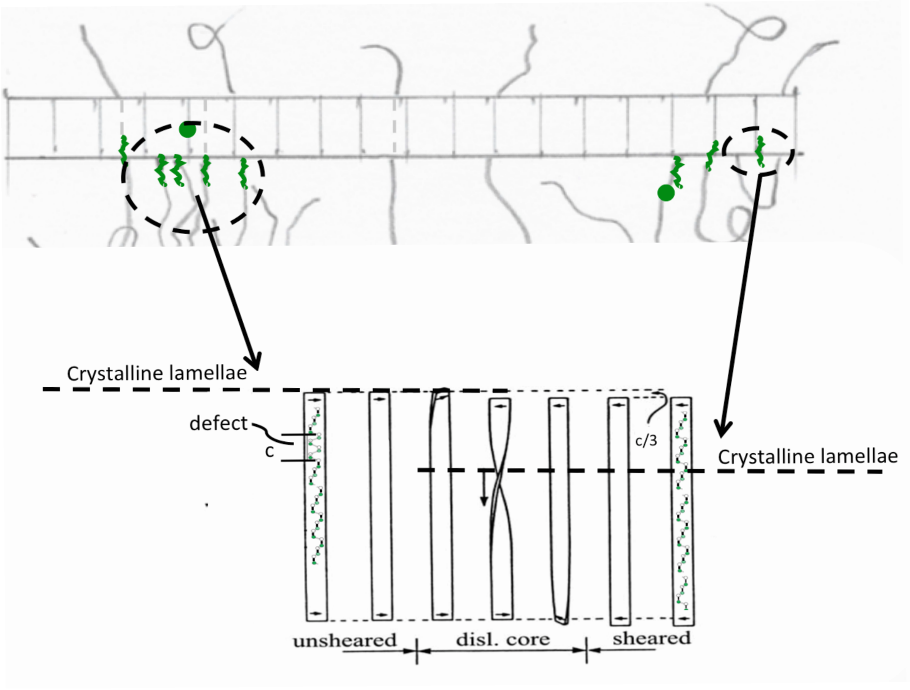

Figure 6.176: Possible phenomenon of RAF diffusion via the helical jumps/dislocation at the interface with the crystalline lamellae under the sole thermal agitation; two cases have been represented in this drawing: on the left hand side, before the chain has diffused into- or after it has diffused from the crystal phase; on the right hand side, the chain is partially in the crystal phase (reworked from [40] and figure 6.175)

6.2 Perspectives

After having focused on the various phases co-existing under usual processing and annealing conditions in iPP, a lot of unknown remain, namely the exact role of the stress transmitters, of the rigid amorphous fraction and its further confinement - caused namely by the transformation of the mesophase into a crystal one - and link with defects or of the competition between local yielding and cavitation. A clearer understanding of the separate influence of the molecular architecture and thermo-mechanical history on these phases, their molecular relaxations and the way they accommodate locally the macroscopic deformation at low characteristic times has to be still achieved, together with a better understanding of the confinement effects on the various nanophases. More specifically, it would be critical to better understand how, during the interactions of the global molecular entangled amorphous network (RAF, condis, stress transmitters, etc.) with the crystalline lamellae, the kinetics, direction and location of defects diffusion operate to accommodate the stress transfer via the strain response.

In order to do so from a real experiment perspective, the main topics are, first, to see and measure how the crystalline lamellae deform under increasing strain, confirming or not the hypothesis of two heterogeneous mechanisms; second, to use quasi-static results to measure the amount of stress transmitters; third, to understand the specificity of each catalyst by seeing and measuring with adapted technologies (in-situ, spectroscopies, ...) the exact composition of the microstructure and how the diffusion of dislocation supports the stress transfer among the phases; finally, to approach the problem of the competition between cavitation and yielding namely by applying the WLF model as the relaxations identified are close to the glass transitions, and therefore the changes in free volume could not be neglected anymore.

From a in-silico perspective, the first step should be to investigate what would be the most relevant scales and tools that would support the development of the experimental program.

More generally, the molecular to micro to macro approach that we have applied in this study is in reality applicable to many semi-crystalline polymers of common use. The presence of the various phases such as RAF and condis crystals was indeed proved for instance in PE, PA6, PET, PB-1 or PLLA just to name a few.

Exploring in a detailed and systematic way the quality of the activation constants and the type of mechanisms at work in relation with both the chemical structure and the thermo-mechanical history at low frequencies is definitely a relevant methodology.

We think that this approach spans the whole chain of knowledge going from the chemistry to the physics of the solid state behaviour in the range of small deformation and fills in some of the gaps existing in the realm of structure/properties relationships.

List of Figures

Bibliography

[1] W. Y. et al, “Tailoring the mechanical properties of binary polypropylene blends with polymorphic and oriented hierarchical structures”, *Polymer Journal*, 2023. DOI: `https://doi.org/10.1038/s41428-023-00773-w`.

[2] O. Lhost, *Polyolefins*, Dec. 2023.

[3] P. Europe, “Plastics: The fast facts 2023”, Plastics Europe, Tech. Rep., 2023. [Online]. Available: `https://plasticseurope.org/wp-content/uploads/2023/10/Plasticsthefastfacts2023-1.pdf`.

[4] R. a. Markets, “Global Polypropylene Industry Report 2023-2028: Markets Thrives Post-COVID as Demand Surges in Automotive and Construction Industries”, Research and Markets, Tech. Rep., Jul. 2023. [Online]. Available: `https://www.researchandmarkets.com/reports/5849391/global-polypropylene-market-analysis-demand?utm_source=GNE&utm_medium=PressRelease&utm_code=45g4sj&utm_campaign=1870480+-+Global+Polypropylene+Industry+Report+2023-2028%3a+Markets+Thrives+Post-COVID+as+Demand+Surges+in+Automotive+and+Construction+Industries&utm_exec=joca220prd`.

[5] Grandviewresearch, “Polypropylene Market Size, Share & Trends Analysis Report By Polymer Type (Homopolymer, Copolymer), By Process, By Application, By End-Use, By Region, And Segment Forecasts, 2023 - 2030”, Grandviewresearch, Tech. Rep., 2022. [Online]. Available: `https://www.grandviewresearch.com/industry-analysis/polypropylene-market#`.

[6] A. Law, L. Simon, and P. Lee-Sullivan, “Effects of thermal aging on isotactic polypropylene crystallinity”, en, *Polymer Engineering & Science*, vol. 48, no. 4, pp. 627–633, Apr. 2008, ISSN: 00323888, 15482634. DOI: `10.1002/pen.20987`. [Online]. Available: `https://onlinelibrary.wiley.com/doi/10.1002/pen.20987` (visited on 11/07/2023).

[7] S. Hellinckx, “Lien entre les mouvements moléculaires et le comportement mécanique du polypropylène”, Ph.D. dissertation, ULB, 1995. [Online]. Available: `https://difusion.ulb.ac.be/vufind/Record/ULB-DIPOT:oai:dipot.ulb.ac.be:2013/212542/Details`.

[8] S. Hellinckx, “A quantitative model describing physical aging in isotactic polypropylenes”, en, *Colloid & Polymer Science*, vol. 273, no. 2, pp. 130–137, Feb. 1995, ISSN: 0303-402X, 1435-1536. DOI: `10.1007/BF00654010`. [Online]. Available: `http://link.springer.com/10.1007/BF00654010` (visited on 12/10/2023).

[9] J. M. Schultz, “Microstructural aspects of failure in semicrystalline polymers”, en, *Polymer Engineering and Science*, vol. 24, no. 10, pp. 770–785, Jul. 1984, ISSN: 0032-3888, 1548-2634. DOI: `10.1002/pen.760241007`. [Online]. Available: `https://onlinelibrary.wiley.com/doi/10.1002/pen.760241007` (visited on 10/06/2023).

[10] C. De Rosa, F. Auriemma, T. Circelli, and R. M. Waymouth, “Crystallization of the and Forms of Isotactic Polypropylene as a Tool To Test the Degree of Segregation of Defects in the Polymer Chains”, en, *Macromolecules*, vol. 35, no. 9, pp. 3622–3629, Apr. 2002, ISSN: 0024-9297, 1520-5835. DOI: `10.1021/ma0116248`. [Online]. Available: `https://pubs.acs.org/doi/10.1021/ma0116248` (visited on 10/09/2023).

[11] D.-W. Van Der Meer, “Structure-Property Relationships in Isotactic Polypropylene”, en, Ph.D. dissertation, University of Twente, Jun. 2003. DOI: `10.3990/1.9789036519144`. [Online]. Available: `https://research.utwente.nl/en/publications/structure-property-relationships-in-isotactic-polypropylene` (visited on 10/05/2023).

[12] J. Varga, “Supermolecular structure of isotactic polypropylene”, en, *Journal of Materials Science*, vol. 27, no. 10, pp. 2557–2579, May 1992, ISSN: 0022-2461, 1573-4803. DOI: `10.1007/BF00540671`. [Online]. Available: `http://link.springer.com/10.1007/BF00540671` (visited on 11/20/2023).

[13] C. Grein, K. Bernreitner, and M. Gahleitner, “Potential and limits of dynamic mechanical analysis as a tool for fracture resistance evaluation of isotactic polypropylenes and their polyolefin blends”, 2004. DOI: `https://onlinelibrary.wiley.com/doi/10.1002/app.20606`.

[14] M. Elvira, P. Tiemblo, and J. Gómez-Elvira, “Changes in the crystalline phase during the thermo-oxidation of a metallocene isotactic polypropylene. A DSC study”, en, *Polymer Degradation and Stability*, vol. 83, no. 3, pp. 509–518, Mar. 2004, ISSN: 01413910. DOI: `10.1016/j.polymdegradstab.2003.08.010`. [Online]. Available: `https://linkinghub.elsevier.com/retrieve/pii/S0141391003003112` (visited on 11/07/2023).

[15] Y. Dauphin, *About Mathematical Modeling in Industrial R&D Context (Solvay - private communication)*, Jun. 2012.

[16] B. Chang, K. Schneider, R. Vogel, and G. Heinrich, “Influence of Annealing on Mechanical $_{c}$-Relaxation of Isotactic Polypropylene: A Study from the Intermediate Phase Perspective”, en, *Macromolecular Materials and Engineering*, vol. 302, no. 11, p. 1 700 291, Nov. 2017, ISSN: 1438-7492, 1439-2054. DOI: `10.1002/mame.201700291`. [Online]. Available: `https://onlinelibrary.wiley.com/doi/10.1002/mame.201700291` (visited on 11/01/2023).

[17] S. Xu, J. Zhou, and P. Pan, “Strain-induced multiscale structural evolutions of crystallized polymers: From fundamental studies to recent progresses”, en, *Progress in Polymer Science*, vol. 140, p. 101 676, May 2023, ISSN: 00796700. DOI: `10.1016/j.progpolymsci.2023.101676`. [Online]. Available: `https://linkinghub.elsevier.com/retrieve/pii/S007967002300031X` (visited on 10/09/2023).

[18] R. Androsch, M. L. Di Lorenzo, C. Schick, and B. Wunderlich, “Mesophases in polyethylene, polypropylene, and poly(1-butene)”, en, *Polymer*, vol. 51, no. 21, pp. 4639–4662, Oct. 2010, ISSN: 00323861. DOI: `10.1016/j.polymer.2010.07.033`. [Online]. Available: `https://linkinghub.elsevier.com/retrieve/pii/S0032386110006464` (visited on 10/31/2023).

[19] M. Cocca, R. Androsch, M. C. Righetti, M. Malinconico, and M. L. Di Lorenzo, “Conformationally disordered crystals and their influence on material properties: The cases of isotactic polypropylene, isotactic poly(1-butene), and poly(l-lactic acid)”, en, *Journal of Molecular Structure*, vol. 1078, pp. 114–132, Dec. 2014, ISSN: 00222860. DOI: `10.1016/j.molstruc.2014.02.038`. [Online]. Available: `https://linkinghub.elsevier.com/retrieve/pii/S0022286014002129` (visited on 11/01/2023).

[20] Q. Zia, H.-J. Radusch, and R. Androsch, “Deformation behavior of isotactic polypropylene crystallized via a mesophase”, en, *Polymer Bulletin*, vol. 63, no. 5, pp. 755–771, Nov. 2009, ISSN: 0170-0839, 1436-2449. DOI: `10.1007/s00289-009-0151-y`. [Online]. Available: `http://link.springer.com/10.1007/s00289-009-0151-y` (visited on 10/27/2023).

[21] Q. Jiang, Y. Zhao, C. Zhang, J. Yang, Y. Xu, and D. Wang, “In-situ investigation on the structural evolution of mesomorphic isotactic polypropylene in a continuous heating process”, en, *Polymer*, vol. 105, pp. 133–143, Nov. 2016, ISSN: 00323861. DOI: `10.1016/j.polymer.2016.10.004`. [Online]. Available: `https://linkinghub.elsevier.com/retrieve/pii/S0032386116309077` (visited on 12/29/2023).

[22] A. Goldberg and S. Hellinckx, “Polyéthylène – La fissuration lente dans tous ses états : De la mesure aux mécanismes de déformation Notice de synthèse Solvay”, Solvay SA, Tech. Rep., Jul. 2003.

[23] A. Goldberg, “Mécanique de rupture - étude bibliographique partie II: Approche micro-macro”, Rapport interne, Solvay, 1996.

[24] A. Kinloch and R. Young, *Fracture behaviour of polymers*, Applied Science Publishers. 1983.

[25] W. Brostow and R. D. Corneliussen, *Failure of Plastics*. 1986. [Online]. Available: `https://api.semanticscholar.org/CorpusID:135607291`.

[26] J. Williams, *Fracture mechanics of polymers*, Chichester : E. Horwood ; New York : Halsted Press. 1984.

[27] A. Goldberg, “Mécanique de rupture - étude bibliographique partie I: Approche théorique”, Rapport interne, Solvay, 1994.

[28] W. EN, *Dislocation*. [Online]. Available: `https://en.wikipedia.org/wiki/Dislocation`.

[29] W. EN, *Burgers vector*. [Online]. Available: `https://en.wikipedia.org/wiki/Burgers_vector`.

[30] W. FR, *Dislocation (Matériaux)*. [Online]. Available: `https://fr.wikipedia.org/wiki/Dislocation_(mat%C3%A9riaux)` (visited on 04/17/2024).

[31] W. Wikipedia NL, *Projectiemodel van een kristalstructuur met een planaire dislocatie. De Burgersvector is in het zwart aangegeven met b, de dislocatielijn in blauw.* [Online]. Available: `https://commons.wikimedia.org/w/index.php?curid=12774796`.

[32] W. Wikipedia NL, *Projectiemodel van een kristalstructuur met een schroefdislocatie.* [Online]. Available: `https://commons.wikimedia.org/w/index.php?curid=2352475`.

[33] M. Mackley, "Polyethylene Polymer Crystallisation", Salcombe, Devon, 2015.

[34] S. Nikolov, I. Doghri, O. Pierard, L. Zealouk, and A. Goldberg, "Multi-scale constitutive modeling of the small deformations of semi-crystalline polymers", en, *Journal of the Mechanics and Physics of Solids*, vol. 50, no. 11, pp. 2275–2302, Nov. 2002, ISSN: 00225096. DOI: 10.1016/S0022-5096(02)00036-4. [Online]. Available: https://linkinghub.elsevier.com/retrieve/pii/S0022509602000364 (visited on 11/16/2023).

[35] W.-G. Hu and K. Schmidt-Rohr, "Polymer ultradrawability: The crucial role of -relaxation chain mobility in the crystallites", en, *Acta Polymerica*, vol. 50, no. 8, pp. 271–285, Aug. 1999, ISSN: 0323-7648, 1521-4044. DOI: 10.1002/(SICI)1521-4044(19990801)50:8<271::AID-APOL271>3.0.CO;2-Y. [Online]. Available: https://onlinelibrary.wiley.com/doi/10.1002/(SICI)1521-4044(19990801)50:8%3C271::AID-APOL271%3E3.0.CO;2-Y (visited on 10/10/2023).

[36] R. H. Boyd, "Relaxation processes in crystalline polymers: Experimental behaviour — a review", en, *Polymer*, vol. 26, no. 3, pp. 323–347, Mar. 1985, ISSN: 00323861. DOI: 10.1016/0032-3861(85)90192-2. [Online]. Available: https://linkinghub.elsevier.com/retrieve/pii/0032386185901922 (visited on 10/06/2023).

[37] K. Schmidt-Rohr and H. W. Spiess', "Chain Diffusion between Crystalline and Amorphous Regions in Polyethylene Detected by 2D Exchange 13CNMR", en, vol. 24, no. 19, 1991.

[38] J.-L. Syi, "Soliton model of the crystalline relaxation", *POLYMER*, vol. 29, June, p. 987, 1988.

[39] R. Seguela, E. Staniek, B. Escaig, and B. Fillon, "Plastic deformation of polypropylene in relation to crystalline structure", en, *Journal of Applied Polymer Science*, vol. 71, no. 11, pp. 1873–1885, Mar. 1999, ISSN: 0021-8995, 1097-4628. DOI: 10.1002/(SICI)1097-4628(19990314)71:11<1873::AID-APP18>3.0.CO;2-I. [Online]. Available: https://onlinelibrary.wiley.com/doi/10.1002/(SICI)1097-4628(19990314)71:11%3C1873::AID-APP18%3E3.0.CO;2-I (visited on 10/24/2023).

[40] S. Nikolov and D. Raabe, "Yielding of polyethylene through propagation of chain twist defects: Temperature, stem length and strain-rate dependence", en, *Polymer*, vol. 47, no. 5, pp. 1696–1703, Feb. 2006, ISSN: 00323861. DOI: 10.1016/j.polymer.2005.12.050. [Online]. Available: https://linkinghub.elsevier.com/retrieve/pii/S0032386105017969 (visited on 04/21/2024).

[41] R. Séguéla, "Plasticity of semi-crystalline polymers: Crystal slip versus melting-recrystallization", en, *e-Polymers*, vol. 7, no. 1, Dec. 2007, ISSN: 1618-7229, 2197-4586. DOI: 10.1515/epoly.2007.7.1.382. [Online]. Available: https://www.degruyter.com/document/doi/10.1515/epoly.2007.7.1.382/html (visited on 10/27/2023).

[42] B. Xiong, "Contribution to the study of elastic and plastic deformation mechanisms of polyethylene and polypropylene as a function of microstructure and temperature", fr, Ph.D. dissertation, 2016.

[43] B. Xiong, O. Lame, J.-M. Chenal, Y. Men, R. Seguela, and G. Vigier, "Critical stress and thermal activation of crystal plasticity in polyethylene: Influence of crystal microstructure and chain topology", en, *Polymer*, vol. 118, pp. 192–200, Jun. 2017, ISSN: 00323861. DOI: 10.1016/j.polymer.2017.05.011. [Online]. Available: https://linkinghub.elsevier.com/retrieve/pii/S0032386117304780 (visited on 02/13/2024).

[44] B. Xiong, O. Lame, J.-M. Chenal, C. Rochas, and R. Seguela, "On the strain-induced fibrillar microstructure of polyethylene: Influence of chemical structure, initial morphology and draw temperature", en, *Express Polymer Letters*, vol. 10, no. 4, pp. 311–323, 2016, ISSN: 1788618X. DOI: 10.3144/expresspolymlett.2016.29. [Online]. Available: http://www.expresspolymlett.com/letolt.php?file=EPL-0006567&mi=c (visited on 02/13/2024).

[45] Y. Men, J. Rieger, and G. Strobl, "Role of the Entangled Amorphous Network in Tensile Deformation of Semicrystalline Polymers", en, *Physical Review Letters*, vol. 91, no. 9, p. 095 502, Aug. 2003, ISSN: 0031-9007, 1079-7114. DOI: 10.1103/PhysRevLett.91.095502. [Online]. Available: https://link.aps.org/doi/10.1103/PhysRevLett.91.095502 (visited on 02/13/2024).

[46] Z. Bartczak and A. Vozniak, "Deformation Instabilities and Lamellae Fragmentation during Deformation of Cross-linked Polyethylene", en, *Polymers*, vol. 11, no. 12, p. 1954, Nov. 2019, ISSN: 2073-4360. DOI: 10.3390/polym11121954. [Online]. Available: https://www.mdpi.com/2073-4360/11/12/1954 (visited on 04/16/2024).

[47] A. Pawlak, A. Galeski, and A. Rozanski, "Cavitation during deformation of semicrystalline polymers", en, *Progress in Polymer Science*, vol. 39, no. 5, pp. 921–958, May 2014, ISSN: 00796700. DOI: 10.1016/j.progpolymsci.2013.10.007. [Online]. Available: https://linkinghub.elsevier.com/retrieve/pii/S0079670013001287 (visited on 11/20/2023).

[48] Y. Wang, T. Wu, and Q. Fu, “Competition of shearing and cavitation effects on the deformation behavior of isotactic polypropylene during stretching”, en, *Polymer*, vol. 273, p. 125 888, Apr. 2023, ISSN: 00323861. DOI: 10.1016/j.polymer.2023.125888. [Online]. Available: https://linkinghub.elsevier.com/retrieve/pii/S0032386123002185 (visited on 11/21/2023).

[49] C. J. Plummer, A. Goldberg, and A. Ghanem, “Micromechanisms of slow crack growth in polyethylene under constant tensile loading”, en, *Polymer*, vol. 42, no. 23, pp. 9551–9564, Nov. 2001, ISSN: 00323861. DOI: 10.1016/S0032-3861(01)00476-1. [Online]. Available: https://linkinghub.elsevier.com/retrieve/pii/S0032386101004761 (visited on 11/20/2023).

[50] A. Pawlak, J. Krajenta, and A. Galeski, “Cavitation phenomenon and mechanical properties of partially disentangled polypropylene”, en, *Polymer*, vol. 151, pp. 15–26, Aug. 2018, ISSN: 00323861. DOI: 10.1016/j.polymer.2018.07.033. [Online]. Available: https://linkinghub.elsevier.com/retrieve/pii/S0032386118306281 (visited on 12/10/2023).

[51] A. Pawlak and A. Galeski, “Cavitation and morphological changes in polypropylene deformed at elevated temperatures”, en, *Journal of Polymer Science Part B: Polymer Physics*, vol. 48, no. 12, pp. 1271–1280, Jun. 2010, ISSN: 0887-6266, 1099-0488. DOI: 10.1002/polb.22020. [Online]. Available: https://onlinelibrary.wiley.com/doi/10.1002/polb.22020 (visited on 12/10/2023).

[52] P. Cerra, D. R. Morrow, and J. A. Sauer, “Deformation of polypropylene single crystals”, en, *Journal of Macromolecular Science, Part B*, vol. 3, no. 1, pp. 33–51, Mar. 1969, ISSN: 0022-2348, 1525-609X. DOI: 10.1080/00222346908217087. [Online]. Available: https://www.tandfonline.com/doi/full/10.1080/00222346908217087 (visited on 10/24/2023).

[53] J. A. Sauer, D. R. Morrow, and G. C. Richardson, “Morphology of Solution-Grown Polypropylene Crystal Aggregates”, en, *Journal of Applied Physics*, vol. 36, no. 10, pp. 3017–3021, Oct. 1965, ISSN: 0021-8979, 1089-7550. DOI: 10.1063/1.1702920. [Online]. Available: https://pubs.aip.org/jap/article/36/10/3017/379235/Morphology-of-Solution-Grown-Polypropylene-Crystal (visited on 10/24/2023).

[54] K.-h. Nitta and K. Odaka, “Influence of structural organization on tensile properties in mesomorphic isotactic polypropylene”, en, *Polymer*, vol. 50, no. 16, pp. 4080–4088, Jul. 2009, ISSN: 00323861. DOI: 10.1016/j.polymer.2009.06.050. [Online]. Available: https://linkinghub.elsevier.com/retrieve/pii/S0032386109005448 (visited on 11/15/2023).

[55] W. J. O’kane, R. J. Young, and A. J. Ryan, “The effect of annealing on the structure and properties of isotactic polypropylene films”, en, *Journal of Macromolecular Science, Part B*, vol. 34, no. 4, pp. 427–458, Nov. 1995, ISSN: 0022-2348, 1525-609X. DOI: 10.1080/00222349508219502. [Online]. Available: https://www.tandfonline.com/doi/full/10.1080/00222349508219502 (visited on 11/15/2023).

[56] K.-H. Nitta and M. Takayanagi, “Tensile yield of isotactic polypropylene in terms of a lamellar-cluster model”, en, *Journal of Polymer Science Part B: Polymer Physics*, vol. 38, no. 8, pp. 1037–1044, Apr. 2000, ISSN: 0887-6266, 1099-0488. DOI: 10.1002/(SICI)1099-0488(20000415)38:8<1037::AID-POLB4>3.0.CO;2-R. [Online]. Available: https://onlinelibrary.wiley.com/doi/10.1002/(SICI)1099-0488(20000415)38:8%3C1037::AID-POLB4%3E3.0.CO;2-R (visited on 11/15/2023).

[57] R. Gao, M. Kuriyagawa, K.-H. Nitta, X. He, and B. Liu, “Structural Interpretation of Eyring Activation Parameters for Tensile Yielding Behavior of Isotactic Polypropylene Solids”, en, *Journal of Macromolecular Science, Part B*, vol. 54, no. 10, pp. 1196–1210, Oct. 2015, ISSN: 0022-2348, 1525-609X. DOI: 10.1080/00222348.2015.1079088. [Online]. Available: http://www.tandfonline.com/doi/full/10.1080/00222348.2015.1079088 (visited on 11/15/2023).

[58] M. Gahleitner, C. Bachner, E. Ratajski, G. Rohaczek, and W. Neil, “Effects of the catalyst system on the crystallization of polypropylene*”, en, *Journal of Applied Polymer Science*, vol. 73, no. 12, pp. 2507–2515, Sep. 1999, ISSN: 0021-8995, 1097-4628. DOI: 10.1002/(SICI)1097-4628(19990919)73:12<2507::AID-APP19>3.0.CO;2-V. [Online]. Available: https://onlinelibrary.wiley.com/doi/10.1002/(SICI)1097-4628(19990919)73:12%3C2507::AID-APP19%3E3.0.CO;2-V (visited on 05/03/2024).

[59] D. Ferrer-Balas, M. Maspoch, A. Martinez, and O. Santana, “Influence of annealing on the microstructural, tensile and fracture properties of polypropylene films”, en, *Polymer*, vol. 42, no. 4, pp. 1697–1705, Feb. 2001, ISSN: 00323861. DOI: 10.1016/S0032-3861(00)00487-0. [Online]. Available: https://linkinghub.elsevier.com/retrieve/pii/S0032386100004870 (visited on 05/03/2024).

[60] K.-h. Nitta and N. Yamaguchi, “Influence of Morphological Factors on Tensile Properties in the Pre-yield Region of Isotactic Polypropylenes”, en, *Polymer Journal*, vol. 38, no. 2, pp. 122–131, Feb. 2006, ISSN: 0032-3896, 1349-0540. DOI: 10.1295/polymj.38.122. [Online]. Available: https://www.nature.com/doifinder/10.1295/polymj.38.122 (visited on 11/15/2023).

[61] A. Menyhard, P. Suba, Z. Laszlo, *et al.*, “Direct correlation between modulus and the crystalline structure in isotactic polypropylene”, en, *Express Polymer Letters*, vol. 9, no. 3, pp. 308–320, 2015, ISSN: 1788618X. DOI: `10.3144/expresspolymlett.2015.28`. [Online]. Available: `http://www.expresspolymlett.com/letolt.php?file=EPL-0005840&mi=c` (visited on 05/03/2024).

[62] T. B. Van Erp, D. Cavallo, G. W. M. Peters, and L. E. Govaert, “Rate-, temperature-, and structure-dependent yield kinetics of isotactic polypropylene”, en, *Journal of Polymer Science Part B: Polymer Physics*, vol. 50, no. 20, pp. 1438–1451, Oct. 2012, ISSN: 0887-6266, 1099-0488. DOI: `10.1002/polb.23150`. [Online]. Available: `https://onlinelibrary.wiley.com/doi/10.1002/polb.23150` (visited on 11/21/2023).

[63] B. Xiong et al., “Amorphous Phase Modulus and Micro–Macro Scale Relationship in Polyethylene via in Situ SAXS and WAXS”, *Macromolecules*, vol. 48, no. 15, pp. 5267–5275, 2015. DOI: `https://doi.org/10.1021/acs.macromol.5b00181`.

[64] T. Kida and M. Yamaguchi, “Role of Rigid–Amorphous chains on mechanical properties of polypropylene solid using DSC, WAXD, SAXS, and Raman spectroscopy”, en, *Polymer*, vol. 249, p. 124 834, May 2022, ISSN: 00323861. DOI: `10.1016/j.polymer.2022.124834`. [Online]. Available: `https://linkinghub.elsevier.com/retrieve/pii/S0032386122003214` (visited on 11/09/2023).

[65] M. Polińska et al, “The Modulus of the Amorphous Phase of Semicrystalline Polymers”, *Macromolecules*, vol. 54, no. 19, pp. 9113–9123, 2021. DOI: `10.1021/acs.macromol.1c01576`.

[66] M. Polińska et al, “Elastic modulus of the amorphous phase confined between lamellae: The role of crystalline component”, *Polymer*, vol. 269, 2023.

[67] G. R. Mitchell and A. Tojeira, Eds., *Controlling the Morphology of Polymers*, en. Cham: Springer International Publishing, 2016, ISBN: 978-3-319-39320-9 978-3-319-39322-3. DOI: `10.1007/978-3-319-39322-3`. [Online]. Available: `http://link.springer.com/10.1007/978-3-319-39322-3` (visited on 10/06/2023).

[68] S. Humbert, O. Lame, and G. Vigier, “Polyethylene yielding behaviour: What is behind the correlation between yield stress and crystallinity?”, en, *Polymer*, vol. 50, no. 15, pp. 3755–3761, Jul. 2009, ISSN: 00323861. DOI: `10.1016/j.polymer.2009.05.017`. [Online]. Available: `https://linkinghub.elsevier.com/retrieve/pii/S0032386109004182` (visited on 10/26/2023).

[69] N. Alberola, M. Fugier, D. Petit, and B. Fillon, “Microstructure of quenched and annealed films of isotactic polypropylene: Part I”, en, *Journal of Materials Science*, vol. 30, no. 5, pp. 1187–1195, Mar. 1995, ISSN: 0022-2461, 1573-4803. DOI: `10.1007/BF00356118`. [Online]. Available: `http://link.springer.com/10.1007/BF00356118` (visited on 10/24/2023).

[70] A. Rozanski and A. Galeski, “Plastic yielding of semicrystalline polymers affected by amorphous phase”, en, *International Journal of Plasticity*, vol. 41, pp. 14–29, Feb. 2013, ISSN: 07496419. DOI: `10.1016/j.ijplas.2012.07.008`. [Online]. Available: `https://linkinghub.elsevier.com/retrieve/pii/S0749641912001179` (visited on 12/10/2023).

[71] C. Jourdan, J. Y. Cavaille, and J. Perez, “Mechanical relaxations in polypropylene: A new experimental and theoretical approach”, en, *Journal of Polymer Science Part B: Polymer Physics*, vol. 27, no. 11, pp. 2361–2384, Oct. 1989, ISSN: 08876266, 10990488. DOI: `10.1002/polb.1989.090271115`. [Online]. Available: `https://onlinelibrary.wiley.com/doi/10.1002/polb.1989.090271115` (visited on 10/11/2023).

[72] N. Brown and I. M. Ward, “The influence of morphology and molecular weight on ductile-brittle transitions in linear polyethylene”, en, *Journal of Materials Science*, vol. 18, no. 5, pp. 1405–1420, May 1983, ISSN: 0022-2461, 1573-4803. DOI: `10.1007/BF01111960`. [Online]. Available: `http://link.springer.com/10.1007/BF01111960` (visited on 10/16/2023).

[73] Y. .-. Huang and N. Brown, “The effect of molecular weight on slow crack growth in linear polyethylene homopolymers”, en, *Journal of Materials Science*, vol. 23, no. 10, pp. 3648–3655, Oct. 1988, ISSN: 0022-2461, 1573-4803. DOI: `10.1007/BF00540508`. [Online]. Available: `http://link.springer.com/10.1007/BF00540508` (visited on 10/16/2023).

[74] J. Yeh and J. Runt, “Fatigue crack propagation in high-density polyethylene”, *Journal of Polymer Science, Part B: Polymer Physics*, vol. 29, no. 3, pp. 371–388, 1991. DOI: `10.1002/polb.1991.090290313`.

[75] H. Beerbaum and W. Grellmann, “The influence of morphology and structure on the crack growth of linear polyethylene”, *European Structural Integrity Society*, vol. 27, pp. 163–174, 2000. DOI: `https://doi.org/10.1016/S1566-1369(00)80016-3`.

[76] W. Krigbaum, R.-J. Roe, and K. Smith, “A theoretical treatment of the modulus of semi-crystalline polymers”, *Polymer*, vol. 5, pp. 533–542, 1964. DOI: `https://doi.org/10.1016/0032-3861(64)90202-2`.

[77] R. Seguela, “Critical review of the molecular topology of semicrystalline polymers: The origin and assessment of intercrystalline tie molecules and chain entanglements”, en, *Journal of Polymer Science Part B: Polymer Physics*, vol. 43, no. 14, pp. 1729–1748, Jul. 2005, ISSN: 0887-6266, 1099-0488. DOI: 10.1002/polb.20414. [Online]. Available: https://onlinelibrary.wiley.com/doi/10.1002/polb.20414 (visited on 10/16/2023).

[78] J. Lefebvre and B. Escaig, “The role of molecular mobility in the yielding of solid polymers”, en, *Polymer*, vol. 34, no. 3, pp. 518–527, 1993, ISSN: 00323861. DOI: 10.1016/0032-3861(93)90544-K. [Online]. Available: https://linkinghub.elsevier.com/retrieve/pii/003238619390544K (visited on 11/16/2023).

[79] R. Séguéla, “Dislocation approach to the plastic deformation of semicrystalline polymers: Kinetic aspects for polyethylene and polypropylene*”, en, *Journal of Polymer Science Part B: Polymer Physics*, vol. 40, no. 6, pp. 593–601, Mar. 2002, ISSN: 0887-6266, 1099-0488. DOI: 10.1002/polb.10118. [Online]. Available: https://onlinelibrary.wiley.com/doi/10.1002/polb.10118 (visited on 11/15/2023).

[80] J. Roetling, “Yield stress behaviour of isotactic polypropylene”, en, *Polymer*, vol. 7, no. 7, pp. 303–306, Jul. 1966, ISSN: 00323861. DOI: 10.1016/0032-3861(66)90025-5. [Online]. Available: https://linkinghub.elsevier.com/retrieve/pii/0032386166900255 (visited on 11/21/2023).

[81] E. Suljovrujic, S. Trifunovic, and D. Milicevic, “The influence of gamma radiation on the dielectric relaxation behaviour of isotactic polypropylene: The relaxation”, en, *Polymer Degradation and Stability*, vol. 95, no. 2, pp. 164–171, Feb. 2010, ISSN: 01413910. DOI: 10.1016/j.polymdegradstab.2009.11.034. [Online]. Available: https://linkinghub.elsevier.com/retrieve/pii/S014139100900384X (visited on 11/09/2023).

[82] N. Olivares and P. Tiemblo, “Physicochemical processes along the early stages of the thermal degradation of isotactic polypropylene I. Evolution of the g relaxation under oxidative conditions”, en, *Polymer Degradation and Stability*, 1999.

[83] M. Hoyos, P. Tiemblo, and J. M. Gómez-Elvira, “The role of microstructure, molar mass and morphology on local relaxations in isotactic polypropylene. The relaxation”, en, *Polymer*, vol. 48, no. 1, pp. 183–194, Jan. 2007, ISSN: 00323861. DOI: 10.1016/j.polymer.2006.11.034. [Online]. Available: https://linkinghub.elsevier.com/retrieve/pii/S0032386106012894 (visited on 10/06/2023).

[84] P. Tiemblo, J. M. Gómez-Elvira, S. G. Beltrán, L. Matisova-Rychla, and J. Rychly, “Melting and Relaxation Effects on the Kinetics of Polypropylene Thermooxidation in the Range 80170 °C”, en, *Macromolecules*, vol. 35, no. 15, pp. 5922–5926, Jul. 2002, ISSN: 0024-9297, 1520-5835. DOI: 10.1021/ma0119373. [Online]. Available: https://pubs.acs.org/doi/10.1021/ma0119373 (visited on 11/07/2023).

[85] J. Arranz-Andrés, B. Peña, R. Benavente, E. Pérez, and M. Cerrada, “Influence of isotacticity and molecular weight on the properties of metallocenic isotactic polypropylene”, en, *European Polymer Journal*, vol. 43, no. 6, pp. 2357–2370, Jun. 2007, ISSN: 00143057. DOI: 10.1016/j.eurpolymj.2007.03.034. [Online]. Available: https://linkinghub.elsevier.com/retrieve/pii/S0014305707001887 (visited on 02/14/2024).

[86] T. Umemura, T. Suzuki, and T. Kashiwazaki, “Impurity effect of the dielectric properties of isotactic polypropylene”, *IEEE Transactions on Electrical Insulation*, vol. EI-17, no. 4, 1982. DOI: https://doi.org/10.1109/TEI.1982.298498.

[87] M. Hoyos, P. Tiemblo, and J. M. Gómez-Elvira, “Influence of microstructure and semi-crystalline morphology on the and mechanical relaxations of the metallocene isotactic polypropylene”, en, *European Polymer Journal*, vol. 45, no. 4, pp. 1322–1327, Apr. 2009, ISSN: 00143057. DOI: 10.1016/j.eurpolymj.2009.01.018. [Online]. Available: https://linkinghub.elsevier.com/retrieve/pii/S0014305709000111 (visited on 11/09/2023).

[88] J. Eichelter, H. Wilhelm, A. Eder, A. Mautner, and A. Bismarck, “Influence of the -relaxation on the high-velocity stretchability of isotactic polypropylene”, en, *Polymer*, vol. 200, p. 122 593, Jun. 2020, ISSN: 00323861. DOI: 10.1016/j.polymer.2020.122593. [Online]. Available: https://linkinghub.elsevier.com/retrieve/pii/S0032386120304249 (visited on 11/09/2023).

[89] B. Read, “Mechanical relaxation in isotactic polypropylene”, en, *Polymer*, vol. 30, no. 8, pp. 1439–1445, Aug. 1989, ISSN: 00323861. DOI: 10.1016/0032-3861(89)90213-9. [Online]. Available: https://linkinghub.elsevier.com/retrieve/pii/0032386189902139 (visited on 11/09/2023).

[90] N. G. McCrum, “The kinetics of the alpha and beta relaxations in isotactic polypropylene”, en,

[91] E. Passaglia and G. M. Martin, “Dependence of mechanical relaxation on morphology in isotactic polypropylene”, en, *Journal of Research of the National Bureau of Standards Section A: Physics and Chemistry*, vol. 68A, no. 5, p. 519, Sep. 1964, ISSN: 0022-4332. DOI: 10.6028/jres.068A.049. [Online]. Available: https://nvlpubs.nist.gov/nistpubs/jres/68A/jresv68An5p519_A1b.pdf (visited on 11/09/2023).

[92] M. Pluta and M. Kryszewski, “Studies of relaxation process in spherulitic and nonspherulitic samples of isotactic polypropylene with different molecular ordering”, en, *Acta Polymerica*, vol. 38, no. 1, pp. 42–52, Jan. 1987, ISSN: 0323-7648, 1521-4044. DOI: `10.1002/actp.1987.010380110`. [Online]. Available: `https://onlinelibrary.wiley.com/doi/10.1002/actp.1987.010380110` (visited on 01/04/2024).

[93] M. Mansfield and R. H. Boyd, “Molecular motions, the relaxation, and chain transport in polyethylene crystals”, *Journal of Polymer Science: Polymer Physics Edition*, vol. 16, no. 7, 1978. DOI: `https://doi.org/10.1002/pol.1978.180160707`.

[94] M. Hoyos, P. Tiemblo, J. M. Gómez-Elvira, L. Rychlá, and J. Rychlý, “Role of the interphase dynamics in the induction time of the thermo-oxidation of isotactic polypropylene”, en, *Polymer Degradation and Stability*, vol. 91, no. 7, pp. 1433–1442, Jul. 2006, ISSN: 01413910. DOI: `10.1016/j.polymdegradstab.2005.10.013`. [Online]. Available: `https://linkinghub.elsevier.com/retrieve/pii/S0141391005004787` (visited on 11/07/2023).

[95] A. Esposito, “From a Three-Phase Model to a Continuous Description of Molecular Mobility in Semicrystalline Poly(Hydroxybutyrate- \emphCo -Hydroxyvalerate)”, 2016. DOI: `10.1021/acs.macromol.6b00384`. [Online]. Available: `https://hal.science/hal-01954226`.

[96] J.-C. Bauwens, “Physique des hauts polymères - Cours ULB”, in 1990.

[97] S. Hellinckx, “Mechanical behaviour of isotactic polypropylenes in the lower and the upper glass transitions ranges”, en, *Colloid & Polymer Science*, vol. 275, no. 2, pp. 116–123, Feb. 1997, ISSN: 0303-402X, 1435-1536. DOI: `10.1007/s003960050060`. [Online]. Available: `http://link.springer.com/10.1007/s003960050060` (visited on 10/05/2023).

[98] H. Eyring, “Viscosity, Plasticity, and Diffusion as Examples of Absolute Reaction Rates”, en, *The Journal of Chemical Physics*, vol. 4, no. 4, pp. 283–291, Apr. 1936, ISSN: 0021-9606, 1089-7690. DOI: `10.1063/1.1749836`. [Online]. Available: `https://pubs.aip.org/jcp/article/4/4/283/207491/Viscosity-Plasticity-and-Diffusion-as-Examples-of` (visited on 10/24/2023).

[99] T. Ree and H. Eyring, “Theory of Non-Newtonian Flow. I. Solid Plastic System”, en, *Journal of Applied Physics*, vol. 26, no. 7, pp. 793–800, Jul. 1955, ISSN: 0021-8979, 1089-7550. DOI: `10.1063/1.1722098`. [Online]. Available: `https://pubs.aip.org/jap/article/26/7/793/161003/Theory-of-Non-Newtonian-Flow-I-Solid-Plastic` (visited on 10/24/2023).

[100] S. Hellinckx and J. .-. Bauwens, “The yield behavior of PVDF and the deformation process at high temperature”, en, *Colloid & Polymer Science*, vol. 273, no. 3, pp. 219–226, Mar. 1995, ISSN: 0303-402X, 1435-1536. DOI: `10.1007/BF00657827`. [Online]. Available: `http://link.springer.com/10.1007/BF00657827` (visited on 10/19/2023).

[101] J.-C. Bauwens, “Relation between the compression yield stress of poly(vinyl chloride) and the loss peak in the -transition range”, en, *Journal of Polymer Science Part C: Polymer Symposia*, vol. 33, no. 1, pp. 123–133, Jan. 1971, ISSN: 0449-2994, 1935-3065. DOI: `10.1002/polc.5070330112`. [Online]. Available: `https://onlinelibrary.wiley.com/doi/10.1002/polc.5070330112` (visited on 11/15/2023).

[102] J. D. Ferry and H. S. Myers, “Viscoelastic Properties of Polymers”, *Journal of The Electrochemical Society*, vol. 108, no. 7, p. 142C, Jul. 1961, Publisher: The Electrochemical Society, Inc. DOI: `10.1149/1.2428174`. [Online]. Available: `https://dx.doi.org/10.1149/1.2428174`.

[103] V. Dorléans, R. Delille, D. Notta-Cuvier, F. Lauro, and E. Michau, “Time-temperature superposition in viscoelasticity and viscoplasticity for thermoplastics”, en, *Polymer Testing*, vol. 101, p. 107 287, Sep. 2021, ISSN: 01429418. DOI: `10.1016/j.polymertesting.2021.107287`. [Online]. Available: `https://linkinghub.elsevier.com/retrieve/pii/S0142941821002361` (visited on 10/11/2023).

[104] T. Kajiyama, T. Okada, A. Sakoda, and M. Takayanagi, “Analysis of the -relaxation process of bulk crystallized polyethylene based on that of single crystal mat”, en, *Journal of Macromolecular Science, Part B*, vol. 7, no. 3, pp. 583–608, Apr. 1973, ISSN: 0022-2348, 1525-609X. DOI: `10.1080/00222347308207887`. [Online]. Available: `https://www.tandfonline.com/doi/full/10.1080/00222347308207887` (visited on 10/11/2023).

[105] U. Kessner, J. Kaschta, F. J. Stadler, C. S. Le Duff, X. Drooghaag, and H. Münstedt, “Thermorheological Behavior of Various Short- and Long-Chain Branched Polyethylenes and Their Correlations with the Molecular Structure”, en, *Macromolecules*, vol. 43, no. 17, pp. 7341–7350, Sep. 2010, ISSN: 0024-9297, 1520-5835. DOI: `10.1021/ma100705f`. [Online]. Available: `https://pubs.acs.org/doi/10.1021/ma100705f` (visited on 10/11/2023).

[106] B. Wunderlich, “Effect of Decoupling of Molecular Segments, Microscopic Stress-Transfer and Confinement of the Nanophases in Semicrystalline Polymers”, en, *Macromolecular Rapid Communications*, vol. 26, no. 19, pp. 1521–1531, Oct. 2005, ISSN: 1022-1336, 1521-3927. DOI: `10.1002/marc.200500488`. [Online]. Available: `https://onlinelibrary.wiley.com/doi/10.1002/marc.200500488` (visited on 10/27/2023).

[107] B. Wunderlich, “Thermodynamic description of condensed phases”, en, *Journal of Thermal Analysis and Calorimetry*, vol. 102, no. 2, pp. 413–424, Nov. 2010, ISSN: 1388-6150, 1572-8943. DOI: `10.1007/s10973-010-0874-x`. [Online]. Available: `http://link.springer.com/10.1007/s10973-010-0874-x` (visited on 10/30/2023).

[108] B. Wunderlich, “Reversible crystallization and the rigid–amorphous phase in semicrystalline macromolecules”, en, *Progress in Polymer Science*, vol. 28, no. 3, pp. 383–450, Mar. 2003, ISSN: 00796700. DOI: `10.1016/S0079-6700(02)00085-0`. [Online]. Available: `https://linkinghub.elsevier.com/retrieve/pii/S0079670002000850` (visited on 10/27/2023).

[109] Q. Zia, R. Androsch, H.-J. Radusch, and S. Piccarolo, “Morphology, reorganization and stability of mesomorphic nanocrystals in isotactic polypropylene”, en, *Polymer*, vol. 47, no. 24, pp. 8163–8172, Nov. 2006, ISSN: 00323861. DOI: `10.1016/j.polymer.2006.09.038`. [Online]. Available: `https://linkinghub.elsevier.com/retrieve/pii/S0032386106011049` (visited on 10/27/2023).

[110] Y. Lu, D. Lyu, B. Xiong, R. Chen, and Y. Men, “Inter-fibrillar tie chains determined critical stress of large strain cavitation in tensile stretched isotactic polypropylene”, en, *Polymer*, vol. 138, pp. 387–395, Feb. 2018, ISSN: 00323861. DOI: `10.1016/j.polymer.2018.01.076`. [Online]. Available: `https://linkinghub.elsevier.com/retrieve/pii/S0032386118301022` (visited on 05/07/2024).

[111] C. Y. Li, “The rise of semicrystalline polymers and why are they still interesting”, en, *Polymer*, vol. 211, p. 123 150, Dec. 2020, ISSN: 00323861. DOI: `10.1016/j.polymer.2020.123150`. [Online]. Available: `https://linkinghub.elsevier.com/retrieve/pii/S0032386120309757` (visited on 05/06/2024).

[112] M. Gahleitner and J.R. Severn, “Designing Polymer Properties”, en, 2008, Publisher: Unpublished. DOI: `10.13140/2.1.1345.0248`. [Online]. Available: `http://rgdoi.net/10.13140/2.1.1345.0248` (visited on 10/06/2023).

[113] W. EN, *Polypropylene*. [Online]. Available: `https://en.wikipedia.org/wiki/Polypropylene`.

[114] G. Natta and P. Corradini, “Structure and Properties of Isotactic Polypropylene”, *Supplemento al volume XV, Serie X del nuovo cimento*, 1960.

[115] V. Busico and R. Cipullo, “Microstructure of polypropylene”, en, *Progress in Polymer Science*, vol. 26, no. 3, pp. 443–533, Apr. 2001, ISSN: 00796700. DOI: `10.1016/S0079-6700(00)00046-0`. [Online]. Available: `https://linkinghub.elsevier.com/retrieve/pii/S0079670000000460` (visited on 11/05/2023).

[116] D. L. VanderHart, R. G. Alamo, M. R. Nyden, M.-H. Kim, and L. Mandelkern, “Observation of Resonances Associated with Stereo and Regio Defects in the Crystalline Regions of Isotactic Polypropylene: Toward a Determination of Morphological Partitioning”, en, *Macromolecules*, vol. 33, no. 16, pp. 6078–6093, Aug. 2000, ISSN: 0024-9297, 1520-5835. DOI: `10.1021/ma992041p`. [Online]. Available: `https://pubs.acs.org/doi/10.1021/ma992041p` (visited on 10/09/2023).

[117] E. B. Bond, J. E. Spruiell, and J. S. Lin, “A WAXD/SAXS/DSC study on the melting behavior of Ziegler-Natta and metallocene catalyzed isotactic polypropylene”, en, *Journal of Polymer Science Part B: Polymer Physics*, vol. 37, no. 21, pp. 3050–3064, Nov. 1999, ISSN: 0887-6266, 1099-0488. DOI: `10.1002/(SICI)1099-0488(19991101)37:21<3050::AID-POLB14>3.0.CO;2-L`. [Online]. Available: `https://onlinelibrary.wiley.com/doi/10.1002/(SICI)1099-0488(19991101)37:21%3C3050::AID-POLB14%3E3.0.CO;2-L` (visited on 10/09/2023).

[118] I. C. Sanchez and R. Eby, “Thermodynamics and Crystallization of Random Copolymers”, [Online]. Available: `https://doi.org/10.1021/ma60047a012`.

[119] W. Hu, “The physics of polymer chain-folding”, en, *Physics Reports*, vol. 747, pp. 1–50, Jul. 2018, ISSN: 03701573. DOI: `10.1016/j.physrep.2018.04.004`. [Online]. Available: `https://linkinghub.elsevier.com/retrieve/pii/S0370157318301042` (visited on 05/06/2024).

[120] S. Bruckner, S. V. Meille, and I. Vittoriopetraccone, “POLYMORPHISM IN ISOTACTIC POLYPROPYLENE”, en,

[121] D. Mileva, R. Androsch, E. Zhuravlev, C. Schick, and B. Wunderlich, “Formation and Reorganization of the Mesophase of Isotactic Polypropylene”, en, *Molecular Crystals and Liquid Crystals*, vol. 556, no. 1, pp. 74–83, May 2012, ISSN: 1542-1406, 1563-5287. DOI: `10.1080/15421406.2012.635912`. [Online]. Available: `http://www.tandfonline.com/doi/abs/10.1080/15421406.2012.635912` (visited on 11/01/2023).

[122] B. Wunderlich and J. Grebowicz, “Thermotropic mesophases and mesophase transitions of linear, flexible macromolecules”, en, in *Liquid Crystal Polymers II/III*, H.-J. Cantow, G. Dall’Asta, K. Dušek, *et al.*, Eds., vol. 60/61, Series Title: Advances in Polymer Science, Berlin, Heidelberg: Springer Berlin Heidelberg, 1984, pp. 1–59, ISBN: 978-3-540-12994-3 978-3-540-38816-6. DOI: 10.1007/3-540-12994-4_1. [Online]. Available: http://link.springer.com/10.1007/3-540-12994-4_1 (visited on 10/30/2023).

[123] V. Vittoria and A. Perullo, “Effect of quenching temperature on the structure of isotactic polypropylene films”, en, *Journal of Macromolecular Science, Part B*, vol. 25, no. 3, pp. 267–281, Sep. 1986, ISSN: 0022-2348, 1525-609X. DOI: 10.1080/00222348608248040. [Online]. Available: https://www.tandfonline.com/doi/full/10.1080/00222348608248040 (visited on 10/25/2023).

[124] W. Rungswang, C. Jarumaneeroj, S. Patthamasang, *et al.*, “Influences of tacticity and molecular weight on crystallization kinetic and crystal morphology under isothermal crystallization: Evidence of tapering in lamellar width”, en, *Polymer*, vol. 172, pp. 41–51, May 2019, ISSN: 00323861. DOI: 10.1016/j.polymer.2019.03.052. [Online]. Available: https://linkinghub.elsevier.com/retrieve/pii/S0032386119302769 (visited on 11/01/2023).

[125] M. Iijima and G. Ströbl, “Isothermal Crystallization and Melting of Isotactic Polypropylene analyzed by Time- and temperature-dependent small-angle X-ray scattering experiments”, *Macromolecules*, vol. 33, p. 5204, 2000.

[126] R. Alamo, G. Brown, L. Mandelkern, A. Lehtinen, and R. Paukkeri, “A morphological study of a highly structurally regular isotactic poly(propylene) fraction”, en, *Polymer*, vol. 40, no. 14, pp. 3933–3944, Jun. 1999, ISSN: 00323861. DOI: 10.1016/S0032-3861(98)00613-2. [Online]. Available: https://linkinghub.elsevier.com/retrieve/pii/S0032386198006132 (visited on 11/10/2023).

[127] G. Strobl, “Crystallization and melting of bulk polymers: New observations, conclusions and a thermodynamic scheme”, en, *Progress in Polymer Science*, vol. 31, no. 4, pp. 398–442, Apr. 2006, ISSN: 00796700. DOI: 10.1016/j.progpolymsci.2006.01.001. [Online]. Available: https://linkinghub.elsevier.com/retrieve/pii/S0079670006000104 (visited on 05/08/2024).

[128] K. Yamada, S. Matsumoto, K. Tagashira, and M. Hikosaka, “Isotacticity dependence of spherulitic morphology of isotactic polypropylene”, en, *Polymer*, vol. 39, no. 22, pp. 5327–5333, Oct. 1998, ISSN: 00323861. DOI: 10.1016/S0032-3861(97)10208-7. [Online]. Available: https://linkinghub.elsevier.com/retrieve/pii/S0032386197102087 (visited on 11/10/2023).

[129] V. Vittoria, “Effect of annealing on the structure of quenched isotactic polypropylene”, en, *Journal of Macromolecular Science, Part B*, vol. 28, no. 3-4, pp. 489–502, Sep. 1989, ISSN: 0022-2348, 1525-609X. DOI: 10.1080/00222348908215238. [Online]. Available: https://www.tandfonline.com/doi/full/10.1080/00222348908215238 (visited on 10/25/2023).

[130] R. Natale, R. Russo, and V. Vittoria, “Crystallinity of isotactic polypropylene films annealed from the quenched state”, en, *Journal of Materials Science*, vol. 27, no. 16, pp. 4350–4354, Aug. 1992, ISSN: 0022-2461, 1573-4803. DOI: 10.1007/BF00541565. [Online]. Available: http://link.springer.com/10.1007/BF00541565 (visited on 10/25/2023).

[131] J. Zhao, J. Qiu, Y. Niu, and Z. Wang, “Evolutions of morphology and crystalline ordering upon annealing of quenched isotactic polypropylene”, en, *Journal of Polymer Science Part B: Polymer Physics*, vol. 47, no. 17, pp. 1703–1712, Sep. 2009, ISSN: 0887-6266, 1099-0488. DOI: 10.1002/polb.21773. [Online]. Available: https://onlinelibrary.wiley.com/doi/10.1002/polb.21773 (visited on 11/01/2023).

[132] Z. Bartczak, “Evaluation of effective density of the molecular network and concentration of the stress transmitters in amorphous layers of semicrystalline polyethylene”, en, *Polymer Testing*, vol. 68, pp. 261–269, Jul. 2018, ISSN: 01429418. DOI: 10.1016/j.polymertesting.2018.04.027. [Online]. Available: https://linkinghub.elsevier.com/retrieve/pii/S0142941818304197 (visited on 05/07/2024).

[133] F. Nilsson, X. Lan, T. Gkourmpis, M. Hedenqvist, and U. Gedde, “Modelling tie chains and trapped entanglements in polyethylene”, en, *Polymer*, vol. 53, no. 16, pp. 3594–3601, Jul. 2012, ISSN: 00323861. DOI: 10.1016/j.polymer.2012.05.045. [Online]. Available: https://linkinghub.elsevier.com/retrieve/pii/S0032386112004594 (visited on 10/16/2023).

[134] S. Nikolov and I. Doghri, “A micro/macro constitutive model for the small-deformation behavior of polyethylene”, en, *Polymer*, vol. 41, no. 5, pp. 1883–1891, Mar. 2000, ISSN: 00323861. DOI: 10.1016/S0032-3861(99)00330-4. [Online]. Available: https://linkinghub.elsevier.com/retrieve/pii/S0032386199003304 (visited on 05/07/2024).

[135] Q. Zia, D. Mileva, and R. Androsch, “Rigid Amorphous Fraction in Isotactic Polypropylene”, en, *Macromolecules*, vol. 41, no. 21, pp. 8095–8102, Nov. 2008, ISSN: 0024-9297, 1520-5835. DOI: 10.1021/ma801455m. [Online]. Available: https://pubs.acs.org/doi/10.1021/ma801455m (visited on 10/27/2023).

[136] A. B. Mathur and G. Mathur, “Thermo-oxidative degradation of isotactic polypropylene film: Structural changes and its correlation with properties”, en, *Polymer*, vol. 23, no. 1, pp. 54–56, Jan. 1982, ISSN: 00323861. DOI: 10.1016/0032-3861(82)90014-3. [Online]. Available: https://linkinghub.elsevier.com/retrieve/pii/0032386182900143 (visited on 11/07/2023).

[137] M. Castejon, P. Tiemblo, and J. Gomez-Elvira, “Photo-oxidation of thick isotactic polypropylene films - part II”, *Polymer Degradation and Stability*, vol. 71, pp. 99–111, 2001.

[138] J. Guisández, P. Tiemblo, and J. Gómez-Elvira, “Change of thermal and dynamic-mechanical behaviour of a metallocene isotactic polypropylene during low-temperature thermo-oxidation”, en, *Polymer Degradation and Stability*, vol. 87, no. 3, pp. 543–553, Mar. 2005. DOI: 10.1016/j.polymdegradstab.2004.10.014. [Online]. Available: https://linkinghub.elsevier.com/retrieve/pii/S0141391004003635 (visited on 11/07/2023).

[139] B. Fayolle, E. Richaud, X. Colin, and J. Verdu, “Review: Degradation-induced embrittlement in semicrystalline polymers having their amorphous phase in rubbery state”, en, *Journal of Materials Science*, vol. 43, no. 22, pp. 6999–7012, Nov. 2008, ISSN: 0022-2461, 1573-4803. DOI: 10.1007/s10853-008-3005-3. [Online]. Available: https://link.springer.com/10.1007/s10853-008-3005-3 (visited on 11/07/2023).

[140] M. Hoyos, P. Tiemblo, and J. M. Gómez-Elvira, “Effect of microstructure on the thermo-oxidation of solid isotactic polypropylene-based polyolefins”, en, *Science and Technology of Advanced Materials*, vol. 9, no. 2, p. 024 404, Apr. 2008, ISSN: 1468-6996, 1878-5514. DOI: 10.1088/1468-6996/9/2/024404. [Online]. Available: http://www.tandfonline.com/doi/full/10.1088/1468-6996/9/2/024404 (visited on 11/07/2023).

[141] P. Tiemblo, J. Manuel Gómez-Elvira, G. Teyssedre, F. Massines, and C. Laurent, “Chemiluminescence spectral evolution along the thermal oxidation of isotactic polypropylene”, en, *Polymer Degradation and Stability*, vol. 65, no. 1, pp. 113–121, Jul. 1999, ISSN: 01413910. DOI: 10.1016/S0141-3910(98)00226-2. [Online]. Available: https://linkinghub.elsevier.com/retrieve/pii/S0141391098002262 (visited on 11/07/2023).

[142] M. Castejon, P. Tiemblo, and J. Gomez-Elvira, “Photo-oxidation of thick isotactic polypropylene films - part I”, *Polymer Degradation and Stability*, vol. 70, pp. 357–364, 2000.

[143] R. F. Saraf and R. S. Porter, “Deformation of semicrystalline polymers via crystal–crystal phase transition”, en, *Journal of Polymer Science Part B: Polymer Physics*, vol. 26, no. 5, pp. 1049–1057, May 1988, ISSN: 0887-6266, 1099-0488. DOI: 10.1002/polb.1988.090260509. [Online]. Available: https://onlinelibrary.wiley.com/doi/10.1002/polb.1988.090260509 (visited on 10/24/2023).

[144] R. F. Saraf and R. S. Porter, “A deformation induced order-disorder transition in isotactic polypropylene”, en, *Polymer Engineering & Science*, vol. 28, no. 13, pp. 842–851, Jul. 1988, ISSN: 0032-3888, 1548-2634. DOI: 10.1002/pen.760281304. [Online]. Available: https://4spepublications.onlinelibrary.wiley.com/doi/10.1002/pen.760281304 (visited on 10/24/2023).

[145] J. Grebowicz, S.-F. Lau, and B. Wunderlich, “The thermal properties of polypropylene”, en, *Journal of Polymer Science: Polymer Symposia*, vol. 71, no. 1, pp. 19–37, Jan. 1984, ISSN: 0360-8905, 1936-0959. DOI: 10.1002/polc.5070710106. [Online]. Available: https://onlinelibrary.wiley.com/doi/10.1002/polc.5070710106 (visited on 10/27/2023).

[146] M. Naiki, T. Kikkawa, Y. Endo, K. Nozaki, T. Yamamoto, and T. Hara, “Crystal ordering of a phase isotactic polypropylene”, en, 2000.

[147] K. Nozaki, Y. Endo, T. Yamamoto, and M. Naiki, “Crystallization of and Phases in Isotactic Polypropylene with Low Ethylene Content: Isothermal Crystallization and Secondary Crystallization”, en, *Journal of Macromolecular Science, Part B*, vol. 42, no. 3-4, pp. 697–707, Jan. 2003, ISSN: 0022-2348, 1525-609X. DOI: 10.1081/MB-120021600. [Online]. Available: https://www.tandfonline.com/doi/full/10.1081/MB-120021600 (visited on 12/10/2023).

[148] A. Mollova, R. Androsch, D. Mileva, M. Gahleitner, and S. S. Funari, “Crystallization of isotactic polypropylene containing beta-phase nucleating agent at rapid cooling”, en, *European Polymer Journal*, vol. 49, no. 5, pp. 1057–1065, May 2013, ISSN: 00143057. DOI: 10.1016/j.eurpolymj.2013.01.015. [Online]. Available: https://linkinghub.elsevier.com/retrieve/pii/S0014305713000335 (visited on 12/10/2023).

[149] E. Andreassen, “Infrared and Raman spectroscopy of polypropylene”, en, in *Polypropylene*, J. Karger-Kocsis, Ed., vol. 2, Series Title: Polymer Science and Technology Series, Dordrecht: Springer Netherlands, 1999, pp. 320–328, ISBN: 978-94-010-5899-5 978-94-011-4421-6. DOI: 10.1007/978-94-011-4421-6_46. [Online]. Available: http://link.springer.com/10.1007/978-94-011-4421-6_46 (visited on 12/14/2023).

[150] F. Auriemma and C. De Rosa, “Crystallization of Metallocene-Made Isotactic Polypropylene: Disordered Modifications Intermediate between the and Forms”, en, *Macromolecules*, vol. 35, no. 24, pp. 9057–9068, Nov. 2002, ISSN: 0024-9297, 1520-5835. DOI: `10.1021/ma020648r`. [Online]. Available: `https://pubs.acs.org/doi/10.1021/ma020648r` (visited on 12/19/2023).

[151] J. C. Randall, “A ^{13} C NMR Determination of the Comonomer Sequence Distributions in Propylene-Butene-1 Copolymers”, en, *Macromolecules*, vol. 11, no. 3, pp. 592–597, May 1978, ISSN: 0024-9297, 1520-5835. DOI: `10.1021/ma60063a032`. [Online]. Available: `https://pubs.acs.org/doi/abs/10.1021/ma60063a032` (visited on 12/19/2023).

[152] P. Hao, V. Laheri, Z. Dai, and F. Gilabert, “A rate-dependent constitutive model predicting the double yield phenomenon, self-heating and thermal softening in semi-crystalline polymers”, en, *International Journal of Plasticity*, vol. 153, p. 103 233, Jun. 2022, ISSN: 07496419. DOI: `10.1016/j.ijplas.2022.103233`. [Online]. Available: `https://linkinghub.elsevier.com/retrieve/pii/S0749641922000201` (visited on 11/17/2023).

[153] M. I. Okereke and A. I. Akpoyomare, “Two-process constitutive model for semicrystalline polymers across a wide range of strain rates”, en, *Polymer*, vol. 183, p. 121 818, Nov. 2019, ISSN: 00323861. DOI: `10.1016/j.polymer.2019.121818`. [Online]. Available: `https://linkinghub.elsevier.com/retrieve/pii/S0032386119308249` (visited on 11/09/2023).

[154] L. S. G. et al, “Discovering and understanding materials through computation”, *Nature Materials*, May 2021. DOI: `https://doi.org/10.1038/s41563-021-01015-1`. [Online]. Available: `https://www.nature.com/articles/s41563-021-01015-1`.

[155] AMI2030, *Materials 2030 Roadmap*, 2022. [Online]. Available: `https://www.ami2030.eu/wp-content/uploads/2022/12/2022-12-09_Materials_2030_RoadMap_VF4.pdf`.

[156] EUMAT, *European Technology Platform for Advanced Engineering Materials and Technologies.* [Online]. Available: `https://www.eumat.eu/en/materials-modelling-and-characterization`.

[157] T. E. M. M. Council, *EMMC Roadmap - Materials modelling and digitalisation of the materials science*, https://zenodo.org/records/4272033, Nov. 2020. [Online]. Available: `https://emmc.eu/emmc-roadmaps/`.

[158] J.-C. Bauwens, “The strain rate and temperature dependence of yield of PC in tension, tensile creep and impact tests”, *Journal of Materials Science*, no. 9, p. 1197, 1974.

[159] P. Béguelin, “Approche expérimentale du comportement des polymères en sollicitation rapide - Béguelin-EPFL_1996”, Ph.D. dissertation, EPFL, 1996.

[160] Y. Wang, S. Chen, T. Wu, and Q. Fu, “Yielding behavior of isotactic polypropylene at elevated temperature understood at the spherulite level”, en, *Polymer*, vol. 281, p. 126 150, Jul. 2023, ISSN: 00323861. DOI: `10.1016/j.polymer.2023.126150`. [Online]. Available: `https://linkinghub.elsevier.com/retrieve/pii/S0032386123004809` (visited on 12/10/2023).

[161] V. Gaucher, *Comportement mécanique des thermoplastiques, polymères semi-cristallins et cristallisables. Bilan et faits marquants des 10 dernières années - UMET Lille*, Dec. 2019.

[162] R. Séguéla and F. Rietsch, “Double yield point in polyethylene under tensile loading”, *J.of Mat.Sc.Letters*, vol. 9, pp. 46–47, 1990.

[163] R. Séguéla, V. Gaucher-Miri, and S. Elkoun, “Plastic deformation of polyethylene and ethylene copolymers: Part II Heterogeneous crystal slip and strain-induced phase change”, *Journal of Material Science*, vol. 33, p. 1801, 1998. [Online]. Available: `https://link.springer.com/article/10.1023/A:1004340902180`.

[164] R. Séguéla, S. Elkoun, and V. Gaucher-Miri, “Plastic deformation of polyethylene and ethylene copolymers: Part I Homogeneous crystal slip and molecular mobility”, *Journal of Material Science*, vol. 33, p. 1273, 1998. [Online]. Available: `https://link.springer.com/article/10.1023/A:1004342113141`.

[165] T. Vu-Khanh and M. El Majdoubi, “Entropy change with yielding and fracture of polypropylene”, en, *Theoretical and Applied Fracture Mechanics*, vol. 51, no. 2, pp. 111–116, Apr. 2009, ISSN: 01678442. DOI: `10.1016/j.tafmec.2009.04.002`. [Online]. Available: `https://linkinghub.elsevier.com/retrieve/pii/S0167844209000238` (visited on 12/18/2023).

[166] J.-C. Bauwens, “Déformation plastique des hauts polymères vitreux soumis á un système de contraintes quelconque”, fr, *Journal of Polymer Science Part A-2: Polymer Physics*, vol. 5, no. 6, pp. 1145–1156, Nov. 1967, ISSN: 0449-2978, 1542-9377. DOI: `10.1002/pol.1967.160050612`. [Online]. Available: `https://onlinelibrary.wiley.com/doi/10.1002/pol.1967.160050612` (visited on 11/15/2023).

[167] O. Darras and R. Séguéla, “Tensile yield of polyethylene in relation to crystal thickness”, en, *Journal of Polymer Science Part B: Polymer Physics*, vol. 31, no. 7, pp. 759–766, Jun. 1993, ISSN: 0887-6266, 1099-0488. DOI: `10.1002/polb.1993.090310702`. [Online]. Available: `https://onlinelibrary.wiley.com/doi/10.1002/polb.1993.090310702` (visited on 11/16/2023).

[168] T. Gómez-del Río and J. Rodríguez, “Compression yielding of polypropylenes above glass transition temperature”, en, *European Polymer Journal*, vol. 46, no. 6, pp. 1244–1250, Jun. 2010, ISSN: 00143057. DOI: `10.1016/j.eurpolymj.2010.02.016`. [Online]. Available: `https://linkinghub.elsevier.com/retrieve/pii/S0014305710001126` (visited on 12/18/2023).

[169] S. Turner, *Mechanical Testing of Plastics*, ISBN: 0 7114 5785 9. [Online]. Available: `https://archive.org/details/mechanicaltestin0000turn`.